Searching for Dark Matter with the ATLAS and CTA Experiments

Ørjan Dale

Dissertation for the degree of philosophiae doctor (PhD)
at the University of Bergen

2016

Dissertation date: 23.06.2016

Acknowledgements

The completion of this thesis is owed to the help and influence of a great number of people, to whom I would like to express my gratitude. First and foremost, I would like to thank my supervisors, Heidi Sandaker and Anna Lipniacka, for their continued support, help and encouragement during the last few years. I am especially grateful for the freedom they have allowed me in my work, in particular during my stay in the US.

Most of my efforts as a PhD student has been within the ATLAS collaboration, where I have greatly benefitted from the vast expertise and know-how of my colleagues. I feel very privileged to have been able to participate and contribute to such an environment, and take part in a piece of HEP history that is the analysis of the first LHC data. I would like to thank all those involved in the ATLAS SUSY with taus working group, and in particular my fellow analysers, for excellent collaboration, their help and hard work, as well as for making the group a good place to work: Steffen Schaepe, Martin Schultens, Anthony Rose and Till Nattermann. A lot of the credit should go to Fabrizio Salvatore and Paul Jackson for expertly leading the group during these years. I would also like to thank Steve McMahon and Maiken Pedersen for their help with the SCT noise monitoring.

I have enjoyed the fruitful collaboration with members of the particle physics group in Bergen: Wolfgang Liebig, Therese Sjursen, Trygve Buanes, Bertrand Martin Dit Latour, Thomas Burgess and Alex Kastanas. Special mentions go to Alex Kastanas for making the summer of 2012 endurable, and Thomas Burgess for introducing me to both particle physics and some of the more obscure elements of pop culture.

Masahiro Morii, Christopher Rogan along with the rest of the LPPC group at Harvard were always very welcoming and including, making my time there both rewarding and fun. I would also like to take the opportunity to thank Fulbright Norway for making this stay possible, and for all their help in practical matters. A special thank you goes to Chris for sharing his extensive knowledge of physics, but also for his refreshing perspectives and, perhaps more importantly, knowing where to watch football at 9 am

in Cambridge. Also, a big thank you to Agnethe and Joe for sharing the Bostonian experience.

I have been fortunate to meet a lot of great people, both in Bergen and elsewhere, during my years in HEP. Although I will not go into names in fear of forgetting someone, it has truly been a pleasure sharing too much coffee, too long breaks, but just the right amount of beer with all of you. Despite the initial language barrier, and some disagreement when it comes to office lighting conditions, Jan Lindroos has been pretty much the perfect office mate, as well as a great friend. I would also like to thank the master crew and the Swede: Anders, Anders, Daniel and Siri.

Finally, I would like to thank my friends and family for providing perspective. My family has, despite my straying from the path of the humanities, always been supportive and taken a keen interest in what I have been up to, for which I am thankful. Hanne has also been of great help in making sure my commas are where they should be. Most of all, I would like to express my sincerest gratitude to Ingrid-Elisabeth for her patience and understanding, that have both undoubtedly been tested during the last years, and for enriching my life immensely.

Abstract

The existence of dark matter has been inferred by several experiments through measurements of its gravitational effects. However, dark matter has not been observed directly, meaning that we do not know what it is made of. Furthermore, the Standard Model of particle physics does not contain a viable dark matter candidate, making new physics beyond the Standard Model necessary to explain dark matter. One possible candidate for particle dark matter is Weakly Interacting Massive Particles (WIMPs). Supersymmetry is an extension of the Standard Model where WIMPs frequently arise. In this thesis two methods of searching for dark matter are investigated. One involves searching for the production of supersymmetric particles at the Large Hadron Collider (LHC), and the other searching for annihilation products of naturally occurring WIMPs with the planned experiment Cherenkov Telescope Array (CTA).

The main part of this thesis, Part II, is devoted to presenting two searches for supersymmetry using data collected by the ATLAS experiment at the LHC at CERN. In both analyses, supersymmetric events are searched for in final states containing jets, $E_{\mathrm{T}}^{\mathrm{miss}}$, and at least one τ lepton. The first search is performed using 4.7 fb^{-1} of data collected at a centre of mass energy of 7 TeV during 2011. The second search makes use of 20.3 fb^{-1} of data collected at a centre of mass energy of 8 TeV in 2012. As no excesses with respect to the Standard Model expectations are observed in either of the searches, upper limits on contributions from new physics are derived. The results are also interpreted in the context of different supersymmetric models, and exclusion limits are set on the model parameters.

In the last part of the thesis, Part III, the expected sensitivity of CTA to WIMP annihilations into monochromatic photon pairs in the Galactic Centre is evaluated. When comparing the projected sensitivity to results from current experimental facilities, it is found that CTA should provide more stringent exclusion limits across a wide range of WIMP masses than achieved by current experiments.

Contents

I Theoretical Background and Motivation 5

List of Figures

List of Tables

Chapter 1

Introduction

The model describing all known elementary particles and their interactions, the Standard Model of particle physics, was developed in the 1970s and has proved remarkably successful. Since its inception it has both accurately predicted new particles and phenomena, and survived increasingly accurate tests of its predictions in particle physics experiments. The most recent, and possibly greatest, triumph of the Standard Model was the 2012 discovery of the Higgs Boson, commonly lauded as the missing piece in the Standard Model jigsaw puzzle. All the particles predicted by the model had now been discovered, and the mechanism for incorporating particle mass in the model was accounted for.

Despite the triumphs of the Standard Model there is strong experimental evidence for the existence of physics phenomena that it does not describe. The perhaps most compelling piece of evidence comes from distance scales far removed from the microscopic distances of subatomic particles, namely the scales of galaxies and galaxy clusters, and the domains of astrophysics and cosmology. There, it has been shown that the universe consists of approximately five times as much of an unknown form of matter, called dark matter, compared to the ordinary, baryonic matter surrounding us every day. As the Standard Model does not provide an explanation for dark matter, we must look to new theories to explain it, while at the same time ensuring that the features of the Standard Model that have resulted in such an extraordinary agreement with particle physics experiments are preserved. The task of particle physics is then to determine the particle type, or types, constituting dark matter along with the model describing such new types of particles.

There are three principal approaches to pinpointing the nature of dark matter – direct detection experiments concerned with measuring collisions between naturally occurring dark matter particles and ordinary matter; indirect detection experiments aiming at measuring the decay or annihilation products of naturally occurring dark matter; and finally, collider experiments that aim to produce and study dark matter particles under laboratory conditions. In this thesis, examples of the two latter approaches will be investigated through analysis of data from the ATLAS experiment at the Large Hadron Collider (LHC) at CERN, along with a study of the expected sensitivity to dark matter signatures at the planned experiment named Cherenkov Telescope Array (CTA).

The main part of this thesis is concerned with one of the most studied extensions of the Standard Model, called supersymmetry. In addition to its many theoretically appealing features it, in many cases, gives rise to a dark matter candidate in the lightest supersymmetric particle (LSP). One of the primary goals of the LHC, and its accompanying experiments, has been to search for manifestations of such a new symmetry. A prominent detector signature expected in collisions where supersymmetric particles of high mass are created, is energetic jets produced as the initial supersymmetric particles decay. Furthermore, an observed transverse momentum imbalance ($E_{\mathrm{T}}^{\mathrm{miss}}$) in the collision is expected to arise from the LSP, and dark matter candidate, escaping detection. Depending on the specific supersymmetric theory, and the preferred decay of the supersymmetric particles, such collisions could also result in final states containing τ leptons.

During my PhD project period I have been one of the main analysers in the ATLAS SUSY with taus working group, where I have worked on the one τ analysis channel. There, I have been one of the principal responsible for all aspects of the analysis including general code development and data management, devising methods for background estimation, defining control regions and optimising signal selections, estimating systematic and theoretical uncertainties, statistical interpretations and combination of the achieved results, as well as documenting results and working through the ATLAS review process towards publications. The work has contributed to three ATLAS publications using the Run I data. The first based on 7 TeV data collected in 2011 and published as an ATLAS paper in the autumn of 2012 [1]; the second a conference note published in the spring of 2013 using 8 TeV data collected in 2012 [2], and also presented at EPS HEP 2013 [3]; before the final publication using the 2012 dataset was published in the autumn of 2014 [4]. The latter result was later included in a paper summarising ATLAS run I SUSY searches for squarks and gluinos [5], and re-interpreted in the context of the pMSSM in [6]. The results from [2] will not be presented here, as they were later superseded by those in [4]. Supporting internal ATLAS documents for the two analyses presented can be found in [7] and [8] respectively.

The last part of the thesis will investigate the prospect of detecting the annihilation products of naturally occurring dark matter in the Galactic Centre. Specifically, the sensitivity of the Cherenkov Telescope Array to Weakly Interacting Massive Particle (WIMP) dark matter annihilating into photon pairs in this region will be investigated. Such a signal is often considered a "smoking gun" signature of dark matter as the monochromatic energy of the resulting photons would result in a striking experimental signature.

Part I of this thesis briefly introduces the theoretical background and motivation for these studies. There, Chapter 2 provides a brief introduction to the main concepts of the Standard Model. Chapter 3 deals with the experimental evidence and most commonly considered candidates for dark matter. Finally, Chapter 4 will discuss the main concepts of supersymmetry and its implications for dark matter. For a more rigorous review of supersymmetry, see for example [9]. Part II presents my own work in searches for supersymmetry in final states with $E_{\mathrm{T}}^{\mathrm{miss}}$, jets and one τ lepton in ATLAS run I data collected in 2011 at a collision energy of 7 TeV, and in 2012 at a centre of mass energy of 8 TeV. Part III introduces the Cherenkov Telescope Array, which is a planned indirect detection experiment, and a study of the expected sensitivity of the experiment to WIMP dark matter annihilating into two photons in the Galactic Centre.

Part I

Theoretical Background and Motivation

Chapter 2

The Standard Model of Particle Physics

According to the Standard Model of particle physics [10, 11] all matter is made of fermions, and the forces acting upon them are mediated by force carrying particles called gauge bosons. Whereas the fermions have half-integer spin, the gauge bosons all have integer spin. Fermions are divided in two categories, named leptons and quarks, and come in three generations. Each generation consists of an up-type and down-type quark with fractional electric charges, a charged lepton and a neutral neutrino. With the exception of the neutrinos, which are close to massless, the fermion masses increase with each generation. The up and down quarks together with the electron and the electron neutrinos are collectively referred to as first generation fermions, and make up the atoms and molecules of the matter that surrounds us every day. The heavier particles belonging to the second and third generations, however, are unstable and will rapidly decay into first generation particles. To create, and study, the short lived and heavier generations of matter a high energy environment is needed, such as the one created when colliding particles using particle accelerators.

The force-carrying gauge bosons – photons, W/Z bosons and gluons – are responsible for transmitting the electromagnetic, weak and strong force respectively. The photon itself is electrically neutral and interacts with all electrically charged particles. The transmitter of the strongest force, the gluon, is – like the photon – massless and electrically neutral, and is responsible for binding atomic nuclei. It acts on particles carrying colour charge, which comes in three values (red, green and blue), namely quarks and gluons themselves. The final force included in the standard model is the weak force. As the name suggests, it is the weakest of the three, and is responsible for radioactive decay. Unlike the other force carriers, the $W^{\pm}$ and Z bosons that mediate the weak force are both massive, and the $W^{\pm}$ additionally have electrical charge ±1. The weak force acts upon all fermions and is the only force that is able to transform fermions between generations. The Standard Model does not include a description of the gravitational force, whose strength is negligible compared to the other forces at the scales relevant to particle physics. Incorporating gravity in a quantum theory of physics has, however, been one of the long standing challenges of physics.

The last of the Standard Model particles is the Higgs boson. Unlike the gauge bosons the Higgs boson carries no spin, making it a scalar boson. It is responsible for giving mass to the fermions and gauge bosons. It was discovered at CERN during my time as a PhD student in the summer of 2012, and was as such the last, and final, Standard Model particle to be discovered.

Formally the Standard Model is described by a renormalisable gauge theory based on the symmetry group $\mathrm{SU}(3)_C \times \mathrm{SU}(2)_L \times \mathrm{U}(1)_Y$. The simplest example of a gauge theory is QED, which describes electromagnetic interactions between charged fermions independently of the other forces. There, the mediator of the electromagnetic force is introduced by requiring invariance of the theory under local, i.e. space-time dependent, U(1) gauge transformations. In the Standard Model, however, the electroweak force is jointly described by the group $\mathrm{SU}(2)_L \times \mathrm{U}(1)_Y$. Similarly to QED, imposing invariance under local gauge transformations gives rise to massless gauge bosons of the electroweak interaction. We know, however, that the carriers of the weak force do in fact have mass. These masses, along with the fermion masses, are generated through a mechanism called electroweak symmetry breaking (ESWB), which gives rise to a neutral scalar boson – the Higgs boson. The strong force is similarly described by quantum chromodynamics (QCD) and the group $\mathrm{SU}(3)_C$, and results in 8 massless force carriers, namely the gluons. The following sections will give a brief, but slightly more formal, overview of the main components of the Standard Model following that found in reference [12]

2.1 Quantum Electrodynamics

Quantum Electrodynamics (QED) describes the electromagnetic interactions of charged particles. The Lagrangian $\mathcal{L}$ for the massless electromagnetic field $A_\mu = (V, A_x, A_y, A_z)$ interacting with a spin-$\frac{1}{2}$ field ψ of bare mass m is given by

$$\mathcal{L}_{\mathrm{QED}} = -\frac{1}{4} F_{\mu\nu} F^{\mu\nu} + \overline{\psi}(i\gamma^\mu D_\mu - m)\psi \tag{2.1}$$

The electromagnetic field tensor, $F_{\mu\nu}$, is given by Equation 2.2, while the covariant derivative, $D_{\mu\nu}$ is given by Equation 2.3.

$$F_{\mu\nu} = \partial_\mu A_\nu - \partial_\nu A_\mu \tag{2.2}$$

$$D_\mu = \partial_\mu - ieA_\mu Q \tag{2.3}$$

e is the unit of electric charge and Q is the charge operator. In this form the QED Lagrangian is invariant under the local U(1) gauge transformations:

$$\psi(x) \to e^{i\alpha(x)}\psi(x) = U(x)\psi(x) \tag{2.4}$$

$$A_\mu(x) \to A_\mu(x) + \partial_\mu \alpha(x) \tag{2.5}$$

The second term of the covariant derivate is introduced to ensure that the Lagrangian is invariant under the above transformation. This in turn introduces an interaction term between the electromagnetic field A_μ and the spin-$\frac{1}{2}$ field ψ, of the form $-e\overline{\psi}\gamma^\mu A_\mu \psi$.

The weak and strong force may be described similarly using the two other symmetry groups of the Standard Model – SU(2) and SU(3). The weak interaction described by the internal symmetry group, SU(2), can be unified with electromagnetic interaction, which is the topic of the next section.

2.2 The Electroweak Model

Just as a Lagrangian with U(1) symmetry can be used to describe electromagnetic interactions, a SU(2) gauge model is suitable to describe weak interactions. The free-field Lagrangian of spin-1/2 fields that transform as doublets is

$$\mathcal{L} = \bar{\psi}(i\gamma^\mu \partial_\mu - m)\psi, \tag{2.6}$$

and once more invariance under local gauge transformations is required

$$\psi(x) \to e^{ig\boldsymbol{\alpha}(x)\cdot\boldsymbol{T}}\psi(x). \tag{2.7}$$

Here $\boldsymbol{T}$ is an operator whose components, T_i, are the generators of SU(2). SU(N) groups are non-abelian meaning their generators do not commute

$$[T_i, T_j] = i\epsilon_{ijk}T_k. \tag{2.8}$$

Equation 2.6 can be made invariant by replacing ∂_μ with a covariant derivate

$$D_\mu = \partial_\mu + ig\boldsymbol{W}_\mu \cdot \boldsymbol{T}, \tag{2.9}$$

provided a triplet of fields $\boldsymbol{W}_\mu$ exist and transform as

$$\boldsymbol{W}_\mu \rightarrow \boldsymbol{W}_\mu + \partial_\mu \boldsymbol{\alpha}(x) + g\boldsymbol{\alpha}(x) \times \boldsymbol{W}_\mu. \tag{2.10}$$

The additional term in the transformation of the field with respect to the QED case is due to the symmetry group being non-abelian. The W-field part of the Lagrangian must also be made invariant which is achieved by adding $-\frac{1}{4}\boldsymbol{W}_{\mu\nu} \cdot \boldsymbol{W}^{\mu\nu}$ to the Lagrangian in Equation 2.6 with

$$\boldsymbol{W}_{\mu\nu} = \partial_\mu \boldsymbol{W}_\nu - \partial_\nu \boldsymbol{W}_\mu - g\boldsymbol{W}_\mu \times \boldsymbol{W}_\nu. \tag{2.11}$$

In addition to the kinetic energy terms, this introduces self-couplings of the $\boldsymbol{W}_\mu$ fields. The self couplings, which are not present in QED, is again a consequence of the non-abelian symmetry group. The triplet $\boldsymbol{W}$ consists of two charged and a neutral boson to transmit the weak force. However, these bosons are massless and do not obey the left-handed structure of charged-current couplings observed experimentally. The solution to these problems, along with the introduction of a unified description of weak and electromagnetic interactions, will be described in the following.

Experimentally, charged-current weak interactions are found to act upon left-handed fermion states only. This is reflected in the Standard Model by the fact that SU(2) gauge symmetry is imposed only on left-handed fermion fields, with left- and right-handed fields defined as

$$\psi_L = \frac{1}{2}(1-\gamma_5)\psi, \qquad \psi_R = \frac{1}{2}(1+\gamma_5)\psi. \tag{2.12}$$

Fermions are classified in weak isospin left-handed doublets, and right handed singlets

$$\begin{pmatrix} \nu_l \\ l \end{pmatrix}_L, \begin{pmatrix} u \\ d \end{pmatrix}_L, \qquad l_R, u_R, d_R \tag{2.13}$$

where l, u, d and ν denote the leptons, up-type quarks, down-type quarks and neutrinos of the Standard Model respectively, and L and R indicate handedness. The associated conserved quantity is weak isospin $\mathbf{T}_L$.

Introducing an additional $\mathrm{U}(1)_Y$ symmetry with conserved quantum number Y, called weak hypercharge, the weak and electromagnetic forces may be collectively described. The relation between these quantum numbers and the electric charge Q is

$$Q = T_3 + \frac{1}{2}Y. \tag{2.14}$$

Right handed fermions transform only under $\mathrm{U}(1)_Y$, while left-handed fermions transform under both $\mathrm{SU}(2)_L$ and $\mathrm{U}(1)_Y$. This leads to the following Lagrangian with separate fermion terms for left and right-handed fields

$$\mathcal{L} = -\frac{1}{4}\mathbf{W}^{\mu\nu} \cdot \mathbf{W}_{\mu\nu} - \frac{1}{4}B^{\mu\nu}B_{\mu\nu} + \bar{\psi}i\gamma^{\mu}D_{\mu}\psi, \tag{2.15}$$

where $\mathbf{W}_{\mu}$ is an SU$(2)_L$ isotriplet, and B_{μ} is an U$(1)_Y$ singlet. B$_{\mu\nu}$ and the covariant derivate, D_{μ}, are defined as

$$\begin{aligned} B_{\mu\nu} &= \partial B_{\nu} - \partial_{\nu}B_{\mu} && (2.16) \\ D_{\mu} &= \partial_{\mu} + ig\mathbf{W}_{\mu} \cdot \mathbf{T} + ig^{'}\frac{1}{2}B_{\mu}Y. && (2.17) \end{aligned}$$

The Lagrangian is invariant under local gauge transformations for SU$(2)_L$ and U$(1)_Y$ independently. In order to have a unified description of the weak and electromagnetic interactions, the neutral term of the covariant derivate must include the electromagnetic term. Therefore W_3 and B can be written as a linear combination of the electromagnetic field A and another neutral field Z

$$\begin{pmatrix} W_3 \\ B \end{pmatrix} = \begin{pmatrix} \cos\theta_W & \sin\theta_W \\ -\sin\theta_W & \cos\theta_W \end{pmatrix} \begin{pmatrix} Z \\ A \end{pmatrix} \tag{2.18}$$

Introducing the above into the covariant derivative and using the relation in Equation 2.14, it is found that

$$g = \frac{e}{\sin\theta_W}, \qquad g^{'} = \frac{e}{\cos\theta_W}. \tag{2.19}$$

For a given θ_W both the gauge couplings, g and $g^{'}$, are determined by the electric charge, e, and the weak and electromagnetic interactions are said to be unified. The theory describes two neutral and two charged fields that correspond to the γ, Z and W$^{\pm}$ gauge bosons respectively. The interaction of these with the fermion fields, ψ, appear from the term in the Lagrangian containing the covariant derivate, as in QED.

As it stands, both the gauge bosons and fermions are massless. A fermion mass term, $m\bar{\Psi}\Psi = m\bar{\Psi}_L\Psi_R + m\bar{\Psi}_R\Psi_L$, for example, would not be invariant under SU$(2)_L$ since the left and right-handed fields transform differently. The mechanism for giving mass to these particles is introduced in the next section.

2.3 The Higgs Mechanism

In the Standard Model the fermion and gauge fields are given masses by introducing a SU$(2)_L$ doublet of scalar fields Φ that spontaneously break the SU$(2)_L \times$U(1) symmetry. This introduces a neutral spin-0 particle, the Higgs boson. Yukawa couplings of Φ to the fermions are responsible for giving mass to the fermions. These couplings will not be discussed further, but it is worth noting that an arbitrary coupling parameter is introduced for each fermion. Meaning that the Higgs mechanism does not in the end explain the fermion mass values.

The term responsible for the gauge boson masses can be written as

$$\mathcal{L}_\Phi = |D_\mu \Phi|^2 - V\left(|\Phi|^2\right), \tag{2.20}$$

where the scalar potential V is

$$V = \mu^2 |\Phi|^2 + \lambda |\Phi|^4. \tag{2.21}$$

And the isodoublet

$$\Phi = \begin{pmatrix} \phi^+ \\ \phi^0 \end{pmatrix}, \tag{2.22}$$

where ϕ^+ and ϕ^0 are complex fields. Classically this potential has a degenerate non-zero minimum for $|\Phi|$ when $\mu^2 < 0$. Which translates to a non-zero vacuum expectation value for $|\Phi|$ in quantum field theory. This non-vanishing vacuum expectation value selects a preferred direction in weak isospin and hypercharge space, breaking the SU(2)×U(1) symmetry in the process. This is referred to as spontaneous symmetry breaking. $\Phi(x)$ can be written as

$$\Phi(x) = \frac{1}{\sqrt{2}} \begin{pmatrix} 0 \\ v + H(x) \end{pmatrix}. \tag{2.23}$$

Introducing the covariant derivate of the physical fields into the Lagrangian, the W and the Z fields acquire mass through their coupling to the Higgs field:

$$M_W = \frac{1}{2} g v, \qquad M_Z = \frac{M_W}{\cos\theta_W}. \tag{2.24}$$

As the photon field does not couple to the Higgs it remains massless. The Higgs mass itself is given by

$$m_H = \sqrt{-2\mu^2}. \tag{2.25}$$

2.4 Quantum Chromodynamics

Strong interactions may be described by a local, non-abelian gauge theory of SU(3) in a manner analogous to the SU(2) case described in Section 2.2. The resulting theory describes particles carrying colour charge – three coloured quarks of each flavour, and eight force carriers of the strong force called gluons. Due to the non-abelian nature of the theory the gluons have self-interactions.

Two important characteristics of QCD are the properties known as confinement and asymptotic freedom. Confinement refers to the fact that coloured particles cannot appear in isolation, but are always confined inside hadrons – such as mesons and baryons, which are bound states of quarks. This is the reason quarks and gluons are observed as jets of hadrons clustered together along the direction of the initial particle at particle colliders. It is due to the fact that as two quarks are pulled apart the strong attraction between them grows, until it becomes energetically favorable for quark pairs to be created from the vacuum forming hadrons. This process is referred to as hadronisation. Asymptotic freedom means that the strong force grows weaker at small distances and high energies. As a consequence quarks behave as free particles inside baryons, such as in the colliding protons at the LHC.

2.5 Shortcomings of the Standard Model

Although the Standard Model has been very successful in predicting and describing observations from particle physics experiments, there are both experimental and theoretical reasons to believe that it does not tell the full story. This has motivated a broad effort, both theoretically and experimentally, in searches for physics beyond the Standard Model that would alleviate these problems. The fact that the theory, as already mentioned, does not incorporate gravity makes it an effective theory valid only below a certain energy cut off scale, and does not allow for a unification of all the forces of nature. Similarly, the couplings of the forces described by the Standard Model do not converge at a common point at higher energy scales, which is a requirement for a unified description of the forces in a Grand Unified Theory (GUT). Other arguments of a more aesthetic nature can be made in that there is no apparent reason, other than the fact that it works, behind the choice of gauge group describing the model. Furthermore, the masses and mixing matrices of the model are free parameters that need to be determined experimentally and inserted into the theory. The lack of an explanation for these measured values is compounded by the fact that they span values of several orders of magnitude without any mechanism in the model to explain such a large range of values, nor why there should be only three generations of fermions.

Perhaps the most compelling theoretical argument for physics beyond the Standard Model is a fine tuning problem called the hierarchy problem. It reflects the fact that the Higgs mass is subject to large quantum corrections that depend on a much larger energy scale, often taken to be the Planck scale, than the electroweak scale of the physical Higgs mass. Therefore a large degree of fine tuning is required for the Higgs mass to remain at the electroweak scale despite the radiative corrections from the particles it couples to. The name hierarchy problem was chosen due to the fact that the problem arises from the difference in order of magnitude between the energy scales involved in the calculation of the Higgs mass corrections. For example the correction to the Higgs mass received from a fermion can be written as

$$\Delta m_H^2 = -\frac{\mid \lambda_f \mid^2}{8\pi^2}\Lambda_{\mathrm{UV}}^2 + \cdots , \tag{2.26}$$

where Λ_{UV}^2 is an ultraviolet energy scale which could be taken to be the energy scale of potential new physics contributions, or the Planck scale, where gravitational effects will become significant. As the top quark is the Standard Model particle with the strongest coupling to the Higgs field it is also the one responsible for the largest quantum correction.

From the experimental point of view, the most noticeable problem of the Standard Model is that in its canonical version the neutrinos are massless. Observations of neutrino mixing have, on the other hand, shown that neutrinos actually have a non-zero mass. There are, however, ways of incorporating massive neutrinos in the Standard Model, where the correct mechanism for generating the masses depend on the nature of the neutrinos, whether they are dirac or majorana particles, which is yet to be determined experimentally. Furthermore, the Standard Model does not explain the observed matter-anti-matter asymmetry in the universe, as it does not provide enough CP-violation. Likewise there is no explanation as to why there is no, or very little, CP-violation related to the strong force, which is often referred to as the strong CP problem. Perhaps the most significant, and certainly the most direct, indication that the Standard Model is not sufficient to describe known physics is the observation of dark matter in astrophysics and cosmology experiments. Convincing arguments can be made that this unknown matter is made of a new species of particles whose origin is yet to be determined by particle physics experiments. The following section will discuss the main evidence for the existence of dark matter, along with possible dark matter candidates.

Chapter 3

Dark Matter

The fact that a large portion of the Universe consist of an, as of yet, unknown type of matter has been established by a series of astrophysical and cosmological measurements carried out over the last several decades. However, the existence of this new type of matter has only been inferred through gravitational effects, leaving its constituents undetermined. Due to the fact that this new type of matter does not exhibit strong or electromagnetic interactions, and hence does not absorb or emit light, it has been dubbed dark matter. Section 3.1 will review the experimental evidence for dark matter, before the possible candidates constituting the observed dark matter are outlined in Section 3.2. These sections are primarily based on [13] and [14] respectively, where more complete reviews can be found.

3.1 Evidence for Dark Matter

The first indication of dark matter [15] appeared already in 1933 when Fritz Zwicky found that the velocity dispersion of the galaxies in the Coma galaxy cluster were such that they could not be explained by the gravitational pull of the visible matter in the cluster alone. From his measurements he inferred that most of the galactic mass was made out of unseen, non-luminous, matter that he called 'dunkle Materie'. Although Zwicky's estimates of the amount of dark matter has later been adjusted, his measurements were the first of many to indicate the presence of a new type of matter, and numerous experiments has pointed towards the existence of dark matter since then.

Additional evidence for dark matter at the scale of galaxy clusters are obtained from gravitational lensing effects, and properties of the X-rays emitted by the hot gas in the clusters. From the equations describing a spherically symmetric, ideal gas in hydrostatic equilibrium the temperature of the gas

Figure 3.1: Galaxy cluster 1E 0657-56, the bullet cluster, formed after the collision of two galaxy clusters. Hot gas detected by Chandra in X-rays is shown in pink, while the mass inferred from gravitational lensing is shown in blue [16].

in a cluster can be described by [13]

$$kT \approx (1.3 - 1.8)\ \mathrm{keV} \left(\frac{M(r)}{10^{14} M_\odot}\right) \left(\frac{1\mathrm{Mpc}}{r}\right), \tag{3.1}$$

where $M(r)$ is the mass within radius r. It turns out that considering the baryonic matter only when calculating $M(r)$ is not sufficient to obtain the observed temperature of $T = 10$ keV, suggesting the existence of additional matter in the clusters.

Gravitational lensing occurs as a direct consequence of Einstein's theory of general relativity which predicts that light, rather than travelling in straight lines, is bent by gravitational fields. Using this effect the gravitational mass of a cluster can be inferred from the distortions observed in the images of background objects, whose light is bent as it is exposed to the cluster's gravitational pull. The most famous result based on gravitational lensing is undoubtedly the bullet cluster, which shows two galaxy clusters colliding [17] as seen in Figure 3.1. As the clusters pass through one-another the baryonic matter, mostly hot gas, interacts, decelerates and leaves shock waves in their wake. From gravitational lensing however, it can be seen that most of the matter in the galaxies pass through practically unperturbed, indicating that most of the matter interacts only weakly with baryonic matter, as well as itself. These measurements at the scale of galaxy clusters imply a dark matter mass density of $\Omega_{DM} \sim 0.2 - 0.3$ [18, 19, 20] in the Universe.

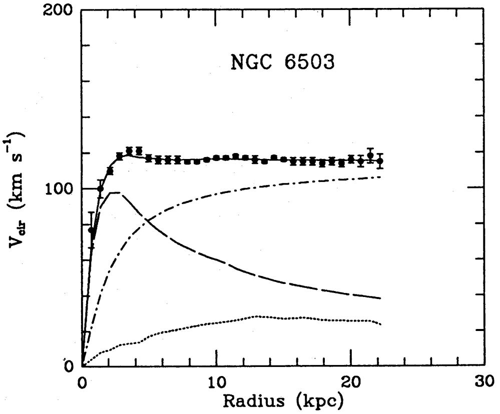

Figure 3.2: Galactic rotation curve where the dotted, dashed and dash-dotted lines are the contributions of gas, disk and dark matter, respectively [21].

Perhaps the most compelling evidence for dark matter are the measurements of galactic rotation curves [22, 21, 23]. The first to measure these rotational velocities of stars and gas as a function of their distance from the galactic center was Vera Rubin towards the late 1970s [22]. She showed that these velocities did not behave as expected when only considering the visible matter of the galaxies. The circular velocity v of an object orbiting a galaxy at radius r is in Newtonian mechanics given by

$$v(r) = \sqrt{\frac{GM(r)}{r}}, \tag{3.2}$$

where the mass inside the orbit $M(r) \equiv 4\pi \int \rho(r) r^2 dr$, and $\rho(r)$ is the mass density profile. If the mass of the galaxy is made out of visible, luminous matter only we would expect the velocities to be falling $\propto 1/\sqrt{r}$ if r lies outside the visible part of the galaxy. Contrary to expectations the measured rotational velocities are seen to remain approximately constant, rather than falling, at large distances from the galactic center. This implies the existence of a galactic dark matter halo with $M(r) \propto r$, and consequently $\rho(r) \propto 1/r^2$. These measurements give a lower bound on the dark matter mass density of $\Omega_{\rm DM} \gtrsim 0.1$ [24].

The most accurate measure of the total amount of dark matter in the universe is obtained through more indirect means – namely fits of cosmological parameters to a range of astrophysics and cosmology measurements. The linchpin of this derivation is the measurement of the Cosmic Microwave Back-

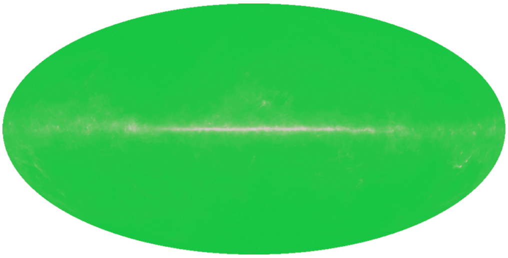

(a) Penzias & Wilson (simulated)

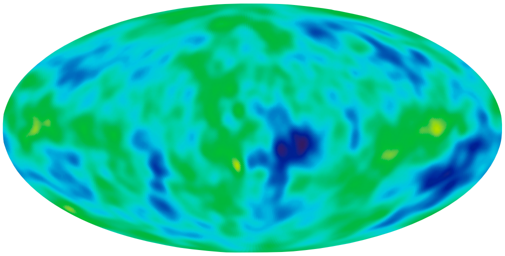

(b) COBE

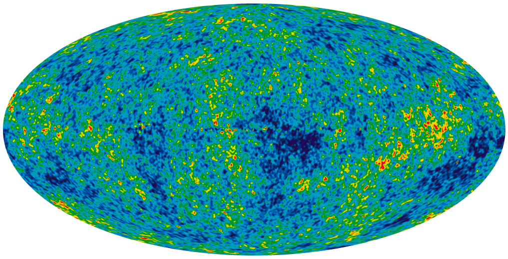

(c) WMAP

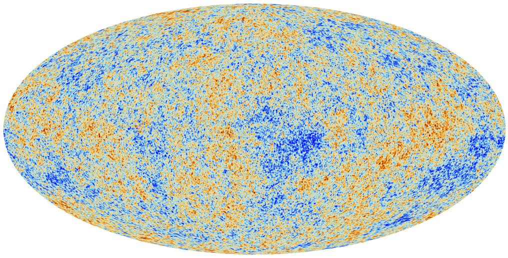

(d) PLANCK

Figure 3.3: Cosmic Microwave Background radiation as seen by different experiments [25, 26, 27, 28, 29, 30]. 3.3(a) is a simulation of the Penzias & Wilson experiment where the region of the galactic disk (central horisontal line) has not been removed as in the other maps.

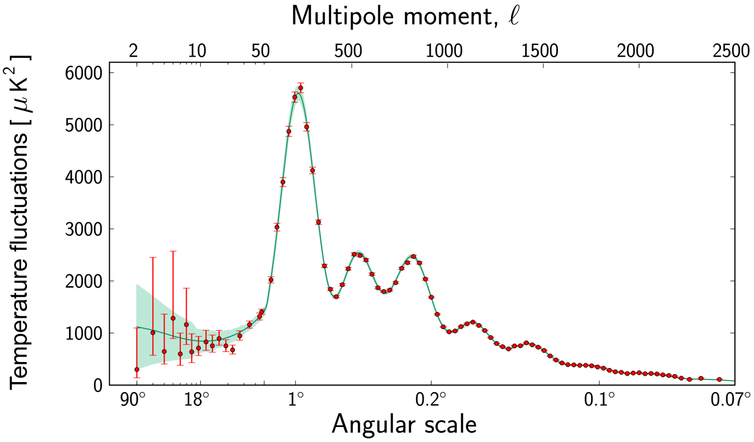

Figure 3.4: CMB power spectrum measured by Planck at different angular scales on the sky [31, 32]. The red dots are Planck measurements, and the green curve shows the best fit of the Standard Model of cosmology.

ground (CMB) that originates from the moment when photons were able to travel freely through the early universe. First discovered by Penzias and Wilson in 1965, in what might be the most inadvertent discovery in the history of modern physics, the CMB has been extensively studied since then. Upon discovering the constant radiation they initially blamed the pigeons residing in their antenna for causing the apparent noise in their experiment. However, it turned out to be the radiation predicted by Gamow in 1948, and later measured to correspond to a black body radiator with a temperature of 2.726 K [13]. Since its discovery, increasingly accurate measurements of this light emitted when the universe was approximately 380 000 years old has helped us determine the age, structure and content of the universe. Figure 3.3 shows the historical development, and dramatic increase in accuracy, of CMB measurements from the initial discovery by Penzias and Wilson, followed by the COBE and WMAP experiments and culminating in the measurements made by Planck.

Although the CMB is almost perfectly isotropic, to the 10^{-5} level, it is the tiny observed CMB anisotropies that constrain cosmological parameters.

These temperature anisotropies are commonly expanded as [13]

$$\frac{\delta T}{T}(\theta, \phi) = \sum_{l=2}^{\infty} \sum_{m=-l}^{l} a_{lm} Y_{lm}(\theta, \phi), \tag{3.3}$$

where $Y_{lm}(\theta, \phi)$ are spherical harmonics. The variance C_l of a_{lm}, which describes the fluctuations observed in the CMB, is given by

$$C_l \equiv \langle \mid a_{lm} \mid^2 \rangle \equiv \frac{1}{2l+1} \sum_{m=-l}^{l} \mid a_{lm} \mid^2. \tag{3.4}$$

Using CMB measurements only, the density of cold, non-baryonic matter is found to be $\Omega_{DM} h^2 = 0.1198 \pm 0.0026$, whereas the number for baryonic matter is $\Omega_b h^2 = 0.02207 \pm 0.00027$ where h is the Hubble constant [13]. Parts of the baryonic matter density will contribute to dark matter in form of MACHOs [33, 34] or cold molecular gas clouds [35]. These dark matter contributions however, are only able to account for a small fraction of the total amount of observed dark matter. In the following any references to dark matter will be to its non-baryonic component unless otherwise specified.

In addition to the total amount of dark matter in the universe, the local amount of dark matter in our vicinity has also been measured. This quantity is especially important for direct and indirect dark matter searches, as they depend on the detection of naturally occurring dark matter. Therefore the potential dark matter detection rates in these experiments depend on both the local dark matter density and velocity distribution. Both these values are obtained mainly through measurements of the rotation curves of the Milky Way yielding a local density [24]

$$\rho_{\mathrm{DM}}^{\mathrm{local}} = (0.39 \pm 0.03) \frac{\mathrm{GeV}}{\mathrm{cm}^3}, \tag{3.5}$$

and mean velocity $\bar{v} \cong 270\mathrm{km/s}$ [13].

3.2 Candidates for Dark Matter

As described in the previous section there is ample experimental evidence for dark matter from astrophysics and cosmology. However, these experiments give no insight into what dark matter is actually made of. In this section, some of the commonly considered dark matter candidates will be introduced with an emphasis on a category of particle dark matter called Weakly Interacting Massive Particles (WIMPs).

A viable candidate for dark matter must meet a set of criteria in order to explain the observed properties of this category of matter. Namely it needs to be stable, weakly interacting and give the correct relic dark matter density. Although absolute stability is not required, it needs to have a lifetime comparable to the age of the universe in order to not have decayed by present times. The candidate must interact very feebly with electromagnetic radiation, otherwise it would not be dark, as well as with other particles and itself to explain the observed dark matter distribution, structures in the universe and the bullet cluster observation. Finally, the production, decay and annihilation of the dark matter candidate must be such that it matches the observed dark matter density.

In the Standard Model there is one particle that fulfils many of the above criteria - namely the neutrino. Being stable, electrically neutral, weakly interacting, and not in the least known to exist, this was one of the first candidates people looked to in the initial attempts to explain dark matter. It turns out, however, that neutrinos are simply not abundant enough to achieve the required dark matter density. Using the measured upper limits on neutrino masses an upper bound on the relic density from neutrinos of $\Omega_\nu h^2 \lesssim 0.07$ can be derived [13]. Furthermore, CMB and large-scale structure data set an upper bound on the same quantity of $\Omega_\nu h^2 \lesssim 0.0062$ [24]. This is due to neutrinos being relativistic particles, often referred to as an example of "hot" dark matter candidates. The problem with "hot" dark matter candidates in general is that they serve to wash out density fluctuations on small distance scales. This indicates a means of structure formation that conflicts with current large-scale structure data, and predicted density fluctuations in the CMB that are in disagreement with both WMAP and Planck measurements [24]. Therefore a suitable dark matter candidate should be "cold", meaning that it should be non-relativistic when galaxy formation started.

Several new particles have also been suggested as possible dark matter candidates. Among these is a particle type similar to the Standard Model neutrinos called sterile neutrinos [36]. These are similar to the neutrinos of the Standard Model, but do not take part in Standard Model weak interactions. Another particle, the axion, was initially suggested to remedy the strong CP problem in the Standard Model and has later been interpreted as a dark matter candidate. Although axions are constrained to be very light ($\lesssim$ 0.01 eV) they would be categorised as cold dark matter due they way they are produced in the early universe [13].

By far the most extensively studied group of dark matter candidates, however, are WIMPs. WIMP is an umbrella term used to describe particles with masses in the GeV to TeV range, and weak scale interactions with the Standard Model sector. An enticing property of such particles is that

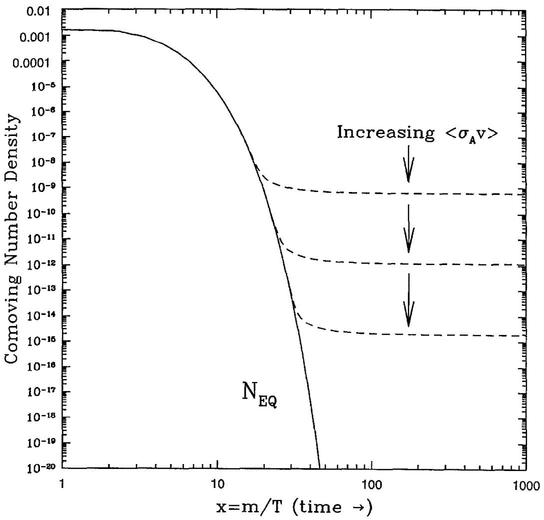

Figure 3.5: WIMP number density in the early universe. The dashed lines are the freeze-out abundance, while the solid line is the equilibrium abundance [14].

they can be shown to give rise to an expected relic dark matter density close to the one observed today. This is often referred to as the WIMP miracle, and builds on simple principles. In the early universe the temperature was high enough for WIMPs to exist in large numbers. The particles were kept in thermal equilibrium by pair-annihilation and, the opposite process, pair-creation of WIMPs. As the universe ages, expands and consequently cools the equilibrium WIMP abundance drops exponentially once the temperature falls below the WIMP mass. However, since the universe expands, the diminishing number of WIMPs will find it increasingly difficult to interact as space between them itself grows. At some point the rate of WIMP annihilation, $\Gamma = \langle\sigma v\rangle n_{WIMP}$, where $\langle\sigma v\rangle$ is the thermally averaged total WIMP annihilation cross section times velocity and n_{WIMP} is the WIMP number density, will drop below the Hubble expansion rate of the universe. At this point the WIMPs will no longer be able to annihilate and drop out of thermal equilibrium, which is often referred to as freeze out. After freeze out the relic dark matter abundance remain essentially unchanged, as shown in Figure 3.5. Freeze out happens at temperature $T_F \simeq m_{\text{WIMP}}/20$ almost independently of the WIMP properties [14]. The present relic density may be calculated following the above considerations and can be expressed, independently of WIMP mass, as [14, 24]

$$\Omega_\chi h^2 \approx const. \cdot \frac{T_0^3}{M_{\rm Pl}^3 \langle \sigma v \rangle} \approx \frac{3 \times 10^{-27} {\rm cm}^3 {\rm s}^{-1}}{\langle \sigma v \rangle}, \tag{3.6}$$

where T_0 is the CMB temperature today and $M_{\rm Pl}$ is the Planck Mass. The fact that the result in Equation 3.6, which contains factors of Planck mass and CMB temperature, gives the correct relic densities in the region of weak interaction cross sections is colloquially referred to as the WIMP miracle. This seeming connection between cosmological and particle physics scales is seen as highly suggestive and therefore indicating that "if there is a stable particle associated with new physics at the electroweak scale, it is the dark matter" [14].

Although Equation 3.6 provides motivation for WIMP dark matter it is worth noting that modifications of the relic density can be introduced in WIMP theories from both the particle physics and the cosmology side, through for example resonance enhancements, so-called coannihilations [37] or dark matter could be composed of more than one particle species [13]. These factors depend on both the specific theory giving rise to the WIMP, as well as the specific parameters of the theoretical model. This brings us to the question of where these WIMPs come from. WIMPs occur naturally in several beyond the Standard Model theories. Commonly studied theories containing WIMPs are Little Higgs, Technicolor and Extra Dimensional models [24, 38]. The perhaps best motivated, and most studied, WIMP candidate is the lightest supersymmetric particle in supersymmetric models, which is also the main focus of this work. The next chapter will therefore introduce supersymmetry in general, and describe supersymmetric dark matter in more detail.

Chapter 4

Supersymmetry

Supersymmetry (SUSY) [39, 40, 41, 42, 43] is an extension of the Standard Model that solves many of its deficiencies by introducing a symmetry between fermions and bosons. In doing so, each Standard Model fermion gets a boson superpartner, while each boson gets a fermion superpartner, with the same properties apart from spin. If supersymmetry was an exact symmetry, the supersymmetric particles, referred to as sparticles, would have the same mass as their Standard Model partners. As sparticles of such masses has not been observed, we know that supersymmetry must be a broken symmetry.

4.1 Fixing the Standard Model

One of the biggest achievements of supersymmetry is its ability to remedy the hierarchy problem. The first order corrections from fermion and scalar loops respectively are shown in Figure 4.1. As seen in Equation 2.26 the first order fermion loop contribution is quadratically divergent. In supersymmetry however, the boson loop correction from the superpartner of the fermion cancels out this quadratic divergence as it has the opposite sign of the fermion contribution. As a result the quadratic divergence is cancelled and only a logarithmic dependence on Λ remains

$$\Delta m_H^2 \approx \frac{1}{16\pi^2}(m_S^2 - m_f^2)\ln\left(\frac{\Lambda}{m_f}\right) \tag{4.1}$$

As seen in the above equation the Higgs mass correction depends on the mass difference between the Standard Model and supersymmetric particles. While the cancellation would be exact for an unbroken supersymmetric theory, the hierarchy problem would be re-introduced in a supersymmetric model where the superpartners are very massive, due to the remaining logarithmic Λ term.

Figure 4.1: One loop corrections to the Higgs mass from a fermion (left) and a scalar (right) [9].

For this reason the masses of the supersymmetric particles are expected to be no higher than about the TeV scale in order for the theory to remain natural [44, 45], i.e. not fine-tuned.

Another salient feature of the theory is the prospect of being able to unify the gauge couplings as seen in Figure 4.2. With the additional particle content of weak scale supersymmetry the equations that describe the running of the coupling strengths from the electroweak to the GUT scale are changed so that the coupling strengths could become equal at higher energies. This could in turn allow for a unified description of the forces.

In Standard Model interactions both lepton and baryon number is conserved. This is no longer the case in supersymmetry, where also the superpartners of the fermions carry lepton and baryon quantum numbers. In particular baryon number violating interactions, that would lead to proton decay through the process $p \to \pi^0 e^+$, are strongly constrained experimentally by the apparent stability of the proton. This problem is often solved by requiring that R-parity [46, 47, 48, 49, 50], which is a multiplicative quantum number, is conserved. R-parity for a particle is defined as

$$R = (-1)^{3(B-L)+2s}, \tag{4.2}$$

where B and L are baryon and lepton number respectively, while s is the spin of the particle. This means that all of the Standard Model particles have $R = 1$ and all sparticles have $R = -1$. Imposing R-parity conservation has important phenomenological implications for supersymmetric models. It means, for example, that sparticles can only be produced in even numbers, and that they can only decay to an odd number of sparticles. Most importantly this makes the lightest supersymmetric particle (LSP) stable, and therefore a viable particle dark matter candidate. Candidates for supersymmetric dark matter will be discussed further in Section 4.3.

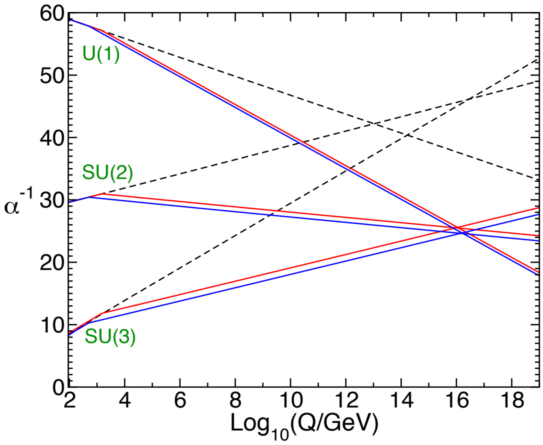

Figure 4.2: Evolution of the inverse gauge couplings in the Standard Model (dashed lines) and MSSM (solid lines) [9]. The difference between the red and blue lines indicate the effect of varying the strong coupling, along with the mass scale where supersymmetric particles enter.

4.2 The Minimal Supersymmetric Standard Model

The minimal supersymmetric extension of the Standard Model (MSSM), as the name implies, contains the minimum of extra particle content beyond that of the Standard Model. This is achieved by associating fermionic superpartners to all Standard Model gauge fields, scalar partners to the fermions, as well as adding one additional Higgs field with one spin 1/2 sparticle associated to each Higgs boson. The fermionic superpartners of the gluon, $W^{\pm}$ and B bosons are called gluinos ($\tilde{g}$), winos ($\tilde{W}^i$) and binos ($\tilde{B}$) – collectively referred to as gauginos. The scalar partners of the quarks and leptons are called squarks and sleptons. The introduction of additional Higgs fields is necessary to give mass to both up and down-type quarks upon EWSB, while at the same time preserving supersymmetry. This results in a total of two Higgs doublets, corresponding to five physical states, where a spin 1/2 Higgsino is associated to each Higgs boson.

The particle content of the MSSM is summarised in Tabled 4.1. There are two squarks, left and right, for each quark and similarly for the leptons. Keeping in mind that the squarks are scalars while the quarks have spin 1/2, this ensures that the bosonic degrees of freedom match the fermionic. In most

Table 4.1: Contents of the MSSM.

Standard model particles/fields		Supersymmetric partners			
		Interaction eigenstates		Mass eigenstates	
Symbol	Name	Symbol	Name	Symbol	Name
$q = u, d, c, s, b, t$	quark	$\tilde{q}_L$, $\tilde{q}_R$	squark	$\tilde{q}_1$, $\tilde{q}_2$	squark
$l = e, \mu, \tau$	lepton	$\tilde{l}_L$, $\tilde{l}_R$	slepton	$\tilde{l}_1$, $\tilde{l}_2$	slepton
$\nu = \nu_e, \nu_\mu, \nu_\tau$	neutrino	$\tilde{\nu}$	sneutrino	$\tilde{\nu}$	sneutrino
g	gluon	$\tilde{g}$	gluino	$\tilde{g}$	gluino
$W^{\pm}$	W-boson	$\tilde{W}^{\pm}$	wino	$\tilde{\chi}^{\pm}_{1,2}$	chargino
H^-	charged Higgs	$\tilde{H}_1^-$	higgsino		
H^+	charged Higgs	$\tilde{H}_2^+$	higgsino		
B	B-field	$\tilde{B}$	bino	$\tilde{\chi}^0_{1,2,3,4}$	neutralino
W^3	W^3-field	$\tilde{W}^3$	wino		
h^0	light scalar Higgs	$\tilde{H}_1^0$	higgsino		
H^0	heavy scalar Higgs	$\tilde{H}_2^0$	higgsino		
A^0	pseudo-scalar Higgs				

models there is no mixing between sfermion flavours, while left-right sfermion mixing is proportional to the corresponding fermion mass. The charged winos and higgsinos mix, resulting in mass eigenstates called charginos. Likewise the neutral higgsinos, wino and bino mix into four Majorana mass eigenstates called neutralinos, where the lightest neutralino is denoted $\tilde{\chi}^0_1$. As there is no ambiguity in doing so, the tilde is often dropped when referring to charginos and neutralinos. The lightest neutralino is often referred to only as χ due to its special role in often being the LSP and a suitable dark matter candidate.

As we know, supersymmetry is not an exact symmetry. It is expected to be broken spontaneously, analogously to EWSB, to give its low-energy appearance. However, as the nature of the symmetry breaking is unknown, terms that break supersymmetry explicitly are rather added to the Lagrangian. These terms are required to be soft, i.e. they should be such that the cancellation of the quadratic divergencies in the Higgs mass correction still occur. The manner of supersymmetry breaking has important phenomenological implications on the theory, and supersymmetric models are often classed by type of symmetry breaking. The supersymmetry breaking terms introduce 105 new parameters of masses, phases and mixing angles in addition to those in the Standard Model. As such it is the supersymmetry breaking terms, rather than supersymmetry in itself, that introduce the large number of free parameters to the theory. To make phenomenological studies of the MSSM tractable, theoretically motivated assumptions are imposed on the parameters of the theory. This reduces the number of free parameters in the theory and leads to distinct supersymmetric models depending on the assumptions applied. In the following some of the most common models, that are relevant to the work in this thesis, will be presented.

Minimal Supergravity

In minimal supergravity (mSUGRA), or constrained MSSM (cMSSM), [51, 52, 53, 54, 55, 56] supersymmetry is broken via gravitational interactions. The number of free parameters in the model is reduced to five by imposing boundary conditions at the Grand Unification scale. These boundary conditions are unification of the gauge couplings, universal trilinear couplings, unification of gaugino masses and universal scalar masses at the GUT scale [56]. When requiring EWSB five free parameters remain:

- m_0: sfermion mass at the GUT scale
- $m_{1/2}$: gaugino mass at the GUT scale
- A_0: trilinear coupling
- $\tan\beta$: ratio of Higgs doublet vacuum expectation values
- sign μ: Higgsino mass parameter sign

Gauge Mediated Symmetry Breaking

Gauge Mediated Symmetry Breaking (GMSB) [57, 58, 59, 60, 61, 62] models are broken by a Standard Model gauge interaction via messenger fields at the scale M_{mes}. The sparticles in the model are proportional to the scale of SUSY breaking, λ. The free parameters in the minimal GMSB models are [61]:

- Λ: the scale of the SUSY breaking
- M_{mes}: the messenger mass scale
- N_5: the number of equivalent messenger fields
- $\tan\beta$: ratio of Higgs expectation values
- sign(μ): Higgsino mass parameter sign

- C_{grav}: the ratio of the physical gravitino mass to its value at the SUSY breaking scale

Λ typically has values of (10-100) TeV and sets the overall mass scale for all MSSM superpartners. Additionally the gaugino and sfermion masses depend on N_5. M_{mes} has to be larger than Λ in order to prevent colour and charge breaking in the messenger sector, and $C_{\text{grav}} \geq 1$ leads to prompt decay of the next-to-lightest supersymmetric particle (NLSP).

The phenomenological MSSM

Another approach to reducing the MSSM parameter space is to a lesser extent based on theoretical arguments, but is rather based on the phenomenological aspects of supersymmetric theory. Commonly a phenomenological MSSM (pMSSM) is constructed by requiring:

- No new sources of CP violation
- no flavour-changing neutral currents
- first and second generation universality

The pMSSM is adaptable and could be described by a number of free parameters ranging from as low as five and up to tens of parameters.

4.3 Supersymmetric Dark Matter

The particle content of the MSSM implies several possible particles that could be the LSP. Most of them do not have the required characteristics of a viable dark matter candidate, however, leaving only a few options for supersymmetric dark matter. Any electrically charged or strongly interacting LSPs may be disregarded as they would bind to ordinary matter, creating anomalously heavy nucleus and nuclei respectively. The presence of such heavy elements is in disagreement with experimental data searching for this type of matter [63, 64, 65]. This leaves the electrically neutral sparticles that are only weakly interacting – the sneutrino, neutralino and gravitino. The latter of the three is the postulated superpartner of the graviton.

Sneutrinos have been shown to give reasonable values for the dark matter relic density for sneutrino masses in the range of about 500 GeV to 2 TeV [13]. However, the scattering cross section of sneutrinos with nucleons is larger than the values allowed by direct dark matter detection experiments [66]. While sneutrino masses between $\mathcal{O}(\text{GeV}) - \mathcal{O}(\text{TeV})$ are excluded by direct detection experiments, very light sneutrinos were excluded at LEP by measuring the invisible Z-boson decay rate [67].

Unlike the sneutrino and the neutrino the gravitino has only gravitational strength interactions. This means that is not expected to have been in thermal equilibrium in the early universe, but it could have been created through decays of heavier supersymmetric particles. Due to the extremely feeble interaction strength of the gravitino the NLSP in supersymmetric scenarios with gravitino LSPs are often metastable. This could lead to striking experimental signatures at colliders of new metastable charged particles, sparticles confined in hadrons along with more conventional experimental signatures. On the other hand there are constraints from cosmology and astrophysics on the mass and lifetime of the NLSP related in particular to the Big-Bang Nucleosynthesis light-element abundance [68]. In GMSB models the relation between the gravitino mass, $m_{\tilde{G}}$, and the masses of the other supersymmetric particles, m_{SUSY} can be approximated by

$$\frac{m_{\tilde{G}}}{m_{\mathrm{SUSY}}} \sim \frac{1}{\alpha_a} \frac{M_S}{M_{Planck}} \ll 1 \tag{4.3}$$

where M_S is the SUSY breaking scale [13]. This means that a very light gravitino generally is the dark matter candidate in GMSB models. The fact that a dark matter candidate with only gravitational strength interactions is very difficult to detect using indirect and direct dark matter experiments underline the importance of varied search strategies, as well as the interplay and complementarity between astrophysics and collider searches.

By far the most commonly considered supersymmetric dark matter candidate is the lightest neutralino. Being an example of WIMP dark matter it enjoys all the appealing aspects of a general WIMP described in Section 3.2. The neutralino mass matrix can in the basis of ($\tilde{B}$, $\tilde{W}_3$, $\tilde{H}_1^0$, $\tilde{H}_2^0$) be written as

$$\mathcal{M}_{\mathrm{N}} = \begin{bmatrix} M_1 & 0 & -M_Z\cos\beta\sin\theta_W & M_Z\sin\beta\sin\theta_W \\ 0 & M_2 & M_Z\cos\beta\cos\theta_W & -M_Z\sin\beta\cos\theta_W \\ -M_Z\cos\beta\sin\theta_W & M_Z\cos\beta\cos\theta_W & 0 & -\mu \\ M_Z\sin\beta\sin\theta_W & -M_Z\sin\beta\cos\theta_W & -\mu & 0 \end{bmatrix},$$

where M_1 and M_2 are the bino and wino mass parameters respectively, and θ_W is the Weinberg angle [68]. The lightest neutralino is a linear combination of $\tilde{B}$, $\tilde{W}_3$, $\tilde{H}_1^0$ and $\tilde{H}_2^0$

$$\chi = N_{11}\tilde{B} + N_{12}\tilde{W}_3 + N_{13}\tilde{H}_1^0 + N_{14}\tilde{H}_2^0. \tag{4.4}$$

The phenomenology of the neutralino is governed by its mass and composition. The latter can be described by defining the gauge fraction, f_G, and higgsino fraction, f_H:

$$f_G = N_{11}^2 + N_{12}^2 \qquad f_H = N_{13}^2 + N_{14}^2. \tag{4.5}$$

An example of this is found when considering mSUGRA or similar scenarios. For most of the parameter space the lightest neutralino is gaugino dominated with a mass at a couple of a few hundred GeV or below. In other regions however, the lightest neutralino will have a larger higgsino fraction, allowing it to be significantly heavier without requiring a highly fine-tuned model.

Part II

Searching for SUSY in ATLAS data

Chapter 5

Introduction to the Analyses

One of the main ways of searching for dark matter, or new particles in general, is at collider experiments. By colliding particles at high energies some of the energy in the collision can be converted to mass, creating new and potentially heavy particles. These would decay almost instantly into lighter Standard Model particles, that in turn are observed by detectors placed at the collision points. From these decay products properties of the initial particle, or particles, produced in the collision can be inferred.

The strongly interacting supersymmetric particles described in the previous section could potentially be produced at high rates at hadron colliders. Assuming R-parity conservations, they would immediately decay into consecutively lighter sparticles accompanied by Standard Model particles, until reaching the lightest supersymmetric particle that is stable. During this chain of decays highly energetic quarks and gluons can be produced, as portions of the coloured sparticle mass is converted to kinetic energy of the much lighter standard model decay products. These quarks and gluons are observed as collections of hadrons, or jets, with large momentum in the detector.

The momentum perpendicular to the direction of the colliding beams is negligible for the initial colliding partons. From momentum conservation it follows that the summed momentum of the resulting particles in the collision should also be negligible in this transverse plane. However, if any of the particles produced in the collision escape detection this does no longer hold, and a transverse momentum imbalance, referred to as missing transverse momentum, would be seen. One source of such momentum imbalance would be the lightest supersymmetric particle as it is only weakly interacting, and therefore would escape the detector unseen.

Furthermore, certain supersymmetric models lead to decays through a $\widetilde{\tau}$ resulting in final states containing a Standard Model τ lepton. This includes, but is not limited to, large portions of the GMSB parameter space where the $\widetilde{\tau}$ is the next-to-lightest supersymmetric particle, and the mSUGRA co-annihilation region that is known to have an acceptable dark matter relic density [69]. Searching for such models motivate studying final states containing τ leptons accompanied by several high energy jets and significant missing transverse momentum, which is the focus of this thesis.

The Large Hadron Collider (LHC) at CERN has, since its inception, collided protons at record energies and rates, bringing more massive and rarer particles than previously accessible within our experimental reach. The ATLAS detector is one of two multi-purpose detectors at the LHC tasked with measuring, recording and interpreting the collisions. The first run period of the LHC saw protons colliding at energies of 7 and 8 TeV from 2010 through 2012. The data recorded by the ATLAS experiment during this period is commonly referred to, and analysed as, distinct datasets corresponding to the year the data was collected. With the increased performance of the LHC after the first year of physics running the combined 2011 and 2012 datasets corresponded to more than a thousandfold increase in collected data compared to the 2010 dataset. Having been privileged enough to have had the opportunity to work with all the data from the first run period, two analyses performed on the full 2011 and 2012 datasets will be presented here.

The work presented builds on experience gained working with the 2010 data that include a search for supersymmetry in two τ final states carried out as part of my master studies [70], and later extended and documented as a CERN internal document [71]. The first results published by ATLAS on supersymmetry searches including τ leptons were two separate analyses, for final states with at least one [72] and two τ leptons [73] respectively, based on the first half of the 2011 dataset. Having joined the ATLAS SUSY with taus analysis team as one of the main analysers after these two early works the first publication using the full 2011 dataset was presented in [1]. This was also the first joint analysis of the previously separate studies of final states with one and two hadronic τ leptons, in addition to final states with a τ and an additional light lepton. Chapter 9 presents this analysis with an emphasis on the results obtained in one τ analysis channel that I was responsible for.

The studies performed using the 2012 dataset resulted in two publications. The first of these [2] was an early publication based on the full 2012 dataset that included a combination of results from the fully hadronic analysis channels. As these result were later superseded by those in [4] they will not be presented here. The final publication on the 2012 dataset [4] is presented in Chapter 10, again with an emphasis on my work in the one τ channel. In addition to also including the analysis channel with light leptons, most of the analysis was reworked with respect to the publication in [2]. This includes almost all of the background simulations being replaced, updated physics object definitions, re-optimisation and addition of signal and control regions, refined background estimation techniques along with additional interpretations of supersymmetric models. Before the analyses are described, both the LHC and the ATLAS experiment are introduced in Chapter 6. Chapter 7 briefly introduces the τ lepton as seen by the ATLAS detector. Finally, Chapter 8 attempts to collectively describe common features of the two analyses presented to avoid unnecessary duplications later on. In the case where something is specific to one of the analyses it has been highlighted in the text.

Chapter 6

The LHC and the ATLAS Experiment

In order to study the known elementary particles and their properties and to discover possible new types of particles we need to be able to produce these under laboratory conditions. This is done using particle colliders which accelerate particles close to the speed of light before crashing them together, making collisions energetic enough to produce new, heavy particles. The two most important properties of a particle collider are the energy of the collisions, allowing heavier particles to be produced, and the rate of collisions, which allows rare particles and processes to be investigated. Naturally we also need be able to record and investigate what happens in these collisions, which is where the detector comes into play. As the heavy particles produced in the collisions have very short lifetimes they decay almost instantly to a collection of other particles. These decay products are measured by the detector, and from their properties their origin is inferred. The salient features of such a detector is, in addition to the accuracy of its measurements, the speed at which it can take and process measurements. This makes the detector able to cope with the high collision frequency of the collider. This thesis is based on analyses of collisions provided by the world's most powerful particle collider, the LHC, and recorded by ATLAS. Both are situated at the European Organisation for Nuclear Research (CERN) and will be introduced in the following sections. Unless otherwise specified the information in the following is taken from [74] and [75] respectively for the LHC and ATLAS experiment sections.

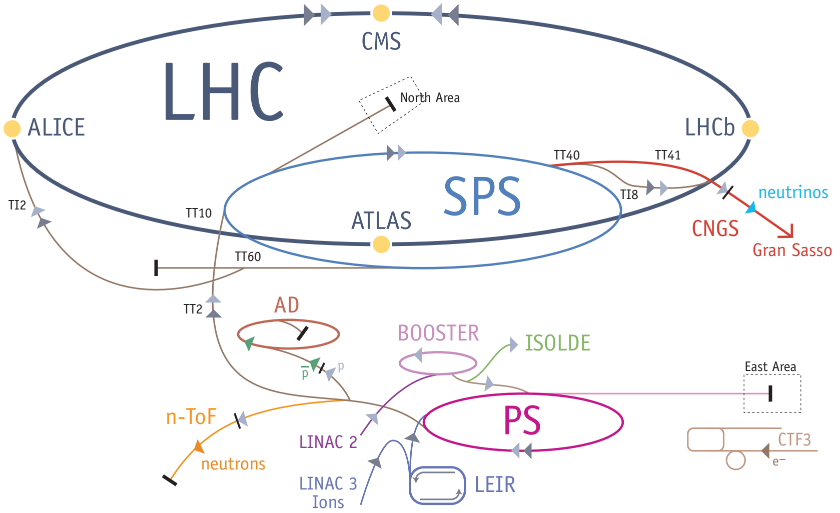

Figure 6.1: The state of the art CERN hadron roller coaster complex [76].

6.1 The Large Hadron Collider

The Large Hadron Collider (LHC) is a circular particle accelerator and collider situated at the French-Swiss border outside Geneva that is designed to collide protons at a centre of mass energy of 14 TeV. The 27 km tunnel that holds the accelerator lies 45-170 m under ground and was built in the late 80s for an earlier CERN collider called LEP. The LHC project was approved by CERN in the mid 90s and in 2000 LEP was closed, to make way for the LHC, having been operational since 1989.

6.1.1 The Life of p

The life of an LHC proton starts out in a bottle of hydrogen where the protons are snugly tucked in by electrons at the centre of hydrogen atoms. The proton is then stripped of its electron and kicked cold, naked and possibly screaming into the PS Booster by the Linac2 linear accelerator at a speed of 31.4%c (50 MeV) [76]. Unfortunately for the poor proton this is only the beginning of a long and dizzying ride through the CERN accelerators as shown in Figure 6.1. Before being lunged into the LHC the proton passes through three successively larger circular accelerators – Proton Synchrotron Booster

(PSB), Proton Synchrotron (PS) and Super Proton Synchrotron (SPS) – reaching a speed of 99.9998%c (450 GeV) [76].

The proton, however, is not alone. The mad scientist bunches 10^{11} protons together and 2808 such bunches make up a beam. During the next 20 minutes or so the proton is given small accelerating kicks by Radio Frequency cavities which are designed to give the proton a maximal speed of 99.9999991%c (7 TeV). Strong, superconducting dipole magnets are used to keep the protons in their orbit, while quadrupole magnets make sure the protons are tightly packed together, forming a nice and focused beam. For the magnets to retain their superconducting properties, and their accompanying 8 T field strength, they are contained in a cryostat system cooled to 2 K by superfluid helium.

At this point the proton is cold, nauseous and most likely tired of being pushed around at the whim of sleep-deprived physicists, when it suddenly sees a blur of long lost proton friends whizzing by – a beam heading in the opposite direction. "So, the others weren't just brought along to keep me company after all", the proton mutters to itself, as he sees a guy he recognises from the hydrogen bottle smash into his best friend, creating an explosive firework of new particles, leaving only bits of his beam mate behind. Soon after, his neighbour suffers the same fate. This excruciating, and most likely traumatising, dance goes on for hours on end as the beams intersect at four interaction points. With the large number of bunches in the beam the bunch crossings are designed to be only 25 ns apart, and the high number of protons in each bunch ensure a high probability of a proton collision occurring during a bunch crossing. Luckily for the proton, there will not be enough time for it to feel the full force of PTSD as one of two fates awaits it: colliding with another proton, possibly creating a Higgs boson or the like, sealing it's place in history as a neon coloured entry in a histogram presented in Comic Sans at a sparsely attended annual conference in the Alps; or being smeared across plates of graphite along with its comrades to the sound of a toilet flushing. After learning of the hardships endured by protons at the LHC we can take heart from the fact that it will take about a million years to accelerate a meagre gram of hydrogen [76], which will help pave the way towards uncharted territory of energy and intensity, as described in the following sections.

6.1.2 Run I Performance

Although the LHC is designed to collide protons at 14 TeV, it has been providing collisions at around half that energy during run I data taking. The reason for this is a that a faulty connection between two superconducting magnets lead to substantial damage to several magnets during initial oper-

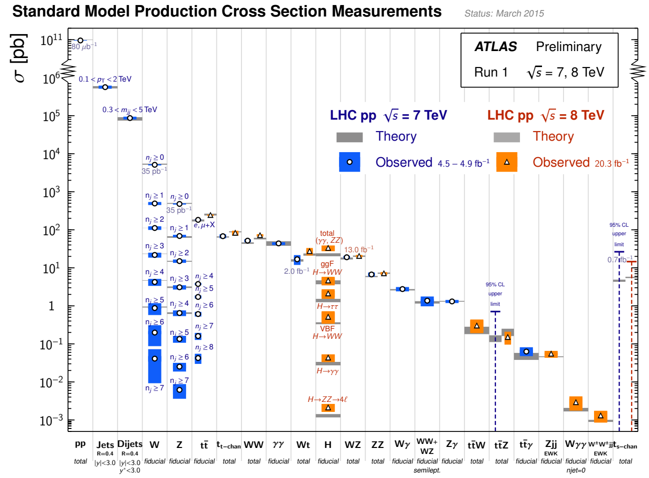

Figure 6.2: Standard Model production cross sections measured by the ATLAS experiment [77].

ation of the LHC in 2008. After being shut down for repairs, the machine resumed operation in late 2009. However, to ensure safe operation, the magnets being the main limiting factor of the achieved energy, the beam energy was reduced to 3.5 TeV for the 2010 and 2011 data taking, before being increased to 4 TeV in 2012 (collectively referred to as Run I). After a shutdown for maintenance and upgrades lasting almost two years from 2013 to 2015, the LHC resumed operation the summer of 2015 (Run II) this time with a beam energy of 6.5 TeV.

In addition to the beam energy another important performance measure is the machine luminosity, L, that depends only on the collider parameters:

$$L = \frac{N_b^2 n_b f_{\text{rev}} \gamma_r}{4\pi \epsilon_n \beta^*} F, \tag{6.1}$$

where N_b is the number of particles per bunch, n_b the number of bunches per beam, f_{rev} the revolution frequency, γ_r the relativistic gamma factor, ϵ_n and β^* are related to the beam geometry and describe the normalised transverse beam emittance and the beta function at the collision point respectively. Finally, F is a geometric luminosity reduction factor from the crossing angle at the interaction point. From the luminosity the number of events produced per second for a given process with cross section, σ, can then be expressed

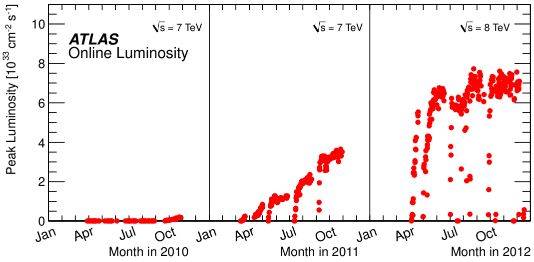

(a) Luminosity

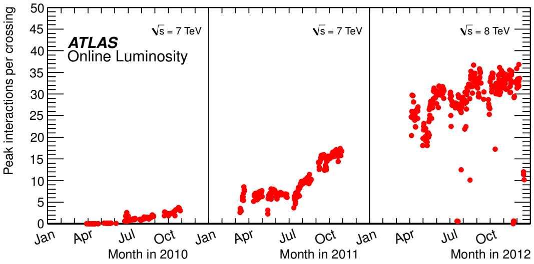

(b) Pile-up

Figure 6.3: Run I pile-up and luminosity conditions as a function of time [78].

as

$$N_{\text{event}} = L\sigma. \tag{6.2}$$

Figure 6.2 shows the Standard Model production cross sections measured by ATLAS experiment during Run I. It indicates the many order of magnitudes spanned by the different processes, and underlines the challenge faced when searching for new low cross section processes. At the design luminosity of 10^{34} cm^{-2}s^{-1} this would result in a total rate of about 600 million particle collisions per second. A commonly used measure for the amount of collected data is the integrated luminosity

$$\mathcal{L} = \int L \, \mathrm{d}t. \tag{6.3}$$

A concept closely related to the achieved instantaneous luminosity is that of pile-up. Pile-up is usually split into two categories – in-time and out-of-time pileup. In-time pile-up is the number of proton collisions per bunch

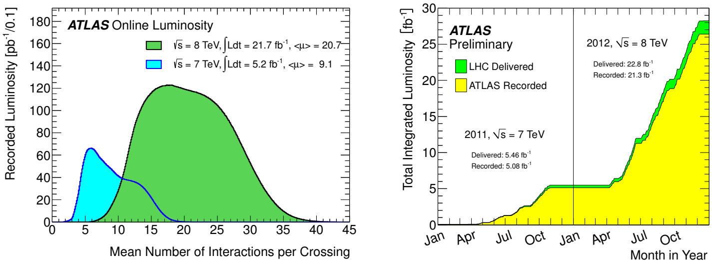

(a) Pile-up (b) Integrated luminosity

Figure 6.4: Pile-up and integrated luminosity for the run I data set [78].

crossing and is purely determined by the LHC machine parameters. Out-of-time pileup refers to remnants of the previous bunch crossing lingering in the detector during later bunch crossings, which naturally also depends on the detector parameters. Figure 6.3 shows how both the peak instantaneous luminosity and in-time pile-up has developed and increased during the run I data taking from 2010 until 2012. The maximal instantaneous luminosity achieved in 2012, close to $8 \cdot 10^{33}$ cm^{-2}s^{-1}, almost doubled that from the previous year.

Figure 6.4 shows the total amount of data collected in 2011 and 2012, along with the pile-up conditions during this period. In 2011 the centre-of-mass energy was 7 TeV, and a total integrated luminosity of 5.2 fb^{-1}with a mean pile-up of 9.1 was collected. The following year the energy was increased to 8 TeV. The mean number of pile-up was more than doubled, with an average value of 20.7. More than four times as much data was collected compared to the previous year, amounting to a total of 20.7 fb^{-1}. During run I the maximal bunch spacing was 50 ns, rather than the design value of 25 ns.

The four main experiments associated with the LHC – ATLAS, CMS, LHCb and ALICE – are located at different interaction points around the LHC ring where the proton beams are made to cross. ALICE studies heavy ion physics during the heavy ion runs of the LHC, while LHCb is purpose built for b-physics and precision measurements of rare processes. The two others, ATLAS and CMS, are multipurpose detectors designed to be sensitive to a wide range of physics processes as well as providing independent cross checks of each other's results using different detector technologies. All data in this thesis is collected by the ATLAS detector, which will be described in more detail in the following sections.

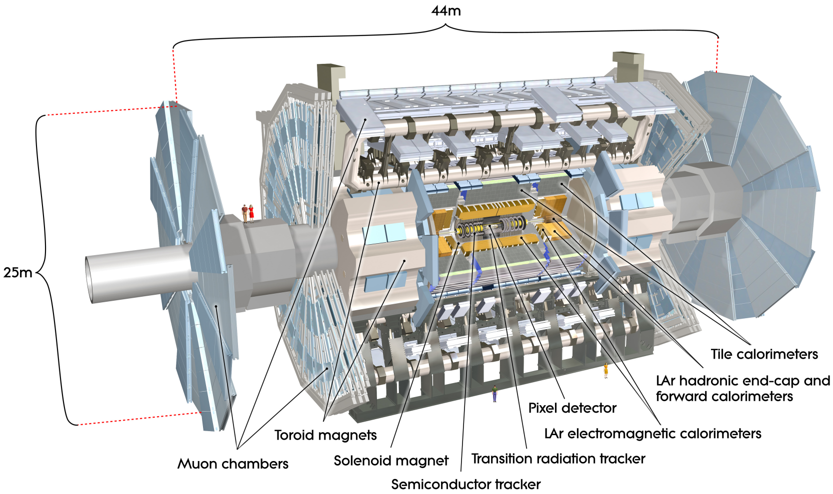

Figure 6.5: Schematic view of the ATLAS detector [79, 75].

6.2 The ATLAS Experiment

The record energy and luminosity of the LHC required development of state of the art detectors able to deal with the challenging LHC environment of high interaction rates, radiation doses, particle multiplicities and energies, in addition to providing accurate measurements for its varied physics programme. ATLAS[1] is one of two multipurpose detectors at the LHC, the other being CMS[2], whose main features will be outlined in the following.

Coordinate system

The ATLAS coordinate system, used extensively throughout this work, is defined with the interaction point as the origin, the z-axis defined along the beam, and the x-y plane transverse to the beam direction. The positive x and y directions are taken to point towards the centre of the LHC ring and upwards respectively. The azimuthal angle ϕ is the angle around the beam axis, while the polar angle θ is the angle from the beam axis. However, when measuring angles from the beam axis the pseudorapidity, $\eta = -\ln\tan(\theta/2)$,

---

[1] A Toroidal LHC ApparatuS

[2] Compact Muon Solenoid

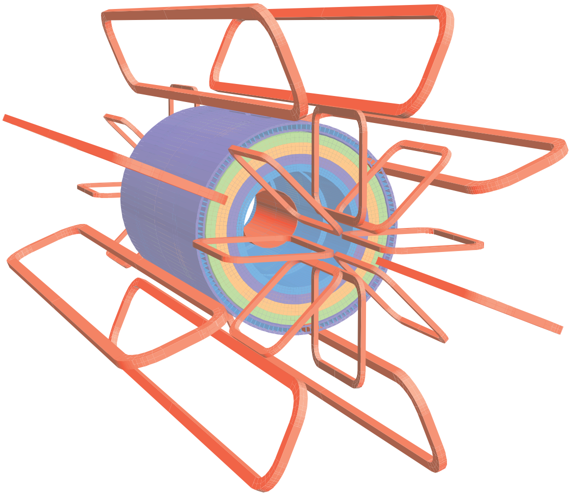

Figure 6.6: Schematic view of the ATLAS magnetic system including the calorimeter steel [75]

is commonly used. Transverse quantities denoted by the subscript T (e.g. p_{T}, $E_{\mathrm{T}}^{\mathrm{miss}}$, etc.) are defined in the transverse (x-y) plane. Often, distances are measured in $\eta - \phi$ space by $\Delta R = \sqrt{\Delta\eta^2 + \Delta\phi^2}$.

6.2.1 Magnet System

In order to measure the momentum of particles the detector takes advantage of the fact that charged particle trajectories are curved in the presence of a magnetic field. The ATLAS magnet system combines two distinct designs – one solenoidal and a toroid magnetic field. Figure 6.6 show the layout of the super conducting magnets providing the ATLAS magnetic field. The solenoid field is aligned with the beam axis, providing a 2 T magnetic field for the inner detector. As the solenoid lies within the ATLAS calorimeters the solenoid layout was optimised to minimise the amount of material in front of the calorimeter to reduce adverse effects on the calorimeter performance. In total the solenoid magnet system contributes $\sim$ 0.66 radiation lengths. The toroidal system is divided into a barrel toroid, consisting of eight characteristic looking coils, and two end-cap toroids resulting in magnetic fields of ranging in strength from 0.5 T to 1 T. To have superconducting properties the ATLAS magnets are cooled to a temperature of 4.5 K.

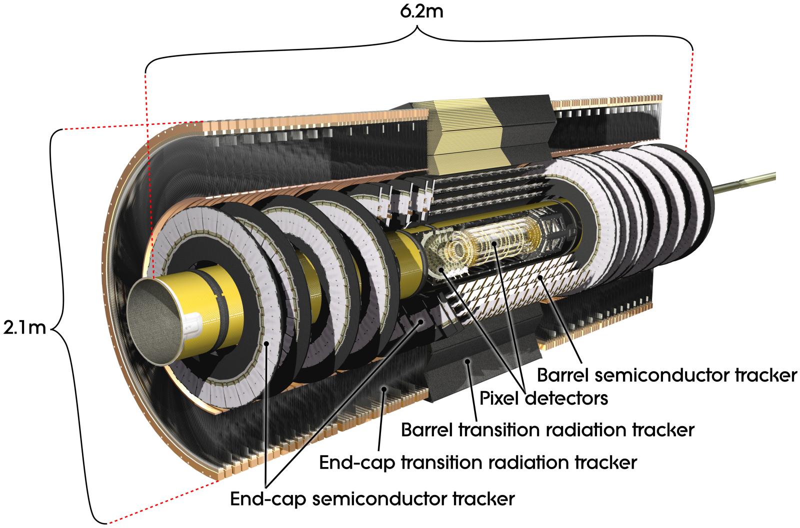

Figure 6.7: Overview of the ATLAS inner detector and its components [75].

6.2.2 Inner Detector

The Inner Detector is located at the very centre of the ATLAS detector. It is responsible for the accurate measurement of particle tracks, allowing particle momenta and track vertices to be precisely determined, in a high track density environment. To achieve the desired performance, measurements are made by three sub-detectors – a pixel tracker, silicon microstrip tracker (SCT) and transition radiation tracker (TRT) based on straw tubes. Figure 6.7 shows the schematic layout of the inner detectors. The other driving factor in the design of the Inner Detector components is the high radiation environment necessitating radiation hard detectors, along with keeping the material budget to a minimum. Figure 6.8 shows the dimensions and placement of the various inner detector components, as well as indicating their coverage in pseudorapidity.

Pixel Detector

The Pixel Detector is situated closest to the beam pipe and consists of three layers of silicon pixels at 50.5 to 122.5 mm from the interaction point in the barrel region. Additionally there are three layers in each end-cap. It

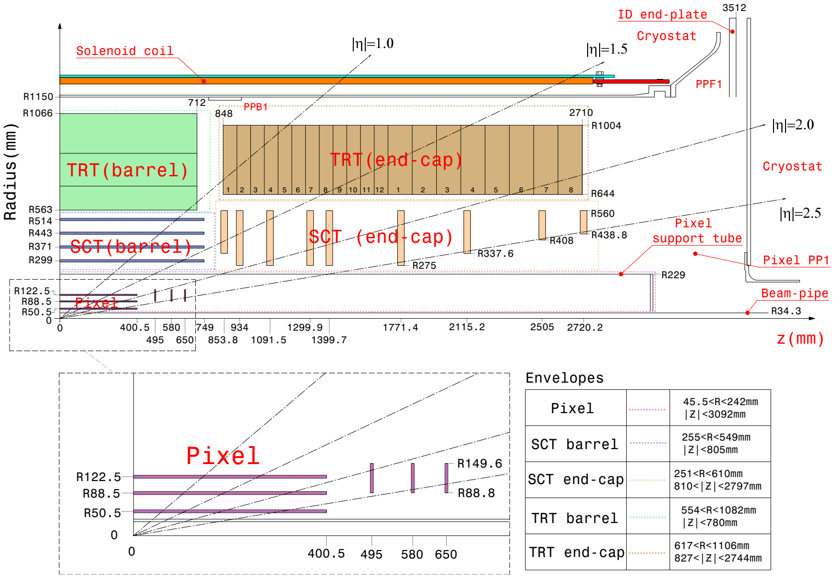

Figure 6.8: Quarter-section of the ATLAS inner detector with dimensions and various pseudorapidities indicated [75].

has a pseudorapidity coverage of $|\eta| < 2.5$ with a $r-\phi$ resolution of 10 μm and z/R resolution of 115 μm provided by $80.4 \cdot 10^6$ pixels. To reduce noise to acceptable levels even after radiation damage, the detector is cooled to a temperature between -5°C and -10°C.

Semiconductor Tracker

Outside of the Pixel Detector we find the Semiconductor Tracker (SCT) consisting of four layers of silicon strip detectors in the barrel region, and 9 layers in each end-cap. Each layer consists of two-sided modules where the strips of each side are rotated with a stereo angle with respect to each other to provide two-dimensional measurements. This results in a $r-\phi$ resolution of 17 μm and z/R resolution of 580 μm from a total of 6.3 million readout channels. Like for the pixel detector, the pseudorapidity coverage is $|\eta| < 2.5$ and the detector is cooled to the same temperature as the pixel detector.

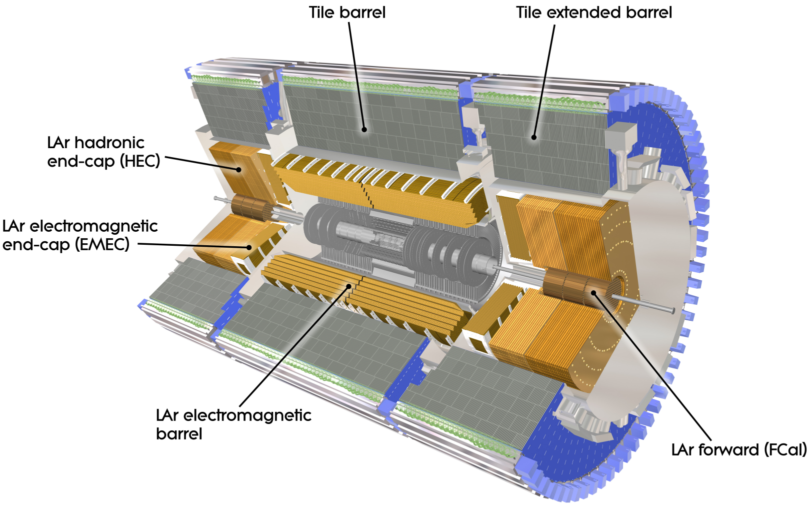

Figure 6.9: Overview of the ATLAS calorimeter system [75].

Transition Radiation Tracker

The outermost component of the inner detector is the Transition Radiation Tracker (TRT) composed of 4 mm diameter straw tubes filled with a Xe, CO_2, O_2 gas mixture. Typically more than 30 (on average 36) track hits are registered in the TRT up to a pseudorapidity of $|\eta| = 2.0$. The straws run parallell to the beam axis in the barrel region, while they are configured radially in wheels in the end-caps, and consist of a total of 351 000 readout channels. The TRT only provides information in the $r - \phi$ direction, where its accuracy is 130 μm per straw, and is operated at room temperature. Additionally, the TRT provides valuable information for particle identifications as electrons may be separated from hadrons, mostly pions, by the amount of transition-radiation photons emitted in the straw tube gas mixture.

6.2.3 Calorimeter System

The ATLAS calorimeters are situated outside the solenoid magnet and are used to measure particle energies and consist of two main components, an electromagnetic and a hadronic calorimeter, with the names indicating the type of particles that are measured. The calorimeters extend to $|\eta| = 4.9$, but the central part ($|\eta| < 2.5$) has the best resolution. Although the calorimeters employ different technologies, they are both sampling calorimeters characterised by absorber material, responsible for stopping and showering the incident particle, interleaved with active material that measures the shower induced in the absorber. From these samples of the shower energy measured in the active components the energy of the incident particle is inferred.

For analyses based on $E_{\mathrm{T}}^{\mathrm{miss}}$, such as many SUSY searches, the calorimeters are particularly important. To accurately estimate $E_{\mathrm{T}}^{\mathrm{miss}}$ in a collision the energy must be measured over almost the full η range, which is achieved by the $|\eta| < 4.9$ coverage, and the calorimeters should have good containment of both hadronic and electromagnetic showers. To this end the electromagnetic calorimeter is greater than 22 radiation lengths in the barrel, and greater than 24 in the end-caps. Good resolution, even for very energetic jets, is achieved by the $\sim$10 interaction lengths of active calorimeter material across the pseudorapidity range.

Electromagnetic calorimeter

The electromagnetic (EM) calorimeter consists of a barrel part ($|\eta| < 1.475$) and two end-cap components ($1.375 < |\eta| < 3.2$) where lead absorber plates are sandwiched by active material of liquid argon (LAr). The EM calorimeter has an accordion geometry, resulting in complete azimuthal symmetry without any cracks. Furthermore, the EM calorimeter is sub-divided into three layers segmented in $|\eta|$, with the first layer being the most finely grained, providing precise position measurement and shower shape information. At $|\eta| < 1.8$ a LAr presampler layer is used to correct for energy lost by electrons and photons before the calorimeter.

Hadronic calorimeter

Responsible for measuring hadrons right outside the EM calorimeter we find the hadronic calorimeter, which has three main components – the Tile Calorimeter, the LAr hadronic end-cap calorimeter and the LAr forward calorimeter. The tile calorimeter uses steel as the absorber material and scintillating tiles as the active material and extends to $|\eta| < 1.7$. The scintillating tiles are read out by wavelength shifting fibers coupled to photomultiplier tubes at two sides. The Hadronic End-cap Calorimeter (HEC) covers the region $1.5 < |\eta| < 3.2$ and uses copper plate absorbers and LAr for the active sampling material. The final component is the Forward Calorimeter

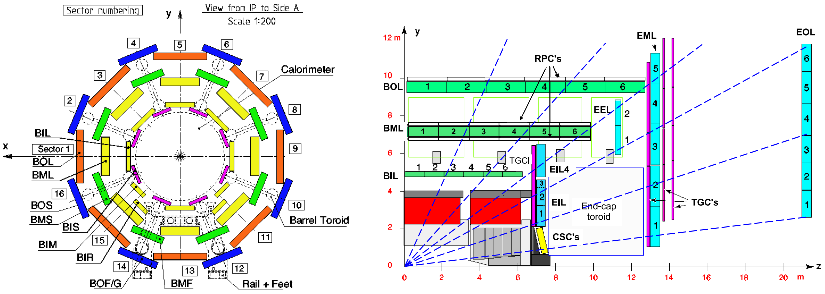

Figure 6.10: Schematic cross section views of the ATLAS muon spectrometer [75].

(FCal) covering $3.1 < |\eta| < 4.9$. It is split into three layers all using LAr for the active material, while the first uses copper for the absorber material, optimised for electromagnetic measurements, the two others have tungsten absorbers used for predominantly for the measurement of hadronic interactions.

6.2.4 Muon Spectrometer

The outermost component of the ATLAS detector is the muon spectrometer designed to detect and measure the momentum of muons, which traverse both the inner detector and calorimeter system, in the region $|\eta| < 2.7$. Their momentum is measured by the deflection of muon tracks in the magnetic field of the air-core toroid magnets. The system is instrumented with separate tracking and triggering chambers with the tracking chambers consisting of three separate layers. Tracking is provided by the Monitored Drift Tubes (MDT's) over most of the $|\eta|$ range, while at large pseudorapidities the Cathode Strip Chambers (CSCs) are responsible for the measurements. The muon trigger system covers a smaller pseudorapidity range than for the tracking ($|\eta| < 2.4$) and consists of the Resistive Plate Chambers (RPC's) in the barrel and Thin Gap Chambers (TGC's) in the end-cap regions. Figure 6.10 shows an overview of the ATLAS muon system.

Table 6.1 summarise the design performance of the ATLAS detector components that are used to construct the physics objects for analysis.

Table 6.1: Summary of the design performance goals of the ATLAS detector (units in GeV).

Detector component	**Resolution**	**Coverage**
Tracking	$\sigma_{p_\mathrm{T}}/p_\mathrm{T} = 0.05\% \times p_\mathrm{T} \oplus 1\%$	$\eta < 2.5$
EM calorimetry	$\sigma_E/E = 10\%/\sqrt{E} \oplus 0.7\%$	$\eta < 3.2$
Hadronic calorimetry	$\sigma_E/E = 50\%/\sqrt{E} \oplus 3\%$	$\eta < 3.2$
	$\sigma_E/E = 100\%/\sqrt{E} \oplus 10\%$	$3.1 < \eta < 4.9$
Muon spectrometer	$\sigma_{p_\mathrm{T}}/p_\mathrm{T} = 10\%$ at $p_\mathrm{T} = 1$ TeV	$\eta < 2.7$

6.2.5 Trigger System

At design operation LHC bunch crossings occur at a frequency of 40 MHz. Given a typical ATLAS event size of about 1-2 MB it is not feasible to read and store all of the collision data. However, as can be seen from Figure 6.2, the vast majority of the collisions produce only low momentum jets. By selecting only collisions with specific properties of the physics processes of interest, the rate of the collected data can be reduced by several orders of magnitude, bringing it down to manageable levels. This first online selection of interesting collisions for storage and further processing is performed by the trigger system. The trigger consists of three levels of event filtering – Level-1 (L1), Level-2 (L2) and event filter (EF). Together the EF and L2 levels form the High-Level Trigger (HLT) and are software based, unlike the L1 trigger, which is based on hardware decisions.

The L1 trigger uses coarse information from the RPC, TGC and calorimeters to search for and select signatures with leptons, jets, $E_\mathrm{T}^\mathrm{miss}$ and large total transverse energy. The calorimeter information is from 0.1×0.1 $\Delta\eta \times \Delta\phi$ trigger towers in the calorimeters. Trigger objects are identified by fixed size $(2 \times 2, 4 \times 4$, etc.) sliding windows of trigger towers. The L1 trigger reduces the data to a maximal rate of 75 kHz, with each trigger decision made within 25 μs of the associated bunch crossing.

The L1 trigger identifies Regions-of-Interest (RoIs) where it has identified possible trigger objects in the event. These RoIs are passed to the L2 trigger which use more finely grained information from these regions to refine the L1 trigger decision. The fact that only the RoI data is used reduces the amount of data that needs to be transferred from the detector readout and is typically only 1-2% of the total event data. The resulting processing time is about 40 ms at an output event rate below 3.5 kHz.

Finally the event is processed by the event filter which uses offline analysis procedures on full events to further reduce the event rate to about 200 Hz. The average processing time of the EF is about four seconds. Both levels of the HLT use algorithms based on the full granularity of the calorimeters and the muons system as well as information from the inner detector to make triggering decisions.

6.2.6 Particle Reconstruction and Identification

Physics analysis objects related to specific particles, or groups of particles, in the detector must be defined when interpreting ATLAS data. These are reconstructed from the raw detector deposits giving tracks in the inner detectors and muon spectrometer along with energy deposits in the calorimeters. By taking advantage of the specific detector signatures of the various particle species the physics objects can furthermore be identified to be of a certain particle type. Figure 6.11 illustrates the basic detector characteristics used to distinguish particle types in the ATLAS detector. The following section will outline the basics of particle reconstruction and identification in ATLAS.

Electrons

Electrons are reconstructed by matching energy deposits in the electromagnetic calorimeter to charged particle tracks in the inner detector. In the central region seed cluster of the calorimeter deposit is required to have $E_{\mathrm{T}} > 2.5$ GeV, and is found using a sliding-window algorithm with a window size of 3×5 in units of 0.025×0.025 in $\eta \times \phi$ space. This cluster is then loosely matched to the extrapolated track by requiring the distance between the two to be within $\Delta\eta < 0.05$. In the transverse plane the distance between the two is required to be $\Delta\phi < 0.1$ in the direction of track curvature, and $\Delta\phi < 0.05$ in the opposite direction, where the different values are introduced to account for radiative bremsstrahlung energy loss. If multiple tracks are matched to the same cluster, tracks with silicon hits are preferred and subsequently the track with smallest ΔR is selected.

The electron cluster is then rebuilt from 3×7 longitudinal towers of cells, and the cluster energy determined. The cluster energy is the sum of four components — the estimated energy deposited in front of the EM calorimeter; the energy measured in the cluster; the estimated energy deposited outside the cluster (lateral leakage); the estimated energy deposited beyond the EM calorimeter (longitudinal leakage). These terms are parametrised, based on simulations, by the measured cluster energies in the presampler and the three longitudinal EM calorimeter layers and depend on the material in the relevant

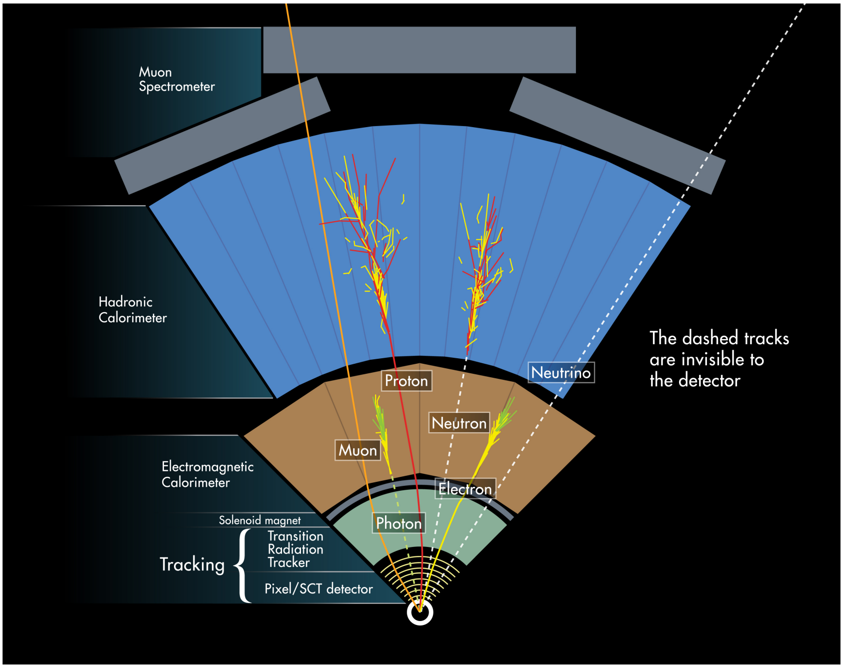

Figure 6.11: Cross section of the ATLAS detector indicating the detector signatures of different particle types and how these are used for particle identification [80].

part of the detector. The reconstructed electron energy is set to the cluster energy, while the direction is determined by the η and ϕ values of the track at the vertex.

In order to separate signal electrons from background electrons (e.g. from photon conversion), and jets faking electrons, cut-based electron identification selections are applied. Three cumulative baseline sets of identification selections has been defined with an increasing level of background rejecting power. The loose selection includes information on the EM calorimeter shower shape and leakage to the hadronic calorimeter. The medium selection adds variables from the EM calorimeter strip layer, track quality requirements and a more stringent track-cluster matching. Finally the tight identification adds further track-cluster matching and track quality criterion, as well as particle identification information from the TRT and explicit requirements agains photon conversions. The selections have been optimised in bins of both electron η and E_{T}.

Muons

The reconstruction and identification of muons is based mainly on information from the Muon Spectrometer (MS) and the inner detector. Muon spectrometer tracks start out as local track segments within each layer of chambers, before tracks from different layers are combined into reconstructed muon spectrometer tracks. In addition to the MS tracking the inner detector provides tracking close to the interaction point.

The reconstructed muons are usually grouped into four categories depending the information going into the reconstruction. Stand-Alone (SA) muons are muons where the tracks are reconstructed only in the MS, and the track is extrapolated back to the interaction point, taking into account energy loss in the calorimeters. SA muons are used mainly to extend the acceptance beyond that covered by the inner detector ($2.5 <| \eta |< 2.7$). The main type of muons are combined muons (CB) for which there exists both ID and MS tracks which are combined to give a muon track. Segment-tagged (ST) muons are muons with an extrapolated ID track matched to at least one local track segment in the MDT or CSC chambers. Finally, a muon is said to be calorimeter-tagged (CaloTag) if a track in the ID is matched to calorimeter energy deposit consistent with a minimum ionizing particle. This category helps recover acceptance in the uninstrumented regions of the MS.

Independent reconstruction algorithms for muons, using different methods, has been used for the ID-MS combination. One of them performs a statistical combination of the track parameters of the SA and ID muons from the covariance matrices, while the other performs a global fit of the muon track to the ID and MS hits. In the latter, applicable quality criteria are also applied to the ID tracks.

Jets

Jets are reconstructed using the anti-k_t algorithm [81] with distance parameter $R = 0.4$. Like other clustering algorithms it iteratively clusters proto jets i and j separated by a distance d_{ij}, and the distance between i and the beam (B) written as d_{iB}. The clustering first finds the smallest of the distances. If the smallest distance is a d_{ij} then i and j are combined, while if it is d_{iB} then i is deemed a jet and removed from the list of proto jets.

Distances are then recalculated and the procedure repeated until the list of proto jets are exhausted.

The anti-k_t algorithm differs from other clustering algorithms, like k_t and Cambridge/Aachen, in the definition of the distances [81]:

$$d_{ij} = min(k_{ti}^{2p}, k_{tj}^{2p}) \frac{\Delta_{ij}^2}{R^2}, \tag{6.4}$$

$$d_{iB} = k_{ti}^{2p}, \tag{6.5}$$

where $\Delta_{ij}^2 = (y_i - y_j)^2 + (\phi_i - \phi_j)^2$ and k_{ti}^{2p}, y_i, ϕ_i are the transverse momentum, rapidity and azimuth angle of proto jet i respectively. The k_t algorithm corresponds to the choice $p = 1$, while choosing $p = 0$ yields the Cambridge/Aachen algorithm. The anti-k_t algorithm is obtained by setting $p = -1$ (i.e. the inverse with respect to the k_t algorithm).

Jets are built from topological calorimeter clusters with positive energy. Topological clusters are groups of calorimeter cells. The clusters are seeded by a cell with high signal-to-noise ratio before neighbouring cells are added iteratively to the cluster being built. The original topo-cluster may be split into separate clusters if cells corresponding to significant local energy maxima in the cluster is found. The topo-cluster energy is defined to be the energy sum of its constituent cells, considered to have zero mass, and direction calculated from a weighted average over its cells.

Missing transverse momentum

An important quantity in SUSY searches is missing transverse momentum, as it could signal the presence of unseen particles in the event. It is defined as the momentum imbalance in the plane perpendicular to the beam line and is taken to be the negative vector sum of all particle momenta in a collision. In addition to real missing transverse momentum from weakly interacting particles there are multiple contributors to fake $E_{\mathrm{T}}^{\mathrm{miss}}$. This includes particles escaping detection at high pseudorapidities, or in inactive regions between calorimeters, dead and noisy readout channels as well as cosmic-ray and beam-halo muons traversing the detector.

$E_{\mathrm{T}}^{\mathrm{miss}}$ is reconstructed by summing contributions mainly from calorimeter energy deposits along with muons reconstructed in the muon spectrometer. The inner detector also contributes by adding information on low p_{T} particles that cannot be measured by the calorimeters or muon spectrometer respectively. The missing transverse momentum is then calculated as:

$$E_{\mathrm{T}}^{\mathrm{miss}} = \sqrt{\left(E_x^{\mathrm{miss}}\right)^2 + \left(E_y^{\mathrm{miss}}\right)^2} \tag{6.6a}$$

$$\phi^{\mathrm{miss}} = \tan^{-1}\left(E_y^{\mathrm{miss}}, E_x^{\mathrm{miss}}\right) \tag{6.6b}$$

The calorimeter terms are calculated from calibrated calorimeter cells as:

$$E_x^{\mathrm{miss,term}} = -\sum_{i=1}^{\mathrm{N_{cell}^{term}}} E_i \sin\theta_i \cos\phi_i \tag{6.7a}$$

$$E_y^{\mathrm{miss,term}} = -\sum_{i=1}^{\mathrm{N_{cell}^{term}}} E_i \sin\theta_i \sin\phi_i \tag{6.7b}$$

where E_i, θ_i and ϕ_i are the energy, polar angle and azimuthal angle respectively. The cells are calibrated according to the physics object they are matched to, and if there is no associated object the cells are included in a dedicated term for soft deposits with LCW calibration applied. The sum runs over cells matched to analysis objects, as well as soft term cells, in the region $|\eta| < 4.5$. To suppress noise only cells belonging to calorimeter topological clusters, unless the clusters are matched to an electron or photon, go into the sum.

The $E_{\mathrm{T}}^{\mathrm{miss}}$ contribution from muons are included by summing the momenta of selected muons

$$E_{x(y)}^{\mathrm{miss},\ \mu} = -\sum_{muons} p_{x(y)}^{\mu}. \tag{6.8}$$

Due to the coverage of the Muon Spectrometer the sum runs over muons in the range $|\eta| < 2.7$. To correctly account for the muon energy deposited in the calorimeters the cases where the muon is close to a jet in the event (non-isolated muon) are treated differently to when it is not (isolated muon).

6.2.7 Monte Carlo Simulations

When searching for new physics in any experiment it is crucial to accurately describe the expected backgrounds in order to draw conclusions on potential signals with any kind of confidence. In ATLAS analyses the modelling of Standard Model backgrounds are heavily reliant on the Monte Carlo simulations of such processes. The accuracy required for these simulations means that in addition to the physics process in the collision, also the high intensity LHC environment and the detailed detector response must be accurately

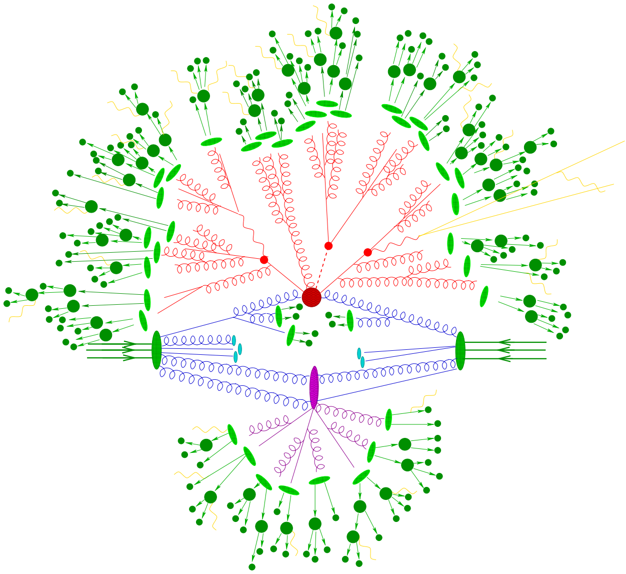

Figure 6.12: Illustration of a simulated event [82].

modelled. The resulting simulations are, as a result, highly complex and under constant development to accurately describe experimental data under challenging and extreme conditions.

ATLAS simulations can roughly be divided into three main components – generation of the physics event; simulation of the detector response; and digitisation of the detector deposits. Several Monte Carlo generators exist which are able to model proton-proton collisions. While the specifics of the physics implementations in the generators are different, the main steps going into the event generation is similar between the generators.

The initial proton-proton collision is described by the hard scattering between partons of the colliding protons. This gives rise to final states containing only elementary particles. To calculate this hard scattering the matrix element of the particle interaction and production, along with the momentum distribution of the initial colliding partons must be known. The matrix element is calculated in perturbative QCD, while the initial momenta are given by the proton parton distribution function (PDF) as exemplified in Figure 6.13. After the initial hard scatter is simulated, additional gluon radiation is added to account for either initial or final state particles radiating gluons. This step is called showering and continues down to a low energy cut-

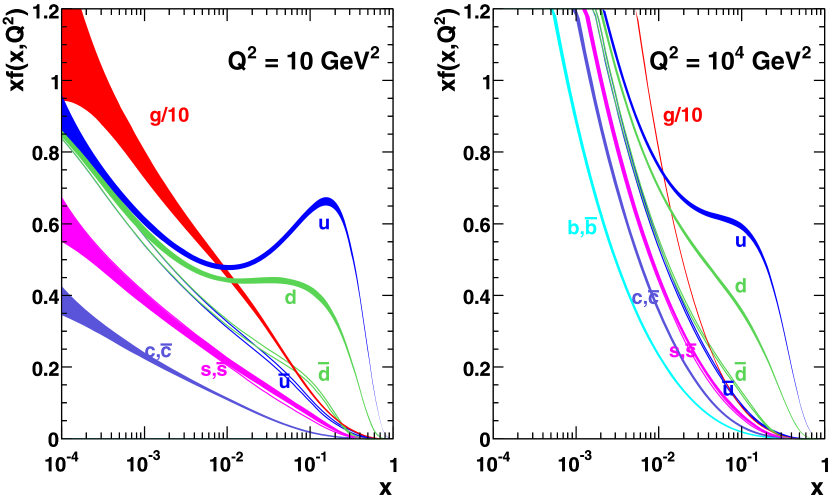

Figure 6.13: Proton parton distribution (MSTW 2008) function at different momentum transfers [85].

off for the radiating particles. In the final step of event generation quarks and gluons are, due to confinement, hadronised into mesons and baryons. This hadronisation step is usually performed differently across generators, and due to the non-perturbative nature of the process generator parameters are tuned to reproduce experimental results [83]. Figure 6.12 illustrates the different components of a simulated event produced by the `SHERPA` generator. For a more complete introduction to the LHC event generators see for example [84].

After the collision itself has been simulated the interaction of the particles with the detector is modeled using GEANT4 [86]. The detector simulation includes the full detector geometry including both active (sensitive detector material) and inactive material (services like cables, cryostats, etc.) and stores the interactions of particles with the detector. These simulated interactions are in the final step transformed (digitised) to the detector output format expected from the readout electronics, that is currents and voltages, in real experimental data. The pileup conditions of the LHC are modelled by overlaying multiple simulated events before the digitisation stage of the simulation [87]. After this step the simulated collision events are passed through reconstruction in the exact same way as real experimental data.

As the GEANT4 detector simulation is very time consuming, an alternative and fast simulation, called AtlFast-II or `AFII` for short, is sometimes used [88]. This algorithm, among other things, uses a parametrised response for the calorimeters, thus significantly reducing the time required for simulating an event. Although the fast simulation is not as accurate as the full detector simulation, the benefits of the increase in simulated statistics it allows for sometimes outweigh the drawbacks of the loss of accuracy.

Chapter 7

The τ Lepton in ATLAS

The τ lepton is the heaviest of the leptons with a mass of 1.777 GeV and a proper decay length of 87 μm, corresponding to a mean lifetime of $290.3 \cdot 10^{-15}$ s [24]. This very short lifetime means that detecting τ leptons with the ATLAS detector is a very different process compared to detecting their leptonic siblings — the electron and the muon. While the lighter leptons are detected directly, the short lifetime of the τ means that it decays before reaching the active regions of the detector. This means that what constitutes a τ from an experimental point of view are the visible decay products of the τ lepton.

There are two possible decay modes for the τ, commonly referred to as hadronic or leptonic decays. The leptonic decays are characterised by decays to a muon or electron along with two neutrinos, while the hadronic decay, as the name suggests, are decays into hadrons accompanied by a neutrino. As the neutrino is only weakly interacting and therefore escapes detection, the only part of the decay that is observed are the leptons or the hadrons. For

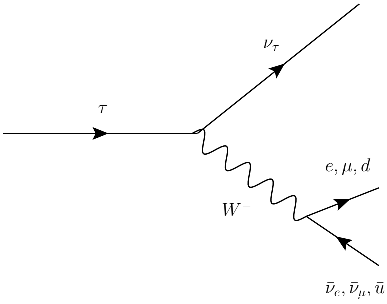

Figure 7.1: Feynman diagram of τ decay.

Table 7.1: Requirements imposed on tracks associated with a reconstructed τ lepton.

p_{T}	> 1 GeV
Pixel hits	≥ 2
SCT hits	≥ 7
Transverse distance τ vertex	$\lvert d_0 \rvert < 1.0$ mm
Longitudinal distance τ vertex	$\lvert z_0 \sin\theta \rvert < 1.5$ mm

the most part electrons and muons originating from τ decays are difficult to distinguish from prompt leptons. It is therefore commonly only the visible decay products of hadronic decays that are referred to when speaking of a τ in ATLAS. This is also the case throughout the ATLAS analyses presented in this thesis. The hadronic τ lepton decays constitute 65% of the total decay modes. Most commonly these decays contain either one or three charged pions, 72% and 22% of the decays respectively, while the remainder mostly contain charged kaons. A large fraction of these decays also contain a neutral pion [24].

A main challenge in identifying hadronic τ decays is to distinguish them from other particles with similar signatures in the detector. It is especially hard to separate a τ decaying into several charged hadrons from jets of hadrons produced when quarks and gluons fragment. Similarly electrons, and sometimes even muons, can be mistakenly identified as a τ decay with a single charged particle. τ leptons are identified using the main characteristics of the τ jet, such as the shower shape and composition, together with information from the reconstructed τ tracks.

7.1 Reconstruction

The input to the τ reconstruction algorithm are anti-k_t jets with a distance parameter of 0.4 satisfying $p_{\mathrm{T}} > 10$ GeV and $\eta < 2.5$ [89]. Furthermore, the event is required to have reconstructed primary vertex with at least three associated tracks [90]. As there are usually multiple simultaneous interactions in an event, and thus also often several primary vertex candidates, the vertex with the highest sum of associated track p_{T} is chosen. However, this is not necessarily the same vertex as the τ originated from. In order to make both τ reconstruction and identification more stable against pile-up the τ vertex is determined by matching the τ candidate tracks to the vertices — choosing the vertex associated with the largest p_{T} summed fraction of τ tracks. This

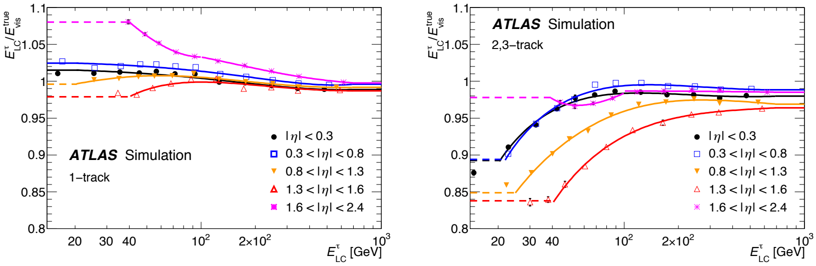

(a) One track (b) Three tracks

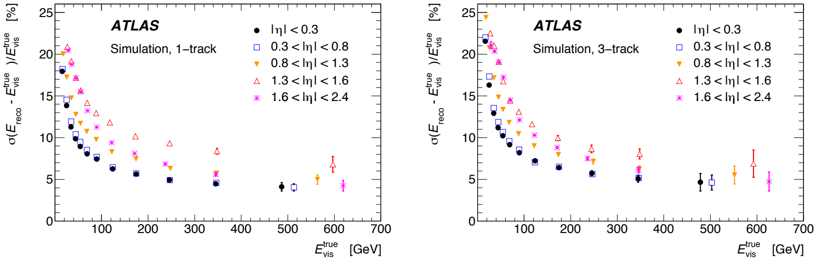

(c) One track (d) Three tracks

Figure 7.2: Response curves (top) for hadronically decaying tau leptons for different pseudorapidity regions [90]. Offline energy resolution (bottom) for hadronically decaying tau leptons for different pseudorapidity regions [90].

vertex is in turn used to determine the τ direction, associated tracks as well as being the basis for calculating identification variables. The τ vertex and the primary vertex are different in about 10% and 1% of events in low and high p_{T} environments respectively [90].

The τ momentum magnitude and direction is calculated by summing topoclusters, at the LC scale and in the tau vertex coordinate system, within $\Delta R < 0.2$ of the jet seed barycenter. Tracks associated with the τ are similarly required to lie within $\Delta R < 0.2$ of the τ direction and satisfy the requirements in Table 7.1. The same requirements are imposed on tracks in the region $0.2 < \Delta R < 0.4$ used for τ identification described in the next section. Furthermore an η- and p_{T}-dependent energy calibration, shown in Figure 7.2, to the hadronic τ energy scale (TES) is applied to match the reconstructed to the true τ energy [91]. This additional energy correction is needed as the calibration already applied to the input jets are not tailored to

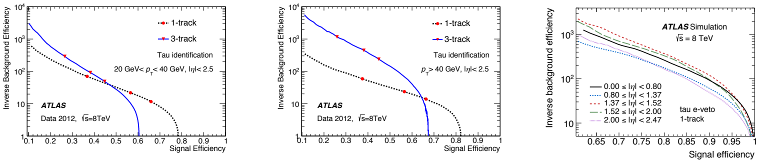

(a) τ ID – low τ p_{T} (b) τ ID – high τ p_{T} (c) Electron veto

Figure 7.3: Inverse background efficiency versus signal efficiency for the offline tau identification (top) and the 1 track τ electron veto (bottom) [90]. The red markers correspond to the loose, medium and tight ID working points. Signal efficiencies are obtained from simulations and include both reconstruction and identification efficiencies. ID background efficiencies are obtained from multijet data, and electron veto background efficiency from simulated $Z \to ee$ events.

the specific hadronic composition, nor the cone size of a τ jet. The resulting τ energy resolution (TER) is shown in Figure 7.2 and ranges from around 20% at low energies to about 5% at high energies.

7.2 Identification

The reconstruction described in the previous section provides little rejection against jets initiated by quarks and gluons. It is therefore necessary with a separate step to identify and distinguish the reconstructed τ candidate from jets and electrons. The following variables are used for τ identification [90]:

Central energy fraction Fraction of transverse energy deposited in the region $\Delta R < 0.1$ with respect to all energy deposited in the region $\Delta R < 0.2$ around the τ candidate.

Leading track momentum fraction The transverse momentum of the highest-p_{T}charged particle in the core region of the τ candidate, divided by the transverse energy sum.

Track radius p_{T}-weighted distance of the associated tracks to the τ direction within a cone of $\Delta R < 0.4$.

Leading track IP significance Transverse impact parameter of the highest-p_{T}track in the core region divided by its estimated uncertainty.

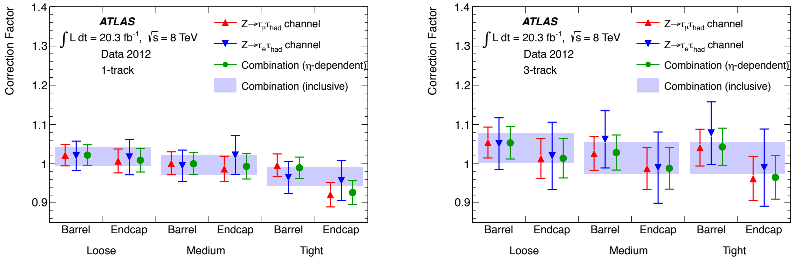

(a) One track (b) Three tracks

Figure 7.4: Identification efficiency corrections applied to hadronically decaying τ leptons [90].

Number of tracks in the isolation region Number of tracks associated with the τ in the $0.2 < \Delta R < 0.4$.

Maximum ΔR The maximum ΔR between a track associated with the τ candidate and the τ direction.

Transverse flight path significance The decay length of the secondary vertex in the transverse plane divided by its estimated uncertainty.

Track mass Invariant mass calculated from the sum of the four-momentum of all tracks.

Track-plus-π^0-system mass Invariant mass of the system composed of the tracks and π^0 mesons.

Number of π^0 mesons Number of π^0 mesons reconstructed.

Ratio of track-plus-π^0-system p_{T} Ratio of the p_{T}estimated using the track + π^0 information to the calorimeter-only measurement.

These variables are used as input to two separate BDT algorithms aimed at identifying single and multi track τ decays respectively. Three working points (loose, medium and tight) corresponding to different τ identification efficiencies are defined, as seen in Figure 7.3. The working point signal efficiencies are to good approximation independent of both τ p_{T} and pile-up

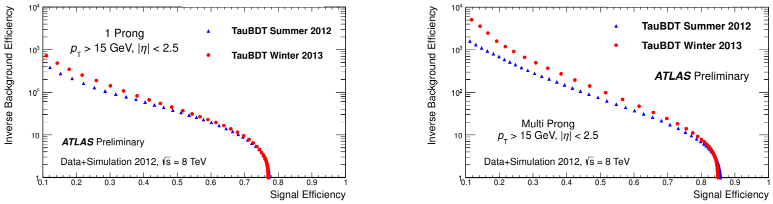

(a) One track

(b) Two and three tracks

Figure 7.5: Comparison of the background and signal efficiencies of the τ identification available in 2012 and 2013 [92].

conditions. Correction factors, shown in Figure 7.4, are also applied to adjust the τ identification efficiency to the level observed in data.

In addition to jets faking a τ lepton, also electron and muons may mimic a single track τ signature in the detector. As for jets though, there are handles to further distinguish an electrons from a τ— transition radiation is more likely to be emitted by an electron; the angular distance of the track to the jet seed direction; the ratio of energy deposited in the EM relative to that in the hadronic calorimeter and the ratio of energy deposited in the outer part of the τ jet cone relative to the total energy. Variables quantifying these differences are combined in a BDT used for electron-τ separation. The performance of the τ electron veto is shown in Figure 7.3. Muons are to a lesser extent misidentified as a τ, but can be further reduced by the standard muon identification along with selections on the EM fraction and track-p_{T} to E_{T} of the calorimeter deposit [90].

Even though this section describes the final τ reconstruction and identification of the 2012 data taking period, that was used for the 8 TeV analysis presented in this thesis, the techniques and approach was similar also for the 2011 data taking. The main improvements of the τ identification and reconstruction between these two periods, in addition to improved performance as can be seen in Figure 7.5, was increased stability against pile-up. This was necessary to deal with the significant increase in simultaneous interactions in 2012 compared to the 2011 data taking period.

Chapter 8

Analysis Overview

There are many shared aspects of the two analyses presented in this thesis. This chapter will attempt to summarise and describe common points, while highlighting any distinctions, and differing features, that are bound to occur in a joint description. The two following chapters will then describe the details and results of the analyses.

8.1 Physics Object Definitions

In both the analyses standard ATLAS physics object definitions are used to define the objects that enter the analyses [93]. These definitions are provided by dedicated performance groups in ATLAS for collaboration wide use in physics analyses. These recommendations, along with other common tools, are in turn collected in a common framework used in the ATLAS Supersymmetry group called `SUSYTools` [94]. For the 7 TeV analysis object definitions equivalent to those in `SUSYTools 00-00-67-01` were implemented, while in the final 8 TeV iteration of the analysis `SUSYTools 00-03-14` was used.

Jets

Jets are reconstructed using the anti-k_t algorithm with a distance parameter of $\Delta R = 0.4$ in $\eta - \phi$ space. Topological calorimeter clusters [95, 96, 97], which aim to reconstruct the shower of particles entering the calorimeter in three dimension, are given as input to the algorithm, and summed as massless four-vectors.

Several jet calibrations are available in ATLAS, and for the 8 TeV edition of this analysis the local cluster weighting (LCW) method [98] was used. This method applies separate energy corrections [95] to topological clusters depending on whether they are deemed to be of hadronic or electromagnetic origin. For the 7 TeV analysis all jets were calibrated at the electromagnetic scale. On top of this a calibration of the jet energy derived from simulations, jet energy scale (JES), was applied to match the calorimeter's response to the true jet energy [95]. Effects caused by additional pile-up activity are accounted for using the jet area subtraction method [99, 100], that estimates pile-up in the event as well as the jet's sensitivity to the estimated pile-up.

As a baseline, jets are required to lie within $|\eta| < 2.8$ and have $p_T >$ 20 GeV. These baseline jets are used for overlap removal, before additional quality and kinematic requirements are imposed on the jets as described in Section 8.2. For the 8 TeV analysis additional selections were applied to the jets to mitigate the effects of the increased amount of pileup in the 2012 data taking relative to that of 2011. The jets were required to have $|\eta| < 2.5$ and $p_T > 30$ GeV and all central jets ($|\eta| < 2.4$) below 50 GeV were required to have a jet vertex fraction above 50%. Jet vertex fraction is defined as the transverse momentum ratio of the sum of jet-matched tracks that originate from the primary vertex, to the sum of all tracks associated with the jet.

b-jet

Jets originating from *b*-quarks are identified using the MV1 jet tagger [101]. The tagger takes advantage of the longer lifetime, and consequently decay length, of *b*-quarks relative to light quarks. This is achieved by using information on the track impact parameters and any secondary vertices along the jet axis [102]. The MV1 algorithm is based on a neural network taking the output of three *b*-jet tagging algorithms (JetFitter+IP3D, IP3D and SV1) as input [101]. Jets with $p_{\mathrm{T}} > 25$ GeV, $|\eta| < 2.5$ that are tagged as *b*-jets by the MV1 algorithm, at the 60% working point, are identified as *b*-jets in the analysis. At the 60% b-tagging efficiency working point, the misidentification rate of light quark or gluon jets was less than one percent in the 7 TeV analysis [103] and less than 0.5% in the 8 TeV analysis.

Electrons

Electrons were required to satisfy $p_{\mathrm{T}}>$ 20 GeV and $\eta<$ 2.47. In addition they were required to pass Medium++ identification [104], and be reconstructed by a cluster-based algorithm [105, 106]. Energy calibrations were applied to electrons in data, while an energy smearing was applied to Monte Carlo electrons [107]. Electron quality requirements were also imposed [108]. This ensured that if the electromagnetic shower of the electron extended to regions containing problematic calorimeter cells, or the electron is in the LAr hole region, they are rejected. Signal electrons in the $\tau+e$ channel are also required to be isolated, meaning that less than 10% of the transverse electron momentum is deposited in the calorimeter within a cone of $\Delta R = 0.2$ of the electron track.

Muons

Muons identified as combined or segment tagged are kept if they satisfy $p_{\mathrm{T}} > 10$ GeV and $|\eta| < 2.4$ [109]. Further quality requirements are applied to the inner detector track of the muon, and additional momentum smearing is applied to Monte Carlo to match observed distributions in data [110]. In the final states including light leptons, muons are also required to be isolated, meaning that less than 1.8 GeV of energy is deposited in the calorimeter within a cone of $\Delta R = 0.2$ of the muon track.

Missing transverse momentum

For the 8 TeV analysis the missing transverse momentum is calculated using the `MET_Egamma10NoTau` algorithm that computes $E_{\mathrm{T}}^{\mathrm{miss}}$ from topological clusters. These clusters are in turn associated with identified objects, electrons, photons, jets and muons, and their energy recalibrated accordingly. Clusters that are not paired with an object are included in the $E_{\mathrm{T}}^{\mathrm{miss}}$ calculation as the `SoftTerm`. The $E_{\mathrm{T}}^{\mathrm{miss}}$ is thus given by:

$$\not{E}_T^{\mathrm{RefFinal}} = \not{E}_T^{\mathrm{RefEle}} + \not{E}_T^{\mathrm{RefGamma}} + \not{E}_T^{\mathrm{RefJet}} + \not{E}_T^{\mathrm{RefMuons}} + \not{E}_T^{\mathrm{SoftTerm}} \tag{8.1}$$

Contributions from electrons and muons are included using the above analysis object definitions, without any isolation criteria. Jets with $p_T > 20$ GeV and without any requirement on η are included with jet energy scale calibration applied. The soft term is computed from remaining locally calibrated topoclusters and tracks. There is no separate treatment for hadronically decaying τ-leptons – these are included in the jet or soft term depending on the p_{T} of the τ jet.

In the 7 TeV analysis $E_{\mathrm{T}}^{\mathrm{miss}}$ is calculated using `MET_Simplified20_-RefFinal`. This a similar scheme to the one outlined above apart from two main differences — it does not contain a dedicated photon term and both the jets and the unassociated clusters are calibrated at the electromagnetic scale [111].

Taus

The details of the reconstruction and identification of hadronically decaying taus are treated in Chapter 7. The one τ part of the analyses uses medium τ identification, while the two τ and τ +lep search channels use the loose τ identification working point.

The Primary Vertex

The primary vertex is required have at least five (four in the 7 TeV analysis) associated tracks of $p_{\mathrm{T}} > 0.4$ GeV. In the case of multiple vertices satisfying these criteria the vertex with the largest summed $\mid p_{\mathrm{T}} \mid^2$ of the associated tracks was chosen [112].

8.2 Event Cleaning

Care is taken to ensure that only good quality data enters the analyses. The first step towards this goal is to require the data to be from a run that is present in a Good Run List (GRL). As the name implies, this is a list of runs that are deemed to contain good quality data that is suitable for analysis. A run is deemed good if the LHC beam conditions are good, and the ATLAS magnet systems are operating at full strength, and all detector subsystems are functioning normally. This will result in the physics objects described above being, mostly, well measured.

Furthermore, the interpretation of an event could be distorted by the presence non-collision, or beam induced, backgrounds, faulty or noisy calorimeter regions, or muons that are not from the primary interaction. All these phenomena could be interpreted as (fake) $E_{\mathrm{T}}^{\mathrm{miss}}$ in the data, and it is therefore important to mitigate their contribution as far as possible. The main sources of these backgrounds are [95]

- Events where a beam proton collides with a gas molecule in the beam pipe vacuum.
- Events caused by interactions between the beam halo protons and the beam collimators.
- Cosmic-ray muons interacting with the detector simultaneously with a collision event.
- Noise in the calorimeters.

- Non operational detector regions.

Events with significant noise or noise bursts, in addition to hardware and readout errors, in the LAr calorimeters are removed using the `larError` flag [93]. Similarly, events with problems in the tile calorimeter are removed by the `tileError` flag in the 8 TeV analysis. For periods G-J in the 8 TeV analysis, additional corrupted tile calorimeter events were rejected using the `TileTripReader` [93]. During the 2012 data-taking part of the read-out system (TTC) was modified such that certain detector conditions could be recovered by a reset of the read-out, without restarting the entire run. However, in the lumiblock following a reset this could result in events with parts of the detector information missing. Such incomplete events were removed using the `coreFlags&0x40000` flag that indicates a TTC reset [93].

Calorimeter energy deposits from noise can be distinguished from those made by particles using the characteristics of these deposits. An important measure in this regard is the pulse in the read-out of the calorimeter cells. The quantity Q_{cell} is defined as the quadratic difference between the measured pulse and the expectation from simulation of the electronics response to a real energy deposit. This variable forms the basis of many of the variables used to distinguish calorimeter noise form real energy deposits [113]:

- f_{HEC}: Fraction of the jet energy in the HEC calorimeter.
- $\langle Q \rangle$: Energy-squared weighted average of Q_{cell} of the jet cells.
- $f_{\text{Q}}^{\text{LAr}}$: Fraction of the energy in the LAr calorimeter cells with $Q_{\text{cell}} > 4000$.
- $f_{\text{Q}}^{\text{HEC}}$: Fraction of the energy in the HEC calorimeter cells with $Q_{\text{cell}} > 4000$.
- E_{neg}: Energy of the jet from cells with negative energy.

Jets from beam induced backgrounds can be distinguished from jets originating from the primary collision by their shower shape, direction, associated tracks and timing with respect to the collision. These hallmarks of jets from beam induced backgrounds, and to some extent jets from cosmic rays, are reflected in the following variables used to remove such jets [113]:

Table 8.1: Selections defining *Looser* bad jets from [113]. If any of the conditions are satisfied the jet is classified as fake.

Non-collision/cosmics	$f_{\mathrm{EM}} < 0.05$ and $f_{\mathrm{ch}} < 0.05$ and $\mid \eta \mid < 2$ $f_{\mathrm{HEC}} > 0.5$ and $\mid f_{\mathrm{Q}}^{\mathrm{HEC}} \mid > 0.5$ and $\langle Q \rangle > 0.8$ $f_{\mathrm{EM}} < 0.05$ and $\mid \eta \mid \geq 2$
Calorimeter noise	$f_{\max} > 0.99$ and $\mid \eta \mid < 2$ $\mid E_{\mathrm{neg}} \mid > 60$ GeV ($f_{\mathrm{EM}} > 0.95$ and $f_{\mathrm{Q}}^{\mathrm{LAr}} > 0.8$ and $\langle Q \rangle > 0.8$ and $\mid \eta \mid < 2.8$)

- f_{EM}: Energy deposited in the electromagnetic calorimeter, divided by the total jet energy.
- $f_{\max}$: Maximal energy fraction in any single calorimeter layer.
- f_{ch}: Ratio of the scalar sum of the p_{T} of the tracks associated with the jet divided by the jet p_{T}.

Table 8.1 shows the criteria used to identify fake jets in the analyses in this thesis. These selection corresponds to the *Looser* bad jet definition that is standard for SUSY analyses. It is designed to reach a signal efficiency for real jets of 99.8%, with a fake jet rejection of about 50% [113]. In the 7 TeV analysis jets above 100 GeV and with $|\eta| < 2.0$ were further required to have charge fraction greater than 2%, or 5% if the electromagnetic fraction of the jet is larger than 90%. This requirement further rejects contribution from cosmic and beam background along with detector noise. In certain runs of the 2012 data taking periods B1 and B2 there was a noisy Tile calorimeter cell that had not been masked in the reconstruction. This was dealt with by removing events in these runs where a jet points towards the problematic cell, and the jet has its highest energy fraction deposited in the second layer of the Tile calorimeter, and this fraction is more than 60% of the total jet energy. The inefficiency introduced by this event veto was found to be negligible [114].

Another source of fake $E_{\mathrm{T}}^{\mathrm{miss}}$ is dead, i.e. non operational, calorimeter regions. Two methods are used to estimate the energy deposited in the dead calorimeter cells. One is a cell level correction that uses information from the neighboring cells, assuming the same energy density. The other, referred to as jet level, uses jet shape information from simulations. This results in two variables that correspond to the fraction of the total jet energy coming from the respective correction, $B_{\mathrm{corr}}^{\mathrm{cell}}$ and $B_{\mathrm{corr}}^{\mathrm{jet}}$. The cell based correction is the default applied in jet reconstruction [115, 116].

In period E to H in the 2011 data taking a hardware failure resulted in missing energy measurement in the LAr calorimeter in the region $0 < \eta < 1.4$ and $-0.8 < \phi < -0.6$, commonly referred to as the "LAr Hole" region [117]. During both the 2011 and 2012 data taking a small fraction of Tile calorimeter cells has been non operational, mainly due to faulty power supplies. Fake $E_{\mathrm{T}}^{\mathrm{miss}}$ arising from these dead detector regions can be significantly reduced by using information on the corrections applied to the jet energies. In the 7 TeV analysis this was done by estimating the contribution to $E_{\mathrm{T}}^{\mathrm{miss}}$ from non operational detector regions by projecting the energy correction applied to the jet onto the direction of $E_{\mathrm{T}}^{\mathrm{miss}}$:

$$\Delta E_{\mathrm{T}}^{\mathrm{miss,\ corr}} = \sum_{\mathrm{jets}} \Delta p_{\mathrm{T}}^{\mathrm{corr}} \cos \Delta\phi(jet, E_{\mathrm{T}}^{\mathrm{miss}}). \tag{8.2}$$

Here the sum runs over jets in the inactive detector regions, and $\Delta p_{\mathrm{T}}^{\mathrm{corr}}$ is the momentum correction applied to the jet using the jet level correction method. Events were vetoed if $\Delta E_{\mathrm{T}}^{\mathrm{miss,\ corr}} > 10$ GeV, or is larger than 10% of the total $E_{\mathrm{T}}^{\mathrm{miss}}$ in the event [117]. Typical rejection factors for fake events are in the range of about 10, with a corresponding signal efficiency of around 99% [118]. In the 8 TeV analysis such events with fake $E_{\mathrm{T}}^{\mathrm{miss}}$ due to non operational cells were removed by vetoing events with a jet above 40 GeV that has more than 5% of its energy from the jet level correction, and that points in the direction of $E_{\mathrm{T}}^{\mathrm{miss}}$ in the event ($\Delta\phi(jet, E_{\mathrm{T}}^{\mathrm{miss}}) < 0.3$) [107]. As the dead material regions are emulated in simulations the cleaning is applied to both data and simulations.

Badly reconstructed, or fake, muons can also be a source of (fake) $E_{\mathrm{T}}^{\mathrm{miss}}$. This includes for example events where particles from very energetic jets travers the calorimeters and enter the muon system (punch through), or incorrect matching of inner detector tracks with hits in the muon spectrometer. Following SUSY group recommendations such events were rejected by vetoing events containing badly reconstructed muons before overlap removal. Finally events containing cosmic muons, identified by their large impact parameter, after overlap removal were rejected [107]. The selections outlined in this section are, together with the primary vertex requirement, applied as a baseline to all parts of the analysis.

Figure 8.1 shows the effect of cleaning and quality requirements described here on data collected in 2012. The selections are clearly seen to reduce the large tail in the $E_{\mathrm{T}}^{\mathrm{miss}}$ distribution, mainly associated with the unphysical

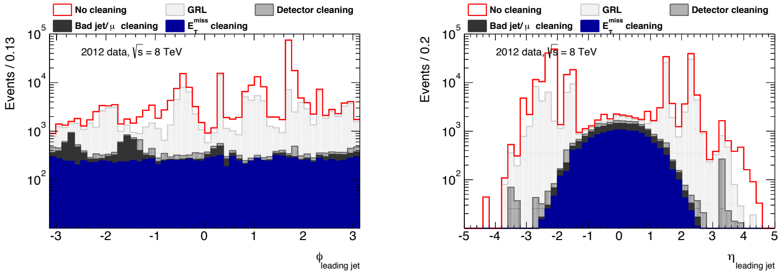

(a) Leading jet ϕ (b) Leading jet η

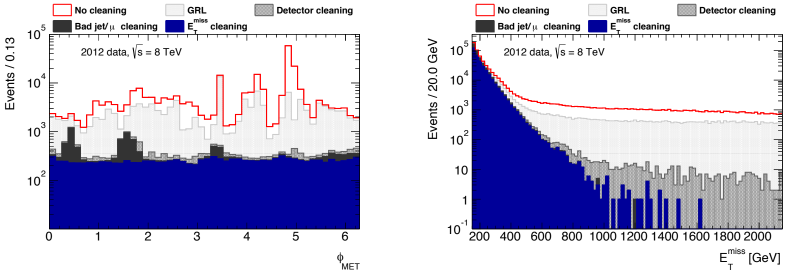

(c) $E_{\mathrm{T}}^{\mathrm{miss}}$ ϕ (d) $E_{\mathrm{T}}^{\mathrm{miss}}$

Figure 8.1: Effect of consecutively applied event cleaning selections on $E_{\mathrm{T}}^{\mathrm{miss}}$ and leading jet variables. The $E_{\mathrm{T}}^{\mathrm{miss}}$ distribution shows dijet events with significant $E_{\mathrm{T}}^{\mathrm{miss}}$, i.e. the selections corresponding to the trigger plateau requirements. The other distributions have a more signal-like selection imposed, with at least two energetic jets ($H_{\mathrm{T}} > 800$ GeV), and significant $E_{\mathrm{T}}^{\mathrm{miss}}$ ($E_{\mathrm{T}}^{\mathrm{miss}}/m_{\mathrm{eff}} > 0.2$) required. Detector cleaning refers to the removal of events with corrupted Tile or LAr information, and treatment of the TTC resets. $E_{\mathrm{T}}^{\mathrm{miss}}$ cleaning refers to the removal of events with energetic jets pointing towards dead Tile regions.

structures observed in the η and ϕ distributions of the leading jet and $E_{\mathrm{T}}^{\mathrm{miss}}$ as a result of problematic or noisy detector regions and non-collision backgrounds.

8.3 Treatment of Overlapping Objects

When analysis objects are found to overlap in the detector it is necessary to solve the ambiguous interpretation and reconstruction of the event, such that only one of the objects are kept. The overlap criteria are based on the geometrical variable $\Delta R = \sqrt{\Delta\phi^2 + \Delta\eta^2}$ that quantifies how close together two objects are in the detector. The conflicting object interpretations are treated by the following criteria:

1. A tau candidate is rejected if it overlaps with either an electron or a muon within $\Delta R < 0.2$.
2. A jet is rejected if it overlaps with a tau or an electron within $\Delta R < 0.2$.
3. A muon is rejected if it overlaps with a jet within $\Delta R < 0.2$.
4. Finally, an electron or a muon is rejected if it overlaps with a jet within $0.2 < \Delta R < 0.4$ since it is then assumed to be originating from a secondary decay within a jet.

8.4 Kinematic Variables

The composite kinematic variables used throughout the analyses are

- The transverse mass between $E_{\mathrm{T}}^{\mathrm{miss}}$ and the τ lepton which is the transverse version of an invariant mass between two objects

  $m_{\mathrm{T}} = \sqrt{2p_{\mathrm{T}}^{\tau}E_{\mathrm{T}}^{\mathrm{miss}}(1 - \cos(\Delta\phi(\tau, p_{\mathrm{T}}^{\mathrm{miss}})))}$

- The transverse scalar sum of the visible analysis objects

  $H_{\mathrm{T}} = p_{\mathrm{T}}^{\tau} + \sum_{\mathrm{jets}} p_{\mathrm{T}}^{\mathrm{jet_i}}$

- The effective mass of the event

  $m_{\mathrm{eff}} = H_{\mathrm{T}} + E_{\mathrm{T}}^{\mathrm{miss}}$

- The minimum azimuthal angle between $E_{\mathrm{T}}^{\mathrm{miss}}$ and the two leading jets in the event

  $\Delta\phi_{\mathrm{min}}^{1,2} = \min\left(\Delta\phi(\mathrm{jet}_1, E_{\mathrm{T}}^{\mathrm{miss}}), \Delta\phi(\mathrm{jet}_2, E_{\mathrm{T}}^{\mathrm{miss}})\right)$

8.5 Standard Model Backgrounds

As can be seen from the previous section the relation between the true constituents resulting from a proton-proton collision and the measured and reconstructed signal deposited in the detector is rather complex. Therefore a careful consideration of how various physics processes will enter in an analysis after detection and full event reconstruction is necessary. This section will briefly summarise the main Standard Model and Supersymmetric processes investigated along with their detector signature characteristics.

Several Standard Model processes can leave detector signatures similar to that of the SUSY signal that is searched for — namely significant $E_{\mathrm{T}}^{\mathrm{miss}}$, multiple high energy jets and a τ lepton. Among the main ones are W and Z bosons produced in association with jets, pairs of top and anti-top quarks and events with multiple jets from QCD processes. The first of these are commonly referred to as electroweak backgrounds.

The electroweak processes may naturally give events with τ leptons from the decay of the bosons in the event. Furthermore, the neutrinos from the same decays are a source of $E_{\mathrm{T}}^{\mathrm{miss}}$ as they escape detection. Events with a Z-boson decaying into a τ pair has no other source of real $E_{\mathrm{T}}^{\mathrm{miss}}$ than the neutrinos from the hadronic τ decay, resulting in most of these events failing selections on $E_{\mathrm{T}}^{\mathrm{miss}}$. On the other hand, events where the Z-boson decays to neutrinos will often have significant $E_{\mathrm{T}}^{\mathrm{miss}}$. Although there is no τ in these events, they can enter the analysis through misidentification of jets as τ leptons, as is the case also for W and $t\bar{t}$ events. Both W and Z bosons can be produced in association with jets leading to events with high jet multiplicities. Even though the cross section for these events is steeply falling with the additional number of jets produced, these processes are still a major source of background due to the initially very high production cross-section of W and Z bosons at the LHC (see Figure 6.2).

Top quarks almost exclusively decay into a b-quark and a W-boson. The topology of events where top quark pairs are produced will therefore largely depend on how the W-boson decays. These events will naturally have large jet multiplicities with at least two b-quarks present and possibly additional jets from hadronic decays of one or both of the W-bosons. As for the electroweak bosons these events may contain both τ leptons and neutrinos from the decay of the W-boson seen in the detector as $E_{\mathrm{T}}^{\mathrm{miss}}$.

Unlike the previous background processes QCD multijet events contain no real sources of τ leptons or missing energy in the event. Rather these events may enter the analysis when both the τ is misidentified and the $E_{\mathrm{T}}^{\mathrm{miss}}$ originates, mainly, from mismeasurements of the objects in the event. While the combination of these two occurring simultaneously might seem unlikely,

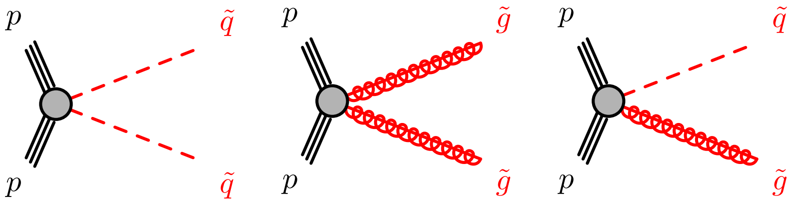

(a) squark-squark (b) gluino-gluino (c) squark-gluino

Figure 8.2: Examples of strong production modes in Supersymmetry.

the very high production cross-section for QCD processes requires that also such events are taken into account.

Like for the background also the characteristics of the supersymmetric signal can be different across the large parameter space spanned by the theory. The following section will take a closer look at examples of supersymmetric models searched for in the analyses presented in this thesis. This will allow us to better understand how to go about searching for these signals in the ATLAS data.

8.6 Supersymmetric Signals

The characteristics of a supersymmetric signal varies not only by the specific supersymmetric model and the region of parameter space, but also the production mechanism and allowed decays of the supersymmetric particles. It is therefore beneficial to tailor a search for SUSY to a specific signature of the model to best exploit the defining features of the targeted signal compared to the Standard Model backgrounds. This both maximises the sensitivity of the joint ATLAS search effort for SUSY, as well as covering as much as possible of the allowed phenomenology within supersymmetric theory. The SUSY searches presented here are designed to target a generic strongly produced supersymmetric signal, i.e. the supersymmetric particles produced in the collisions are squarks and gluinos as exemplified in Figure 8.2. Such a signal has the advantage of a comparatively large production cross-sections, even for higher sparticles masses, compared to other production modes. Figure 8.3 shows the fraction of strong production and the total cross section for the three signal grids investigated, giving a rough indication of where the analyses are expected to be most sensitive.

For all the simulated signal samples, cross-sections are calculated to

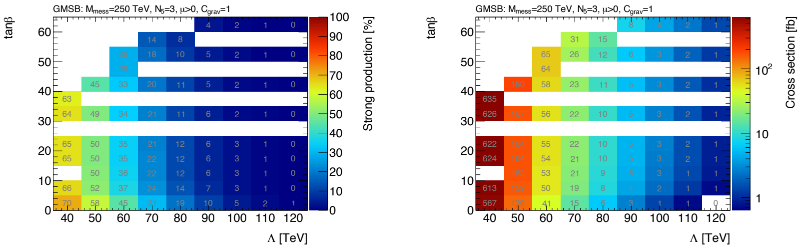

(a) GMSB (b) GMSB

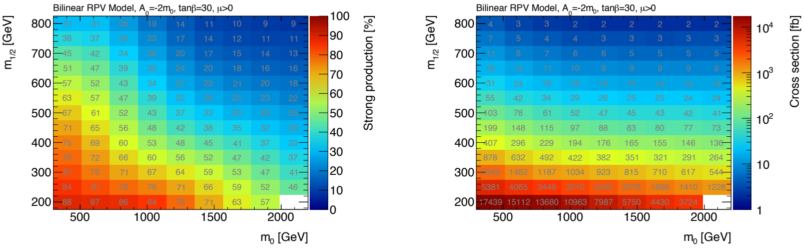

(c) bRPV (d) bRPV

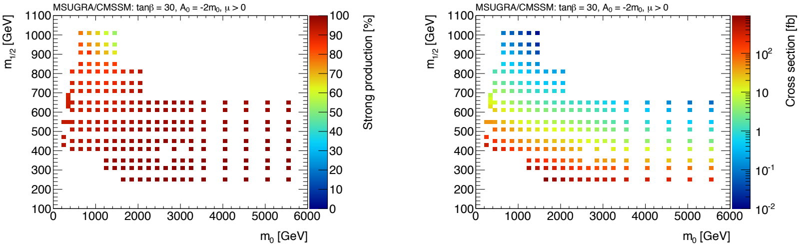

(e) mSUGRA (f) mSUGRA

Figure 8.3: Fraction of total cross section that is strongly production (left) and total cross section (right) in the investigated signal grids.

next-to-leading order with soft gluon emission included at next-to-leading-logarithmic accuracy [119, 120, 121, 122]. Both the nominal signal cross-sections, and their uncertainties, are taken from an envelope of predictions where different PDFs along with factorisation and renormalisation scales are used. The procedure is described in detail in for example [123].

Additionally, a sparticle mass hierarchy where the produced sparticles are significantly heavier than the lightest sparticles are targeted. This type of signal is characterised by several energetic jets produced in the decay of the initial sparticles along with $E_{\mathrm{T}}^{\mathrm{miss}}$ from the lightest sparticle escaping detection, assuming that R-parity is conserved. No further requirements are placed on the LSP, and interpretations are made in models where either the gravitino or the neutralino is the LSP in addition to a model where the LSP is unstable (R-parity not conserved). Furthermore a τ is required at some step of the decay chain — this occurs for example when the $\tilde{\tau}$ is the next-to-lightest sparticle where the $\tilde{\tau}$ then decay into a τ and the LSP. This is of particular interest as the mass mixing in large portions of the parameter space of many models leads to the $\tilde{\tau}$ being the NLSP. Additionally, these regions often also have a relic dark matter density that is consistent with experimental measurements, as is the case for the mSUGRA co-annihilation region. The following sections will describe the specific slices of parameter space of the models that are investigated in this work.

There are a host of other searches for Supersymmetry in ATLAS, and most of them largely complement each other. Some are designed to search for SUSY events where the sparticles produced are sleptons or charginos (electroweak production); the initial sparticles are third generation squarks; specific types of particles in the final state; intermediate Standard Model bosons in the decay chains; long lived sparticles; compressed sparticle mass spectra, to name a few. Although the results, when interpreted in the context of a specific model, might be similar and therefore may seem redundant, they are, by virtue of targeting different signal types, gleaning important and separate pieces of information from the available data. This approach of leaving no stone unturned is clearly sensible, given that we have little indication of what we are actually looking for within the vast possibilities of SUSY phenomenology.

8.6.1 GMSB

In the following work GMSB models are studied in the Λ-$\tan\beta$ plane for $M_{\mathrm{mes}}=250\,\mathrm{TeV}$, $N_5=3$, $\mathrm{sign}(\mu)=+$ and $C_{\mathrm{grav}}=1$. The free parameters are chosen to limit the event topologies to the final states of interest. The chosen C_{grav} avoid long NLSP lifetimes; N_5 ensures a $\tilde{\tau}$ NLSP across large portions

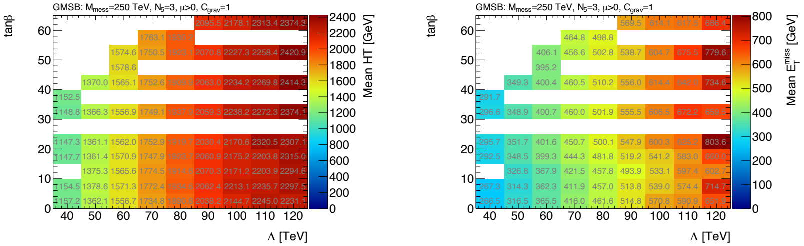

(a) H_{T} (b) $E_{\mathrm{T}}^{\mathrm{miss}}$

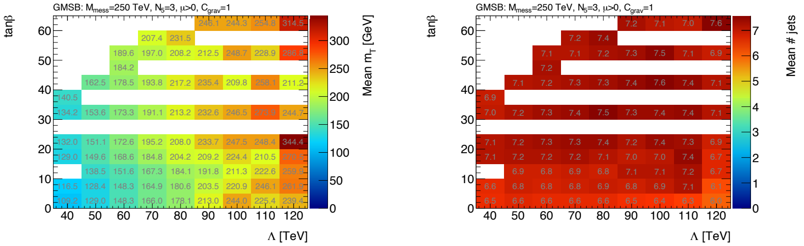

(c) m_{T} (d) Number of jets

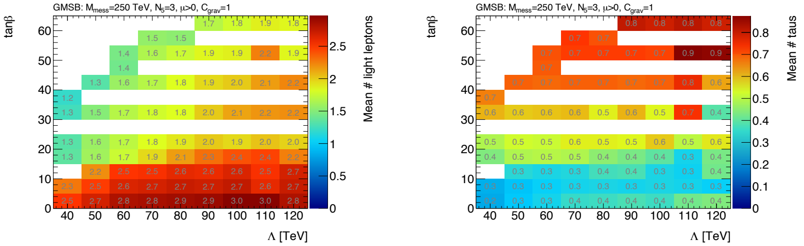

(e) Number of electrons and muons (f) Number of medium taus

Figure 8.4: Main kinematic properties of the GMSB signal grid at a centre-of-mass energy of 8 TeV. All quantities are reconstructed with objects as defined in Section 8.1.

of the parameter space, giving τ rich final-states. The chosen parameters also ensure that squark/gluino pair production is the dominant production mechanism. Previous results from LEP [124, 125, 126] exclude $\tilde{\tau}$ NLSP masses below 87 GeV in GMSB models assuming pair production of $\tilde{\tau}$ sleptons and subsequent prompt decay of the $\tilde{\tau}$ into a τ and a gravitino.

Due to the increasing sparticle masses with the SUSY breaking scale the cross-section is strongly dependent on Λ, while there is very little cross-section dependence on $\tan\beta$. Additionally, Λ and $\tan\beta$ are the most important model parameters for the event topology. Figure 8.4 shows the main kinematic properties relevant for this analysis across the chosen GMSB grid. As expected, for increasing Λ, and therefore sparticle masses, the dimensional variables, $E_{\mathrm{T}}^{\mathrm{miss}}$ H_{T}, m_{T}, are increasing. The number of reconstructed jets with transverse momentum above 30 GeV are close to uniform and equal to 7 across the grid. The mean number of reconstructed electrons and muons are highest at low $\tan\beta$ where the slepton is NLSP, while the mean number of τ leptons are increasing with $\tan\beta$ as the $\tilde{\tau}$ is NLSP in this region. For intermediate $\tan\beta$, the CoNLSP region, the slepton and $\tilde{\tau}$ are almost mass degenerate.

8.6.2 mSUGRA

While the relatively high Higgs Boson mass is difficult to accommodate in large portions of the parameter space, there are regions where the Higgs Boson mass is in agreement with the value observed at the LHC [127, 128, 129]. One such parameter choice is $A_0 = -2m_0$, $\tan\beta = 30$ and sign $\mu = +1$. Additional motivation for searches with τ leptons in this grid stems from the fact that the $\tilde{\tau}$ is the NLSP in a region where the Dark Matter relic density is compatible with measurements performed by WMAP and Planck [130, 131]. In this so-called coannihilation region the small mass splitting between the neutralino LSP and stau NLSP will allow the two particles to coannihilate in the early universe, reducing the abundance of relic dark matter to experimentally acceptable levels [37]. The stau NLSP will give final states containing τ leptons from the decay into the LSP. However, due to the small mass splitting the produced τ leptons often have low momentum – possibly too low to be reconstructed by the ATLAS detector.

Figure 8.5 shows the main kinematic properties of the mSUGRA grid studied here. H_{T}, $E_{\mathrm{T}}^{\mathrm{miss}}$, m_{T} all increase roughly with increasing values of $m_{1/2}$. The mean number of reconstructed jets along with electrons and muons is highest at high m_0 and lowest in the coannhilation region ranging from 6-10 and 0.2-0.7 respectively. While the grid in general is not very τ rich, with the mean number of τ leptons usually below 0.1, the number is almost

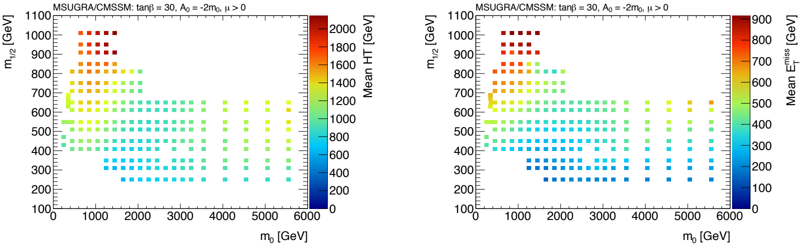

(a) H_{T} (b) $E_{\mathrm{T}}^{\mathrm{miss}}$

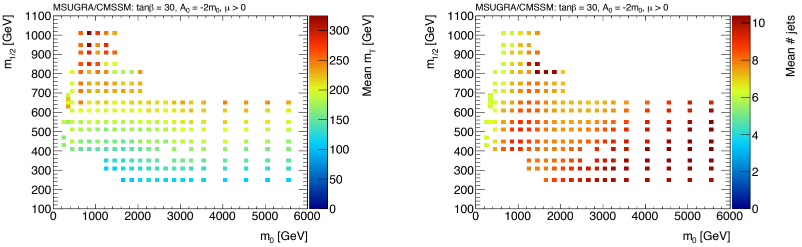

(c) m_{T} (d) number of jets

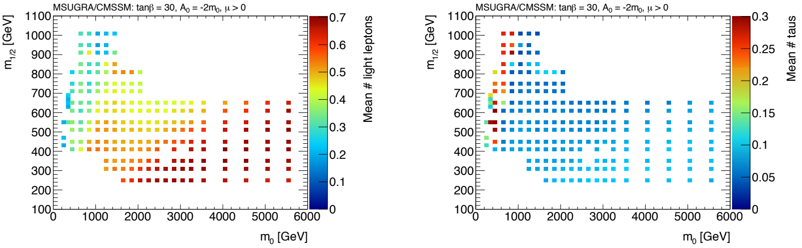

(e) number of electrons and muons (f) number of medium taus

Figure 8.5: Main kinematic properties of the mSUGRA signal grid at a centre-of-mass energy of 8 TeV. All quantities are reconstructed with objects as defined in Section 8.1.

three times as large in most of the coannihilation region. The mean number of τ leptons is seen to drop again at the points in the coannihilation region with the lowest values of m_0, where the energy of the produced τ is below the reconstruction threshold.

8.6.3 bRPV

The bRPV [132, 133] grid has the same model parameters as the mSUGRA grid, but has bilinear R-parity and lepton number violating terms. The bRPV terms lead to mixing of gauginos, higgsinos and neutrinos into mass eigenstates. From this connection between neutrinos and neutralinos the RPV parameters are chosen [134] to be consistent with constraints from neutrino oscillation experiments [135]. The decay chains are as for the R-parity conserving case, except for the LSP decay. The LSP decay is required to be prompt ($c\tau < 5$ mm) and the lightest neutral Higgs mass to be consistent with the observed value. The R-parity violating couplings give τ leptons in the final state from decays of the neutralino LSP into Z and W-bosons, or τ leptons in association with a W-boson or neutrinos [136].

Figure 8.6 shows the main kinematic characteristics of the bRPV grid under investigation. Both $E_{\mathrm{T}}^{\mathrm{miss}}$ and H_{T} in the grid are seen to increase with higher $m_{1/2}$ and lower m_0. Compared to the models of the previous section a comparatively high H_{T} and low $E_{\mathrm{T}}^{\mathrm{miss}}$ is observed. m_{T} increase with increasing $m_{1/2}$ while the mean number of electrons and muons are almost uniform across the grid and equal to 1. The jet multiplicity is also comparatively high, with numbers ranging from 7 to almost 11. The mean number of reconstructed τ leptons is around 0.2-0.3 for most of the grid. In the corner of high $m_{1/2}$ and low m_0 however, where neutralino pair-production is the dominant production process, this is almost doubled.

8.6.4 nGM

Natural gauge mediation (nGM) [137] is a simplified model, based on general gauge mediation (GGM) [138], with constraints from fine tuning arguments imposed. All sparticles that are not relevant to the fine tuning of the Higgs sector are decoupled, leaving light Higgsinos, a light stop, a light gluino and a light gravitino LSP. This results in minimal fine tuning while all current collider constraints are satisfied. Furthermore the stau is required to be the NLSP to have tau rich final states. Assuming coloured production to be dominant, limits on the gluino mass can be set by assuming that the gluino is the only light coloured sparticle.

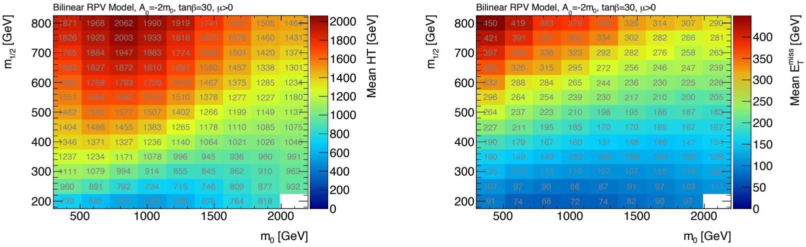

(a) H_{T} (b) $E_{\mathrm{T}}^{\mathrm{miss}}$

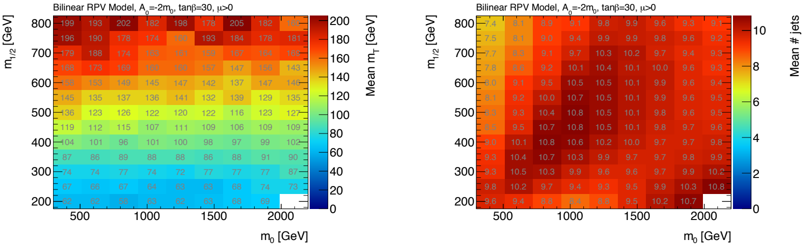

(c) m_{T} (d) number of jets

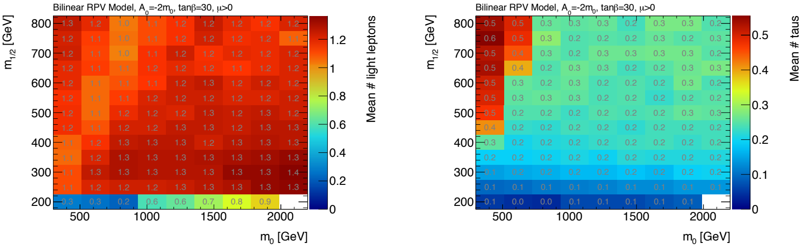

(e) number of electrons and muons (f) number of medium taus

Figure 8.6: Main kinematic properties of the bRPV signal grid at a centre-of-mass energy of 8 TeV. All quantities are reconstructed with objects as defined in Section 8.1.

The resulting model therefore consists of gluino pair production followed by one of the decay chains consistent with the sparticle mass spectra:

- $\tilde{\mathrm{g}} \rightarrow g\tilde{\chi}^0_{1,2} \rightarrow g\tilde{\tau}\tau \rightarrow \tilde{G}g\tau\tau$
- $\tilde{\mathrm{g}} \rightarrow \tilde{\chi}^0_{1,2}q\bar{q} \rightarrow \tilde{\tau}\tau q\bar{q} \rightarrow \tilde{G}\tau\tau q\bar{q}$
- $\tilde{\mathrm{g}} \rightarrow qq'\tilde{\chi}^{\pm}_1 \rightarrow qq'\nu_\tau\tilde{\tau} \rightarrow \tilde{G}qq'\nu_\tau\tau$

As the resulting final states all contain at least two τ leptons, the one τ part of the analysis was not found to add any significant sensitivity to the other analysis channels in the context of this model. Therefore no nGM interpretation was made in the one τ analysis. However, combined limits were set by the three other channels in the plane spanned by the gluino and stau masses.

8.7 Separating SUSY Signals from Standard Model Backgrounds

From the characteristics of the backgrounds and the Supersymmetric signals of the previous section we can begin to determine how to best select events to pick out a potential signal from the huge amount of Standard Model background processes. A simple selection on variables generally distinguishing the targeted signals from Standard Model bakgrounds is found, in order to remain inclusive with respect to supersymmetric models and sections of parameter space. At the same time the selection is optimised to be maximally sensitive to the discovery of such generic signal topologies. To this end, a selection of signal points from each of the three signal models of the previous section is chosen to represent the variation of the kinematics, seen from Figures 8.4-8.6, within the model. Values obtained from the optimisation are then chosen that form a good compromise of sensitivity across the models and parameter variations.

The figure of merit used for the optimisation is the modified Asimov approximation of discovery significance [139]:

$$z_A \equiv \sqrt{2\left\{(N_{\mathrm{sig}}+N_{\mathrm{BG}})ln\left[\frac{(N_{\mathrm{sig}}+N_{\mathrm{BG}})(N_{\mathrm{BG}}+\sigma^2_{N_{\mathrm{BG}}})}{N^2_{\mathrm{BG}}+(N_{\mathrm{sig}}+N_{\mathrm{BG}})\sigma^2_{N_{\mathrm{BG}}}}\right]-\frac{N^2_{\mathrm{BG}}}{\sigma^2_{N_{\mathrm{BG}}}}ln\left[1+\frac{N_{\mathrm{sig}}\sigma^2_{N_{\mathrm{BG}}}}{N_{\mathrm{BG}}(N_{\mathrm{BG}}+\sigma^2_{N_{\mathrm{BG}}})}\right]\right\}}$$

where N_{sig} and N_{BG} are respectively the expected number of signal and background events passing the selection and σ_{BG} is the uncertainty on the expected background yield. The background uncertainty is taken to be a

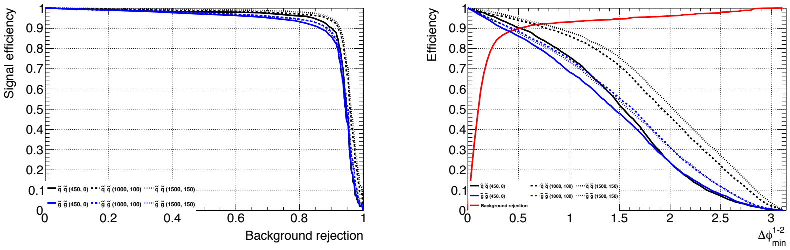

(a) Bckg. rejection vs signal efficiency

(b) Selection efficiencies

Figure 8.7: $\Delta\phi(jet_{1/2}, E_{\mathrm{T}}^{\mathrm{miss}})$ Background rejection versus signal efficiency, and signal and background selection efficiencies against selection value. Background is multijet MC (JXZW) and signals are simplified SUSY models with squark-squark or gluino-gluino production and direct decay into the LSP at centre-of-mass energy of 8 TeV.

flat 25% throughout this section. This is a modified version of the Asimov significance [140]:

$$z_A \equiv \sqrt{2\left[(N_{\mathrm{sig}} + N_{\mathrm{BG}})\ln\left(1 + \frac{N_{\mathrm{sig}}}{N_{\mathrm{BG}}}\right) - N_{\mathrm{sig}}\right]}\;,$$

that does not take background uncertainties into account and therefore overestimates the expected significance. The main advantage of this significance measure over the familiar and more intuitive $N_{\mathrm{sig}}/\sqrt{N_{BG}}$, that it reduces to in the large-statistics limit, is that it more accurately describes the true significance also in cases where N_{sig} is not small compared to N_{BG}, as shown in [141].

The optimisation shown in this section is carried out after basic event and trigger selection using the objects presented in the previous section. Furthermore, all Standard Model contributions in the analyses are considered, except for in Figure 8.7, with corrections obtained from data applied and the signal is weighted by their process dependent NLO cross-sections. As the optimisation, naturally, was carried out before the analysis was finalised, the background estimates are not the final ones obtained in the analysis, but the differences are, in any case, small. Although this section presents optimisation for a centre of mass energy of 8 TeV and an integrated luminosity of 20.3 fb^{-1} the qualitative conclusions hold equally well for the 7 TeV analysis. The selection values applied for the two signal regions in the 8 TeV analysis are indicated by the solid and dashed gray lines in Figures 8.9-8.11.

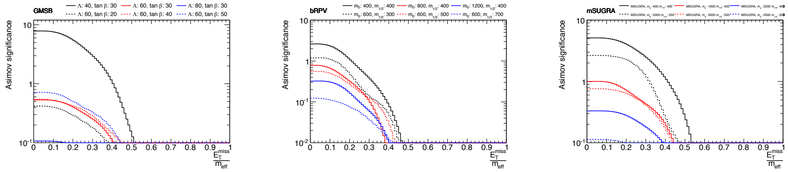

(a) GMSB (b) bRPV (c) mSUGRA

Figure 8.8: Significance of $E_{\mathrm{T}}^{\mathrm{miss}}/m_{\mathrm{eff}}$ selection at centre-of-mass energy of 8 TeV after basic pre-selection of events with moderately high $E_{\mathrm{T}}^{\mathrm{miss}}$ and H_{T}.

Multijet Rejection

Due to the large cross-section of QCD multijet events coupled with the difficulty of accurately simulating events that are sensitive to detector mismeasurements, separate selections are applied to remove contributions from this process. Two common approaches to achieve this, is to remove events where $E_{\mathrm{T}}^{\mathrm{miss}}$ points in the same azimuthal direction as one of the energetic jets in the event, as this is indicative of mismeasurement of the jet creating fake $E_{\mathrm{T}}^{\mathrm{miss}}$ in the event. Another approach that also efficiently removes such events, is to require that the $E_{\mathrm{T}}^{\mathrm{miss}}$ correspond to a certain fraction of the total transverse momentum in the event. Jet mismeasurement giving $E_{\mathrm{T}}^{\mathrm{miss}}$ will often be proportional to the jet energy and it would take a large mismeasurement, which is less likely, to give significant $E_{\mathrm{T}}^{\mathrm{miss}}$ relative to the jet energy.

Both analyses apply a selection on the azimuthal angle between $E_{\mathrm{T}}^{\mathrm{miss}}$ and the two leading jets in the event, $\Delta\phi(jet_{1/2}, E_{\mathrm{T}}^{\mathrm{miss}})$. Figure 8.7 shows the background rejection versus signal efficiency, and efficiencies for a given selection value on this quantity after a pre-selection requiring moderately high $E_{\mathrm{T}}^{\mathrm{miss}}$ and H_{T}. The signal used to show the efficiency of the selection is a simplified model of pair-production of squarks or gluinos directly decaying into the LSP, while the background in this case refers to multijet simulations only. A selection on $\Delta\phi(jet_{1/2}, E_{\mathrm{T}}^{\mathrm{miss}}) > 0.4$ is seen to reject close to 90% of the multijet contribution while retaining almost 90% signal efficiency for different production mechanisms and sparticle masses. While being an efficient way of removing multijet events, the selection on $E_{\mathrm{T}}^{\mathrm{miss}}/m_{\mathrm{eff}}$ was removed and replaced with a selection on $E_{\mathrm{T}}^{\mathrm{miss}}$ to suppress the multijet contribution in the 8 TeV edition of the analysis. The reason for this choice is demonstrated in Figure 8.8, where the selection is seen to significantly reduce the sensitivity to R-parity violating signals due to the relatively lower $E_{\mathrm{T}}^{\mathrm{miss}}$ in such models.

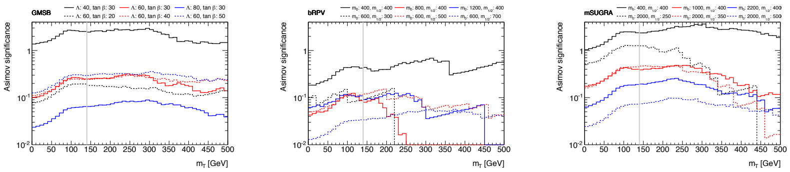

(a) GMSB (b) bRPV (c) mSUGRA

Figure 8.9: Significance of m_{T} selection at centre-of-mass energy of 8 TeV after basic pre-selection and QCD Multijet rejecting selection of events.

Such a selection would also reduce the sensitivity to signal topologies with significant jet activity.

Transverse Mass (m_{T})

The transverse momentum can be used to efficiently reduce large portions of the electroweak backgrounds. In particular W+jets events, where the transverse mass is limited to the W-boson mass when both $E_{\mathrm{T}}^{\mathrm{miss}}$ and the τ lepton originates from the W-boson decay products. This is, however, not necessarily true for events where the τ is from a misidentified jet and no such bounding by the W mass holds. Therefore, a higher fraction of events containing misidentified τ leptons are in general found at higher m_{T} values compared with below the W mass.

Similar effects, albeit less pronounced, are also observed in $t\bar{t}$ events and Z+jets events. In the case of $t\bar{t}$, real τ leptons and portions of $E_{\mathrm{T}}^{\mathrm{miss}}$ originate from a W-boson decay, giving rise to a similar m_{T} shape to that of W+jets. For Z+jets where the Z-boson decay into a τ pair, similar behaviour is also seen due to the comparable mass scales of the two bosons, although $E_{\mathrm{T}}^{\mathrm{miss}}$ in these events is usually insufficient to produce high m_{T} values. Z-bosons decaying into neutrinos are likewise more prominent at large m_{T} values, due to the presence of significant real $E_{\mathrm{T}}^{\mathrm{miss}}$ from neutrinos combined with a fake τ.

For similar reasons the m_{T} selection is not a very efficient discriminator of QCD multijet events, as there is no connection between the origin of the τ and the fake $E_{\mathrm{T}}^{\mathrm{miss}}$ in these events. Such events result in a bump in the m_{T} spectrum, whose position is determined by the τ energy threshold and the $E_{\mathrm{T}}^{\mathrm{miss}}$ trigger threshold selection. As both the p_{T} distribution of the fake τ and the $E_{\mathrm{T}}^{\mathrm{miss}}$ distributions for such events are steeply falling, most events of this type have values for the variables just above their threshold

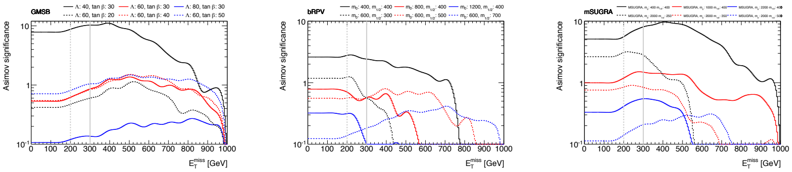

(a) GMSB (b) bRPV (c) mSUGRA

Figure 8.10: Significance of $E_{\mathrm{T}}^{\mathrm{miss}}$ selection at centre-of-mass energy of 8 TeV after basic pre-selection, multijet rejecting selection and selection on m_{T}.

values. Combined with an almost uniform angular distribution between $E_{\mathrm{T}}^{\mathrm{miss}}$ direction and the τ lepton, this gives rise to a peaking structure at the scale of the selections applied to $E_{\mathrm{T}}^{\mathrm{miss}}$ and τ p_{T}.

Signal, on the other hand, is close to flat in this variable with the distribution shifted to higher values with increasing Λ in GMSB and $m_{1/2}$ in bRPV and mSUGRA as seen in Figures 8.4-8.6. Figure 8.9 shows the Asimov significance for the selected points in the GMSB, bRPV and mSUGRA grids. The significance shapes are very similar for all points, allowing for a common selection value without sacrifice of sensitivity in any of the models. The second peaking structure of the background is also reflected in the significance curves at m_{T} values around 100 GeV. Additionally, the lack of sample statistics is apparent for a couple of the bRPV grid points due to the 150 GeV selection on $E_{\mathrm{T}}^{\mathrm{miss}}$ already imposed due to trigger efficiency requirements. A selection of m_{T} greater than 140 GeV is indicated in the figure and imposed before the optimisation of $E_{\mathrm{T}}^{\mathrm{miss}}$ in the following section. This value is slightly higher than the optimal choice with respect to maximising the significance, but was chosen to also take control region statistics into consideration.

Missing Transverse Momentum ($E_{\mathrm{T}}^{\mathrm{miss}}$)

For $E_{\mathrm{T}}^{\mathrm{miss}}$ there are backgrounds where there is naturally occurring missing energy from neutrinos escaping detection, and those where $E_{\mathrm{T}}^{\mathrm{miss}}$ is predominantly from mismeasurements of the other event objects. The former is particularly relevant for electroweak backgrounds and especially $Z \to \nu\nu$. There, the final state is dominated by neutrinos escaping detection, giving rise to significant real $E_{\mathrm{T}}^{\mathrm{miss}}$ in the event. An example of the latter is multijet events where the dominant effect giving rise to $E_{\mathrm{T}}^{\mathrm{miss}}$ is mismeasurements.

The R-parity conserving signal is characterised by having higher $E_{\mathrm{T}}^{\mathrm{miss}}$

than the backgrounds due to an additional weakly interacting particle escaping detection in addition to the neutrino, namely the lightest supersymmetric particle. For the R-parity violating grid, bRPV, the LSP is unstable and decays into Standard Model particles than can be detected and therefore in general have lower $E_{\mathrm{T}}^{\mathrm{miss}}$ than for the R-parity conserving cases. Figure 8.10 shows significance curves for selecting high $E_{\mathrm{T}}^{\mathrm{miss}}$ values for selected points in the three models after the pre-selection and m_{T} selection is applied. It is clear that the R-parity conserving models favours higher cut values than the R-parity violating model along with low $m_{1/2}$ points in the mSUGRA grid. To be sensitive also to these lower $E_{\mathrm{T}}^{\mathrm{miss}}$ topologies the 8 TeV edition of the analysis uses two signal regions, one of which has a looser selection on $E_{\mathrm{T}}^{\mathrm{miss}}$.

Transverse Scalar Sum (H_{T})

The transverse scalar sum, H_{T}, of an event quantifies the total amount of transverse energy in an event. It can be defined in several ways depending on which objects are included in the sum. In the analyses in this work all jets and τ leptons, as defined in Section 8.1, are included. Supersymmetric events where the mass difference between the produced sparticle and the LSP is large, generally have high H_{T} due to the long decay chains and large available kinematic phase space for the decays. Contributions to H_{T} are, through the high number of decay products, the highly energetic objects created in the decay, or a combination of the two. Selecting on H_{T} is therefore an indirect choice of the supersymmetric mass splitting, and mass scale, targeted by the analysis. Analyses based on such selections, in general, have a lower sensitivity to compressed, i.e. small sparticle mass splittings, scenarios where the decay products have low momentum – possibly to the extent that they are not reconstructed.

For the models investigated here, mass splittings are generally large and typically $\mathcal{O}(\mathrm{TeV})$, resulting in significant H_{T}. In particular the GMSB, bRPV and certain parts of the mSUGRA grids are characterised by several highly energetic jets. Figure 8.11 shows significance curves for points in the three models after selections on multijet rejecting variables, m_{T}, and $E_{\mathrm{T}}^{\mathrm{miss}}$ have have been applied. Generally large H_{T} selections are preferred across the grids, but with some remaining dependence on the selection of a specific point and model. When selecting a H_{T} value to define a signal region, there are also other considerations to take into account. One is the background composition of a potential signal region, another is selecting a value which yields good sensitivity to points with cross-sections that could be excluded, or discovered, with the available dataset.

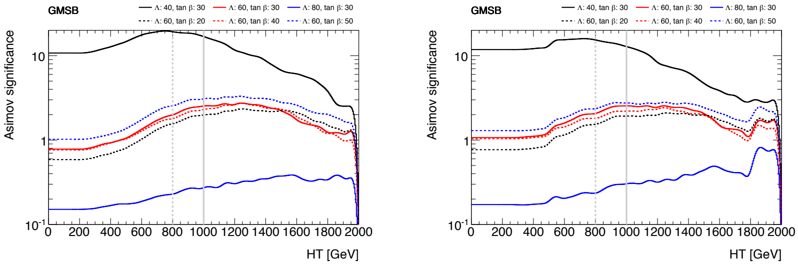

(a) GMSB (b) GMSB

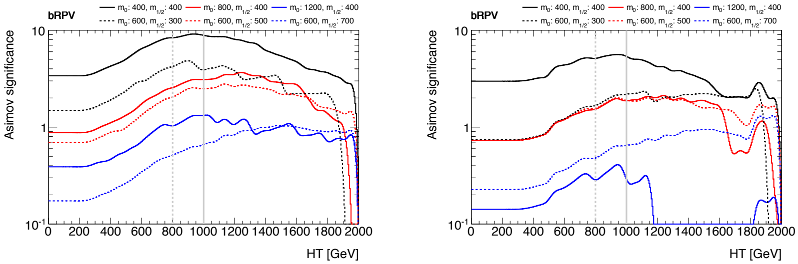

(c) bRPV (d) bRPV

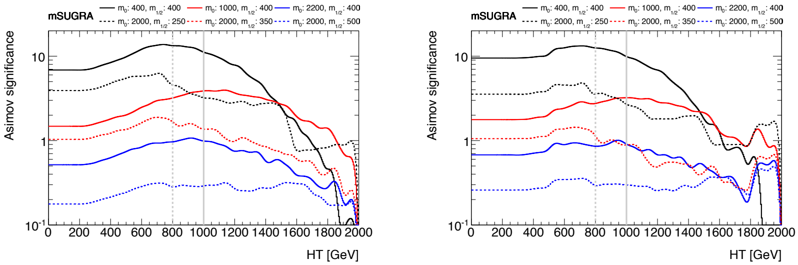

(e) mSUGRA (f) mSUGRA

Figure 8.11: Significance of H_{T} selection at centre-of-mass energy of 8 TeV after basic pre-selection, multijet rejecting selection and selection on m_{T} and $E_{\mathrm{T}}^{\mathrm{miss}}$.

8.8 Background Estimation Techniques

Even though ATLAS simulations are remarkably detailed and accurate they are not without uncertainties. There are uncertainties related to all steps of the simulation from the initial hard interaction in production cross-sections and event topologies; the subsequent showering process of the initial partons; the modelling of the underlying pile-up events; to the simulation of the detector configuration and response. SUSY searches are also concerned with an extreme part of phase space that is located in the tails of the simulated distributions. Unlike the bulk of the simulations these are often a bigger challenge to simulate accurately both due to the lack of experimental data to tune the simulation to, and the tendency for small discrepancies in the simulations to grow as you approach the tails.

A vital part of any analysis is therefore to verify that the simulations accurately describe the data in the kinematic regime relevant to the analysis. If that is not the case the simulations need to be corrected, in either shape or normalisation, to match observations in the data. Another approach is to avoid the use of simulations altogether and rather use the data directly to estimate a given background. Such methods of estimating background processes using the data are often referred to as data-driven methods and are vital to ensure that background processes are under control and well understood. Without these methods and the confidence they lend to the backgrounds estimates, it would be impossible to distinguish a poorly modelled background from a potential supersymmetric signal.

The following sections will outline the background estimation methods that are common to both the 7 and the 8 TeV analyses. Methods applied that are unique to one or the other will be treated separately in the corresponding analysis sections.

8.8.1 Multijet Background

For QCD multijet events there is a large uncertainty associated with the normalisation of the simulated background. Additionally, the main features that make it relevant to a search for Supersymmetry are predominantly caused by detector effects, mismeasurements and misidentifications rather than real physics objects in the events. This applies, for example, to the $E_{\mathrm{T}}^{\mathrm{miss}}$, usually originating from mismeasured jets, and the τ, which is predominantly a misidentified QCD jet. Such effects, often referred to as fake, are notoriously challenging to model. It is therefore particularly important that the estimates of this background are as data-driven as possible, with only a minimal dependence on Monte Carlo predictions.

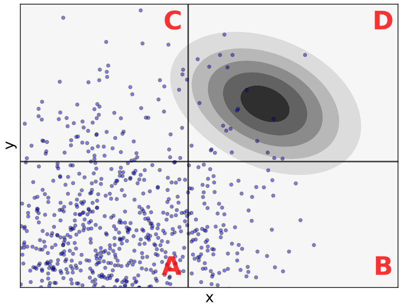

Figure 8.12: Schematic illustration of ABCD method for estimating background using two uncorrelated and signal enhancing variables. Inspired by [143, 142].

ABCD

A commonly used method in high energy physics is the so-called ABCD method [142]. It allows the background rate in a region defined by two signal enhancing cuts to be estimated from the data, under the assumption that the two variables are uncorrelated for the background. Figure 8.12 illustrates the method where the small background contribution in the signal enriched region D can be estimated from the high statistic background dominated regions A–C. Assuming that the two variables are uncorrelated, the background contribution in region D can be expressed as $\mu_D = \mu_B \mu_C / \mu_A$, where μ_i is the background contribution in region $i \in \{A, B, C, D\}$.

As the background contributions are taken from data the above expression furthermore assumes that there is no, or negligible, signal contamination in regions A, B and C. Additionally it assumes that a single source contributes to the background, or that the background may be treated as such. If there is other known and well modelled backgrounds in the regions, these may be subtracted from the observed event counts.

In the context of the analyses presented here the ABCD method has been applied to estimate the multijet background in the signal region. The method is based on two uncorrelated variables, one $E_{\mathrm{T}}^{\mathrm{miss}}$ based and the other related to τ identification, to select a region with enhanced signal contribution and remove the bulk of the multijet contribution. Although there is some added complexity related to application of the method compared to the instructional example presented here, the conceptual basis of the method remains.

τ Misidentification Factor

Among the problems related to multijet estimates using Monte Carlo simulations is the insufficient simulated statistics when requiring the presence of a τ in the event. Additionally, the modelling of τ misidentification rates of QCD jets in simulations might not accurately reflect those observed in the data. To circumvent these challenges a partly data-driven multijet estimate was developed where a τ candidate is taken from simulations before the event is weighted by a misidentification probability determined from data.

No identification criteria are applied to the selected τ candidate, which greatly increases the available statistics in the sample, and therefore also reduces the statistical uncertainty on the estimate. The probability of one of these τ candidates passing the nominal τ identification is calculated from data as a function of the τ p_{T}.

As a starting point a τ candidate is randomly selected from the data in a multijet dominated control region. It is then checked whether or not this τ candidate has also passed the nominal τ selection by matching the τ candidate in ΔR to any nominal τ leptons that might be present in the event. The probability of a randomly chosen looser tau to be identified as nominal tau may then be expressed as

$$P\left(\text{nominal } \tau \;\middle|\; \text{loose } \tau\right) = \frac{N^{\text{loose \& tight}}}{N^{\text{loose}}}$$

Where N^{loose} and $N^{\text{loose \& tight}}$ are the number of selected looser taus and looser taus that also pass nominal tau selection respectively binned in p_T of the tau.

To estimate the multijet contribution a τ candidate is chosen randomly in the simulation, and is used like a regular τ to calculate other event variables. All selections are then applied to the event just as for other events. The probability, as determined above, is then applied as an event weight to obtain the correct normalisation and shape of the estimated background. Unlike the ABCD method described before, which only outputs event yields, this method result in full distributions that are well suited for plotting. For this reason the method is adopted to indicate the contribution from QCD multijets in figures.

8.8.2 Electroweak Background

For electroweak backgrounds Monte Carlo simulations are relied upon for estimating backgrounds. The normalisation of the simulations could, however, be incorrect due to potential deviations between simulated and observed selection efficiencies induced from differences in the real and simulated detector response. Additionally, the normalisation is influenced by theoretical uncertainties from calculations of the cross section of the process. Correct normalisation can be obtained by scaling the simulations to the background rates observed in data in dedicated control regions.

A control region (CR) is constructed to be enriched with a given background while at the same time remaining in a kinematic regime close to that of the signal region. Dedicated control regions for each background allow separate studies of the process in question, making it possible to pin down potential mismodelling in the simulations with respect to the data. Control regions are defined to have similar kinematics to the signal region as the method hinges on the derived normalisation factors also being valid in the signal region where the backgrounds are to be estimated. In general, the choice of control regions is a trade off between the statistical uncertainty from the diminishing statistics in the kinematic region close to the signal region, and the systematic uncertainty induced in the transfer from the control to the signal region, which increases with the distance of the extrapolation. In practice control regions are not exclusively comprised of one background type, making it necessary to simultaneously take into account multiple sources of backgrounds in several control regions.

Data-Driven Scaling Factors From Matrix Inversion

With a set of n control regions for n backgrounds contributing to the observed event count in each region, the observed event counts for the regions can be expressed as a matrix equation

$$\begin{bmatrix} O_1^{\text{data}} \\ \vdots \\ O_n^{\text{data}} \end{bmatrix} = \begin{bmatrix} N_{11}^{\text{MC}} & \cdots & N_{n1}^{\text{MC}} \\ \vdots & \ddots & \vdots \\ N_{1n}^{\text{MC}} & \cdots & N_{nn}^{\text{MC}} \end{bmatrix} \times \begin{bmatrix} \omega_1 \\ \vdots \\ \omega_n \end{bmatrix} \tag{8.3}$$

N_{ij}^{MC} is the background contribution from MC simulation in control region j for process i. The vector of scaling factors, ω, is to be applied to background i in all control regions, in order for the normalisation of the individual MC simulations to agree with the observed data. The observed data, N_i^{data}, in each region includes contributions from other backgrounds, not included in the matrix equation. Therefore, these other backgrounds are subtracted to leave only the data contribution from backgrounds included in the matrix equation

$$O_i^{\text{data}} = N_i^{\text{data}} - \sum_{\text{other bgs.}} N_i^{\text{MC}} \tag{8.4}$$

The scaling factors, ω_i, can be obtained by inverting the above matrix equation

$$\omega = \mathbf{N}^{-1}\mathbf{O} \tag{8.5}$$

Furthermore, the uncertainties and correlations of the scaling factors are obtained by repeating the procedure in a large number of toy Monte Carlo experiments. For each toy all values are varied within their respective uncertainties and the scaling factors recalculated. The simulated background predictions are assumed to be normally distributed, while the observed data is varied according to a Poisson distribution. The resulting spread of the distribution of the scaling factors under these variations represent the uncertainty.

8.9 Systematic Uncertainties

In addition to purely statistical uncertainties, there are a number of systematic uncertainties that need to be accounted for when interpreting the results of the analyses. These quantify the degree of uncertainty associated with our detector measurements, simulations as well as theoretical uncertainties and choice of background estimation methods. The influence of these uncertainties on the analyses are investigated by varying the affected quantity according to their ascribed uncertainty, and re-doing the whole analysis with the systematically shifted parameter. This includes re-calculation of correction factors from control regions and full background estimates. With the change propagated through the whole analysis chain, potential correlations between control and signal region contributions are propagated to a systematic variation on the final signal region estimates. This section describes common sources of systematic uncertainties for the two analyses presented. Any method and analysis specific uncertainties along with further details are given in the corresponding Chapters 9 and 10.

8.9.1 Experimental Uncertainties

Experimental uncertainties are related to uncertainty of the measurement, reconstruction and identification of the physics objects used in the analysis. These are evaluated by dedicated performance groups and provided through software packages interfaced with `SUSYTools`.

Jet Related Uncertainties

Jet energy scale (JES) is the uncertainty related to the correspondance between the calorimeter response and the jet energy [95, 144, 145, 146]. It is determined by varying the modelling of underlying physics, hadronic showers and detector configurations in simulations, along with comparing the pseudorapidity dependent jet response in data and simulations. After the energy of the jets in the event are rescaled this change is propagated to the missing transverse momentum, which is recalculated with the new jet collection

$$E_T^{\prime miss} = E_T^{miss} + \sum_{jets} p_T - \sum_{jets} p_T^{\prime}, \tag{8.6}$$

where corrected values are primed.

Likewise the jet energy resolution (JER) is only known with a finite precision. From studies comparing the spread of the p_{T} imbalance in dijet events in data and simulations the uncertainty has been estimated to be of the order of 10%. This is accounted for by a p_{T} and η dependent smearing of the simulated jets in the event. As before, the change is also propagated to the missing transverse momentum.

Whether or not a jet is tagged as originating from a b-quark is used to separate the W+jets from the top control regions. Uncertainties in this classification has been applied according to the c-quark and b-quark jet tagging efficiencies, as well as the rate of misclassification of these types of quark jets [101].

Signal jets are required to pass a selection on the jet vertex fraction (JVF) to enhance the selection of jets from the hard process relative to jets from pileup interactions. An uncertainty related to this method of mitigating pileup effects is applied.

Tau Related Uncertainties

As for jets, there is also an energy scale uncertainty related to the τ energy measurement [91]. The uncertainty, derived by the Tau Working Group, is determined by truth studies in Monte Carlo by varying parameters affecting the τ energy reconstruction (event generator, showering model, pileup and detector properties). The provided uncertainty depends on p_{T}, η and the number of tracks associated with the τ and is typically in the range 2-4%. Unlike the jets, there is no propagation of the energy shift to $E_{\mathrm{T}}^{\mathrm{miss}}$. This is justified by the fact that there is no τ term in the $E_{\mathrm{T}}^{\mathrm{miss}}$ calculation, and thus any uncertainty on the energy scale should be covered by the JES uncertainty.

Additionally, there are uncertainties related to the τ identification efficiency [89], that have been studied using $Z \to \tau\tau$ and $W \to \tau\nu$ events. This is taken into account by reweighing simulated events containing a true τ, and thus increasing or decreasing the τ identification efficiency, according to the size of the measured uncertainty. The reweighing depends on the τ identification working point and the number of tracks of the τ.

$E_{\mathrm{T}}^{\mathrm{miss}}$ Related Uncertainties

Missing transverse momentum is, as previously indicated, sensitive to measurement uncertainties of any of the objects entering the $E_{\mathrm{T}}^{\mathrm{miss}}$ calculation. Uncertainties on the analysis objects, apart from τ leptons, which are counted as jets, are propagated to the $E_{\mathrm{T}}^{\mathrm{miss}}$ calculation, as for the jets. In addition to the analysis objects, $E_{\mathrm{T}}^{\mathrm{miss}}$ is also sensitive to uncertainties on the soft term — low momentum physics objects and other calorimeter energy deposits (noise, pileup activity, etc.). Variations are also applied to the measured energy scale for this term, and an energy resolution smearing is applied [111].

Other Uncertainties

Simulations are weighted to closely match the pileup conditions observed in the data. Remaining uncertainties relating to differing pileup conditions in the data and simulations are accounted for by varying the pileup reweighing within 10% of its nominal value, following SUSY working group recommendations.

For background estimates that are taken directly from Monte Carlo, rather than from data-driven methods, an uncertainty is applied to account for the uncertainty on the recorded integrated luminosity of the data [147].

8.9.2 Theory and Simulation Uncertainties

Uncertainties related to a specific choice of Monte Carlo generator, or parameters within a generator, are taken into account by comparing simulations from different generators, or with generator parameters varied. This allows the effects of using different approaches for matrix element calculations, parton showering and the modelling of hadronisation and the underlying event to be investigated. For the 7 TeV analysis generator parameters were varied, rather than comparing different generators, to estimate generator uncertainties. The difference between the estimates are taken as the generator uncertainty, also accounting for the statistical uncertainty on the alternative generator. For this comparison no shape re-weighting is applied to the generators in order to see the uncorrected variations between the generators. The effect of the generator choice on other backgrounds through correlations in signal regions and background estimates is also taken into account.

Additionally, the main kinematic variables used for extrapolating between control and signal regions are checked for possible generator biases in the transfer between these regions. Unless otherwise specified the uncertainty of the transfer from the control region to the signal region is assumed covered by the generator systematic. This is based on the assumption that the observables extrapolated over are well described by the simulations — this is thoroughly checked through comparisons with data.

In addition to the experimental uncertainties listed above, theoretical uncertainties (PDF, renormalisation and factorisation scale and strong coupling) on signal cross sections are also applied per production process for the various signal grid points to arrive at a theoretical uncertainty of the predicted signal yield.

8.10 Statistical Interpretation

This section aims to review the main ingredients of commonly used statistical procedures relevant to searches for new physics with the ATLAS detector. It draws from standard statistics texts in high energy physics such as the ones found in [140, 143, 24].

One of the main components of an analysis is the statistical interpretation of the results to quantify the level of agreement between a given model and observed data in order to test predictions from competing models. To this end we specify a hypothesis, H, such that the probability of finding the data, $\boldsymbol{x}$, under the assumption of this hypothesis is $P(\boldsymbol{x}|H)$. A hypothesis we want to test (the null hypothesis) is usually denoted by H_0 and an alternative hypothesis by H_1. A test of H_0 is defined by specifying a subset of the data space (the critical region), w, such that the probability to observe the data there is less then a small chosen value, α,

$$P(\boldsymbol{x} \in w|H_0) \leq \alpha. \tag{8.7}$$

α is referred to as the size or significance level of the test. Consequently, if the data is observed in w, the hypothesis H_0 is rejected at the chosen significance level. While there are a number of subsets w satisfying the above criterion the critical region is selected to maximise the probability of observing the data there, assuming the alternative hypothesis. Figure 8.14 illustrates the principle behind the statistical test.

There are two types of errors associated with such hypothesis tests. Rejecting H_0 if it is true is referred to as type I error. By construction this happens with a probability equal to the size of the test, α. On the other hand, accepting H_0 when it is false is referred to as type II error. The probability of such an error is one minus the power of the test with respect to H_1. The power is defined as the probability to reject H_0 if H_1 is true.

Similarly, if we want to quantify the level of agreement between observed data, $\boldsymbol{x}_{\text{obs}}$, and the hypothesis H, a significance test is performed. This is done by calculating the p-value of the observed data. This is the probability, assuming H, of finding data with at least as much incompatibility with H as in the observed data. Again, the ambiguity in defining greater incompatibility is solved by requiring greater compatibility with an alternative hypothesis.

Commonly the p-value is translated into an equivalent quantity called significance, Z, defined by

$$Z = \Phi^{-1}(1 - p), \tag{8.8}$$

where Φ^{-1} is the inverse of the cumulative standard Gaussian distribution, or the quantile of the standard Gaussian. In particle physics a significance of $Z = 5$ is commonly required to claim discovery of new physics. Translated into a null hypothesis p-value this corresponds to $2.9 \cdot 10^{-7}$. Figure 8.13 illustrates the relation between significance and p-value, along with the p-values corresponding to different significance levels.

In a number counting experiment with b expected background events and s expected signal events the mean expected number of events can be written as $\mu s + b$, where μ specifies the strength of the signal process. The number of observed events n can be modelled as a Poisson distribution where the probability of observing n events is

$$P(n|\mu) = \frac{(\mu s + b)^n}{n!} e^{-(\mu s + b)}. \tag{8.9}$$

The likelihood function $L(\mu)$ is equivalent to $P(n|\mu)$ with n fixed. Therefore the likelihood for background only, i.e. $\mu = 0$, can be denoted L_b, while the likelihood for background with an additional signal contribution, $\mu \neq 0$, may be denoted L_{s+b}. To test these hypotheses it is necessary to chose a function that maps the data to a single real number — a so-called test statistic. Although there is an infinite number of ways to define a test statistic, the Neyman-Pearson lemma [148] states that the test statistic that maximises

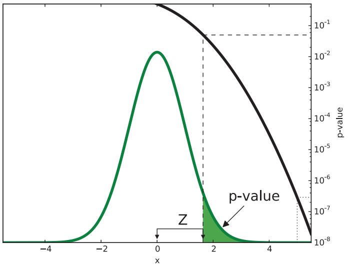

Figure 8.13: Illustration of the relation between p-value and significance. The p-value corresponding to a significance level, Z, is the integral of the tail of a standard Gaussian (green) at a distance Z standard deviations from the mean of the distribution. The black curve shows the p-value as function of the significance. The dashed and dotted lines indicate a p-value of 0.05 and significance level of 5σ respectively.

the power of the test for a fixed size is the likelihood ratio

$$\lambda = \frac{L_{s+b}}{L_b}. \tag{8.10}$$

The above number counting model assumes that there are no uncertainties on background and signal estimates, leaving the signal strength as the only free parameter. When additional free parameters, nuisance parameters, are introduced to describe the expected number of events, the Neyman-Pearson lemma no longer holds. In particular, care needs to be taken due to the p-value dependence on the nuisance parameters. In a frequentist approach the null hypothesis would have to be rejected for all values of nuisance parameters in order to be discarded.

Including nuisance parameters, the likelihood can be expressed as

$$L(\mu, \boldsymbol{\theta}; n, \mathcal{G}) = \mathrm{Pois}(\mu, \boldsymbol{\theta}) \prod_{\mathcal{S}} G(\theta_i), \tag{8.11}$$

where the Poisson expectation now depend on the nuisance parameters, $\boldsymbol{\theta}$. The product over the nuisance parameters, $\mathcal{S} \in \{\theta_1, \ldots, \theta_n\}$, of Gaussian constraint, G, for parameter θ_i given by the unit Gaussian

$$G(\theta_i) = \frac{1}{\sqrt{2\pi}} e^{-\theta_i^2/2}. \tag{8.12}$$

In the frequentist interpretation the global observable, corresponding to the maximum likelihood estimate of θ_i measured in data, would fluctuate about the true value according to this distribution upon repeating the experiment. For clarity, the dependence of the likelihood function on the data and the measured global observables, $\mathcal{G}$, are included explicitly in the above expression, but will be suppressed from here on. The resulting influence on the nominal signal and background yields, s_0 and b_0, are

$$s(\boldsymbol{\theta}) = s_0 \prod_{\mathcal{S}} (1 + \theta_i \sigma_i^s) \tag{8.13a}$$

$$b(\boldsymbol{\theta}) = b_0 \prod_{\mathcal{S}} \left(1 + \theta_i \sigma_i^b\right), \tag{8.13b}$$

where σ_i represents a one standard deviation fluctuation of the nuisance parameter θ_i.

A frequentist procedure for determining p-values when the likelihood includes nuisance parameters is based on the profile likelihood ratio

$$\lambda(\mu) = \frac{L(\mu, \hat{\hat{\boldsymbol{\theta}}}(\mu))}{L(\hat{\mu}, \hat{\boldsymbol{\theta}})}. \tag{8.14}$$

The maximum likelihood estimates $\hat{\mu}$ and $\hat{\boldsymbol{\theta}}$ are the values that maximise the likelihood function $L(\mu, \boldsymbol{\theta})$. Likewise the conditional maximum likelihood estimates $\hat{\hat{\boldsymbol{\theta}}}(\mu)$ are the values maximising the likelihood for a fixed μ. Choosing the nuisance parameters depending on μ is referred to as profiling and $\hat{\hat{\boldsymbol{\theta}}}(\mu)$ as the profiled value of $\boldsymbol{\theta}$. It is worth noting that $\lambda(\mu)$ is independent of the nuisance parameters, $\boldsymbol{\theta}$, as these have been eliminated by profiling.

Typically, two different test statistics based on the profile likelihood ratio are used for discovery and exclusion of a signal with positive signal strength μ. For discovery we would like to test, and possibly reject, the background only hypothesis ($\mu = 0$) by using the test statistic

$$q_0 = \begin{cases} -2 \ln \lambda(0) & \hat{\mu} \geq 0 \\ 0 & \hat{\mu} < 0 \end{cases} \tag{8.15}$$

Here, higher values of q_0 correspond to increasing disagreement between data and the background only hypothesis. Additionally, negative $\hat{\mu}$ are not considered incompatible with the background only hypothesis in the context of discovery of a positive signal contribution.

To set upper limits on the signal strength parameter μ the null is the signal-plus-background hypothesis with critical region corresponding to typical data values for the alternative background only hypothesis. This is quantified by the test statistic

$$q_\mu = \begin{cases} -2\ln\lambda(\mu) & \hat{\mu} \leq \mu \\ 0 & \hat{\mu} > \mu \end{cases} \tag{8.16}$$

where again higher values quantify a larger degree of incompatibility, and $\hat{\mu}$ larger than the tested signal strength is not considered incompatible with the null (signal-plus-background) hypothesis.

For both the discovery and exclusion test statistic increasing incompatibility corresponds to increasing values of q, meaning that the p-value can be written as

$$p_{\mu,\theta} = \int_{q_{\mu,obs}}^{\infty} f(q_\mu|\mu, \boldsymbol{\theta}) dq_\mu. \tag{8.17}$$

Here $q_{\mu,obs}$ is the q value obtained for the observed data and $f(q_\mu|\mu, \boldsymbol{\theta})$ is the distribution of q_μ. Two problems in the above formula are immediately clear – the p-value depends on the nuisance parameters and the distribution of the test statistic needs to be determined. In this work two common methods are applied to circumvent these obstacles – one based on the asymptotic behaviour of the profile likelihood ratio and the other on generating ensembles of pseudo-experiments to estimate the profile likelihood ratio distribution using Toy Monte Carlo techniques.

The procedure referred to as the asymptotic approximation is based on theorems by Wilks [149] and Wald [150]. These state that asymptotically the test statistic distribution is described by a chi-square distribution that is independent of the nuisance parameters. Furthermore, results in [140] show that the variance on the maximum likelihood estimate of μ can be estimated by constructing the Asimov dataset where the number of events are equal to the expected number. These approximations yield simple expressions for the nuisance parameter independent p-value, p_μ, and significance, Z_μ:

$$p_\mu = \Phi\left(\sqrt{q_\mu}\right) \tag{8.18}$$

$$Z_\mu = \sqrt{q_\mu} \tag{8.19}$$

where Φ is the cumulative distribution of the standard Gaussian. In reality data samples are finite and the above approximations are therefore not exact, meaning that the p-value will have some residual dependence on the nuisance parameters.

The test statistic distribution can also be obtained using Monte Carlo methods. By generating an ensemble of pseudo experiments, or toys, where both the number of events and global observables are drawn randomly according to the model, the required distributions can be constructed to calculate the necessary integrals. A large ensemble of pseudo experiments are

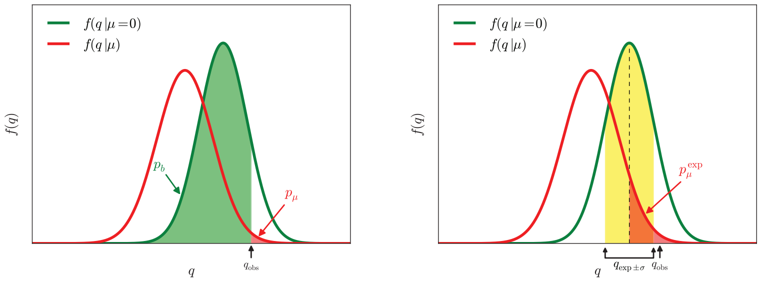

(a) Observed (b) Expected

Figure 8.14: Illustration of test statistic distributions under the background only and signal-plus-background hypotheses. The shaded areas indicate the p-value for background only (green) and with an additional signal of strength μ (red). The right hand plot indicates how expected upper limits, with uncertainties, on the signal-plus-background model are obtained by using the q-value corresponding to the median of the background only distribution, median$\pm\sigma$ quantiles for the uncertainties, to calculate the p-value integral.

needed to reliably populate the tails of the distribution, that are integrated over, making the method computationally expensive. Knowing that the test statistic distribution is close to independent of the nuisance parameters it is not necessary to calculate p-values for all $\boldsymbol{\theta}$. Any remaining dependence on the nuisance parameters are taken care of by using the conditional maximum likelihood estimate of the nuisance parameters when calculating the p-value

$$p_\mu = \int_{q_{\mu,obs}}^{\infty} f(q_\mu|\mu, \hat{\hat{\boldsymbol{\theta}}}(\mu, \mathrm{obs}))dq_\mu. \tag{8.20}$$

This is a natural choice as larger p-values correspond to better agreement with the data. It therefore yields an estimate of the largest p-value for any nuisance parameter values, or equivalently the ability to reject a hypothesis for any $\boldsymbol{\theta}$. This approach is referred to as profile construction.

Special care is taken to avoid excluding models to which one has little sensitivity, as exemplified in Figure 8.15. In the case of a downward fluctuation relative to the background expectation arbitrarily small signal rates could be excluded. By construction this would occur at a rate equal to the size of the test (e.g. 5% for a 95% CL upper limit). This undesirable effect is remedied by taking into account the p-value under the background only

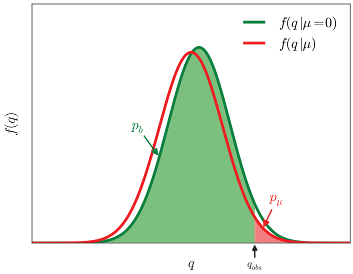

Figure 8.15: Test statistic distributions for μ value that is virtually indiscernible from the background only hypothesis. The shaded areas indicate the ingredients of the CL_S method. In the case of an observed downward fluctuation, as for q_{obs} indicated here, arbitrarily small μ could be excluded considering p_μ alone. This is remedied in the CL_S method by taking into account the size of $1 - p_b$ relative to p_μ.

hypothesis

$$p_b = 1 - \int_{q_{\mu,obs}}^{\infty} f(q_\mu|0, \hat{\hat{\boldsymbol{\theta}}}(\mu = 0, \mathrm{obs}))dq_\mu. \tag{8.21}$$

The CL_S upper limit is then defined by

$$p_\mu^{\mathrm{CL_S}} = \frac{p_\mu}{1 - p_b}. \tag{8.22}$$

In the case of low sensitivity the test statistics for background and signal-plus-background will be similar, meaning that p_μ and $1 - p_b$ are of similar magnitude, resulting in a large p-value, while for high sensitivity the expression approaches p_μ. This conservative approach for calculating limits is referred to as the CL_S method [151].

The analyses presented here are split into search channels with final states containing exactly one, more than one and at least one hadronically decaying τ in combination with an electron or muon. These search channels are constructed to be orthogonal and therefore statistically independent. This means that their results can be combined by considering the total likelihood function for all search channels

$$L_{\mathrm{combined}}(\mu, \boldsymbol{\theta}) = \prod_{i \in \mathrm{channels}} L_i(\mu, \boldsymbol{\theta}_i), \tag{8.23}$$

where $L_i(\mu, \boldsymbol{\theta}_i)$ are the individual search channel likelihoods. Results are obtained by applying the same procedures to the combined likelihood as described throughout this section.

Chapter 9

Analysis of 7 TeV Data

Between March 13th and October 30th in 2011 the LHC provided proton-proton collisions at a centre-of-mass energy of 7 TeV. During this period a total integrated luminosity of 5.46 fb^{-1} was delivered. The ATLAS experiment recorded approximately 93% of this data, of which about 90%, or 4.57 fb^{-1}, was deemed suitable for use in physics analyses. This subset of the data contains only good quality physics objects as flagged by DQ after data reprocessing. Furthermore, the data taking period saw an average number of pileup events of $\sim$9.1, as seen in Figure 9.1.

Compared with the total integrated luminosity of 35 pb^{-1} collected in 2010, this constituted a marked increase in the amount of data available for analysis. Results based on the 2011 dataset therefore saw a significant improvement in the experimental reach and sensitivity to signatures from new physics with respect to the previous year. The analysis presented here builds on previous analyses [72, 73] of τ based supersymmetric signatures using parts of the 2011 dataset. This analysis was the first search for supersymmetry in τ final states using the entire 2011 dataset, and it was also the first to combine previously separate analyses distinguished by τ multiplicity and light lepton content. The larger dataset and combination of final states contributed to a significant increase in sensitivity compared to the first supersymmetry searches in τ final states.

The analysis was based on three final states that were made orthogonal by construction to allow for combination of the individual results. Two analysis channels were defined by the presence of exactly one, or at least one hadronically decaying τ, while the third investigated events with an additional electron or muon in the final state. Through the similarities of the final states the analysis channels benefited greatly from shared techniques, experience and procedures throughout the analysis process. The following

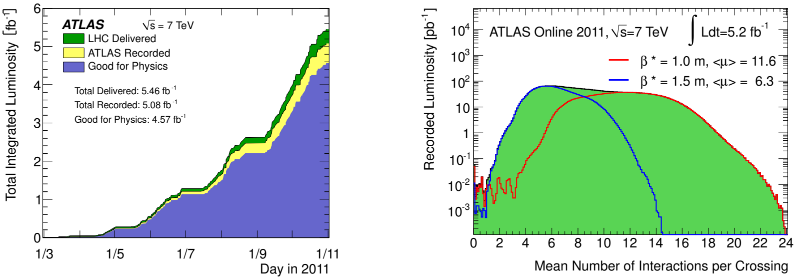

(a) Luminosity

(b) Pileup

Figure 9.1: 2011 data taking conditions – integrated luminosity and mean number of interactions per bunch crossing [78].

chapter will describe the analysis with emphasis on the final state with exactly one hadronically decaying τ, for which I was one of the main analysts.

9.1 Dataset and Monte Carlo Samples

Table 9.1 shows the runs, periods and the corresponding integrated luminosity constituting the full 2011 dataset used in the analysis. Period A and B1 are not included as the ATLAS magnets were switched off during these periods. Additionally, period C was taken at a lower collision energy, 2.76 TeV, while heavy ions were collided in period N. Both period C and N are therefore not included in the analysis. Applying the standard SUSY working group Good Run List, this amounts to a total integrated luminosity of 4.7 fb^{-1}. This is slightly higher than what is flagged as suitable for physics in Figure 9.1. As only a subset of all the physics objects are used in the

Table 9.1: Data from the 2011 $\sqrt{s}$ = 7 TeV proton-proton run used in the analysis. Amounting to a total integrated luminosity of 4713 pb^{-1}.

Runs	Period	$\int$ L dt [pb^{-1}]
178044 – 178109	B2	11.7
179710 – 186493	D – I	1453
186516 – 187815	J – K	817
188902 – 191933	L – M	2432

Table 9.2: Generators used for simulation of relevant Standard Model background processes. All Monte Carlo simulations are from the MC11c production campaign.

Process	Generator	Alternative Generator
$t\bar{t}$	`MC@NLO`	`ALPGEN`
Single top	`MC@NLO` and `ACER`	-
W/Z+jets	`ALPGEN`	-
Diboson	`MC@NLO`	`SHERPA`
Drell-Yan	`ALPGEN`	-
Multijet	`PYTHIA`	-

analysis the remaining objects are not required to pass quality requirements, resulting in a larger fraction of the data being available for analysis.

All Monte Carlo simulations used for analysis are official and centrally produced SUSY D3PDs with production tag `p832`. Table 9.2 shows the generators used for simulation of the Standard Model background processes that are relevant for the considered final states. In the case of $t\bar{t}$ and diboson backgrounds the alternative generators are used to estimate the uncertainty introduced from the choice of generator. For a full list of the Monte Carlo samples used, along with number of simulated events, cross sections, k-factors and filter efficiencies, see Section A.1.

`ALPGEN` [152] is used to simulate W+jets, Z+jets and Drell-Yan events, using `CTEQ6L1` [153] to describe the parton distribution functions. Events are simulated with up to five jets associated with the Z bosons, and up to six jets with the W bosons. Drell-Yan is in the following defined as Z/γ^* events where the invariant mass of the resulting lepton pair is below 40 GeV. All top quark production, except single top t-channel production, and diboson pair production is simulated using `MC@NLO` [154, 155, 156] and the next-to-leading-order parton distribution functions `CT10` [157]. `JIMMY` [158] simulates the underlying event, while `Herwig` [159] is used for fragmentation and hadronisation. τ lepton decays are simulated using the `TAUOLA` [160, 161] package that correctly accounts for spin effects. Multijet background is simulated with `PYTHIA 6.4.25` [162], using the `AUET2B` tune [163], and `MRST2007 LO`* PFDs [164].

The GMSB signal samples are generated on a grid with parameter values ranging from $10-80$ TeV in Λ, and $2-67$ in $\tan\beta$. The supersymmetric mass spectra in this grid are obtained using `ISAJET 7.80` [165] and grid points are then simulated using `Herwig++ 2.4.2` [166] and `MRST2007 LO`* PFDs.

Table 9.3: Triggers used in the analysis along with the period they were applied.

Trigger	Stream	Period
`EF_j75_a4tc_EFFS_xe45_loose_noMu`	`JetTauETMiss`	B2 – I
`EF_j75_a4tc_EFFS_xe55_loose_noMu`	`JetTauETMiss`	J – M
`EF_mu15_mu10_EFFS`	`Muon`	B2 – I
`EF_mu15_mu10_EFFS_medium`	`Muon`	J – M

9.2 Event Selection

The signature that is searched for is characterised by $E_{\mathrm{T}}^{\mathrm{miss}}$ produced by the escaping LSP, along with the production of associated jets and a τ lepton. Data events from the `JetTauETMiss` stream were therefore required to pass a trigger, the one with lowest threshold without a prescale applied, selecting events with large $E_{\mathrm{T}}^{\mathrm{miss}}$ and a high-p_{T} jet. For period B2 through I this was `EF_j75_a4tc_EFFS_xe45_loose_noMu`, while for the remainder of the periods this was a trigger with a slightly raised $E_{\mathrm{T}}^{\mathrm{miss}}$ threshold (`EF_j75_a4tc_EFFS_xe55_loose_noMu`). These triggers require the highest p_{T} jet to have p_{T} greater than 75 GeV at the EF level, while the $E_{\mathrm{T}}^{\mathrm{miss}}$ must be larger than 45 and 55 GeV respectively. Table 9.3 shows the triggers used in the analysis, the physics stream they belong to and the periods in which they were operational. There is, however, not a one-to-one correspondence between the objects at the trigger level and the ones used in a physics analysis. As the triggering decision of an event needs to happen quickly, to cope with the high collision rates of the LHC, only a cursory interpretation of the event and its objects are available to the triggering algorithm compared to the refined offline reconstruction that is later applied. To avoid introducing triggering biases in the analysis it is therefor necessary to find the corresponding values for the analysis objects where the trigger is close to fully efficient. It was found that requiring two jets, one with $p_{\mathrm{T}} > 130$ GeV and the other with $p_{\mathrm{T}} > 30$ GeV, as well as $E_{\mathrm{T}}^{\mathrm{miss}} > 130$ GeV and $E_{\mathrm{T}}^{\mathrm{miss}} > 150$ GeV respectively, ensured that the trigger was close to 99% efficient. This requirement was applied to both data and Monte Carlo events.

Furthermore, basic quality requirements were imposed on the events as described in Section 8.2. All data events were required to be part of a run present in the Good Run List (GRL). The events were also required to have a reconstructed primary vertex, have no jets flagged as bad after overlap removal, or muons that are consistent with cosmic rays. Events where the LAr calorimeter reports an error are discarded, and events where either a jet or a τ has large corrections from the LAr hole treatment were also removed. Events with two loose τ leptons, or an electron or muon were rejected to ensure orthogonality with the other analysis channel. This allows for statistical combination of the results obtained in the three search channels. Finally, a medium τ in the event was required.

9.2.1 Signal Region

In order to reject the Standard Model backgrounds, and enhance the signal fraction in the selected region, selections are imposed following the discussion in Section 8.7. To reduce the contribution from QCD multijet processes it is required that $E_{\mathrm{T}}^{\mathrm{miss}}/m_{\mathrm{eff}} > 0.3$ and $\Delta\Phi(\mathrm{jet}, E_{\mathrm{T}}^{\mathrm{miss}}) > 0.3$. For both m_{eff} and $\Delta\Phi(\mathrm{jet}, E_{\mathrm{T}}^{\mathrm{miss}})$ only the two leading jets are included. Requiring $m_{\mathrm{T}} >$ 110 GeV removes large parts of the electroweak backgrounds — in particular W+jets background. The final selection of $H_{\mathrm{T}} >$ 775 GeV was selected optimising the exclusion reach in the GMSB grid. Table 9.4 summarises the selections defining the signal region in the one tau channel of the analysis. Signal region selection efficiency and acceptance for the GMSB signal grid is shown in Section A.2.

9.2.2 Control Regions

To estimate and constrain Standard Model backgrounds, dedicated control regions (CRs) that are orthogonal to the signal region and have an enhanced contribution of a specific type of background process are defined. Except for in the Z+jets CR, the nominal event pre-selection is applied to all control regions, as described in the Section 9.2. The control region for QCD multijet processes is defined by inverting the cuts applied to suppress this background when defining the signal region. Furthermore, it is split into sub-regions defined by the τ content in the region. Selecting $m_{\mathrm{T}} <$ 70 GeV after pre-selection and the multijet rejecting cuts defines control regions for W+jets and top. Requiring a b-tagged jet within this region defines the top control region, while the W+jets region is required to not contain any b-tagged jets. A control region for Z+jets is defined by selecting events with two oppositely charged muons in a mass window around the Z-boson mass. Unlike the other control regions the Z+jets CR selects events from the `Muon` stream passing a di-muon trigger. The individual control regions are further described where the corresponding background estimations are introduced in Section 9.3. Table 9.4 summarises the control regions defined in this analysis.

Table 9.4: Selections defining signal and control regions after basic preselection of events including trigger plateau selections. m_{T}, H_{T} and $m_{\mu,\mu}$ are in units GeV.

Region	$\Delta\phi_{\mathrm{min}}$	$E_{\mathrm{T}}^{\mathrm{miss}}/m_{\mathrm{eff}}$	m_{T}	H_{T}	b-tag	$m_{\mu,\mu}$
Signal	> 0.3	> 0.3	> 110	> 775	–	–
Top (true τ)	> 0.3	> 0.3	< 70	–	Yes	–
Top (fake τ)	> 0.3	> 0.3	> 110	< 775	Yes	–
W+jets (true τ)	> 0.3	> 0.3	< 70	–	No	–
W+jets (fake τ)	> 0.3	> 0.3	> 110	< 775	No	–
Z+jets	–	–	–	–	–	$\in [66, 116]$
QCD multijet	< 0.3	or < 0.3	–	–	–	–

9.3 Estimating Standard Model Backgrounds

The following section describes the methods applied to ensure that the modelling of the main Standard Model background processes accurately describe those observed in data, and to produce robust estimates of the background contributions to the signal region. Dedicated data-driven estimation techniques are used for Z+jets, W+jets, top quark and QCD multijet events.

9.3.1 Z+jets

One of the main backgrounds in the analysis is events where a Z-boson is created in association with jets. In particular, events where the Z-boson decays into a pair of neutrinos are relevant for the kinematic regions studied. Such events have real missing energy from the neutrinos, while the τ is faked by one of the associated jets. Final states with Z-boson decays into τ-leptons also contribute to the analysis. It is particularly significant in the W+jets, top and multijet control regions where the requirements on $E_{\mathrm{T}}^{\mathrm{miss}}$ and m_{T} are relaxed compared to those for the signal region. When demanding high $E_{\mathrm{T}}^{\mathrm{miss}}$ and m_{T} for the signal region this contribution is small compared to the final states with decays into neutrinos due to the lack of real missing energy in these events. The cases where the Z-boson decays into light leptons, muons or electrons, are almost negligible due to the vetoes to light leptons applied in the analysis. However, these events can be used to estimate and validate the number of expected events with Z-boson decays into neutrinos, which are

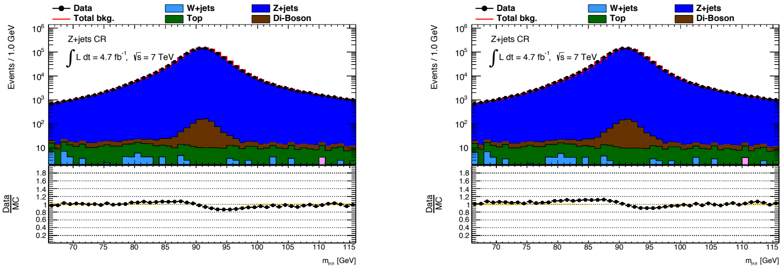

(a) Inclusive (unscaled)

(b) Inclusive (scaled)

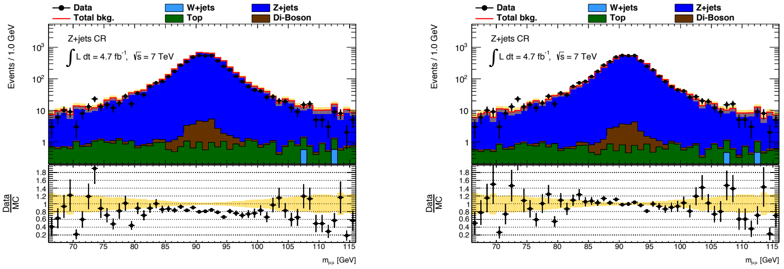

(c) With pre-selection (unscaled)

(d) With pre-selection (scaled)

Figure 9.2: Z-boson mass peak constructed from the di-muon invariant mass. The left hand side figures are unscaled, while the right hand side plots have an overall scaling factor applied to correct the offset in normalisation between data and MC. The lower plots are in a kinematic region similar to the signal region and are used to determine the Z+jets scale factor used throughout the analysis.

Table 9.5: Number of events in the Z+jets control region with pre-selections as described in the text.

	nominal	**inclusive**
W+jets	1.1 ± 0.8	100 ± 15
Diboson	26.9 ± 1.1	960.7 ± 6.5
$t\bar{t}$	39.4 ± 1.4	46.1 ± 4.9
Z+jets	5834 ± 54	1 136 870 ± 1045
Total SM	5902 ± 58	1 138 400 ± 823
Data	4794	1 019 580
SF_Z	0.81 ± 0.01	0.960 ± 0.001

otherwise challenging to treat due to the lack of kinematic handles in such events.

From lepton universality the Z+jets events should be identical except for the flavour of the lepton in the Z-boson decay. Therefore, Z+jets estimates in the signal region, dominated by Z decays into neutrinos, are corrected by a scale factor obtained from the data/MC agreement in a dedicated Z+jets control region with Z decays into muons. To this end, events from the `Muon Stream` are required to pass one of the di-muon triggers listed in Table 9.3. Furthermore, events are required to pass the same GRL and vertex requirements as previously described. To obtain a Z+jets dominated region two isolated muons with $|\eta| < 2.4$ and $p_{\mathrm{T}} > 20$ GeV were selected and required to have invariant mass within a window of the Z-boson mass — 66 GeV $< m_{\mu,\mu} <$ 116 GeV. For the control region to be kinematically similar to the defined signal region two jets with $p_{\mathrm{T}} > 130$ GeV and $p_{\mathrm{T}} > 30$ GeV respectively were also required in the events. To suppress top background in the region, a veto against b-tagged jets was also applied.

Figure 9.2 shows the invariant mass of the muon pair in the control region with and without the selection on the two leading jets applied, before and after scaling with the obtained scaling factor. In both cases the region is clearly dominated by Z+jets events. There is some peaking background from diboson events, along with a small, flat contribution from top and W+jets events. The slight offset of the muon peak in data with respect to Monte Carlo indicates that the calibrations applied to the selected muons in Monte Carlo is entirely sufficient to reproduce the muons observed in data. Since for our purpose only the overall normalisation of the peak is of interest, rather than the shape, this does not influence the result of this exercise. From the number of observed events in this region, shown in Table 9.5, a scaling factor of $0.81 \pm 0.01^{\text{stat}}$ is obtained. When no jet requirement is applied the obtained scaling factor is $0.960 \pm 0.001^{\text{stat}}$, which is in agreement with the dedicated ATLAS measurement [167]. Furthermore, several cross-checks of the scaling factor were performed — dependence on the top scaling factor; control region definition (jet and muon transverse momentum requirement, τ requirement). As a final cross-check $E_{\text{T}}^{\text{miss}}$ in the event was recalculated by adding the vectorial transverse momentum sum of the muons to $E_{\text{T}}^{\text{miss}}$. This emulates the contribution to $E_{\text{T}}^{\text{miss}}$ from neutrinos escaping detection in Z→ $\nu\nu$ events and allows the definition of the control region to be brought closer to that of the signal region. In this instance the nominal $E_{\text{T}}^{\text{miss}}$ selection was applied, to the corrected definition of $E_{\text{T}}^{\text{miss}}$, to define the Z+jets control region.

9.3.2 W+jets and Top

As the protons that are collided contain up-type valence quarks these collisions are more likely to produce a positively, rather than a negatively, charged W-boson. As the charge of the W-boson is carried by the lepton it decays into, this results in a larger fraction of events containing positively, compared to negatively charged leptons. Assuming there is no preferred lepton charge for other processes, including W+jets events with a fake τ, it is possible to estimate contributions from W-bosons with true τ leptons using the charge asymmetry observed in data [168, 169]. Taking the ratio of positive to negative W-boson production, r_{MC}, from Monte Carlo:

$$r_{\text{MC}} = \frac{\sigma(pp \to W^+)}{\sigma(pp \to W^-)} \tag{9.1}$$

then the estimated number of W+jets events is

$$N_W = N_W^+ + N_W^- = \frac{r_{\text{MC}} + 1}{r_{\text{MC}} - 1} \left(N_{\text{data}}^+ - N_{\text{data}}^- \right) \quad . \tag{9.2}$$

where N_{data}^+, N_{data}^- are respectively the number of events with a positively and negatively charged lepton in data. With $r_{\text{MC}} = 2.15 \pm 0.05$ and $N_{\text{data}}^+ - N_{\text{data}}^- = 502$ the W+jets contribution with a true τ is estimated to be 1376 ± 41 in the control region. With the corresponding number from Monte Carlo being 1831 ± 19 this yields a correction factor for W+jets with a true τ of

$$\omega_W^{\text{true}} = 0.75 \pm 0.04^{\text{stat}} \pm 0.03^{\text{syst}} \tag{9.3}$$

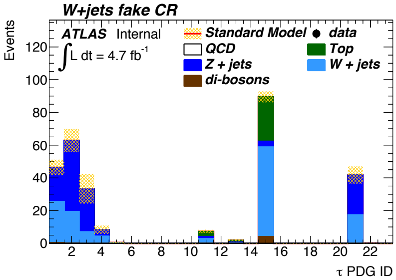

Figure 9.3: True origin of reconstructed τ in the fake τ dominated W+jets control region. Monte Carlo ID numbers below 1-4 correspond to light quarks and 21 to gluons. A true τ has ID 15 while 11 and 13 are electrons and muons respectively. $t\bar{t}$ τ fakes are not included in the figure.

The stability of this estimate with respect to pile-up and control region definition was also checked and found to be negligible. Furthermore, the method was cross-checked using muons in place of taus.

Top background with a true τ was estimated by a template fit of the number of b-tagged jets in a true τ dominated control region. The templates, one for top and one for other backgrounds, were taken from Monte Carlo and fit to the data to determine the relative fraction of top in the control region. Comparing this to the Monte Carlo estimate results in a scaling factor of

$$\omega_{\text{top}}^{\text{true}} = 1.39 \pm 0.08^{\text{stat}}{}^{+0.06}_{-0.08}{}^{\text{syst}} \tag{9.4}$$

As misidentified τ leptons are often not as well described by Monte Carlo as true τ leptons, separate scaling factors are determined based on the origin of the τ lepton. This allows the simulations to be weighted according to their composition of true and fake τ leptons. To this end the W+jets and top control region of the previous section, which is primarily dominated by events with true τ leptons, is extended to a high m_{T} region where the dominant contribution is from events with a fake τ. As before, this region is split into top and W+jets dominated sections by imposing a requirement on the number of b-tagged jets. To keep the control region separate from the signal region the signal region selection on H_{T} is inverted. Figure 9.3 shows the true and fake τ content in the fake dominated W+jets control region. The fake τ contribution is seen to most commonly originate from light quarks, with a significant contribution also from gluon jets. Comparatively the misidentification of electrons and muons as hadronic τ leptons is seen to be negligible.

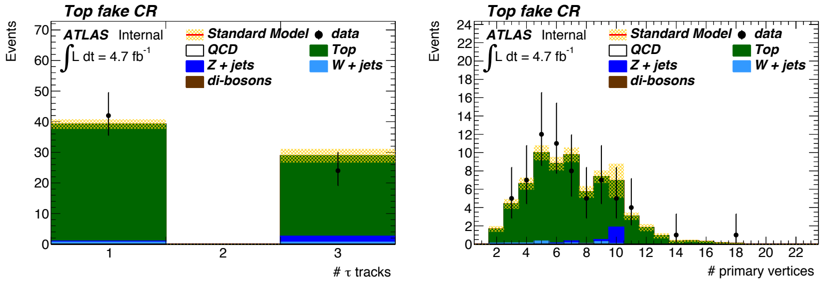

(a) Top fake CR (b) Top fake CR

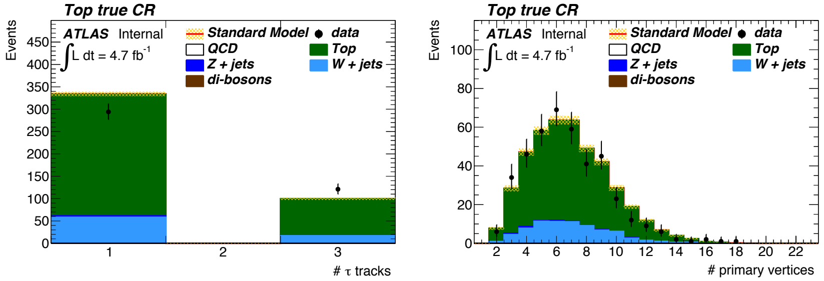

(c) Top true CR (d) Top true CR

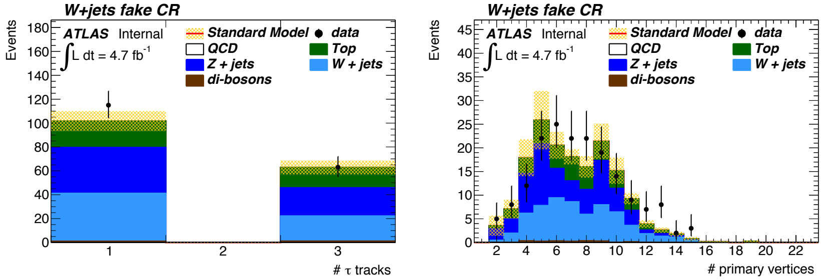

(e) W+jets fake CR (f) W+jets fake CR

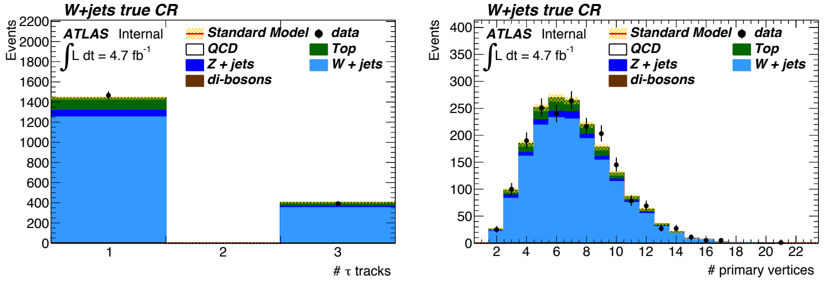

(g) W+jets true CR (h) W+jets true CR

Figure 9.4: Kinematic distributions in the top/W+jets control region after scaling factors are applied.

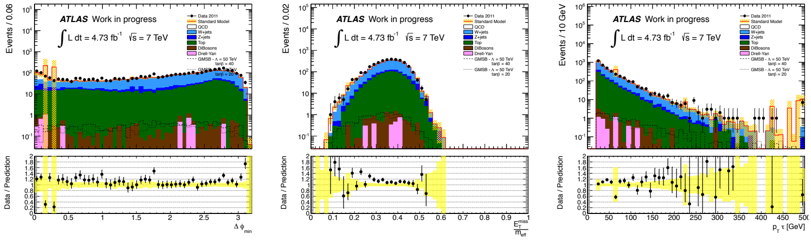

(a) $\Delta\Phi(\text{jet}, E_{\text{T}}^{\text{miss}})$ (b) $E_{\text{T}}^{\text{miss}}/m_{\text{eff}}$ (c) τ p_{T}

Figure 9.5: Distributions of kinematic variables after electroweak scaling factors have been applied.

Kinematic distributions in the resulting control regions for W+jets and top quark events, split by dominant τ lepton origin, are shown in Figure 9.4. Using these control regions and solving the matrix equation for the scaling factors yield

$$\begin{bmatrix} \omega_W^{\text{true}} \\ \omega_W^{\text{fake}} \\ \omega_{\text{top}}^{\text{true}} \\ \omega_{\text{top}}^{\text{fake}} \end{bmatrix} = \begin{bmatrix} 0.91 \pm 0.03^{\text{stat}} + 0.05^{\text{syst}} \\ 0.32 \pm 0.28^{\text{stat}} + 0.17^{\text{syst}} \\ 1.32 \pm 0.10^{\text{stat}} + 0.13^{\text{syst}} \\ 1.92 \pm 0.41^{\text{stat}} + 0.22^{\text{syst}} \end{bmatrix} . \tag{9.5}$$

As an additional check, the stability of these scaling factors with respect to the choice of m_{T} defining the regions was studied and found to be within statistical uncertainties.

For the final background estimates the scaling factors for misidentified τ leptons obtained from the matrix method are used together with the true τ scaling factors from the charge ratio and template fit methods. Figure 9.5 shows three validation distributions after pre-selection and with the above scaling factors applied. The corrected Monte Carlo distributions are seen to reproduce those observed in data.

9.3.3 Multijets

Multijet events are characterised by containing mismodelled τ leptons and $E_{\text{T}}^{\text{miss}}$ from mismeasurement, both of which are difficult to accurately model in simulations. Additionally, the uncertainties on the production cross section of this process is significant, and the statistics of the simulated samples are often insufficient in the parts of phase space where such backgrounds are able to mimic a supersymmetric signal. Although its contribution in the signal

Table 9.6: Definitions of QCD regions used in ABCD method.

	Extra Loose τ	Nominal τ
$\Delta\phi_{\text{min}} < 0.3$	Control region A	Control region B
$\Delta\phi_{\text{min}} > 0.3$	Control region C	Signal region D

region is usually small relative to other backgrounds, to a certain degree by construction, it is therefore important to control by estimates based on measurements in data.

Two methods of estimating this background are applied and the multijet enriched control region in Table 9.4 defined to both validate and develop these estimates. Figure 9.6 shows the most relevant kinematic distributions for this analysis in the multijet control region without requiring a τ in the event. The observed agreement between data and simulation is seen to be very good for all the distributions. It is also clear that the multijet events are mostly situated at low $\Delta\Phi(\text{jet}, E_{\text{T}}^{\text{miss}})$, $E_{\text{T}}^{\text{miss}}/m_{\text{eff}}$ and $E_{\text{T}}^{\text{miss}}$ as expected. The apparent discontinuity at 150 GeV in the $E_{\text{T}}^{\text{miss}}$ distribution is due to the two different $E_{\text{T}}^{\text{miss}}$ trigger plateau cuts, at 130 GeV and 150 GeV, used in the analysis.

ABCD

The two variables defining the ABCD regions are the τ identification and $\Delta\Phi(\text{jet}, E_{\text{T}}^{\text{miss}})$, as shown in Table 9.6. These uncorrelated variables together define a signal-like region when their nominal signal region selection values are applied. Conversely, when the τ identification is loosened and the nominal $\Delta\Phi(\text{jet}, E_{\text{T}}^{\text{miss}})$ requirement is inverted, orthogonal and multijet enriched regions are selected. The looser τ definition differs from the nominal in that the τ jet-identification requirement is removed. If an event contains more than one such looser τ, not overlapping with any of the two leading jets in the event, one of them is selected at random. The looser τ is then treated like a regular τ in further event selection and when calculating kinematic variables.

Ideally, the ABCD method would directly output the signal region multijet estimate. However, due to the limited amount of multijet background remaining after all other signal region selections are applied, relative to the electroweak backgrounds, this is not feasible. Such non-multijet dominated ABCD regions would leave the method sensitive to effects other than the multijet contribution that is attempted estimated. To increase the relative

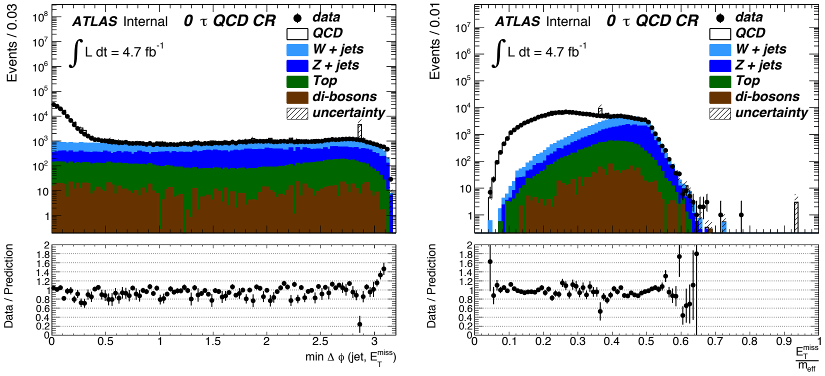

(a) $\Delta\Phi(\text{jet}, E_{\mathrm{T}}^{\mathrm{miss}})$ (b) $E_{\mathrm{T}}^{\mathrm{miss}}/m_{\mathrm{eff}}$

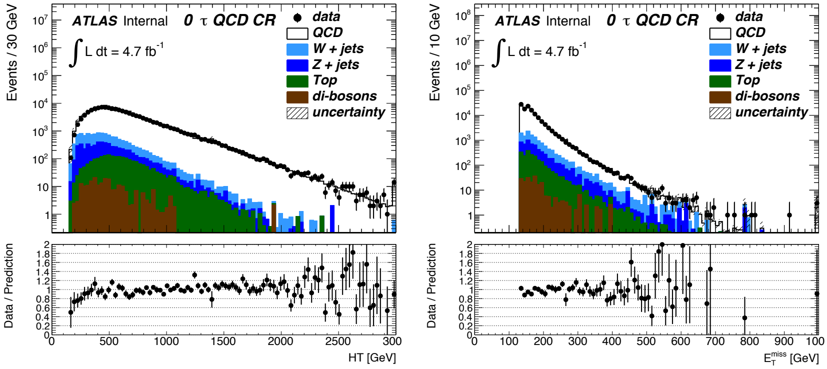

(c) H_{T} (d) $E_{\mathrm{T}}^{\mathrm{miss}}$

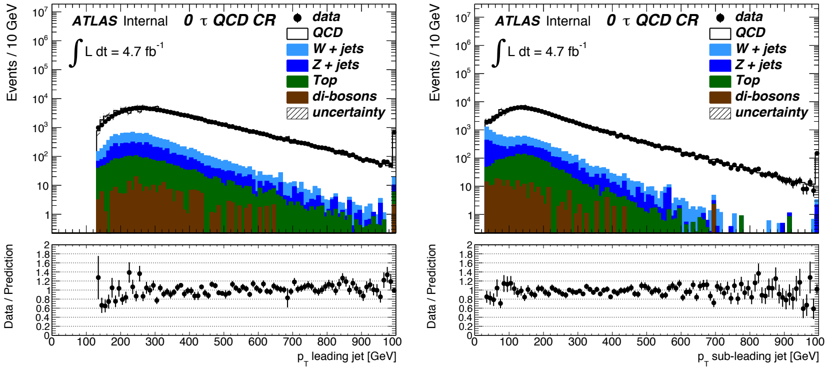

(e) jet$_1$ p_{T} (f) jet$_2$ p_{T}

Figure 9.6: Multijet control region selection without requiring a τ.

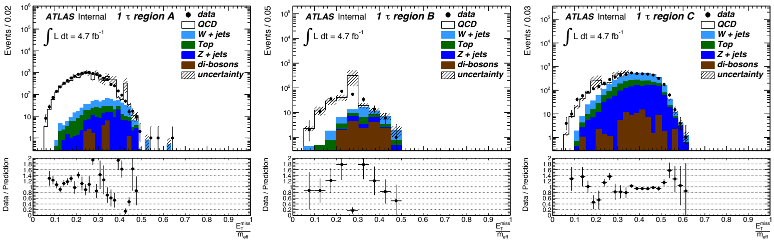

Figure 9.7: $E_{\mathrm{T}}^{\mathrm{miss}}/m_{\mathrm{eff}}$ distributions in regions used in the ABCD method. The discrepancies between the observed data and non-QCD simulation is seen to be in regions dominated by QCD multijet events. In particular region C, which mainly consists of non-QCD processes is also dominated by QCD multijet events for $E_{\mathrm{T}}^{\mathrm{miss}}/m_{\mathrm{eff}} < 0.3$.

multijet contribution, the nominal selection apart from the selection on H_{T} and $E_{\mathrm{T}}^{\mathrm{miss}}/m_{\mathrm{eff}}$ is applied to the region where the ABCD estimate is calculated. To further reduce the electroweak contamination in region C, and thus reduce the method's dependence on the electroweak scaling factors, the selection on $E_{\mathrm{T}}^{\mathrm{miss}}/m_{\mathrm{eff}}$ is inverted in region C. Figures 9.8 and 9.7 show the background processes contributing to the ABCD regions, along with the observed data of each region. The overall contribution of multijet Monte Carlo is seen to describe the data reasonably well. However, the simulation is affected by a low number of events with high event weights and correspondingly large uncertainties, which emphasises the need for data-driven estimates of this background.

Two methods are used to determine the contribution from multijet events in data within the ABCD regions — a simple method based on subtraction of electroweak contributions from simulations, and a more statistically robust method based on a maximum likelihood estimate.

For the subtraction based method the multijet contribution is determined by subtracting simulated electroweak contributions, with their respective scaling factors applied, from the observed data

$$N_{\mathrm{A,B,C}}^{\mathrm{QCD}^*} = N_{\mathrm{A,B,C}}^{\mathrm{data}} - N_{\mathrm{A,B,C}}^{\mathrm{non-QCD}} \tag{9.6}$$

This allows the number of multijet events in the signal like region D, for $E_{\mathrm{T}}^{\mathrm{miss}}/m_{\mathrm{eff}} < 0.3$, to be estimated by

$$N_{\mathrm{D}}^{\mathrm{QCD}^*} = \frac{N_{\mathrm{B}}^{\mathrm{QCD}^*}}{N_{\mathrm{A}}^{\mathrm{QCD}^*}} N_{\mathrm{C}}^{\mathrm{QCD}^*} \tag{9.7}$$

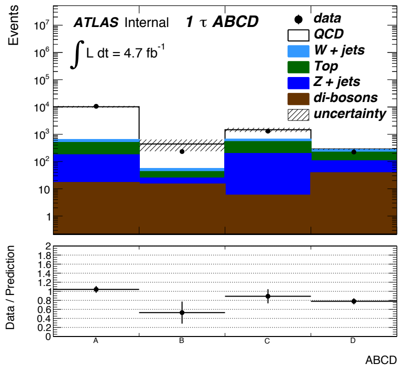

Figure 9.8: Background contributions and data in the ABCD regions used to estimate QCD multijet contributions to the signal region.

In order to obtain an estimate in the signal region this estimate is scaled by the ratio of multijet events, taken from simulation, in the region with $E_{\rm T}^{\rm miss}/m_{\rm eff}$ inverted to that including the nominal $H_{\rm T}$ and $E_{\rm T}^{\rm miss}/m_{\rm eff}$ selection. This ratio is taken from the high statistics region A under the assumption that these variables are independent of those defining the ABCD. This yields $N_{\rm D}^{\rm QCD*} = 9.9 \pm 1.0^{\rm stat}$ and in the final signal region $N^{\rm QCD*}_{\rm D,\ E_T^{miss}/m_{eff}>0.3\ \&\ H_T>775GeV} = N^{\rm QCD*}_{\rm SR} = 0.17 \pm 0.04^{\rm stat}$. The estimate was also calculated taking the ratio from the two other regions, varying the τ definition in the ABCD, and with and without the electroweak scaling factors applied to the regions with a looser τ. The maximal difference between the estimates was taken as an additional systematic on the method. Furthermore, the robustness of the method with respect to the selection values on the multijet reducing cuts, $\Delta\Phi(\text{jet}, E_{\rm T}^{\rm miss})$ and $E_{\rm T}^{\rm miss}/m_{\rm eff}$, was checked. Figure 9.9 shows the multijet signal region estimates for various of these selection values.

A full likelihood based approach [142], that is both statistically robust and takes into account the possible presence of a signal in the ABCD regions, can also be adopted. The predicted rates for the non-QCD background components are denoted by $\mu^{\rm nQCD}_{D;A,B,C}$ and are taken from MC with appropriate scaling factors applied. A possible signal contribution in region D is denoted by μ. The signal leakage into the other regions is expressed in terms of μ and a signal acceptance factor into this region taken from Monte Carlo in a sample GMSB signal. Then there is the multijet background to be estimated which is completely data-driven. Denoting the component in the

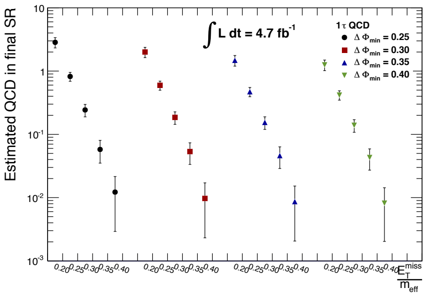

Figure 9.9: Signal region estimates from the ABCD method for different multijet rejecting selections.

search region D as μ^{QCD}, we describe the ABCD-relation between the other three components with two additional nuisance parameters τ_B and τ_C. The estimated rates in the 4 regions are thus described by:

$$\begin{aligned}
\mu_A &= a\mu + \mu_A^{\mathrm{nQCD}} + \mu^{\mathrm{QCD}}\tau_B\tau_C \\
\mu_B &= b\mu + \mu_B^{\mathrm{nQCD}} + \mu^{\mathrm{QCD}}\tau_B \\
\mu_C &= c\mu + \mu_C^{\mathrm{nQCD}} + \mu^{\mathrm{QCD}}\tau_C \\
\mu_D &= \mu + \mu_D^{\mathrm{nQCD}} + \mu^{\mathrm{QCD}}
\end{aligned}$$

The likelihood function is the product of the four likelihoods for the counting experiments in the four regions:

$$L(n_A, n_B, n_C, n_D \Big| \mu, \theta_\mu) = \prod_{i=A,B,C,D} \frac{e^{-\mu_i}\mu_i^{n_i}}{n_i!}$$

The maximum likelihood fit to data yields $\mu^{\mathrm{QCD}} = 9.9 \pm 1.0$. This yields an estimate of 0.13 ± 0.03 events in the signal region, which is the same as obtained from the simpler subtraction method.

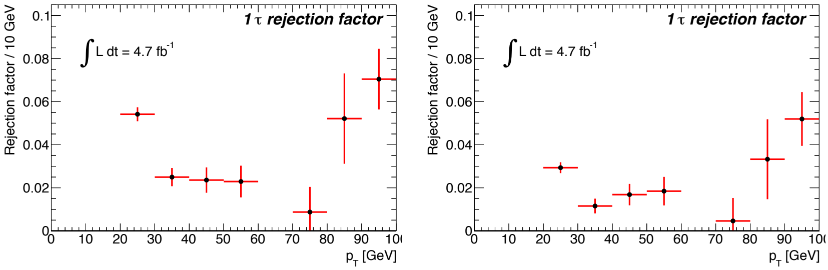

(a) Loose τ ID

(b) Medium τ ID

Figure 9.10: Fake τ identification factors for QCD multijet events.

τ Misidentification Factor

When requiring a τ in the multijet control region, the insufficient statistics of the simulations make these unsuitable both for plotting and for determining signal region estimates. Therefore, the method based on weighting of τ candidates, that greatly increases the available statistics, was used to both cross-check the signal region estimate from the ABCD method, and for indicating multijet contributions in plots.

As a starting point, a looser τ is selected at random from data in the multijet control region. The probability of a randomly chosen looser tau to be identified as a nominal tau is then calculated, as described in the Section 8.8.1. To increase the number of selected τ leptons there is no selection on m_{T} applied to the multijet control region. The overall probability, not binned in p_{T}, of identifying a looser τ as nominal was found to be consistent with the m_{T} selection applied. To minimise the contribution from electroweak processes and therefore contribution from real τ leptons, the electroweak estimates from simulations are subtracted from the data. The resulting probabilities can bee seen in Figure 9.10 and agrees with similar results in the 2τ analysis channel.

For all plots including multijet contributions it is the estimate using the weighted looser τ that is used. Figure 9.11 shows good data and Monte Carlo agreement for the main kinematic distributions in the multijet control region with a nominal τ using the method described in this section for the multijet distributions.

Furthermore, the signal region estimate from the ABCD method was cross-checked using the method. A comparison of the signal region estimates, that are found to be in good agreement, is shown in Table 9.7. Also,

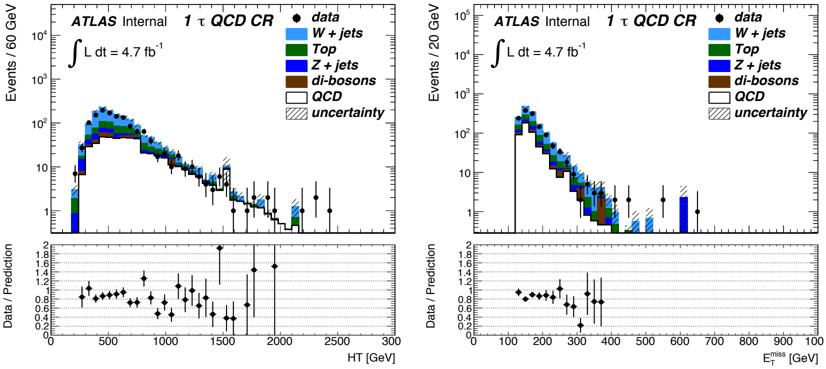

(a) H_{T} (b) $E_{\mathrm{T}}^{\mathrm{miss}}$

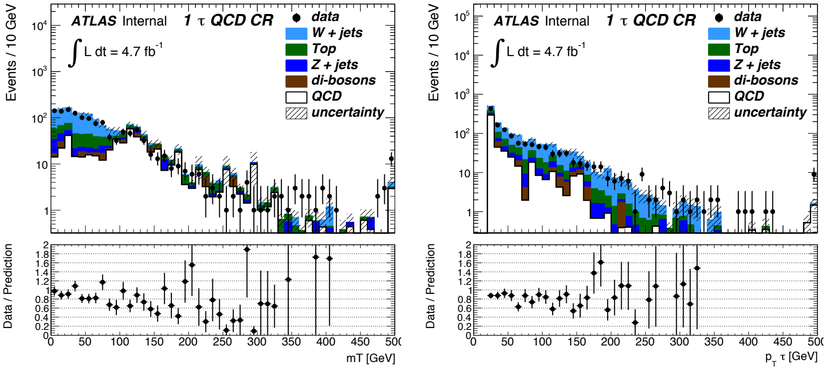

(c) m_{T} (d) τ p_{T}

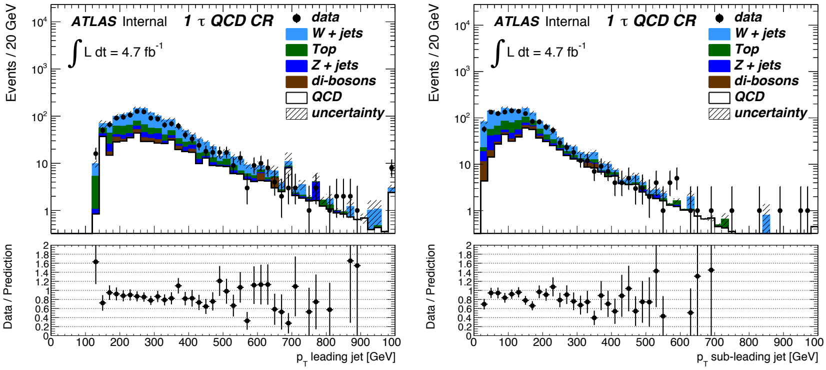

(e) jet_1 p_{T} (f) jet_2 p_{T}

Figure 9.11: τ multijet control region distributions. The multijet contributions are from weighting looser τ candidates.

Table 9.7: Estimated QCD signal region contributions from the investigated methods. No scale indicates that the non-QCD contributions to the extra loose tau region are not scaled with the electroweak scale factors. Uncertainties are statistical only.

Methode	ABCD subtr. no scale	ABCD subtr.	Weighted extra loose
QCD in SR	0.13 ± 0.03	0.17 ± 0.04	0.48 ± 0.21

the multijet contribution in the electroweak control regions are found to be negligible using this methods. Typical contaminations are at, or below, the percent level.

9.3.4 Other Backgrounds

The small contributions from diboson and Drell-Yan events in this analysis are taken from Monte Carlo. For both of these backgrounds there is a small contribution observed in the control regions, while no events survive the signal region selection. Upper bounds on the contributions in the signal region were set, taking into account the amount of statistics available in the simulations.

9.4 Systematic Uncertainties

For each of the detector related systematics outlined in Section 8.9 the systematic uncertainty on the signal region estimate is calculated by propagating the relevant change through the whole analysis chain including recomputation of the scale factors. To disentangle the statistical and systematic effect, the H_{T} selection is relaxed to 600 GeV when evaluating the systematic uncertainties.

Additionally, systematic uncertainties are attributed to the chosen method for estimating the multijet and W+jets background. The 50% uncertainty on the multijet estimate accounts for the dependence of the method on the electroweak scale factors. Similarly, the 21% uncertainty on the W+jets estimate with a true τ covers the discrepancy between the scaling factor obtained from the charge asymmetry and the matrix inversion method.

Another systematic uncertainty is attributed to the Monte Carlo generator choice and extrapolation from the control to the signal region. For W+jets and multijets these uncertainties are assumed to already be covered by the systematic uncertainties attributed to the choice of method. For $t\bar{t}$ the nominal estimates are compared to that obtained using predictions from

Table 9.8: Overview of relative systematic and statistical uncertainties on signal region background estimates.

Systematic	QCD	W+jets (truth)	W+jets (fake)	Top (truth)	Top (fake)	Z+jets	di-boson
JER	0.33	<0.002	1.1	-0.06	0.14	0.23	<0.002
JES up	0.16	0.03	1.4	0.02	0.15	0.23	-0.33
JES down	-0.09	-0.22	-0.90	-0.04	-0.10	<0.002	<0.002
TES up	0.03	<0.002	0.07	-0.007	0.13	0.23	<0.002
TES down	0.06	<0.002	0.20	-0.13	-0.10	<0.002	<0.002
Tau ID	0.07	0.06	-0.01	0.06	0.07	0.06	0.07
Pile-up re-wgt.	0.01	<0.002	0.20	-0.02	-0.05	<0.002	<0.002
ST scale up	0.01	<0.002	<0.002	<0.002	<0.002	<0.002	<0.002
ST scale down	-0.06	<0.002	<0.002	<0.002	<0.002	<0.002	<0.002
ST res. up	0.04	<0.002	<0.002	<0.002	<0.002	<0.002	<0.002
ST res. down	-0.01	<0.002	<0.002	<0.002	<0.002	<0.002	<0.002
Bjet up	-0.02	0.05	0.33	-0.10	-0.08	0.02	<0.002
Bjet down	0.04	-0.05	-0.07	0.09	0.08	-0.02	<0.002
Bjet light up	0.01	-0.01	0.01	-0.02	-0.04	-0.004	-0.003
Bjet light down	0.01	0.01	-0.06	-0.003	0.04	0.004	0.003
Method	0.50	0.21	—	—	—	—	—
Generator Di-Bos.	—	<0.002	<0.002	<0.002	<0.002	0.05	0.04
Generator $t\bar{t}$	—	—	—	0.15	0.15	—	—
Theory/Extrapol.	—	0.30	0.27	0.26	0.26	—	—
Total syst. unct.	0.63	0.39	1.65	0.33	0.40	0.57	0.34
Stat. unctertainty	0.21	0.70	1.13	0.38	0.81	1.0	—

`POWHEG` and `AcerMC` [170] generators, resulting in a 15% uncertainty. For diboson events, a similar comparison yields a 25% uncertainty in the control regions. As no diboson events pass the signal region selection, an upper limit on the signal region contribution, corresponding to one MC event with a weight of 0.04, is assumed. In addition, an uncertainty on the total integrated luminosity of 3.9% [171] is applied to the diboson estimate, as this is determined from pure Monte Carlo predictions scaled to the recorded amount of integrated luminosity, rather than a data-driven approach.

From Table 9.8 the main systematic uncertainties are seen to be the ones related to the jet measurement — namely the jet energy resolution and jet

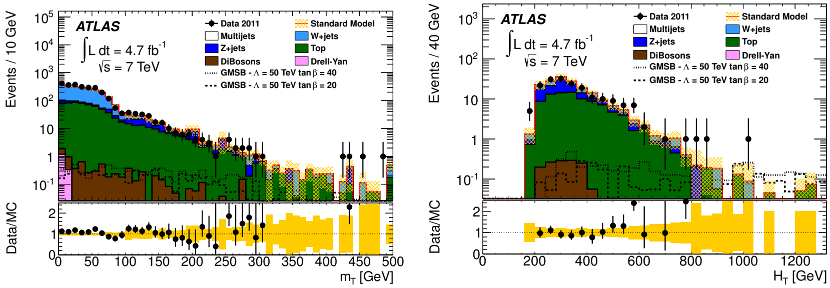

(a) m_{T} (b) H_{T}

Figure 9.12: Distributions of the final two variables defining the signal region after all selections, apart from the variable shown, have been applied. The uncertainties shown are statistically only. The yellow band represents the uncertainties of the background estimates while Poisson errors are shown for the data points.

energy scale. Followed by uncertainties related to generators, method and theoretical uncertainties along with the τ energy scale.

9.5 Results and Interpretation

Table 9.9 shows the remaining events in data and Monte Carlo for the last selections applied in the analysis after the appropriate scale factors obtained in the previous sections are applied. Again, the data and Monte Carlo agreement is seen to be good. After both the multijet rejecting selections are applied, the multijet contribution is reduced by more than two orders of magnitude. Likewise, the m_{T} selection removes close to two orders of magnitude of the W+jets background, while also removing a significant fraction of Top and Z+jets. The final selection on H_{T} removes about an order of magnitude across all backgrounds.

Figure 9.12 shows the distribution of the final two variables that define the signal region, with all other selections applied up until the selection on the variable shown. The resulting total number of background events in the signal region is $1.31 \pm 0.37^{\mathrm{stat}} \pm 0.65^{\mathrm{syst}}$ compared to 4 observed data events. Having observed slightly more events in the data than expected from Standard Model background only, this begs the question how significant such a discrepancy is. The probability of the expected background yielding 4 or more observed events is 5.3%, whereas the probability for such a fluctuation

Table 9.9: Cut-flow for the selection defining the signal region after baseline event selection showing expected Standard Model backgrounds and data. Background estimates are from simulations with scale factors applied to top, W+jets and Z+jets, except for the final estimate of QCD events, which is obtained by a data-driven method. The errors are statistical only.

After cut	$1\ \tau$	$\Delta\phi_{\mathrm{min}}$	$E_{\mathrm{T}}^{\mathrm{miss}}/m_{\mathrm{eff}}$	m_{T}	H_{T}
W+jets	2045 ± 114	1951 ± 107	1593 ± 89	34 ± 15	0.30 ± 0.16
Top	890 ± 55	834 ± 50	680 ± 41	90 ± 14	0.61 ± 0.25
QCD	456 ± 222	28 ± 10	3.7 ± 3.6	< 3.5	0.17 ± 0.04
Z+jets	243 ± 15	205 ± 14	157 ± 13	52 ± 8	0.22 ± 0.22
Drell-Yan	4.1 ± 1.2	2.2 ± 0.9	1.5 ± 0.8	< 0.36	< 0.36
Di-boson	9.0 ± 1.0	7.8 ± 0.9	5.8 ± 0.6	1.5 ± 0.3	< 0.05
Total SM	3656 ± 256	3028 ± 120	2441 ± 99	178 ± 22	1.31 ± 0.37
Data	3751	3370	2673	184	4

in one or more of the four signal regions is 19.6%. Detector event displays for the four observed data events in the signal region are shown in Section A.3.

The expected GMSB signal ranges from $\mathcal{O}$(0.01-1000) across the grid with a typical statistical and systematic uncertainty around 10-20%, while the uncertainty of the signal production cross section typically is around 20%. Combining this information, the 95% CL limit shown in Figure 9.13 is set for the GMSB grid. The expected exclusion is indicated by the dashed black line with the one standard deviation uncertainty band in yellow. The observed limit is shown in solid red. The dark grey region is theoretically excluded due to unphysical sparticle mass values, while the orange, cyan and light grey areas are limits obtained by OPAL [126]. The figure also indicates the NLSP of a given region – slepton, coNLSP and stau respectively going from low to high $\tan\beta$. The dashed-dotted vertical grey lines indicate the gluino mass and is seen to depend on Λ.

The effect of the upward fluctuation in data observed in the signal region is seen by the observed limit being weakened compared to the expected exclusion. The exclusion reach in Λ increases with $\tan\beta$ and at $\tan\beta$ values around 40 the expected exclusion reaches Λ values of ~ 50. The observed exclusion extends to a maximum of ~ 44 for similar $\tan\beta$ values. For the observed exclusion this corresponds to gluino masses ranging between 800-1000 GeV going from low to high $\tan\beta$.

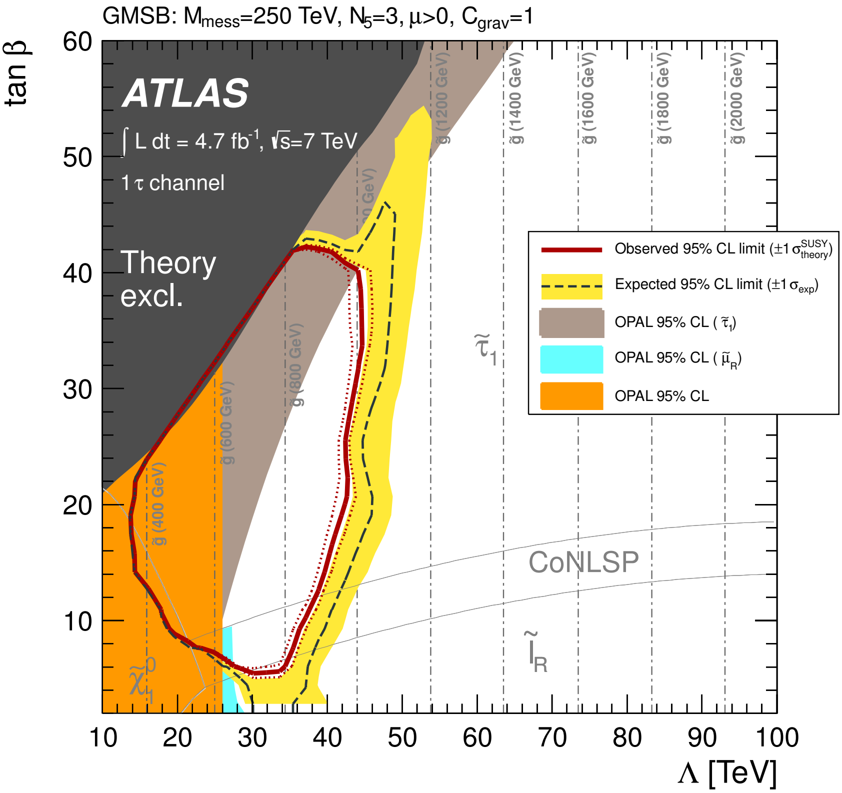

Figure 9.13: Observed and expected 95% CL exclusion limit in the GMSB plane spanned by Λ and $\tan\beta$. The yellow band indicate the $\pm\sigma$ uncertainty on the expected exclusion, while the red dotted line indicates the theoretical uncertainty on the signal cross section [172].

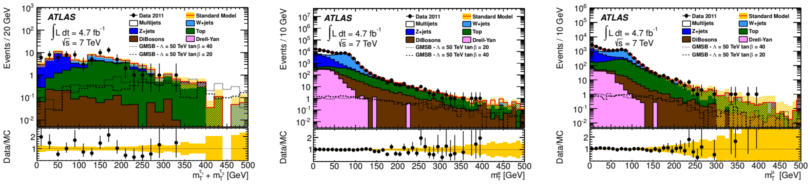

(a) 2τ (b) $\tau+e$ (c) $\tau+\mu$

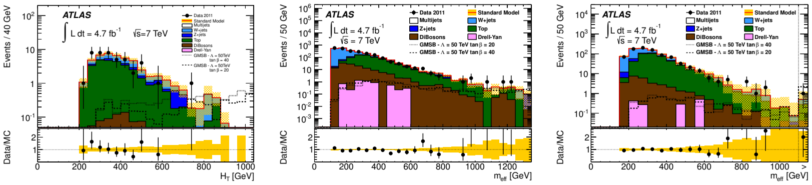

(d) 2τ (e) $\tau+e$ (f) $\tau+\mu$

Figure 9.14: Signal region kinematic distributions for 2τ and τ+lepton analysis channels [172].

9.6 Other Search Channels and Combination

In addition to the results obtained in the 1τ channel described in the previous sections, the analysis consists of three additional search channels – 2τ, $\tau+e$ and $\tau+\mu$. The 2τ channel is based on the same trigger as the 1τ analysis, and consequently applies the same trigger plateau selection. Furthermore, also the multijet reducing selections ($E_{\mathrm{T}}^{\mathrm{miss}}/m_{\mathrm{eff}} > 0.3$ and $\Delta\Phi(\mathrm{jet}, E_{\mathrm{T}}^{\mathrm{miss}}) > 0.3$) are shared between the two search channels. Additionally two τ leptons passing loose identification is required, while events with light leptons are vetoed. The loosening of the τ identification with respect to that applied in the 1τ channel is offset by the additional fake background suppression achieved from the additional τ. Furthermore, the two remaining signal enhancing selections are like the 1τ channel based on m_{T} and H_{T}. The sum of the transverse masses of the two τ leptons with $E_{\mathrm{T}}^{\mathrm{miss}}$ is required to be larger than 100 GeV, while H_{T} is required to be larger than 650 GeV. The distributions of these two final variables are shown in Figure 9.14. Also the background estimation techniques for the channels is similar to those applied and described in the previous sections. Electroweak backgrounds are scaled by factors obtained from dedicated control regions for top, W+jets and Z+jets using the matrix inversion method. Multijet contributions are estimated by scaling looser τ candidates in Monte Carlo simulations by a identification specific identification factor. In the end no significant excess

Table 9.10: Number of expected background events and data yields in the four final states discussed. The 95 % confidence level (CL) upper limits on the number of observed (expected) signal events and corresponding cross-section from any new physics scenario that can be set are also shown for each analysis channel.

–	1τ	2τ	$\tau+\mu$	$\tau+e$
Multijet	$0.17 \pm 0.04 \pm 0.11$	$0.17 \pm 0.15 \pm 0.36$	< 0.01	0.22 ± 0.30
W + jets	$0.31 \pm 0.16 \pm 0.16$	$1.11 \pm 0.67 \pm 0.30$	$0.27 \pm 0.21 \pm 0.13$	$0.24 \pm 0.17 \pm 0.27$
Z + jets	$0.22 \pm 0.22 \pm 0.09$	$0.36 \pm 0.26 \pm 0.35$	$0.05 \pm 0.05 \pm 0.01$	$0.17 \pm 0.12 \pm 0.05$
Top	$0.61 \pm 0.25 \pm 0.11$	$0.76 \pm 0.31 \pm 0.31$	$0.36 \pm 0.18 \pm 0.26$	$1.41 \pm 0.27 \pm 0.84$
Diboson	< 0.05	$0.02 \pm 0.01 \pm 0.07$	$0.11 \pm 0.04 \pm 0.02$	$0.26 \pm 0.12 \pm 0.11$
Drell-Yan	< 0.36	$0.49 \pm 0.49 \pm 0.21$	< 0.002	< 0.002
Total background	$1.31 \pm 0.37 \pm 0.65$	$2.91 \pm 0.89 \pm 0.76$	$0.79 \pm 0.28 \pm 0.39$	$2.31 \pm 0.40 \pm 1.40$
Data	4	1	1	3
Obs. (exp.) upper limit on number of signal events	7.7 (4.5)	3.2 (4.7)	3.7 (3.4)	5.2 (4.6)
Obs. (exp.) upper limit on visible Cross-Section (fb)	1.67 (0.95)	0.68 (0.99)	0.78 (0.72)	1.10 (0.98)

with respect to the Standard Model expectation is found in the signal region and upper limits on potential contributions from new physics processes are set.

The methods and selections applied in the τ+lepton channels are slightly different from the other two due to the presence of the light leptons. These channels use triggers based on the presence of a single electron or muon. The muon trigger also needs one jet in the event to fire, making it necessary to require a leading jet p_{T} of 50 GeV to be in a region where the trigger is close to fully efficient. Unlike the two other channels there is no additional selection on $E_{\mathrm{T}}^{\mathrm{miss}}$ or transverse momentum of jets. At least one τ passing loose identification is then required in addition to a muon or electron. The two final selections applied to define the signal region are common between the $\tau+e$ and $\tau+\mu$ channels. The first is similar to that of the two other channels with a selection on $m_{\mathrm{T}} > 100$ GeV to reduce electroweak backgrounds. The only difference being that the transverse mass is calculated using the light lepton rather than the τ. The final selection is on $m_{\mathrm{eff}} > 1$ TeV, which is just a linear combination of the H_{T} and $E_{\mathrm{T}}^{\mathrm{miss}}$ selections applied in the other analysis channels. This means that the phase space probed is very similar across all channels. As for the other channels, the matrix inversion method is used to derive scaling factors for the top and W+jets background. Multijet backgrounds are estimated using the matrix method, described in for example [173], where the light lepton identification is varied to determine the contribution from fake leptons. As for the other channels, results are found to be consistent with Standard Model background only and exclusion limits are set.

In all search channels the observed data is found to be consistent with the Standard Model only hypothesis. Table 9.10 shows the signal region background expectations and observations in data for all search channels. Since no significant deviations with respect to the background are observed combined exclusion limits on the GMSB grid is set as seen in Figure 9.15. Values of Λ below 45 TeV are excluded at 95% CL independent of $\tan\beta$. The maximal exclusion reached in Λ is 58 TeV. This corresponds to a exclusion of gluino masses in the model ranging from 1000-1250 GeV. Here the results from all search channels are used and included in the total likelihood function. Additionally, model independent upper limits on contributions from any new physics processes in these regions are set, as shown in Table 9.10. In Section A.4 a comparison of the individual 95% CL observed search channel limits are shown. A comparison of the combined observed limit presented here with the limit obtained in the ATLAS dilepton search [173] on the same dataset is also shown. The τ search is seen to provide the strongest exclusion at large $\tan\beta$ where the models have τ rich final states, while the dilepton exclusion limit

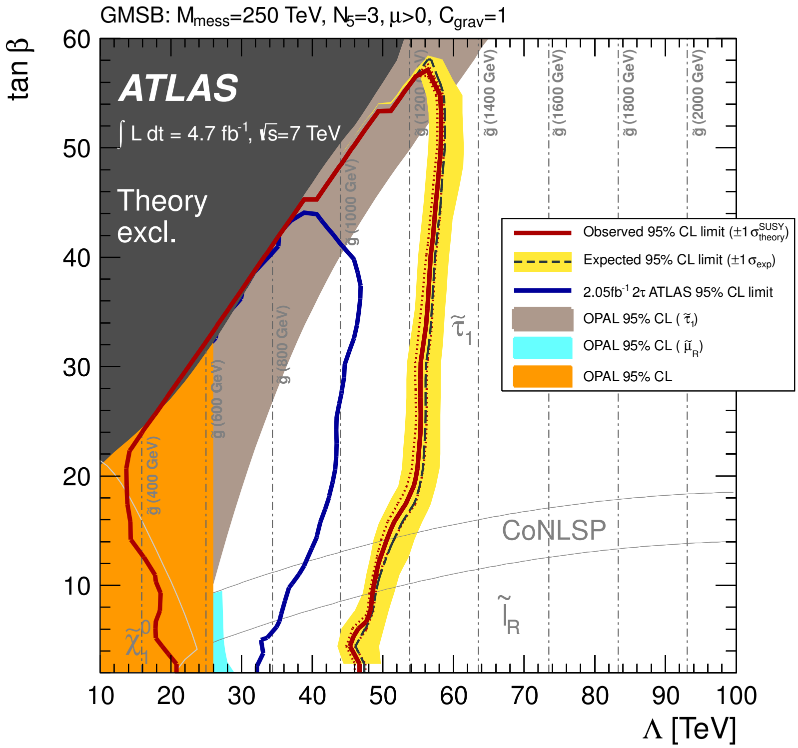

Figure 9.15: Combined exclusion at 95% CL obtained in the GMSB plane when combining the results of the four analysis channels. The blue line shows the previous observed exclusion obtained by the 2τ analysis, using about half of the total dataset used in this analysis [172].

is the strongest at low tan β as the slepton LSP there leads to an increase in final states with light leptons.

Chapter 10

Analysis of 8 TeV Data

Following the successful running of both the LHC and the associated experiments the previous year, the 2012 data taking period saw an increase in the centre-of-mass energy from 7 to 8 TeV. In addition to the increased beam energy, more than five times as much data was collected over the course of 2012 compared to the year before, as seen in Figure 10.1. With the increase in both energy and collected data, searches extended their reach to higher sparticle masses and lower production cross sections than previously accessible. With increasingly large portions of supersymmetric parameter space being probed, the final results of the first LHC run period saw a significant improvement upon previous ATLAS results.

The increase in the amount of collected data was largely made possible by the increased number of interactions per bunch crossing in the 2012 collisions compared to the year before. While this allowed more particle collisions to be studied, the additional interaction vertices were also a challenge from an analysis point of view due to the increased complexity of the events. Naturally this will make the matching of a physics object to a specific vertex more difficult, while at the same time object reconstruction could be influenced by energy deposits from pileup interactions. In particular, low p_{T} jets from pileup interactions being attributed to the primary, hard interactions could potentially be problematic. This meant that both accurate description of pileup in simulations, and physics objects and kinematic variables being robust with respect to pileup was even more important in the analysis of the 2012 dataset. The τ identification, for instance, underwent significant improvement, making it more stable against pileup effects, between the two data taking periods.

The analysis of the 8 TeV dataset collected in 2012 builds on the analysis performed on the 7 TeV dataset from 2011. The main components remain unchanged — orthogonal analysis channels with differing τ and light lepton

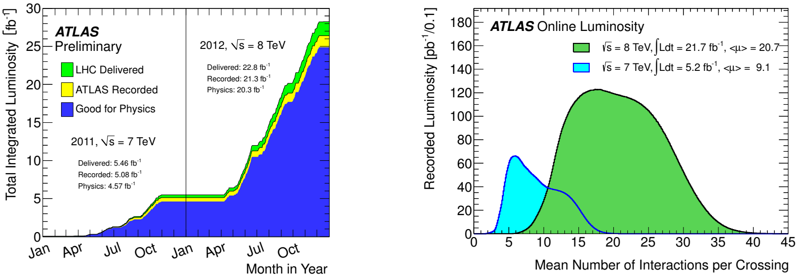

(a) Luminosity (b) Pileup

Figure 10.1: 2012 data taking conditions compared to the previous year – integrated luminosity and mean number of interactions per bunch crossing [78].

content; large $E_{\mathrm{T}}^{\mathrm{miss}}$ and total transverse momentum in the event to target strongly produced SUSY along with the main background estimation techniques remaining unaltered. Despite the similarities, there are several improvements with respect to the first iteration of the analysis. In all analysis channels the selections were fully re-optimised to the new energy and integrated luminosity. Results were interpreted in additional SUSY models and multiple new signal regions were defined to target different signal characteristics. In total, the number of signal regions were increased from 4 to 14 between the two analyses. Background estimation techniques were modified, improved upon or new methods were applied including the selections defining the control regions. Great care was taken to understand the effects of different Monte Carlo generators, including the simulation of the detector response, and pileup dependence of the analysis. Also the simulated statistics in the nominal Standard Model background samples were increased. Finally, the performance of physics objects used was also improved by the relevant performance groups to the benefit of the analysis. While there, unfortunately, was no sign of new physics in the final results, the sum of these changes allowed for a significant increase in the achieved exclusion reach in SUSY parameter space.

10.1 Dataset and Monte Carlo Samples

The proton-proton collisions analysed were collected from April 12th to December 6th of 2012 at a centre-of-mass energy of 8 TeV. During this period

Table 10.1: Generators used for simulation of relevant Standard Model background processes. All Monte Carlo simulations are from the MC12a production campaign.

Process	Generator	Alternative Generator
$t\bar{t}$	`POWHEG+PYTHIA (AFII)`	`ALPGEN`
Single top	`MC@NLO` & `ACER`	-
W/Z+jets	`SHERPA` (massive c/b)	`ALPGEN`
Diboson	`SHERPA`	`POWHEG+PYTHIA`
Multijet	`PYTHIA`	-

the LHC delivered 22.8 fb^{-1} of data, of which 21.3 fb^{-1} was recorded by the ATLAS experiment corresponding to just above 93% of the total delivered. After requiring that the data is from a run contained in the standard SUSY group Good Run List, `v61-pro14-02_DQDefects-00-01-00_PHYS_-StandardGRL_All_Good`, a total integrated luminosity of 20.3 fb^{-1} is left for analysis. Both data and Monte Carlo are officially produced SUSY D3PDs with tag `p1512` for Monte Carlo, and `p1542` for data.

The generators used to simulate the Standard Model background processes are listed in Table 10.1, while a full list of Monte Carlo samples used in the analysis can be found in Section B.1. The leading-order cross sections calculated by the generators for the simulated samples are corrected by k-factors provided centrally by the SUSY group to their next-to-next-to-leading order values.

The $t\bar{t}$ samples are simulated using ATLAS fast simulation (`AFII`) for the detector response, rather than full ATLAS simulation. `POWHEG r2129` was used in conjunction with `PYTHIA 6.246` for the event generation using `CT10` PDFs. While the fast simulation uses parametrised detector response, and therefore is not as accurate as the full simulation, the reduced CPU time needed to simulate an event means that a much larger number of events may be generated, thus reducing the statistical uncertainty of the estimates derived from the sample. The accuracy of the fast simulation was extensively checked against data and full simulation to ensure that it was satisfactory, especially the modelling of the τ content was investigated. Additionally, the simulated $t\bar{t}$ samples were reweighed in bins of true p_{T} of the $t\bar{t}$ system to agree with the most recent measurements of the $t\bar{t}$ differential cross-section [174]. Systematic uncertainties on the chosen generator were evaluated using samples simulated using `ALPGEN` with up to four associated partons produced. Single top events are simulated by `MC@NLO 4.06` with `HERWIG 6.520` show-

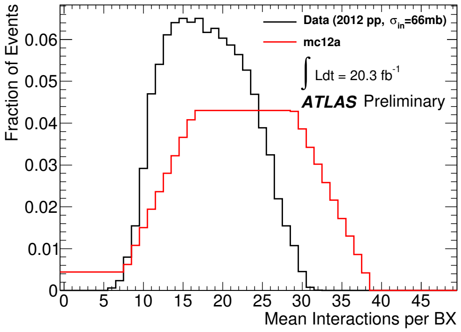

Figure 10.2: Simulated pileup conditions in MC12a production Monte Carlo and the actual distribution observed in data [78].

ering for the $s-$ and $Wt-$channel production (`CT10` PDF), and `ACER 3.8` with `PYTHIA 6.246` showering for the t channel (`CTEQ6L1` PDF).

Processes with vector bosons produced in association with jets are simulated using the `SHERPA 1.4.1` generator with massive c and b quarks, and `CT10` PDFs. Samples binned in transverse momentum of the boson are combined with inclusive samples by requiring the samples to be orthogonal in the boson p_{T}. The low-p_{T} W/Z+jets samples are simulated using `AFII` to model the detector response, while the remaining samples use the full GEANT4 based detector simulation. These samples are also split into boson decay mode and quark flavour. Furthermore, they are reweighed by correction factors binned in true transverse momentum of the boson to account for observed mismodelling in data of the boson p_{T} in kinematic regions of high $E_{\mathrm{T}}^{\mathrm{miss}}$ and leading jet p_{T}. These correction factors were first derived in the context of the ATLAS stop-charm search [175], but were found to be applicable in the phase space considered in this analysis as well. Generator systematics were obtained from W/Z+jets samples simulated using `ALPGEN 2.14`, that accounts for production of up to five accompanying partons, using `CTEQ6L1` PDFs. For these samples fragmentation and hadronisation are performed with `HERWIG 6.520`, and `JIMMY` is used to simulate the underlying event.

Diboson samples are simulated by `SHERPA`, while Drell-Yan contributions are found to be small by studying events generated by `ALPGEN`. Since the contribution is small and Drell-Yan samples have significant overlap with the Sherpa Z+jets samples, Drell-Yan samples has been omitted throughout the analyses. Both contributions from a Standard Model Higgs boson and production of $t\bar{t}$ in association with a vector boson were checked and found to be negligible and are consequently omitted throughout. Alternative diboson simulations, using `POWHEG r2129` together with `PYTHIA 8.165`, were used to evaluate systematic uncertainties.

Two further reweightings are applied in order for the simulations to accurately reproduce the data — pileup and b-tag reweighing. Even though simulations are performed including a best guess of the expected pileup conditions, the simulations are later corrected to the actual pileup conditions observed in data by applying weights based on the mean number of interactions per bunch crossing. This is done using the ATLAS `PileupReweighting` tool. Figure 10.2 shows the simulated pileup conditions compared to that observed in 2012 data. In regions where b-tags are used weights depending on the truth, light and heavy jet content and the b-tagging algorithm are applied to correct for the differences in b-tagging efficiencies and fake rates between simulations and data.

The signal samples studied are produced using `PYTHIA 6.246`, with the `CTEQ6L1` PDF set, except for the bRPV model where `HERWIG++ 2.5.2` was used.

Tau lepton decays were mainly simulated using `TAUOLA 2.4`, and for the modelling of the underlying event the ATLAS AUET2B tune was primarily used. The exception to this was events produced with `SHERPA`, `HERWIG++ 2.5.2` or `PYTHIA 8.165` where τ lepton decays were simulated within the generator, and the built-in `SHERPA`, UEEE [176], AU2 [177] tunes were respectively used for the underlying event modelling. Additionally, the $t\bar{t}$ samples generated using `POWHEG` uses the Perugia 2011C tune [178].

10.2 Event Selection

As for the 7 TeV analysis the hadronic analysis channels are based on a trigger requiring a high p_{T} jet and $E_{\mathrm{T}}^{\mathrm{miss}}$. To keep the trigger rate at the desired level for the new running conditions the $E_{\mathrm{T}}^{\mathrm{miss}}$ and jet p_{T} trigger thresholds were slightly raised with respect to their 7 TeV values. Throughout the data taking period the lowest unprescaled $E_{\mathrm{T}}^{\mathrm{miss}}$ and jet p_{T} trigger, `EF_j80_a4tchad_xe100_tclcw_veryloose`, was required to have fired. This trigger requires that $E_{\mathrm{T}}^{\mathrm{miss}}$ and leading jet p_{T} at EF level satisfy: $E_T^{\mathrm{miss,EF}} > 100$ GeV and leading jet $p_T^{\mathrm{EF}} > 80$ GeV. The trigger is seeded by the trigger `L2_j75_c4cchad_xe45` at L2, that in turn is seeded by `L1_J30_XE40` at L1. To find the corresponding offline thresholds at which the trigger is close to fully efficient, data events triggered by an independent trigger based on a single, isolated muon are studied. Muon stream events passing the trigger

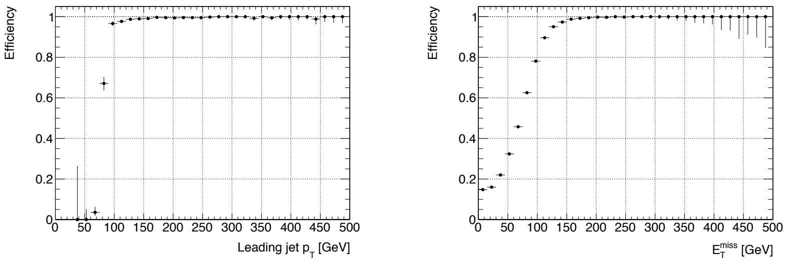

(a) Leading jet p_T turn-on

(b) $E_\mathrm{T}^\mathrm{miss}$ turn-on

Figure 10.3: Trigger turn-on curves in $E_\mathrm{T}^\mathrm{miss}$ and leading jet p_T for `EF_j80_a4tchad_xe100_tclcw_veryloose` in period B data events selected by `EF_mu24i_tight`.

`EF_mu24i_tight` and basic event cleaning from period B data taking were selected. Additionally, the events were required to contain an offline muon and two analysis jets. From these events the efficiency of the $E_\mathrm{T}^\mathrm{miss}$ part of the trigger is calculated as a function of offline $E_\mathrm{T}^\mathrm{miss}$. To test the $E_\mathrm{T}^\mathrm{miss}$ term of the combined trigger, only events where the jet term is close to fully efficient, leading jet $p_\mathrm{T}>$ 130 GeV and sub-leading jet $p_\mathrm{T}>$ 30 GeV, is used when calculating the efficiency. Similarly, the efficiency of the jet term is calculated as a function of leading jet p_T, when requiring the $E_\mathrm{T}^\mathrm{miss}$ term to be at its plateau, $E_\mathrm{T}^\mathrm{miss} > 160$ GeV. The resulting efficiencies are shown in Figure 10.3.

The efficiency is also checked for correlations between $E_\mathrm{T}^\mathrm{miss}$ and leading jet p_T, as shown in Figure 10.4, where the efficiency is calculated as function of these two variables simultaneously using the same selection of events as before.

The trigger is seen to be close to fully efficient around $E_\mathrm{T}^\mathrm{miss} > 150$ GeV, leading jet $p_\mathrm{T}>$ 130 GeV and sub-leading jet $p_\mathrm{T}>$ 30 GeV. These selection values are applied in the analysis to ensure that the trigger is close to fully efficient. Figure 10.5 shows the fraction of the total number of events passing the offline trigger threshold selections for the three signal grids considered in the analysis. For the GMSB grid around 50-60% satisfy this requirement for most parts of the grid. The mSUGRA grid is close to fully efficient across the whole grid but drops to around 60% for the lowest $m_{1/2}$ values. In general the bRPV grid has the lowest efficiency, ranging from around 10% at low $m_{1/2}$ values to about 70% at high, due to the lower $E_\mathrm{T}^\mathrm{miss}$ due to the LSP decay. As these efficiencies also include weak production modes, the selection efficiency

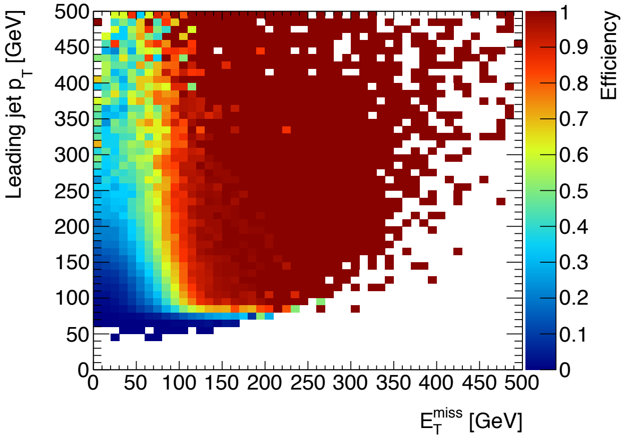

Figure 10.4: Trigger efficiency of `EF_j80_a4tchad_xe100_tclcw_veryloose` in period B data events selected by `EF_mu24i_tight`.

of only strong production processes is generally expected to be higher due to the increased presence of high momentum jets for such production modes.

As for the 7 TeV analysis events are required to pass a common, basic event selection. This involves requiring a primary vertex as defined in Section 8, removing corrupt or noisy events, jets or muons showing signs of problems with reconstruction or measurements, or muons consistent with cosmic rays.

The selection of τ leptons and electrons and muons is unchanged with respect to the 7 TeV analysis — events are required to contain exactly one medium τ, and no additional electrons, muons or loose τ leptons. The QCD multijet rejecting selection on $\Delta\Phi(\text{jet}, E_{\text{T}}^{\text{miss}})$ is kept at 0.3, while the fixed selection on $E_{\text{T}}^{\text{miss}}/m_{\text{eff}}$ was removed as it was found to be inefficient for certain signal models and in particular the bRPV grid, as seen in Figure 8.8. Even when removing this selection the multijet contribution was found to be of a manageable magnitude in the signal regions when separate selections on $E_{\text{T}}^{\text{miss}}$ and H_{T} were applied. The requirement on τ p_{T} was raised to 30 GeV to reduce the influence of Z→ $\nu\nu$ background and possible pileup effects which are most prominent at low p_{T} with negligible loss in signal efficiency.

Signal Region Selection

The effect of the trigger selection requirements described above on the main Standard Model backgrounds, as well as an example supersymmetric

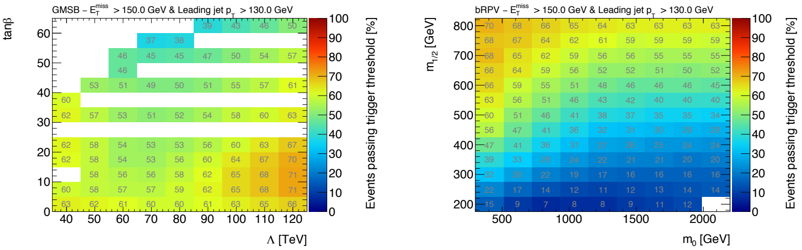

(a) GMSB (b) bRPV

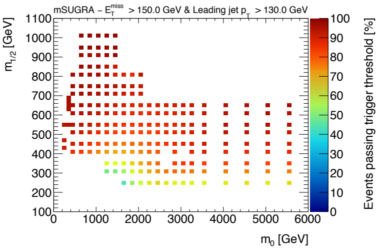

(c) mSUGRA

Figure 10.5: Efficiency, including weak production, of the trigger plateau selection for the three signal grids considered in the analysis.

signal is shown in Figure 10.6. In particular the $E_{\mathrm{T}}^{\mathrm{miss}}$ requirement is seen to remove many orders of magnitudes of Standard Model background processes, mainly multijet events, while at the same time only resulting in a comparatively modest loss of signal events. Furthermore the requirement on the leading and next-to-leading jet p_{T} removes Standard Model processes at the same time as strongly produced signal with large mass splitting between the initially produced squark/gluino and LSP remain virtually unaffected by the selection. The additional jet requirement prevents a significant fraction of Z→ $\nu\nu$ events from entering the analysis.

In addition to the event cleaning and quality and trigger selection requirements that are common to all regions investigated in the analysis, three additional selections are applied to define the signal regions. The first of these is the m_{T} selection that was raised slightly from its 7 TeV value to 140 GeV. While this increase does not yield a significant gain in sensitivity for most supersymmetric signals it allows the control regions to be defined in such a way as to contain more events and therefore reduces the uncertainty on the backgrounds estimated form these regions. Figure 10.7 shows

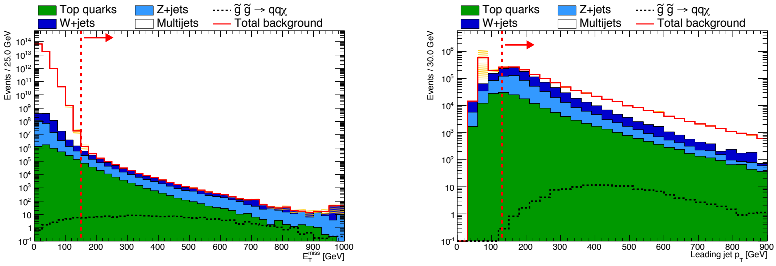

(a) $E_{\mathrm{T}}^{\mathrm{miss}}$

(b) Leading jet p_{T}

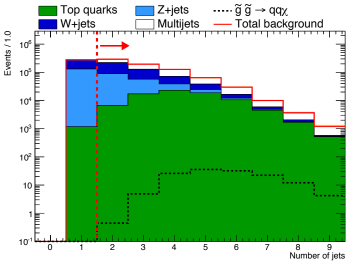

(c) Number of jets

Figure 10.6: Distributions of trigger variables showing the trigger selections, consecutively applied, indicated by the dashed red line and the direction of the selection by the arrow. Signal is illustrated by a simplified model of pair-produced gluinos decaying into quarks and a neutralino.

the main backgrounds and a dummy signal for the variables defining the signal region selection in the analysis. The figures show the distributions with the selections imposed consecutively.

The final two selections were like before applied to $E_{\mathrm{T}}^{\mathrm{miss}}$ and H_{T}. These variable values vary to some degree across the studied signal grids, as they directly relate to the parameters of mass scales that defines the 2D planes that are studied. For this reason two signal regions were defined by different cuts on these two variables to capture the properties of different parts of these grids. For the GMSB grid larger values of both $E_{\mathrm{T}}^{\mathrm{miss}}$ and H_{T} are preferred, with the favoured value of H_{T} steadily increasing with Λ, as seen in Section 8.7. A selection of $E_{\mathrm{T}}^{\mathrm{miss}} > 300$ GeV and $H_{\mathrm{T}} > 1$ TeV was found to be close to optimal in the region around the expected exclusion limit of ~ 60 GeV. Larger H_{T} and $E_{\mathrm{T}}^{\mathrm{miss}}$ values are also preferred for higher values of $m_{1/2}$ in the bRPV and mSUGRA grids. For low $m_{1/2}$ in the mSUGRA grid and across

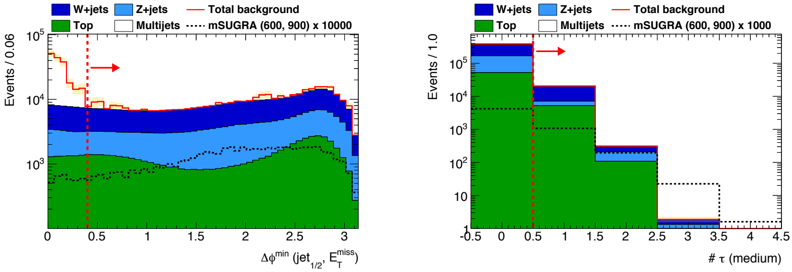

(a) $\Delta\Phi(\text{jet}, E_{\mathrm{T}}^{\mathrm{miss}})$ (b) Number of medium τ leptons

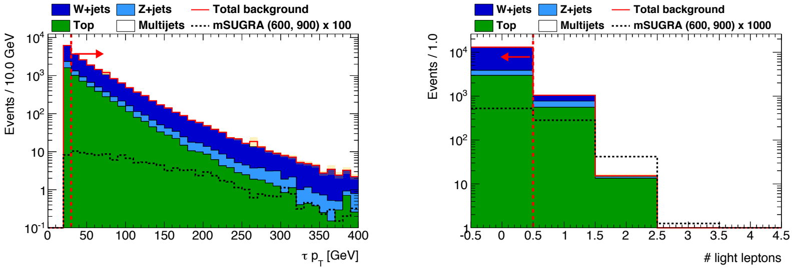

(c) τ p_{T} (d) Number of electrons and muons

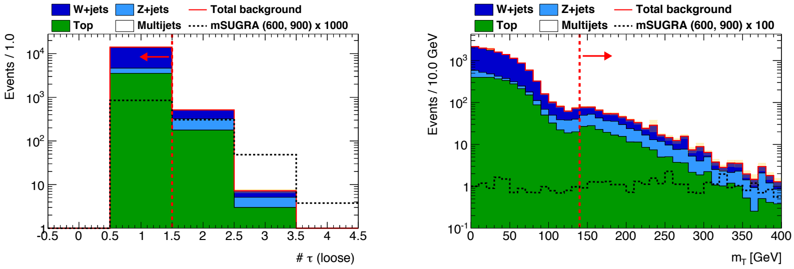

(e) Number of loose τ leptons (f) m_{T}

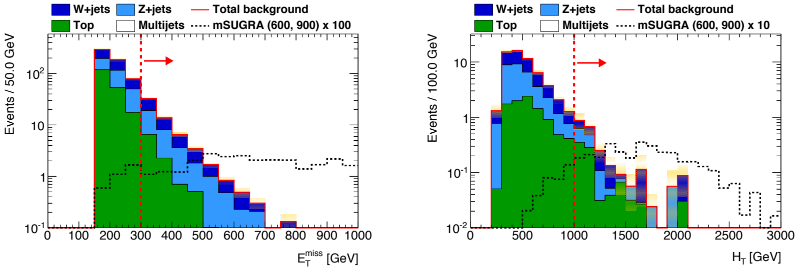

(g) $E_{\mathrm{T}}^{\mathrm{miss}}$ (h) H_{T}

Figure 10.7: Selections defining the tight signal region of the analysis. Distributions shown have all previous selections applied. The selections are indicated by the dashed red line and the direction of the selection by the arrow. Signal is illustrated by the mSUGRA point with $m_0 = 600$ GeV and $m_{1/2} = 900$ GeV. To make the signal visible in the figures it has been scaled by a factor ranging from 10-10000.

Table 10.2: Signal region selection criteria

	1τ Loose SR	1τ Tight SR
Trigger selection	$p_{\mathrm{T}}^{\mathrm{jet1}} > 130$ GeV, $p_{\mathrm{T}}^{\mathrm{jet2}} > 30$ GeV $E_{\mathrm{T}}^{\mathrm{miss}} > 150$ GeV	
Taus	$N_{\tau}^{\mathrm{medium}} = 1$ $p_{\mathrm{T}} > 30\,\mathrm{GeV}$	
Light leptons	$N_{\ell}^{\mathrm{baseline}} = 0$	
Multijet rejection	$\Delta\phi(\mathrm{jet}_{1,2}, p_{\mathrm{T}}^{\mathrm{miss}}) > 0.4$, $\Delta\phi(\tau, p_{\mathrm{T}}^{\mathrm{miss}}) > 0.2$	
Signal selections	$m_{\mathrm{T}} > 140\,\mathrm{GeV}$	
	$E_{\mathrm{T}}^{\mathrm{miss}} > 200\,\mathrm{GeV}$ $H_{\mathrm{T}} > 800\,\mathrm{GeV}$	$E_{\mathrm{T}}^{\mathrm{miss}} > 300\,\mathrm{GeV}$ $H_{\mathrm{T}} > 1000\,\mathrm{GeV}$

the bRPV grid, however, lower values of $E_{\mathrm{T}}^{\mathrm{miss}}$ are preferred. To improve sensitivity in this region a loose signal region was defined where the selections were relaxed to $E_{\mathrm{T}}^{\mathrm{miss}} > 200$ GeV and $H_{\mathrm{T}} > 800$ GeV. Both the GMSB and the bRPV grids in general have high jet activity and resulting large values of H_{T}. For both these signal regions it could improve the sensitivity to cut harder on H_{T}. However, as a selection on H_{T} does not provide significant reduction of multijet events on its own, it is necessary to select a combination of a $E_{\mathrm{T}}^{\mathrm{miss}}$ and H_{T} that together ensures that multijet events do not become the main background in the analysis, due to the difficulties in modelling this background and its systematic uncertainty accurately. For this reason the combined selection on $E_{\mathrm{T}}^{\mathrm{miss}}$ and H_{T} was chosen so that multijet contribution in the signal region would not exceed 10% when defining the signal regions, even though a larger significance could be obtained by a more stringent H_{T} selection and larger multijet contribution when not considering additional uncertainties this would introduce.

Figure 10.8 shows the corresponding selection efficiencies across the grids for the loose signal region. Signal events are seen to be most efficiently selected at high $\tan\beta$, where the τ is the NLSP, and at lower values of Λ, where strong production processes are more prominent than electroweak production mechanisms. Similarly, events at high $m_{1/2}$ and low m_0 are most efficiently selected in the bRPV grid due to the increased presence of τ leptons, and generally larger values of $E_{\mathrm{T}}^{\mathrm{miss}}$ in this region compared to the rest of the grid. The same is true also for the mSUGRA grid, where the imposed selection is most efficient along the co-annihilation region where the $\tilde{\tau}$ LSP

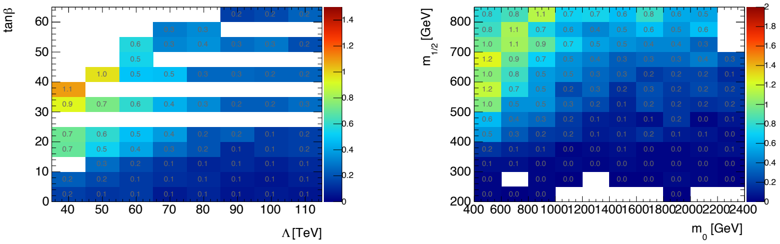

(a) GMSB (b) bRPV

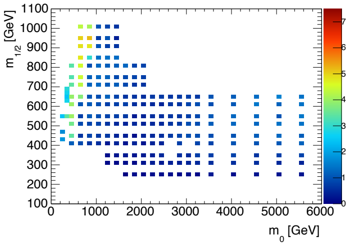

(c) mSUGRA

Figure 10.8: Signal region selection efficiency × acceptance for the loose signal region in the GMSB, bRPV and mSUGRA signal grids.

leads to events with τ final states. A full overview of signal acceptance and efficiencies in all grids for both signal regions can be found in Section B.4.

Figure 10.9 shows the expected 95% CL exclusion reach for the two signal regions in the three signal grids that are considered using the modified Asimov significance as the significance measure. The tight signal region shown on the right hand side is seen to be most sensitive for the GMSB grid and at high $m_{1/2}$ in the bRPV and mSUGRA grids as expected. The loose signal region, on the other hand, extends the exclusion at low $m_{1/2}$ in both the mSUGRA and the bRPV grids.

Control Region Selection

Control regions for the various Standard Model background processes are defined after the common selections outlined at the start of this section. A QCD multijet dominated control region is constructed by requiring that

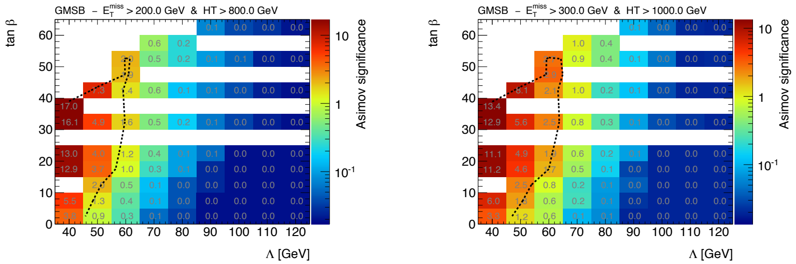

(a) Loose signal region (b) Tight signal region

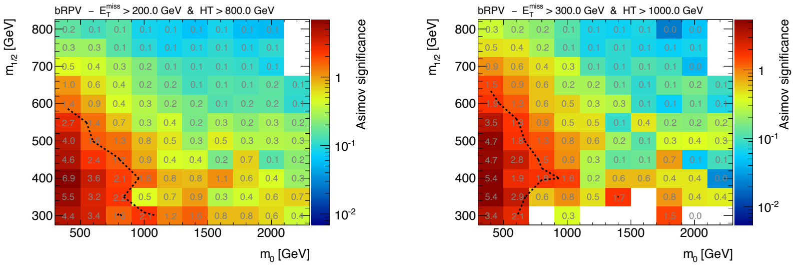

(c) Loose signal region (d) Tight signal region

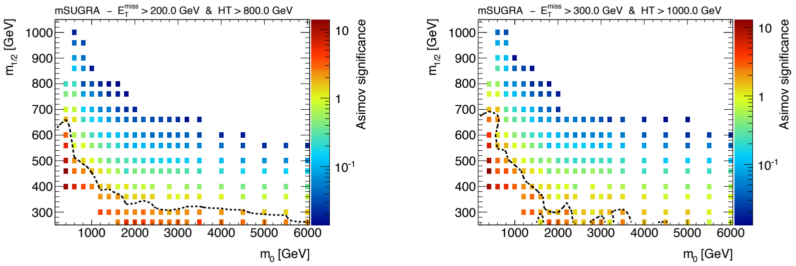

(e) Loose signal region (f) Tight signal region

Figure 10.9: The expected exclusion in the GMSB, mSUGRA and bRPV signal grids for the loose and tight signal regions. The expected exclusion is indicated by the contour where the modified Asimov significance with a background uncertainty of 25% is equal to 1.64 corresponding to a one-sided expected 95% CL upper limit.

Table 10.3: QCD Multijet control region selection.

Control region	Selection
QCD Multijet	$\Delta\Phi(\text{jet}, E_{\mathrm{T}}^{\mathrm{miss}}) < 0.4$ $E_{\mathrm{T}}^{\mathrm{miss}}/m_{\mathrm{eff}} < 0.4$

events satisfy the selections on the multijet rejecting variables $\Delta\Phi(\text{jet}, E_{\mathrm{T}}^{\mathrm{miss}})$ and $E_{\mathrm{T}}^{\mathrm{miss}}/m_{\mathrm{eff}}$ as shown in Table 10.3. This region is then further split by the τ content into sub-regions with no tau lepton, a reconstructed tau candidate, or a nominal τ passing medium identification criteria.

Four control regions are constructed for W+jets, Z+jets and top quarks backgrounds. W+jets and Z+jets processes are treated together in a common control region due to the similarities in both the physics process and the generator used to simulate it. The top control regions are designed in a similar fashion, with the two being distinguished by the requirement on a b-tagged jet in the event. In addition to the control regions being split by dominant processes, they are also separated into regions containing mostly a true or fake τ lepton to allow separate scaling factors to be determined for these two cases. This allows possible differences in the accuracy of the modelling of true relative to fake τ leptons in simulation to be corrected individually. The main selection to separate true from fake τ leptons is on m_{T} where there is a larger contribution from fake τ leptons at high m_{T}. To further enhance the separation into true and fake τ leptons, additional selections on the τ p_{T} and the azimuthal angle between the τ and the direction of $E_{\mathrm{T}}^{\mathrm{miss}}$ are applied. These additional requirements also increase the available statistics in the fake control regions, and to some extent compensate for the reduction in statistics with respect to the 7 TeV analysis experienced due to the raised trigger thresholds and the minimal τ transverse momentum required. The full selection defining the control regions for the electroweak backgrounds are shown in Table 10.4. All the electroweak control regions have multijet rejection selections applied to reduce the contribution from this process. As for the signal region $\Delta\Phi(\text{jet}, E_{\mathrm{T}}^{\mathrm{miss}}) > 0.4$ is required. Additionally, $\Delta\phi(\tau, p_{\mathrm{T}}^{\mathrm{miss}}) > 0.2$ was required for all control regions as this was found to remove multijet events, appearing at low m_{T}, whose shape was not accurately described by the statistics limited multijet Monte Carlo. Finally, $m_{\mathrm{T}} < 140$ GeV was required to keep the control regions orthogonal to the signal region selection.

All control regions are constructed such that the signal contamination from the considered signal grids are negligible. This allows Monte Carlo scaling factors to be derived using the control regions without taking into

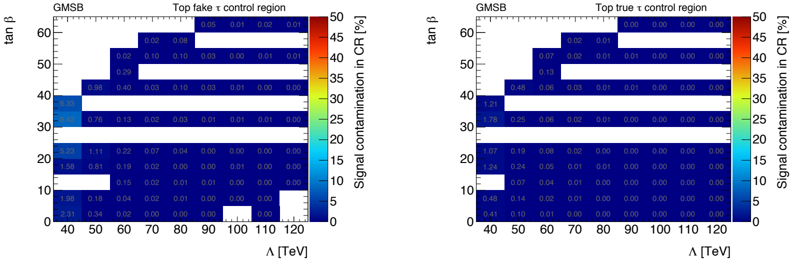

(a) Top fake CR (b) Top true CR

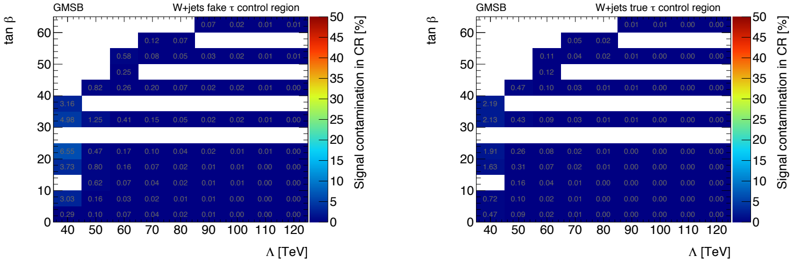

(c) W/Z fake CR (d) W/Z true CR

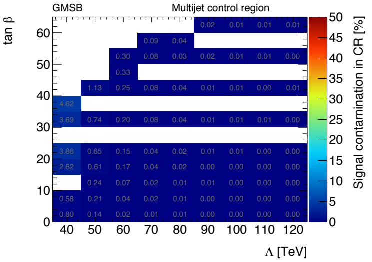

(e) QCD Multijet CR

Figure 10.10: Contamination in the Standard Model background control regions from the GMSB grid evaluated in the analysis.

Table 10.4: Overview of the control regions employed for the background estimation of W, Z and top quark backgrounds. Trigger requirements and selected objects are identical to the signal region requirements. A multijet rejection cut $\Delta\phi(\mathrm{jet}_{1,2}, p_{\mathrm{T}}^{\mathrm{miss}}) > 0.4$ is applied in all CRs.

	$N_{b\text{-jet}} = 0$	$N_{b\text{-jet}} > 0$
$m_{\mathrm{T}} < 90\,\mathrm{GeV}$ or $\Delta\phi(\tau, p_{\mathrm{T}}^{\mathrm{miss}}) < 1.0$ or $p_{\mathrm{T}}^{\tau} > 55\,\mathrm{GeV}$	CR W/Z true τ	CR Top true τ
$90\,\mathrm{GeV} < m_{\mathrm{T}} < 140\,\mathrm{GeV}$ and $\Delta\phi(\tau, p_{\mathrm{T}}^{\mathrm{miss}}) > 1.0$ and $p_{\mathrm{T}}^{\tau} < 55\,\mathrm{GeV}$	CR W/Z fake τ	CR Top fake τ

account possible contributions from signal models. Additionally, it allows the exclusion limits for the models to be calculated from the signal region only without simultaneous fits to the control regions when evaluating the hypothesis tests. Figure 10.10 (see Figures B.2 and B.1 for mSUGRA and bRPV) shows the contamination in all control regions across the GMSB signal grid. For the GMSB grid the contamination is typically well below a percent across the grid with the exception of the lowest Λ where it reaches a maximum of about 7%. These values have, however, already been excluded by previous searches. In the region of the expected exclusion the signal contamination ranges from 0.01-0.4%. The contamination from the bRPV grid is also typically below a percent except in the corner of low m_0 and $m_{1/2}$. Even in this region the level of contamination is within the tolerance of the analysis, except for the top fake control region where contaminations reach $\mathcal{O}(10)\%$. This region has, however, been excluded by other ATLAS searches and therefore no special treatment due to this contamination was considered. Something similar is observed for the contamination from mSUGRA where typical values are below 1%, while at the lowest $m_{1/2}$ it reaches 15-20% in the top fake control region. As the analysis presented here has highest sensitivity at low m_0 and moderate $m_{1/2}$, where the signal contamination is low, it does not contribute significantly to the region with problematic signal contamination, compared to other ATLAS searches. It is evident from the expected exclusion of the tight signal region, that goes into the final combination of results, that it does not have significant exclusion power in this region, and as such does not influence the final exclusion in the region of high signal contamination in this grid. For this reason no special treatment

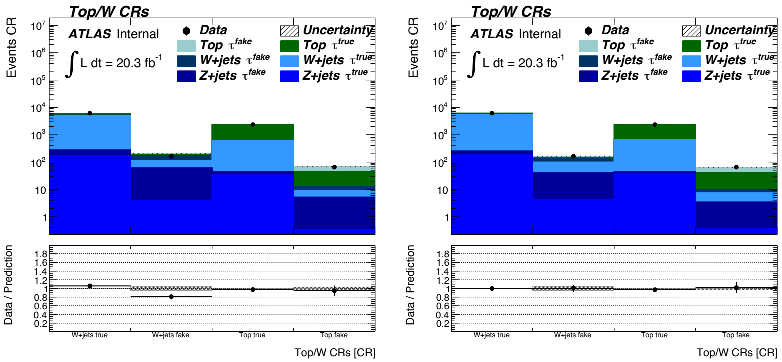

(a) Before scaling

(b) After scaling

Figure 10.11: W/Z+jets and top control region contributions before and after the derived scaling factors are applied to the individual processes split by true and fake τ content.

of the signal contamination in this region is considered in the interpretation of the obtained results.

10.3 Estimating Standard Model Backgrounds

The main methods for background estimates remain from the 7 TeV iteration of the analysis. Matrix inversion is used to determine scale factors for the electroweak backgrounds, while the QCD multijet contribution is determined by an ABCD method, with alternative methods as a cross-checks.

10.3.1 Electroweak Backgrounds

With the control regions defined in Table 10.4, the scale factors for top and W/Z+jets, split into components for true and fake τ leptons, were calculated. The validity of treating the W+jets and Z+jets with common scale factors was ensured by scale factor cross-checks with the 2τ analysis. Figure 10.12 shows the resulting scale factors that are obtained. The lower statistics in the fake τ regions is reflected in the wider distributions and increased uncertainties on the corresponding scale factors. Including the systematic uncertainties the electroweak scale factors are given by

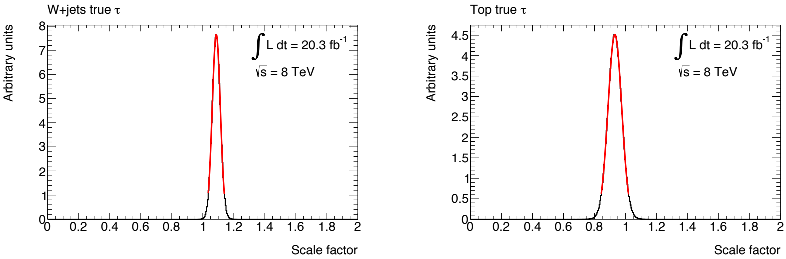

(a) W/Z+jets true scale factor (b) Top true scale factor

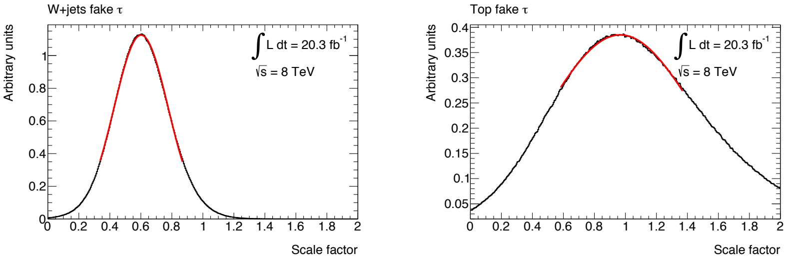

(c) W/Z+jets fake scale factor (d) Top fake scale factor

Figure 10.12: Electroweak scale factors for events with true and fake τ leptons obtained from the electroweak control regions.

$$\begin{bmatrix} \omega_W^{\mathrm{true}} \\ \omega_W^{\mathrm{fake}} \\ \omega_{\mathrm{top}}^{\mathrm{true}} \\ \omega_{\mathrm{top}}^{\mathrm{fake}} \end{bmatrix} = \begin{bmatrix} 1.09 \pm 0.03^{\mathrm{stat}} + 0.11^{\mathrm{syst}} \\ 0.60 \pm 0.18^{\mathrm{stat}} + 0.11^{\mathrm{syst}} \\ 0.93 \pm 0.05^{\mathrm{stat}} + 0.10^{\mathrm{syst}} \\ 0.98 \pm 0.52^{\mathrm{stat}} + 0.34^{\mathrm{syst}} \end{bmatrix} . \tag{10.1}$$

The stability of the scale factors in 10.1 with more stringent multijet rejecting selections applied to the CRs have been checked to ensure that the lack of a data driven multijet estimate in these regions does not affect the obtained scale factors. Applying a selection of $E_{\mathrm{T}}^{\mathrm{miss}}/m_{\mathrm{eff}} > 0.3$ resulted in changes that were all well within the statistical uncertainty of the estimates, indicating that there is negligible multijet contribution that is unaccounted for in these regions.

That there are no background processes unaccounted for in the control regions is further supported by the distributions of some important kinematic variables in these regions, shown in Figures 10.13-10.14. No significant shape differences between the simulations and the data are seen in the various distributions indicating that any remaining discrepancies can be attributed to simple normalisation offsets of the simulation as derived when solving the above matrix equation.

Figure 10.11 shows the Standard Model process contributing to the control regions before, and after the derived scaling factors are applied. The most significant deviation between the simulation and the observed data before scaling is seen in the W/Z+jets control regions, where the simulation overshoots the data in the fake τ region, and slightly underestimates the data in the true τ region.

In general, the simulation of events with a true τ accurately describes the observed data, resulting in scale factors close to unity. For events with a fake τ, on the other hand, the simulations tend to overestimate the τ fake rate relative what is seen in data, resulting in scale factors below one. This was also observed, and extensively studied, in previous iterations of the analysis, and is observed across the four analysis channels of the analysis.

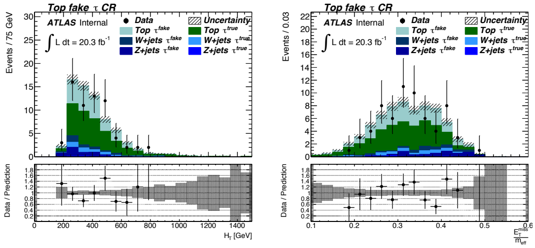

(a) Top fake - H_T (b) Top fake - $E_\mathrm{T}^\mathrm{miss}/m_\mathrm{eff}$ (c) Top fake - τ p_T

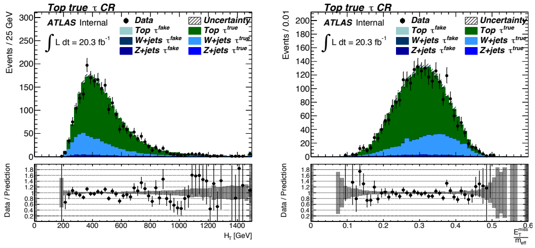

(d) Top true - H_T (e) Top true - $E_\mathrm{T}^\mathrm{miss}/m_\mathrm{eff}$ (f) Top true - τ p_T

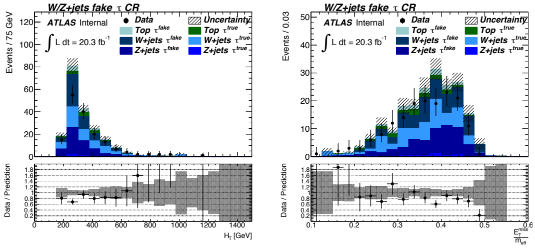

(g) W/Z fake - H_T (h) W/Z fake - $E_\mathrm{T}^\mathrm{miss}/m_\mathrm{eff}$ (i) W/Z fake - τ p_T

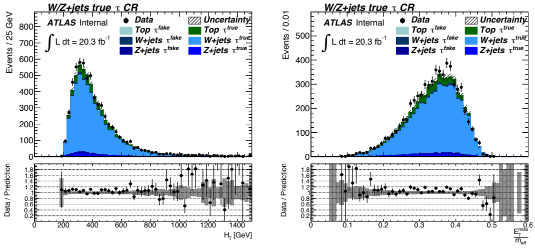

(j) W/Z true - H_T (k) W/Z true - $E_\mathrm{T}^\mathrm{miss}/m_\mathrm{eff}$ (l) W/Z true - τ p_T

Figure 10.13: Kinematic distributions in the W/Z+jets and top control regions after scaling factors are applied.

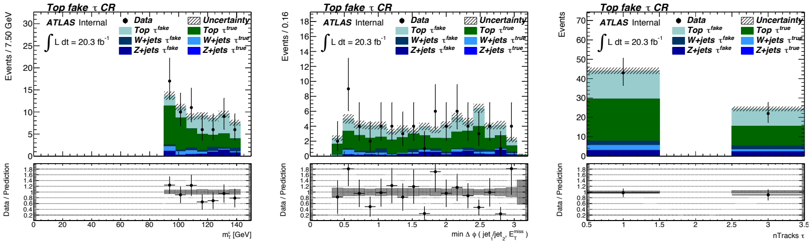

(a) Top fake - m_{T} (b) Top fake - $\Delta\Phi(\mathrm{jet}, E_{\mathrm{T}}^{\mathrm{miss}})$ (c) Top fake - # taus

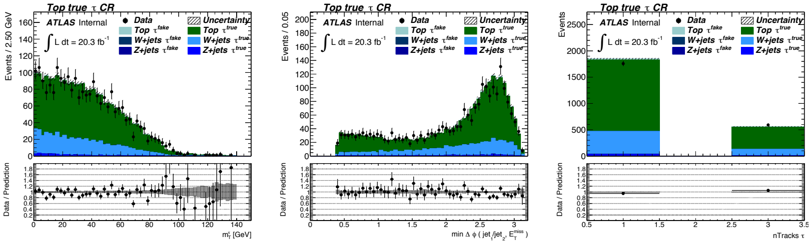

(d) Top true - m_{T} (e) Top true - $\Delta\Phi(\mathrm{jet}, E_{\mathrm{T}}^{\mathrm{miss}})$ (f) Top true - # taus

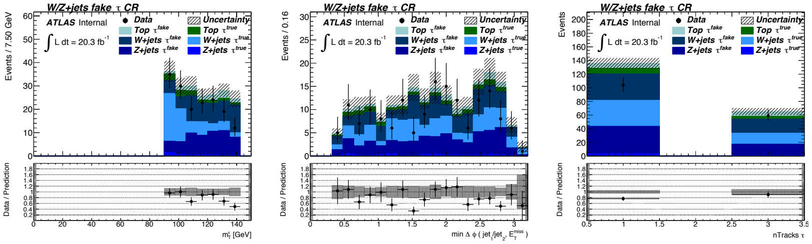

(g) W/Z fake - m_{T} (h) W/Z fake - $\Delta\Phi(\mathrm{jet}, E_{\mathrm{T}}^{\mathrm{miss}})$ (i) W/Z fake - # taus

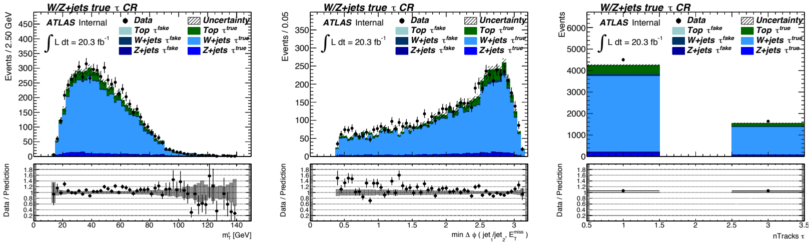

(j) W/Z true - m_{T} (k) W/Z true - $\Delta\Phi(\mathrm{jet}, E_{\mathrm{T}}^{\mathrm{miss}})$ (l) W/Z true - # taus

Figure 10.14: Kinematic distributions in the W/Z+jets and top control regions after scaling factors are applied, continued.

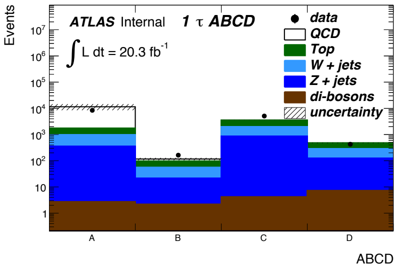

Figure 10.15: Standard Model background process contributing to the ABCD regions along with the observed data in the regions. A selection of $E_{\mathrm{T}}^{\mathrm{miss}} <$ 200 GeV is required in region C.

10.3.2 Multijets

The nominal estimate of contributions from QCD multijets in the signal region is from an ABCD method based on τ identification and $\Delta\Phi(\mathrm{jet}, E_{\mathrm{T}}^{\mathrm{miss}})$. For plotting, and as a cross-check to the nominal method, an estimate is also performed using τ candidates from simulations with weights for the τ fake rate determined from data applied. Finally, a commonly used technique called jet smearing was used as a further cross-check.

ABCD

The main method of multijet estimation, as for the 7 TeV analysis, is the ABCD method. The same variables are used to define the ABCD, the main difference being that the inversion of $E_{\mathrm{T}}^{\mathrm{miss}}/m_{\mathrm{eff}}$ in region C is replaced by inversion of $E_{\mathrm{T}}^{\mathrm{miss}}$ only. The definition of the ABCD regions is shown in Table

Table 10.5: Definitions of control region used when estimating the multijet background. General pre-selection, trigger plateau and m_{T} selections are applied for all regions.

	Very loose tau	Nominal tau
$\Delta\phi(\mathrm{jet}_{1,2}, p_{\mathrm{T}}^{\mathrm{miss}}) < 0.4$	Region A	Region B
$\Delta\phi(\mathrm{jet}_{1,2}, p_{\mathrm{T}}^{\mathrm{miss}}) > 0.4$ $E_{\mathrm{T}}^{\mathrm{miss}} < 200/300$ GeV	Region C	Region D

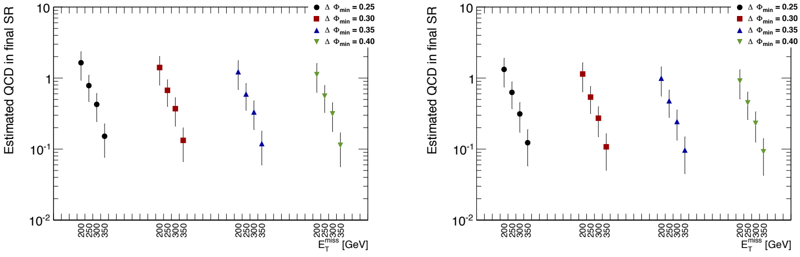

(a) Loose SR – $H_\mathrm{T} > 800$ GeV (b) Tight SR – $H_\mathrm{T} > 1$ GeV

Figure 10.16: ABCD method signal region estimates for combinations of $E_\mathrm{T}^\mathrm{miss}$ and $\Delta\Phi(\mathrm{jet}, E_\mathrm{T}^\mathrm{miss})$ selections for the two signal regions separated by the H_T selection imposed.

10.5. For all regions the analysis pre-selection, selections on $E_\mathrm{T}^\mathrm{miss}$ and jet p_T to ensure a fully efficient trigger and the m_T selection have been applied.

A very loose τ is required to have passed the same identification criteria as a nominal τ, except for the jet BDT criteria. It is additionally required not to overlap with any of the two leading jets in the event. The very loose τ is used just as a nominal τ to calculate other event variables depending on the τ content of the event. In region C the $E_\mathrm{T}^\mathrm{miss}$ selection defining the signal region is inverted to increase the relative fraction of multijets to electroweak processes in the region, thus removing some of the method's dependence on the scale factors derived for these.

Figure 10.15 shows the various background processes contributing to the ABCD regions. Apart from in region A a significant contamination from electroweak processes is seen in all regions. With respect to previous iterations of the analysis the contributions from QCD Multijets are reduced by the increased trigger thresholds, in particular for $E_\mathrm{T}^\mathrm{miss}$, the increased m_T selection and the reduced fake rate of the improved τ identification algorithm.

The estimate in region D is obtained by subtracting the electroweak contributions, with the appropriate scale factors applied, from the data in the regions and solving the ABCD equation. The estimate in region D is for all analysis cuts defining the signal region applied, except with the $E_\mathrm{T}^\mathrm{miss}$ selection inverted and without the final H_T selection. To obtain the signal region estimate the estimate in region D is multiplied by the ratio of multijet events, taken from simulation, in the signal region to those in region D. To reduce the statistical uncertainty of the estimate the ratio is taken from the multijet-rich region A, under the assumption that it is independent

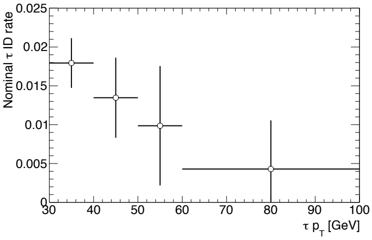

Figure 10.17: p_{T} dependent τ identification fake rate of very loose τ candidates.

of the azimuthal angle between the two leading jets and $E_{\mathrm{T}}^{\mathrm{miss}}$ in the event. As a cross-check of the method the ratio was also calculated from region C and from data in region A. The results were found to be consistent with the nominal values in both cases. Figure 10.16 shows the obtained signal region estimates for different values of the final $E_{\mathrm{T}}^{\mathrm{miss}}$ and $\Delta\Phi(\mathrm{jet}, E_{\mathrm{T}}^{\mathrm{miss}})$ selections defining the signal regions.

Due to significant non-mulitjet contamination in region C, the ABCD estimates will depend on the W/Z+jets and top scale factors. The scale factor dependence on the τ identification could also influence the method. To account for this dependence, estimates were derived without scale factors applied, and with them applied only to the regions with nominal τ leptons. The conservative estimate where scale factors were applied to all ABCD regions was taken as the nominal estimate. A 100% method uncertainty was assigned to this estimate to account for the observed differences in the choices of calculation of the ratio, treatment of electroweak scale factors, and differences with respect to the methods described in the following sections. The resulting multijet background estimates are $0.23 \pm 0.10^{\mathrm{stat}}$ and $1.12 \pm 0.49^{\mathrm{stat}}$ in the tight and loose signal regions respectively.

Weighted τ Candidates

For use in plotting distributions and as a cross-check of the ABCD method weighting of τ candidates was also performed. The probability, as a function of p_{T}, for a very loose τ candidate, as used in the ABCD method, to be identified as a nominal τ was calculated in the QCD control region. To determine if a τ candidate was also identified as a nominal τ the two particles were ΔR-matched. If a nominal τ was found to lie within a cone of $\Delta R < 0.1$ of the τ candidate the two particles were assumed to be the same. Subtracting

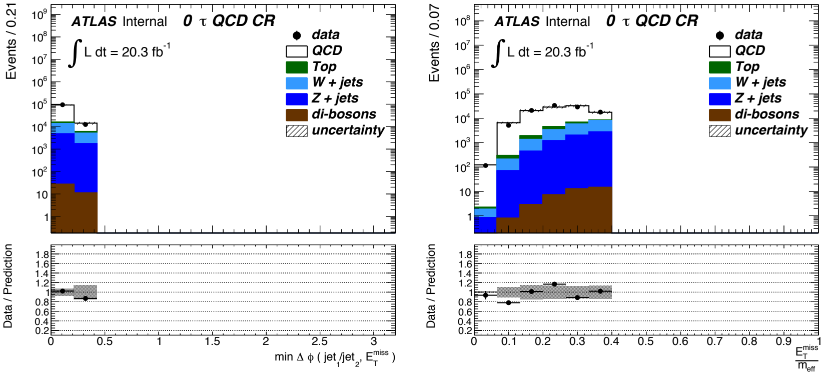

(a) $\Delta\Phi(\text{jet}, E_{\mathrm{T}}^{\mathrm{miss}})$ (b) $E_{\mathrm{T}}^{\mathrm{miss}}/m_{\mathrm{eff}}$

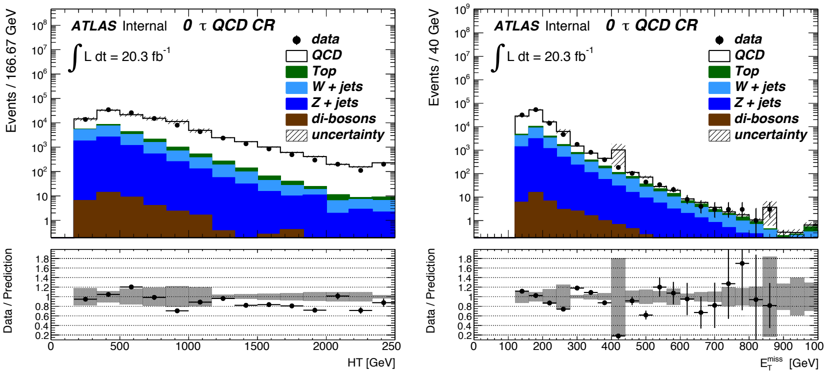

(c) H_{T} (d) $E_{\mathrm{T}}^{\mathrm{miss}}$

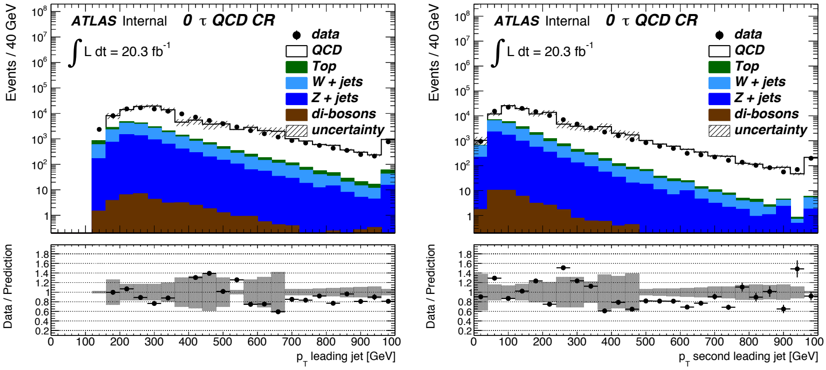

(e) leading jet p_{T} (f) sub-leading jet p_{T}

Figure 10.18: Main kinematic distributions of the multijet control region without any requirements on the number of τ leptons in the event imposed. Statistical uncertainties only.

W/Z+jets and top background processes, with scale factors applied, from the data the probability of a τ candidate to pass nominal τ selection, seen in Figure 10.17, was calculated.

The overall normalisation of the QCD multijet Monte Carlo was determined in the multijet control region without any τ requirement imposed. Figure 10.18 shows the main kinematic distributions after electroweak scaling factors, and the multijet Monte Carlo normalisation factor have been applied. Good agreement, within the statistical uncertainties, between simulations and data are observed. The relatively large statistical uncertainty, and resulting uneven distributions, at low jet p_{T} and H_{T} is due to the lower p_{T} slices of the multijet Monte Carlo samples dominating this part of the distributions. These samples have relatively large event weights, e.g. low statistics, compared to the observed event counts making parts of the distributions sparsely populated. This effect is also enhanced partly due to the high $E_{\mathrm{T}}^{\mathrm{miss}}$ selection required to satisfy the trigger plateau requirement. The same effect is also seen with single high weight events from the lower p_{T} samples being prominent in for example the $E_{\mathrm{T}}^{\mathrm{miss}}$ distribution.

Figure 10.19 shows the main kinematic distributions of the same multijet control region containing a nominal τ. The indicated multijet contribution is obtained by applying the above τ fake rate factors to events containing a very loose τ candidate. In general, the agreement between simulations and data is found to be good. For both the τ p_{T} and the $E_{\mathrm{T}}^{\mathrm{miss}}$ distributions the multijet estimates are seen to nicely cover the remaining discrepancies between the electroweak processes and the data at low τ p_{T} and $E_{\mathrm{T}}^{\mathrm{miss}}$. It is, however, clear that the limited multijet Monte Carlo statistics lead to sparsely populated distribution tails.

A comparison of the signal region estimates obtained from the ABCD method and using weighted τ candidates can be seen in Table 10.6. The quoted uncertainties are statistical only. In general, the estimate from weighted τ candidates is seen to be lower than the estimates from the ABCD method although they are consistent within errors. The relative uncertainties on the estimates are also of the same magnitude.

Method	ABCD w/MC ratio	ABCD w/data ratio	Very Loose Tau
Loose SR	1.12 ± 0.49	1.99 ± 0.28	0.61 ± 0.20
Tight SR	0.23 ± 0.10	0.34 ± 0.08	0.09 ± 0.06

Table 10.6: Comparison between multijet estimates using scaled extra loose taus and the ABCD method. Uncertainties on the estimates are statistical only.

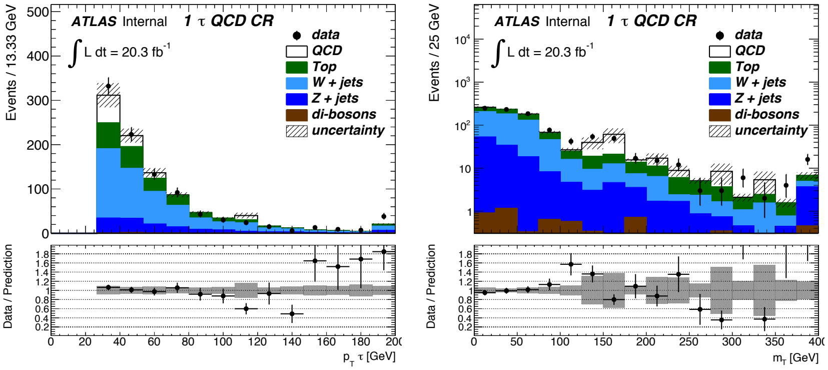

(a) τ p_{T} (b) m_{T}

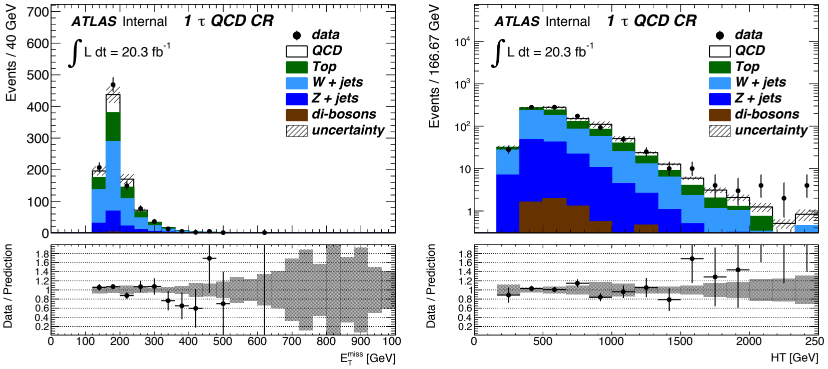

(c) $E_{\mathrm{T}}^{\mathrm{miss}}$ (d) H_{T}

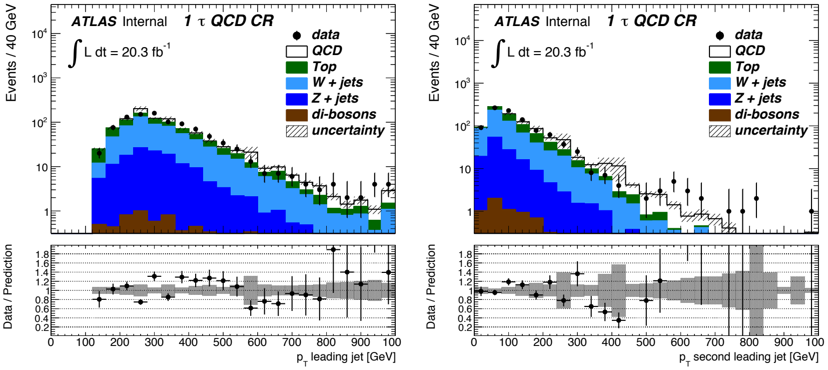

(e) leading jet p_{T} (f) sub-leading jet p_{T}

Figure 10.19: Main kinematic distributions of the 1 τ multijet control region. Contributions from multijet processes are from weighted very loose τ candidates in QCD Monte Carlo. Statistical uncertainties only.

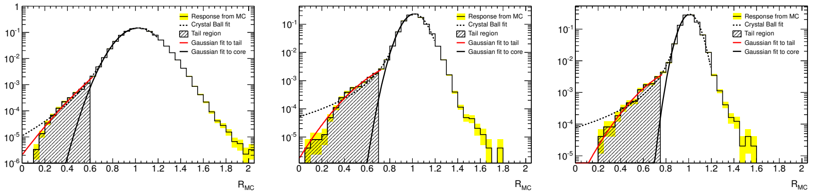

(a) 40 GeV $< p_T^{\text{true}} <$ 60 GeV (b) 140 GeV $< p_T^{\text{true}} <$ 160 GeV (c) 540 GeV $< p_T^{\text{true}} <$ 560 GeV

Figure 10.20: Example jet p_{T} response functions derived from QCD Monte Carlo with separate Gaussian fits to the the core and tail regions of the distribution [179].

Jet Smearing

A commonly used method within the ATLAS collaboration is the so-called jet smearing method [179] that was first applied in [180]. The method is based on the assumption that the QCD multijet contributions in the kinematic phase space relevant to SUSY searches, e.g. high $E_{\mathrm{T}}^{\mathrm{miss}}$, are due to jet mis-measurements. Under this assumption pseudo-data with high $E_{\mathrm{T}}^{\mathrm{miss}}$ may be constructed from well measured multijet events by smearing the jets according to their measurement uncertainty. The jet energy measurement uncertainty is quantified by the response function of the jet energy measurement and is measured in Monte Carlo and validated and modified by observations in data. The jet response function, R, giving the fluctuation in measured jet p_{T} is given by

$$R = \frac{p_T^{\text{reco}}}{p_T^{\text{true}}}. \tag{10.2}$$

Figure 10.20 shows example jet energy response functions derived from simulations. The jets in the events are then smeared with the appropriate response function and the missing transverse energy recalculated as

$$\not{E}_T' = \not{E}_T + \sum_{\text{jets}} (p_T' - p_T), \tag{10.3}$$

where primed variables indicate smeared quantities.

The selection of seed events is based on data events passing single jet triggers in the `JetTauEtmiss` stream. Events passing one of the triggers `EF_-j55/j80/j110/j180/j220/j280/j360/j460_a4tchad`, not containing light leptons, passing nominal event cleaning are used as a starting point for the method. All but the two highest threshold single jet triggers have been pre-scaled during the entire 2012 data taking period. Figure 10.21 shows

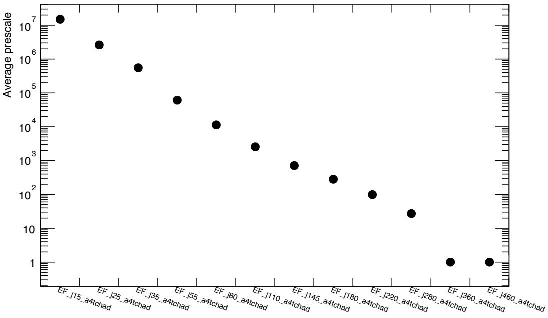

Figure 10.21: Average pre-scales of the single jet triggers used for seed selection in the jet smearing method.

the average pre-scales, obtained from per event pre-scales information from the `TriggerDecisionTool`, for the triggers. Event weights are assigned to the events according to the pre-scale of the highest threshold, fully efficient trigger that fired in the event. Seed events, i.e. well measured events in data in a region dominated by QCD multijet events, are chosen by a selection on the $E_{\mathrm{T}}^{\mathrm{miss}}$ significance

$$S = \frac{E_{\mathrm{T}}^{\mathrm{miss}}}{\sqrt{\sum E_T}} < 0.6\ \mathrm{GeV}^{\frac{1}{2}}. \tag{10.4}$$

Each seed event is smeared a thousand times. The fraction of the total number of smears that result in the nominal trigger requirements being satisfied, is applied as an additional event weight. The smeared event content is taken from the first smear iteration passing trigger requirements, in order to avoid duplication of the τ content in the event.

One of the main appeals of the jet smearing methods is that the τ content is taken directly from the data, avoiding possible bias from τ mismodelling in simulations. To regain correct normalisation after the smearing iterations, the pseudo-data is normalised in the QCD multijet control region without any τ requirement.

Figure 10.22 shows the obtained kinematic distributions in the 0 τ control region after normalisation of the pseudo-data. The main multijet rejecting variables, $\Delta\Phi(\mathrm{jet}, E_{\mathrm{T}}^{\mathrm{miss}})$ and $E_{\mathrm{T}}^{\mathrm{miss}}/m_{\mathrm{eff}}$, are seen to be well modelled and the higher statistics in the pseudo-data sample compared to the multijet simulations is evident. The distributions of data for H_{T} and jet p_{T} is, however, seen to be harder than what is obtained in the pseudo-data from jet smearing.

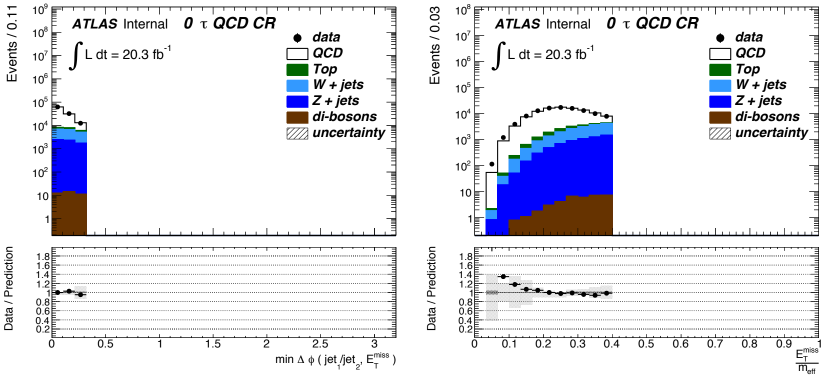

(a) $\Delta\Phi(\text{jet}, E_{\mathrm{T}}^{\mathrm{miss}})$ (b) $E_{\mathrm{T}}^{\mathrm{miss}}/m_{\mathrm{eff}}$

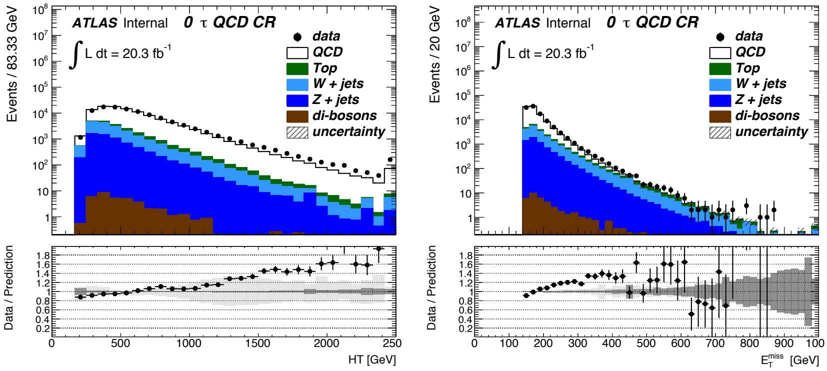

(c) H_{T} (d) $E_{\mathrm{T}}^{\mathrm{miss}}$

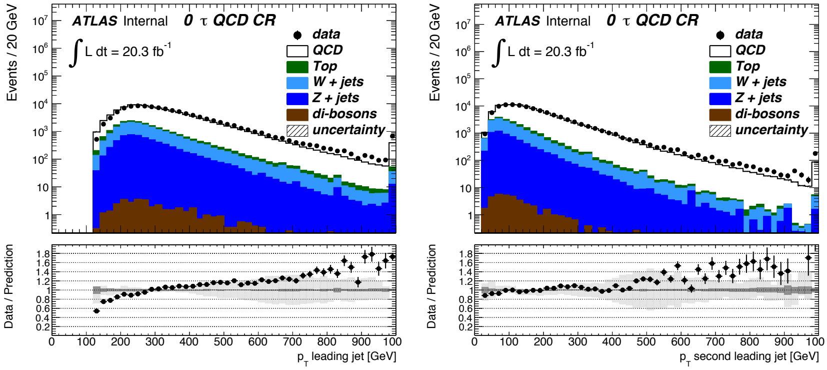

(e) leading jet p_{T} (f) sub-leading jet p_{T}

Figure 10.22: Distributions obtained by jet smearing in the QCD control region without any requirement on the τ. The pseudo-data is normalised to the observed data in the region. The dark shaded areas indicate the statistical uncertainty, while the light grey area indicate systematic uncertainties.

These differences in shape are slightly larger than the estimated systematic uncertainty of the method indicated by the light grey shaded area.

Figure 10.23 shows the QCD multijet control region containing a τ lepton, where the multijet distribution is obtained by the jet smearing method. Despite the shape differences in the 0 τ QCD multijet control region, the distributions in data are here are seen to be mostly well described by the estimated backgrounds, while there are some discrepancies in the very tails of the H_T distribution. Again, the improved statistics with respect to multijet Monte Carlo is seen in for example the QCD multijet dominated peak of the m_T distribution, at around 150 GeV, that arise due to selections on the variables used to calculate m_T.

Due to the discrepancies seen in the multijet control region without a τ requirement, the method is used only as a cross-check to the nominal method. As such, it lends credence to the other two approaches in underpinning the behaviour, and low levels of multijet contributions to the portions of phase space defined by the signal region selection. The application of the method also serves as a proof of principle, and as a starting point for future iterations of the analysis. The inherent potential of the method is clear with a significant increase in statistics and the mismodelling of jets as τ leptons taken directly from data. There are several potential factors that could contribute to the observed level of shape mismodelling, and that could be resolved by further studies. This includes biases introduced by the seed selection and the chosen smearing parameters (light/heavy quark content, criteria of jets to be smeared, $E_\mathrm{T}^\mathrm{miss}$ soft term smearing, angular smearing, etc.). Additionally, the jet response functions have been derived in the context of the zero lepton SUSY search. As the event cleaning criteria between the two analyses are not identical, there could be differing sources of fake $E_\mathrm{T}^\mathrm{miss}$ resulting in slightly different jet response functions between the analyses. Also, a dedicated τ smearing, using a response function specific to τ leptons, could potentially improve the description of fake $E_\mathrm{T}^\mathrm{miss}$ from mismeasurements of the τ leptons.

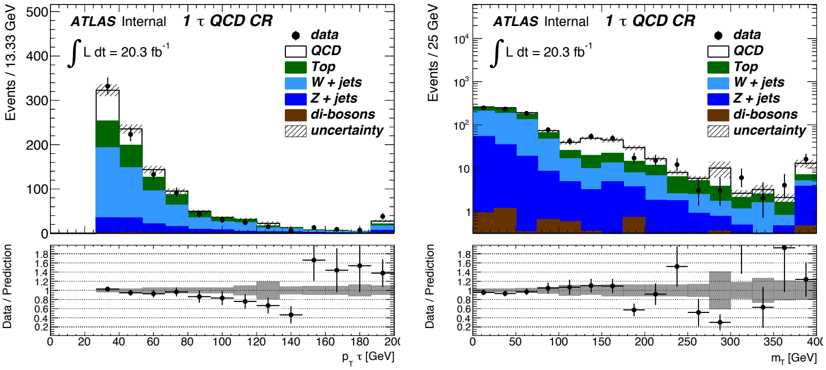

(a) $\tau\ p_{\mathrm{T}}$ (b) m_{T}

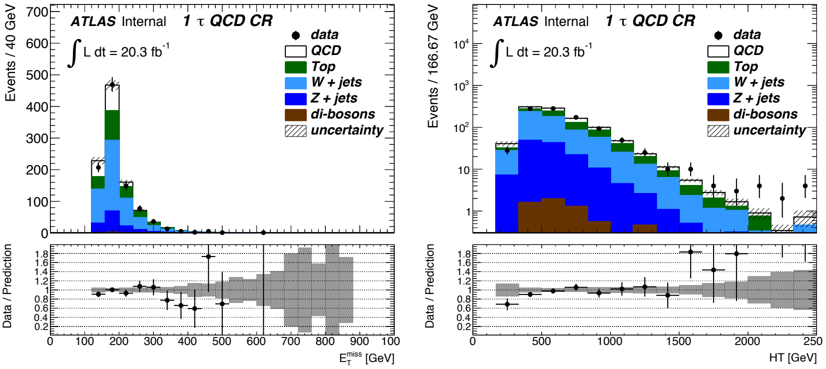

(c) $E_{\mathrm{T}}^{\mathrm{miss}}$ (d) H_{T}

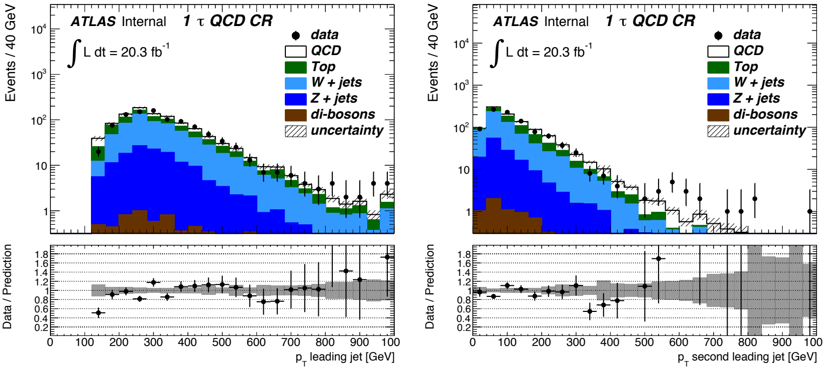

(e) leading jet p_{T} (f) sub-leading jet p_{T}

Figure 10.23: Distributions obtained by jet smearing in the multijet control region with a τ. The dark shaded areas indicate the statistical uncertainty, while the light grey areas indicate systematic uncertainties.

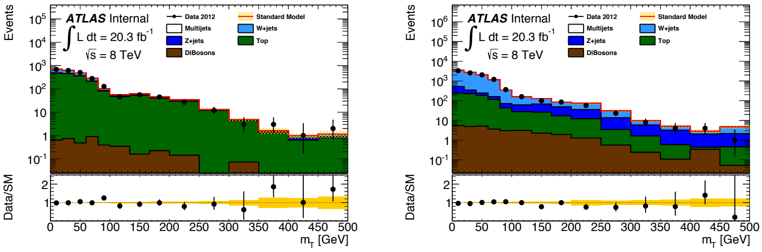

(a) Top background validation (b) W/Z+jets background validation

Figure 10.24: Validation of Top and W/Z+jets modelling after scaling factors are applied. The uncertainties are statistical only.

10.4 Validating the Background Estimates

The modelling of the electroweak backgrounds and the derived scaling factors are validated by splitting events after the trigger plateau selection, one τ requirement and QCD multijet rejection into regions dominated by top and W/Z+jets respectively by requiring, or vetoing, b-tagged jets in the event. The m_{T} distributions in these regions are shown in Figure 10.24. In addition to being one of the main, and final, selection variables, m_{T} is a complex, composite variable that includes both information on the τ, $E_{\mathrm{T}}^{\mathrm{miss}}$ and their angular separation. Therefore, it would be sensitive to mismodelling of any of these quantities. The simulated distributions are seen to accurately describe the data across the full range of the distribution. This includes the regions that were not used to define the control regions and, importantly, the part of the distribution that goes into the signal region definition. The distributions are also well modelled in both regions dominated by true τ leptons, low m_{T}, and fake τ leptons at moderate to high m_{T}. For the W/Z+jets control region the relative contribution of Z+jets to W+jets events vary across the variable range. The accurate description of the data for differing relative contributions vindicates the use of a common scale factor for the individual W+jets and Z+jets contributions.

Further kinematic distributions validating the Standard Model background modelling are shown in Figure 10.25. For all distributions apart from $\Delta\Phi(\mathrm{jet}, E_{\mathrm{T}}^{\mathrm{miss}})$ all selections apart from the two final selections on m_{T} and H_{T} have been applied. In the case of $\Delta\Phi(\mathrm{jet}, E_{\mathrm{T}}^{\mathrm{miss}})$ (Figure e) the selection on $\Delta\Phi(\mathrm{jet}, E_{\mathrm{T}}^{\mathrm{miss}})$ is also removed. In all figures electroweak backgrounds have the appropriate scale factors applied, while the multijet contribution is obtained from scaling of τ candidates. The background estimates are seen to

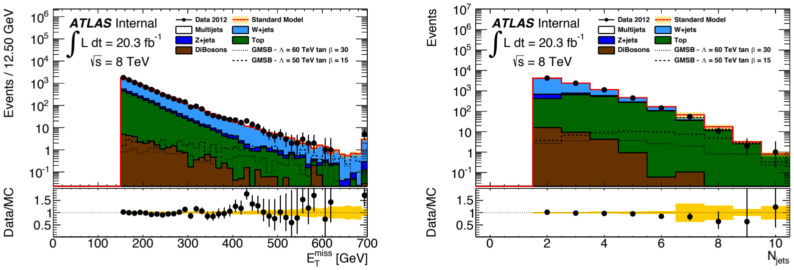

(a) $E_{\mathrm{T}}^{\mathrm{miss}}$ (b) number of jets

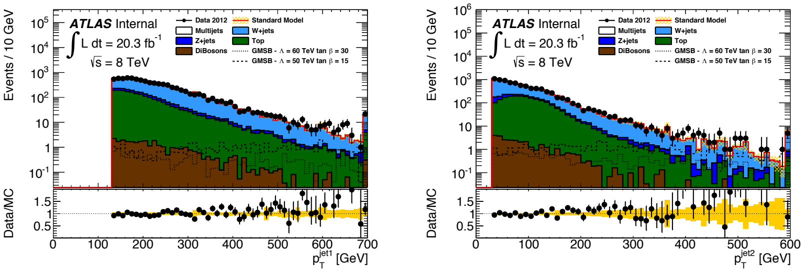

(c) leading jet p_{T} (d) sub-leading jet p_{T}

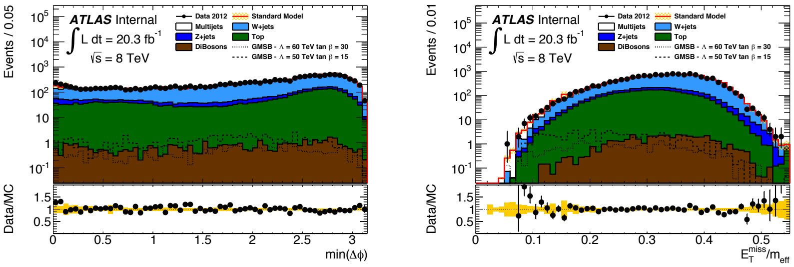

(e) $\Delta\Phi(\mathrm{jet}, E_{\mathrm{T}}^{\mathrm{miss}})$ (f) $E_{\mathrm{T}}^{\mathrm{miss}}/m_{\mathrm{eff}}$

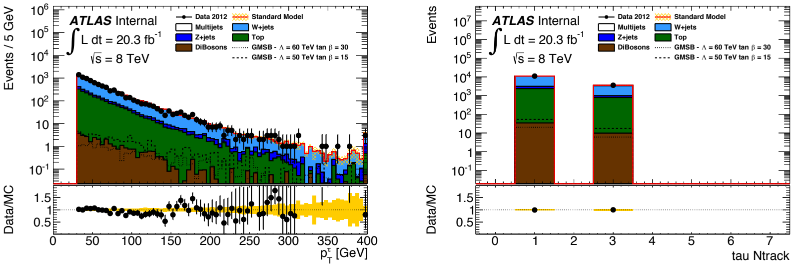

(g) τ p_{T} (h) τ tracks

Figure 10.25: Distributions of the main kinematic variables of the analysis after pre-selection, trigger plateau requirements, the multijet rejecting selection (except in Figure *e*)) and the τ requirement. W/Z+jets and top backgrounds are scaled by the appropriate scale factors, and multijets events are obtained from weighted τ candidates. Uncertainties are statistical only.

accurately model the observed data for all the kinematic distributions investigated within the statistical uncertainties indicated in the figures. Additional uncertainties from theory, the methods applied and experimental uncertainties are not shown in the figure, but are considered in the final interpretation of the results.

10.5 Systematic Uncertainties

The influence of the systematic uncertainties described in Section 8.9 are considered for all backgrounds relevant to the signal region. The size of experimental uncertainties such as uncertainties related to measurement, reconstruction and identification efficiencies and other detector-related effects are evaluated by dedicated performance groups in ATLAS. The recommendations provided by the performance groups are implemented in the analysis by varying the response of the uncertainties by their $\pm 1\sigma$ values and repeating the whole analysis, including the full background estimates, for each systematic variation considered. For example, the scale of the jet energy measurements is shifted up and down according to their uncertainty, and every jet in the event has their energy modified according to this shift. Every jet-dependent quantity in the event is also recalculated, and the full analysis is re-done with the energy shifted jets. The same procedure is applied to all the experimental systematic uncertainties. Additional systematics on methods and from the choice of generators are treated individually in each analysis channel.

Background Uncertainties

When the systematic variations are considered the uncertainty associated with a given background, is the deviation between the nominal signal region estimate and the systematically varied estimate. Since the Monte Carlo statistics remaining in the signal regions are limited for many of the backgrounds, the estimate of the systematic uncertainty will be artificially enlarged by the statistical uncertainty in the region. As a measure to counteract this effect, relative systematic uncertainties are derived in a region with smaller statistical uncertainties by relaxing the final selection on H_{T}. This method is applied to all backgrounds based on Monte Carlo simulations.

Uncertainty introduced through the choice of generator used to model the physics processes are accounted for by performing the analysis with an alternative generator and comparing the results to the nominal signal region estimates. As the normalisation of the electroweak Monte Carlo is corrected

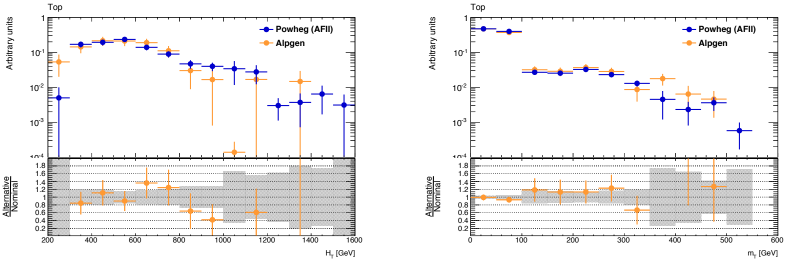

(a) H_{T}– $t\bar{t}$ (b) m_{T}– $t\bar{t}$

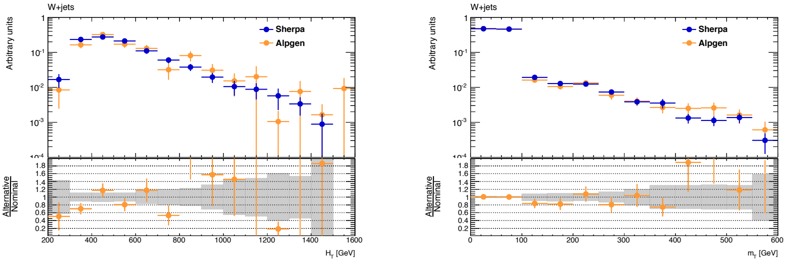

(c) H_{T}– W+jets (d) m_{T}– W+jets

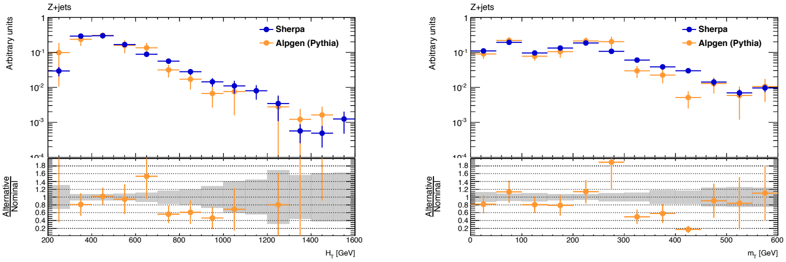

(e) H_{T}– Z+jets (f) m_{T}– Z+jets

Figure 10.26: Comparison of the nominal and alternative $t\bar{t}$, W+jets and Z+jets generators for the two final variables defining the analysis signal region. The distributions are normalised to unity.

to describe data, any offsets in normalisation between generators would be corrected for by the background estimation techniques and as such should not introduce a systematic uncertainty. Differences in the modelled shapes of variables extrapolated over going from the control regions, where the simulations are adjusted to describe data, to the signal regions would, however, lead to systematic uncertainties from the generator choice. Figures 10.26 and B.3 – B.5 compare the shapes of the nominal (blue) and alternative (orange) generators for the main variables and backgrounds of the analysis. The distributions are obtained after all selections, apart from on m_{T} and H_{T}, are implemented. For all background processes and variables, the differences between the generators are, as expected, seen to be small. In particular, the distributions that are extrapolated over, m_{T} and H_{T}, going from the control to the signal region are seen to agree within the statistical uncertainties. From the distributions the statistical uncertainties of the generated samples are also visible, where the sample with the largest available statistics in each case was taken to be the nominal one resulting in a significantly improved description of the distribution tails and accompanying reduction of the statistical uncertainty.

Tables 10.7 and 10.8 show a breakdown of the relative systematic and statistical uncertainties of the loose and tight signal regions respectively. Correlations among the different background contributions under a systematic variation are taken into account when considering the total estimated background in a signal region. A common nuisance parameter per systematic variations is introduced for all background processes, except for the generator statistical uncertainty, which is treated as uncorrelated across the backgrounds. Naturally, any background specific systematic uncertainties introduce nuisance parameters only on the background in question.

From Tables 10.7 and 10.8 the dominant systematic uncertainties are seen to arise from the choice of Monte Carlo generators, jet and τ measurement and the multijet estimates. The combined Monte Carlo generator related uncertainty in the loose and tight signal regions are respectively 19% and 30% and is the dominant source of uncertainty in both signal regions. In both regions the uncertainty of the multijet estimate is close to 10%. The jet and τ energy scale uncertainties are of a similar magnitude, and in the loose signal region they are both 3.6%, while in the tight signal region they are 4.0% and 1.3% respectively. The jet energy resolution uncertainty is also of a similar magnitude at 2.8% and 9.7% in the loose and tight signal regions. Finally, the uncertainty related to pile-up is comparatively small at 1% in both regions.

Systematic	Total	QCD	W+jets (true)	W+jets (fake)	Top (true)	Top (fake)	Z+jets (true)	Z+jets (fake)	di-boson
JES up	-0.017	-0.346	0.006	-0.032	0.086	-0.053	0.110	0.069	0.030
JES down	0.056	0.390	-0.055	0.078	-0.066	0.139	0.164	0.035	-0.132
JER	-0.029	-0.278	0.021	-0.065	0.035	-0.023	0.146	-0.051	0.211
TES up	-0.045	-0.140	-0.011	-0.055	0.014	-0.111	-0.028	-0.041	0.063
TES down	0.029	0.283	-0.035	-0.006	-0.004	0.077	0.029	-0.012	-0.132
TauId up	0.004	0.022	0.004	-0.002	0.004	-0.004	0.013	-0.002	0.036
TauId down	-0.004	-0.022	-0.004	0.002	-0.004	0.005	-0.014	0.002	-0.036
TauElV up	-0.004	-0.007	-0.002	0.007	-0.002	-0.014	-0.002	-0.005	0.002
TauElV down	0.004	0.007	0.002	-0.007	0.002	0.014	0.002	0.005	-0.002
ST up	-0.004	-0.009	-0.018	0.019	-0.005	0.006	0.169	-0.026	-0.006
ST down	0.019	0.007	0.021	0.008	0.025	0.028	0.013	0.025	0
ST res	-0.027	-0.146	-0.003	-0.019	-0.021	0.023	0.185	-0.065	0
JVF up	0.001	0.002	-0.002	0.003	0.001	0.002	0.003	0.003	0
JVF down	<0.001	<0.001	-0.004	0.001	0.001	-0.004	-0.004	0.001	0
Pileup up	0.010	0.050	-0.005	0.023	0.004	-0.003	0.019	0.025	-0.047
Pileup down	-0.009	-0.051	-0.009	-0.004	0.006	-0.008	-0.039	-0.016	0.030
BJet up	<0.001	0	-0.009	-0.007	0.032	-0.014	-0.009	-0.007	0
BJet down	0.002	0	-0.014	-0.037	0.041	0.042	-0.014	-0.037	0
CJet up	-0.002	0	0.013	0.034	-0.038	-0.037	0.013	0.034	0
CJet down	-0.002	0	-0.005	-0.004	0.010	-0.014	-0.005	-0.004	0
B Mistag up	0.002	0	0.005	0.004	-0.010	0.014	0.005	0.004	0
B Mistag down	<0.001	0	0.009	0.006	-0.032	0.016	0.009	0.006	0
Method QCD	0.104	1	0	0	0	0	0	0	0
Top generator	0.142	-0.089	0.001	0.053	0.143	0.600	0.001	0.053	0
Top gen MC stat	0.054	0	0	0	0.189	0.216	0	0	0
W,Z generator	0.125	0.031	0.212	0.494	0.177	-0.137	0	0.054	0
W,Z gen MC stat	0.065	0	0.194	0.246	0	0	1	0.269	0
Diboson gener.	-0.004	0	-0.001	-0.009	0.001	0.008	-0.001	-0.009	-0.054
Db gen MC stat	0.009	0	0	0	0	0	0	0	0.202
Total syst.	0.241	1.136	0.292	0.563	0.312	0.668	1.041	0.300	0.327
Stat. uncertainty	0.13	0.44	0.17	0.33	0.16	0.55	0.57	0.31	0.38
Total uncertainty	0.27	1.22	0.34	0.65	0.35	0.87	1.19	0.43	0.50

Table 10.7: Systematic and statistical uncertainties for the loose signal region. The uncertainties are relative variations of the predicted number of background events. The grouping of several background types in one row for the “gen MC stat” sources is only for display purposes, in the analysis they have been treated as uncorrelated sources.

Systematic	Total	QCD	W+jets (true)	W+jets (fake)	Top (true)	Top (fake)	Z+jets (true)	Z+jets (fake)	di-boson
JES up	-0.043	-0.290	-0.047	0.050	0.013	-0.068	0.051	-0.020	0.013
JES down	-0.042	-0.140	-0.118	0.069	-0.015	0.035	0.154	0.013	-0.296
JER	-0.098	0.019	-0.164	-0.011	-0.158	-0.247	-0.064	-0.058	0.275
TES up	-0.012	-0.039	0.008	-0.027	0.013	-0.007	-0.028	-0.051	0
TES down	-0.005	0.245	-0.102	-0.010	-0.022	0.076	0.028	0.024	-0.296
TauId up	0.007	0.022	0.011	-0.002	0.006	-0.004	0.012	-0.002	0.038
TauId down	-0.007	-0.022	-0.012	0.002	-0.007	0.005	-0.013	0.002	-0.038
TauElV up	-0.007	-0.007	-0.002	-0.006	-0.002	-0.029	-0.002	-0.005	0.005
TauElV down	0.007	0.007	0.002	0.005	0.002	0.029	0.002	0.005	-0.005
ST up	-0.025	0.010	-0.017	0.012	-0.006	-0.011	-0.014	-0.005	-0.296
ST down	0.021	0.002	-0.010	0.021	0.007	0.072	0.013	0.047	0
ST res	-0.016	0.006	-0.003	-0.001	-0.004	-0.063	-0.001	-0.027	0
JVF up	<0.001	0.002	0.003	0.003	0.001	0.002	0.003	-0.012	0
JVF down	-0.001	-0.002	-0.004	0.001	0.001	-0.004	-0.004	0.001	0
Pileup up	0.019	0.026	0.064	0.005	0.032	-0.033	-0.001	0.039	-0.067
Pileup down	-0.013	-0.013	-0.059	0.030	-0.014	0.004	-0.005	-0.024	0.045
BJet up	<0.001	0	-0.009	-0.007	0.032	-0.014	-0.009	-0.007	0
BJet down	0.002	0	-0.014	-0.037	0.041	0.042	-0.014	-0.037	0
CJet up	-0.002	0	0.013	0.034	-0.038	-0.037	0.013	0.034	0
CJet down	-0.003	0	-0.005	-0.004	0.010	-0.014	-0.005	-0.004	0
B Mistag up	0.003	0	0.005	0.004	-0.010	0.014	0.005	0.004	0
B Mistag down	<0.001	0	0.009	0.006	-0.032	0.016	0.009	0.006	0
Method QCD	0.096	1	0	0	0	0	0	0	0
Top generator	-0.147	-0.130	0.001	0.053	-0.986	0.233	0.001	0.053	0
Top gen MC stat	0.095	0	0	0	0.013	0.557	0	0	0
W,Z generator	0.226	-0.135	0.565	1.252	0.177	-0.137	0	-0.065	0
W,Z gen MC stat	0.135	0	0.464	0.820	0	0	1	0.304	0
Diboson gener.	-0.008	0	-0.001	-0.009	0.001	0.008	-0.001	-0.009	-0.104
Db gen MC stat	0.022	0	0	0	0	0	0	0	0.334
Total syst.	0.349	1.050	0.759	1.500	1.016	0.676	1.008	0.329	0.520
Stat. uncertainty	0.19	0.43	0.34	0.43	0.50	0.69	0.42	0.40	0.63
Total uncertainty	0.40	1.13	0.83	1.56	1.13	0.97	1.09	0.52	0.82

Table 10.8: Systematic and statistical uncertainties for the tight signal region. The uncertainties are relative variations of the predicted number of background events. The grouping of several background types in one row for the “gen MC stat” sources is only for display purposes, in the analysis they have been treated as uncorrelated sources.

Signal Uncertainties

In addition to the uncertainties on the background estimates, discussed in the previous section, the signal uncertainties also need to be taken into account when interpreting results and setting limits in the context of the considered signal models. Figure 10.27 (Figues B.9 and B.8 for mSUGRA and bRPV) summarises the relative uncertainties on the signal region signal contributions for the GMSB model. The systematic uncertainty shown is the combined uncertainty from the detector related uncertainties considered in the previous section. In addition to the statistical uncertainty on the signal region estimate, the theoretical uncertainty on the production cross-section of the supersymmetric signal is also shown. The latter is obtained by varying the NLLO signal cross-sections per SUSY production process within their uncertainty.

Applying more stringent selections to define a signal region naturally increases the statistical uncertainty on the signal region estimates, as seen when going from the loose to the tight signal region in Figures 10.27, B.8 and B.9. For the GMSB grid the statistical uncertainties vary from 6-27% in the loose signal region, while the corresponding numbers for the tight signal region are 8-43%. In the region around the 95% CL expected exclusion limit, however, the statistical uncertainty is typically between 10% and 15%. The bRPV model grid considered suffers from a lack of statistics in regions of low acceptance, typically at low $m_{1/2}$ and/or high m_0, resulting in large statistical uncertainties in these regions. However, the low statistics region coincides with the region of high control region contamination, where the analysis is not expected to be sensitive, and therefore does not pose a problem for the interpretation of results. Towards high $m_{1/2}$ the typical statistical uncertainty is around 10%, while at lower $m_{1/2}$ the statistical uncertainty can reach above 50% with typical values of around 30%. For the mSUGRA grid the statistical uncertainty increases with decreasing $m_{1/2}$. The loose signal region uncertainties range from 5-25%, with uncertainties of 5-50% seen for the tight signal region. For the regions around the expected exclusion, the statistical uncertainty ranges from around 5-20% in both signal regions.

The systematic uncertainties in the GMSB grid are typically in the range of 10-20%, with some higher values observed that are likely due to statistical fluctuations. For the bRPV grid, values are naturally influenced by the limited signal region statistic. Typical values are in the range 5-30%, with larger fluctuations seen in the low statistics regions of the grid. The mSUGRA systematic uncertainties are typically below 15%, with larger uncertainties at low $m_{1/2}$.

For all the considered model grids the cross-section uncertainty has a

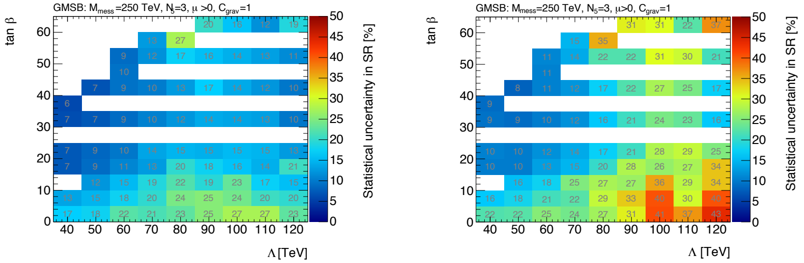

(a) Statistical uncertainty (b) Statistical uncertainty

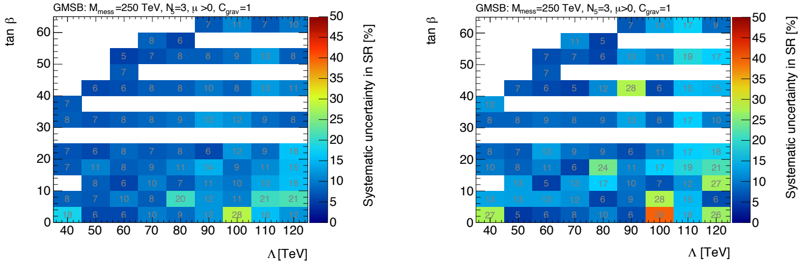

(c) Systematic uncertainty (d) Systematic uncertainty

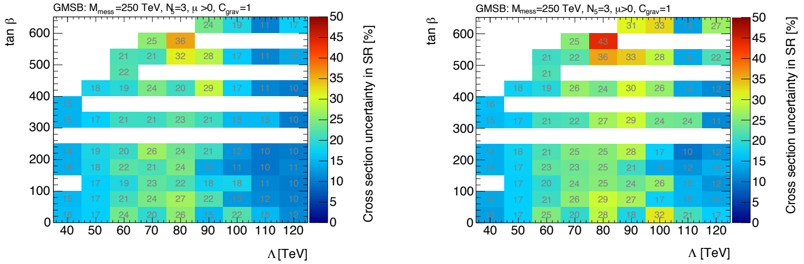

(e) Cross-section uncertainty (f) Cross-section uncertainty

Figure 10.27: Relative signal region uncertainties for the GMSB grid. The left hand column show uncertainties in the loose signal region, while the tight signal region uncertainties are to the right.

larger dependence on the grid parameters than the other uncertainties. This is due to the cross-section uncertainties depending on the supersymmetric production mechanism, which in turn depends on the grid parameters and the composition of events entering the signal region. The GMSB grid uncertainties range from 15-30%, while in the region of the expected exclusion typical values are 20-25%. The cross-section uncertainties in the bRPV grid are of a similar magnitude, varying between 15-30% across the grid, with values around the exclusion limit around 15-25%. The mSUGRA uncertainties range from 15-50% with typical values around the expected exclusion in the region of 15-30%.

Table 10.9: Cut-flow for the selection defining the loose signal region after baseline event selection showing expected Standard Model backgrounds and data. Background estimates are from simulations with scale factors applied to top, W+jets and Z+jets, except for the final estimate of multijet events that is obtained by a data-driven method described in the QCD background section. The uncertainties are statistical only.

After cut	$1\ \tau$	$\Delta\phi_{\mathrm{min}}$	$E_{\mathrm{T}}^{\mathrm{miss}}$	m_{T}	H_{T}
W+jets	10316 ± 297	5940 ± 179	2394 ± 75	97 ± 18	3.1 ± 0.6
Top	3050 ± 173	1956 ± 125	702 ± 45	78 ± 23	3.9 ± 1.0
QCD	255 ± 53	24 ± 18	5.1 ± 3.1	0.6 ± 0.2	1.12 ± 0.49
Z+jets	911 ± 77	430 ± 63	159 ± 31	72 ± 20	1.9 ± 0.6
Di-boson	44 ± 2	30 ± 2	15 ± 1	4.5 ± 0.5	0.47 ± 0.18
Total SM	14576 ± 356	8381 ± 228	3275 ± 93	252 ± 35	10.5 ± 1.4
Data	14629	8353	3187	224	12

Table 10.10: Cut-flow for the selection defining the tight signal region after baseline event selection showing expected Standard Model backgrounds and data. Background estimates are from simulations with scale factors applied to top, W+jets and Z+jets, except for the final estimate of multijet events that is obtained by a data-driven method described in the QCD background section. The uncertainties are statistical only.

After cut	$1\ \tau$	$\Delta\phi_{\mathrm{min}}$	$E_{\mathrm{T}}^{\mathrm{miss}}$	m_{T}	H_{T}
W+jets	10316 ± 297	5940 ± 179	408 ± 13	19.8 ± 3.0	0.73 ± 0.20
Top	3050 ± 173	1956 ± 125	89 ± 6	9.9 ± 3.1	0.82 ± 0.33
QCD	255 ± 53	24 ± 18	0.1 ± 0.1	0.1 ± 0.1	0.23 ± 0.10
Z+jets	911 ± 77	430 ± 63	24 ± 6	14.8 ± 4.1	0.42 ± 0.15
Di-boson	44 ± 2	30 ± 2	3.5 ± 0.5	1.3 ± 0.3	0.16 ± 0.09
Total SM	14576 ± 356	8381 ± 228	525 ± 15	46 ± 6	2.36 ± 0.44
Data	14629	8353	532	44	3

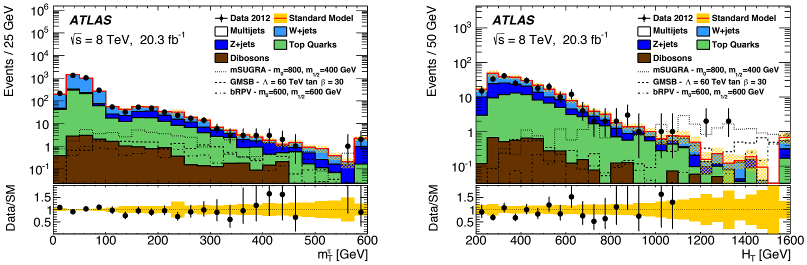

(a) Loose signal region – m_{T} (b) Loose signal region – H_{T}

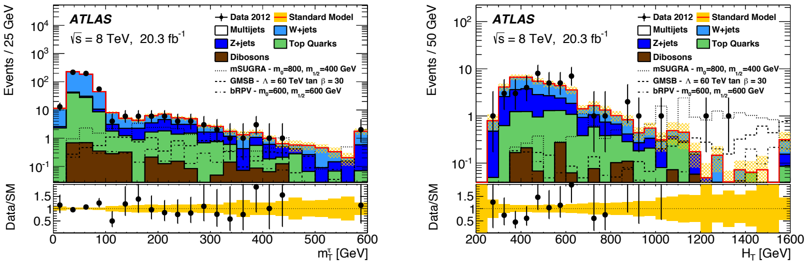

(c) Tight signal region – m_{T} (d) Tight signal region – H_{T}

Figure 10.28: Distributions of the final two variables defining the signal regions with all selections, but the variables plotted, applied. The uncertainties shown are statistical only.

10.6 Results and Interpretations

Tables 10.9 and 10.10 show the background estimates, obtained as described in the previous section, for the Standard Model backgrounds compared with the number of events observed in the data in the loose and tight signal regions respectively. Good agreement between data and estimated Standard Model background is observed at all stages of event selection, even where different background processes are dominant.

The two final kinematic distributions defining the signal regions, m_{T} and H_{T}, are shown in Figure 10.28 with all other selections applied. No excess with respect to the observed Standard Model background is seen, and the detailed breakdown of the background contributions, including systematic uncertainties, are shown in Table 10.11. Both signal regions have a slightly larger fraction of $t\bar{t}$ and W+jets events with a true rather than fake τ: 57% and 54% of the expected events, respectively, contain a true τ. The Z+jets

Table 10.11: Signal region background expectations, observed data and 95% CL upper limits on contributions from new physics.

–	Loose SR	Tight SR
Multijet	$1.12 \pm 0.49\,^{+1.27}_{-1.12}$	$0.23 \pm 0.10 \pm 0.24$
W + jets	$3.13 \pm 0.57 \pm 1.10$	$0.73 \pm 0.20 \pm 0.69$
Z + jets	$1.89 \pm 0.56 \pm 1.58$	$0.42 \pm 0.15 \pm 0.14$
Top	$3.87 \pm 0.99 \pm 1.62$	$0.82 \pm 0.34 \pm 0.46$
Diboson	$0.47 \pm 0.18 \pm 0.16$	$0.16 \pm 0.10 \pm 0.09$
Total background	$10.5 \pm 1.4 \pm 2.6$	$2.4 \pm 0.4 \pm 0.8$
Data	12	3
Obs (exp) limit on signal events	11.7 ($10.1^{+3.6}_{-2.6}$)	5.9 ($5.3^{+1.8}_{-1.3}$)
Obs (exp) limit on vis. cross section (fb)	0.58 (0.50)	0.29 (0.26)
Discovery p-value $p(s = 0)$	0.37	0.37

contribution, however, consisting mainly of Z-bosons decaying to neutrinos, has an expectation of more than 90% of the events containing a misidentified τ in both regions.

The total estimated background in the loose signal region, including systematic uncertainties, is $10.5 \pm 1.4 \pm 2.6$, while 12 events are observed in the data. The corresponding numbers for the tight signal region is a background expectation of $2.4 \pm 0.4 \pm 0.8$ with 3 events observed in the data. In both signal regions the observed data is consistent with the background only expectations and 95% CL limits are therefore set on contributions from new physics processes. Event displays for the three data events in the tight signal region are shown in Figure B.10.

Model independent upper limits set using 10 000 toy Monte Carlo pseudo experiments and the $\mathrm{CL_S}$ criterion are shown in Table 10.11. The observed 95% CL upper limits on the signal region contributions from new physics are 11.7 and 5.9 events in the loose and tight signal regions respectively. This corresponds to an observed limit on the visible cross section of 0.58 fb and 0.29 fb in the two regions. In both regions a discovery p-value, that is the p-value under the background only hypothesis, of 0.37 is obtained.

In addition to the model independent limits, the results are interpreted in context of GMSB, mSUGRA and bRPV. From the signal region expectations of the various models shown in Figure 10.29, along with the background and signal uncertainties discussed in the previous section, 95% CL limits are set on the GMSB, mSUGRA and bRPV model parameters in the parameter

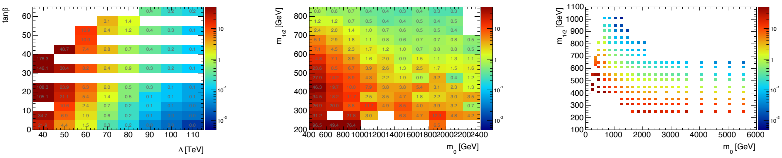

(a) Loose SR - GMSB (b) Loose SR - bRPV (c) Loose SR - mSUGRA

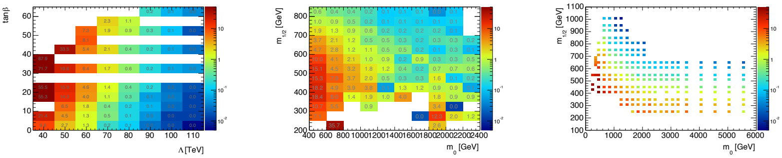

(d) Tight SR - GMSB (e) Tight SR - bRPV (f) Tight SR - mSUGRA

Figure 10.29: Signal expectations for the two signal regions for the three grids investigated in the analysis.

planes investigated. The limits, shown in Figure 10.30, are obtained using the Asymptotic approximation with the CL_S criterion and the Profile likelihood test statistic, as described in Section 8.10. Correlations between the uncertainties for the various background contributions and the signal are accounted for by introducing common nuisance parameters in the Likelihood function. Figure B.11 shows the obtained expected and observed CLs values across the three considered grids.

In Figure 10.30 the dashed black line indicates the expected exclusion reach with the yellow band representing the 1σ statistical and systematic uncertainty on the expected background and signal contributions. The solid red line shows the observed exclusion obtained from the observation made in the data. Around the observed limit the effect of shifting the theoretical uncertainty on the signal cross-section according to its uncertainty is shown by the dotted red line. The same conventions are used for other model dependent exclusion limits included in this work.

The limits are seen to agree with the expected exclusion reach obtained using a simplified significance measure in Figure 10.9. The limit obtained from the tight signal region alone is seen to be a significant improvement compared to the combined exclusion limit of the 7 TeV analysis, with a typical improvement in the exclusion reach in Λ of about 5 TeV in the GMSB model. The results is also a significant improvement on the preliminary results published on the same dataset as seen in Figure B.12. Typical expected

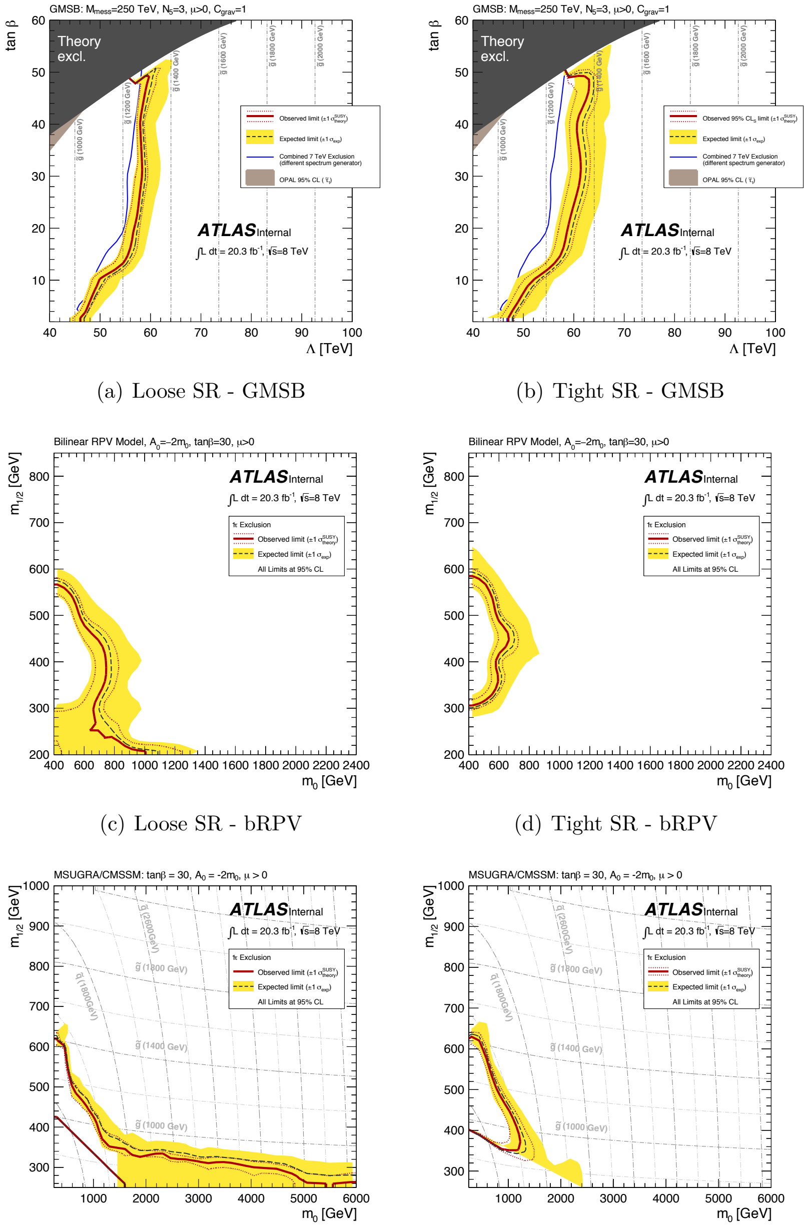

(a) Loose SR - GMSB (b) Tight SR - GMSB

(c) Loose SR - bRPV (d) Tight SR - bRPV

(e) Loose SR - mSUGRA (f) Tight SR - mSUGRA

Figure 10.30: 95% CL upper limits on the GMSB, bRPV and mSUGRA signal grids.

Table 10.12: Selections defining the 2τ analysis channel signal regions.

Requirement	Inclusive SR	bRPV SR	GMSB SR	nGM SR
Trigger selection	$p_{\mathrm{T}}^{\mathrm{jet1}} > 130$ GeV, $p_{\mathrm{T}}^{\mathrm{jet2}} > 30$ GeV $E_{\mathrm{T}}^{\mathrm{miss}} > 150$ GeV			
Taus	$N_{\tau}^{\mathrm{loose}} \geq 2$ $p_T > 20\,\mathrm{GeV}$			
Light leptons	$N_{\ell}^{\mathrm{baseline}} = 0$			
Multijet rejection	$\Delta\phi(\mathrm{jet}_{1,2}, p_{\mathrm{T}}^{\mathrm{miss}}) \geq 0.3$			
$m_T^{\tau_1} + m_T^{\tau_2}$ [GeV] >	150		250	
$H_{\mathrm{T}}^{2\mathrm{j}}$ [GeV] >	1000			600
$N_{\mathrm{jet}} \geq$	-	4		

GMSB 95% CL exclusion values are improved by almost 10 TeV compared to the previous one tau analysis result. The maximal observed exclusion reach is seen to be around 62 TeV compared to 56 TeV previously. Furthermore, values of Λ below 47 TeV are excluded at 95% CL independently of $\tan\beta$.

The strongest exclusions at high $m_{1/2}$ values in both the mSUGRA and bRPV grids are achieved in the tight signal region. There, maximal observed exclusion values at 95% CL 580 GeV and 630 GeV for bRPV and mSUGRA respectively. The loose signal region provides the strongest exclusions at low m_0. An observed exclusion of around 750 GeV in m_0 is reached at values of $m_{1/2}$ close to 400 GeV in bRPV. In mSUGRA $m_{1/2}$ values below 280 GeV are excluded for m_0 values up to 6 TeV by the loose signal region.

However, to fully benefit from the orthogonal design of the analysis channels, the results from the individual channels are combined and upper limits on the signal models are derived by combining the individual analysis channel results. The following sections will briefly describe the results of the other analysis channels.

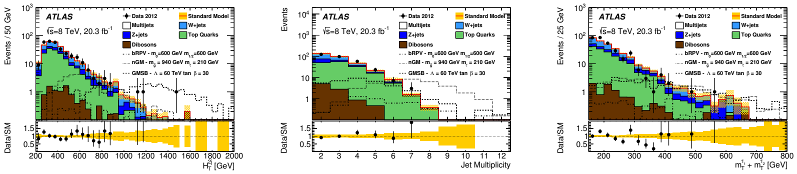

(a) H_{T} (b) Number of jets (c) $m_T^{\tau_1} + m_T^{\tau_2}$

Figure 10.31: Signal region kinematic distributions in the 2τ analysis [4].

10.7 Combining Search Channel Results

The other analysis channels, are as in the 7 TeV analysis, defined by the presence of at least two τ leptons, or a τ in addition to an electron or muon. For each of these three final states four signal regions are defined, targeting the range of main kinematics observed in the GMSB, mSUGRA, bRPV and nGM signal model grids. This means that the full analysis consists of a total of 14 independent signal regions, all targeting strongly produced SUSY with τ lepton final states.

All the analysis channels share a similar structure to the one τ channel described in the previous section, with the main selections performed on $E_{\mathrm{T}}^{\mathrm{miss}}$, H_{T} and jet multiplicity variables. Table 10.12 shows the selections defining the 2τ signal regions. Except for the selection of two loose τ leptons and an additional requirement on the number of jets, the 2τ signal regions are based on selections on the same variables as in the one τ analysis – jet and $E_{\mathrm{T}}^{\mathrm{miss}}$ trigger selections; light lepton veto; $\Delta\Phi(\mathrm{jet}, E_{\mathrm{T}}^{\mathrm{miss}})$ for multijet rejection and signal selection using the transverse mass and $H_{\mathrm{T}}^{\mathrm{2j}}$. The only subtle differences are that the sum of the transverse mass of the two τ leptons is used, in addition to only the two leading jets going into the calculation of the $H_{\mathrm{T}}^{\mathrm{2j}}$ variable. Figure 10.31 shows the kinematic distributions of the three last variables used to define the signal regions. Good agreement within the indicated statistical uncertainties is observed between the estimated backgrounds and the observed data.

The selections defining the τ+lepton signal regions are shown in Table 10.13. Unlike the other two search channels, the event selection here is based on a single lepton trigger. The trigger requirement therefore requires an isolated lepton with $p_{\mathrm{T}} > 25$ GeV. The remaining event selection is similar to the other two channels, except that the light lepton is used to calculate m_{T}, and a selection on m_{eff} replaces the H_{T} selection in the other channels. Figure 10.32 shows the final kinematic distributions defining the signal regions in t

Table 10.13: Selections defining the τ+lepton signal regions.

	GMSB SR	nGM SR	bRPV SR	mSUGRA SR
Trigger selection	$p_{\mathrm{T}}^{\ell} > 25$ GeV			
Taus	$N_{\tau}^{\mathrm{loose}} \geq 1$ $p_T > 20\,\mathrm{GeV}$			
Light leptons	$N_{\ell}^{\mathrm{signal}} = 1, \quad N_{\mathrm{other\ lep}}^{\mathrm{baseline}} = 0$			
Multijet rejection	$m_{\mathrm{T}}^{\ell} > 100$ GeV			
m_{eff} [GeV] $>$	1700	-	1300	-
$E_{\mathrm{T}}^{\mathrm{miss}}$ [GeV] $>$	-	350	-	300
$N_{\mathrm{jet}} \geq$	-	3	4	3

τ+lepton analysis channels. In general, good agreement is observed between the estimated background distributions and the data within the statistical uncertainties.

Table 10.14 compares the expected Standard Model background contributions and observed data in these signal regions. The observed data is overall seen to be in good agreement with the background only expectations. The most notable deviations between the expected background and the observed data are seen in the τ+e nGM and τ+μ bRPV signal regions. In the τ+e nGM the background expectation is $4.3 \pm 0.9 \pm 2.0$, while 8 events are observed in the data corresponding to a discovery p-value of 0.15. An expected background contribution of $2.5 \pm 0.6 \pm 1.0$ events and 7 events observed in data yields a discovery p-value of 0.04 in the τ+μ bRPV signal region. Considering the large number of signal regions investigated in the analysis, this observed deviation between the data and the expectation from background processes alone does not constitute a significant indication of new physics contributions. By construction, an experiment is expected to yield a discovery p-value ≤ 0.05 in one out of every 20 experimental trials, given that the background only (null) hypothesis is true. Similarly, the probability of observing at least one deviation beyond the 95% CL in 14 statistically independent signal regions, not considering any systematic correlations, assuming the background only hypothesis is 51%.

In addition to the lack of global statistical significance, the deviations are not seen in the signal regions aimed at similar final state kinematic signatures. For example, while there is an excess in the observed data in the τ+μ bRPV signal region there are, albeit small and well within one sigma, deficits in

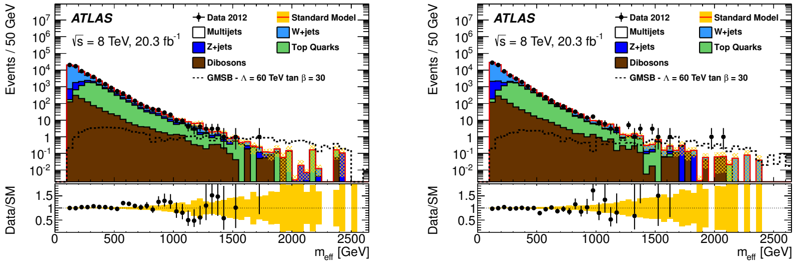

(a) τ+e – GMSB

(b) τ+μ – GMSB

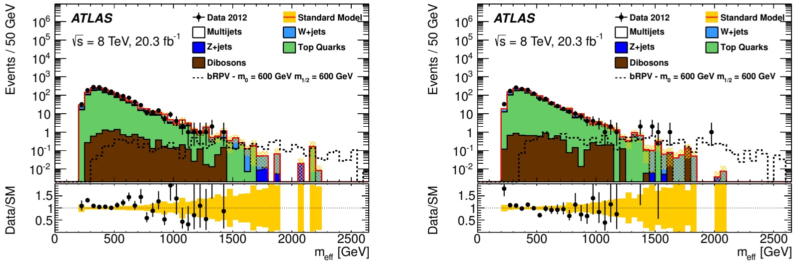

(c) τ+e – bRPV

(d) τ+μ – bRPV

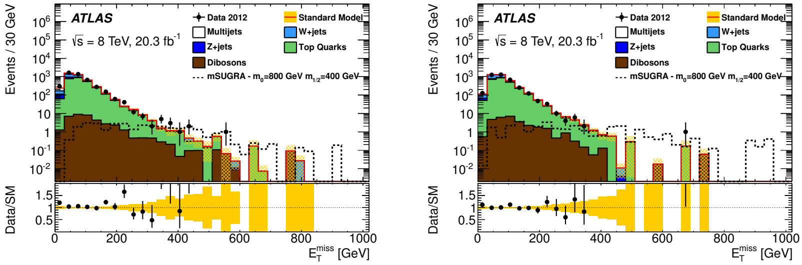

(e) τ+e – mSUGRA

(f) τ+μ – mSUGRA

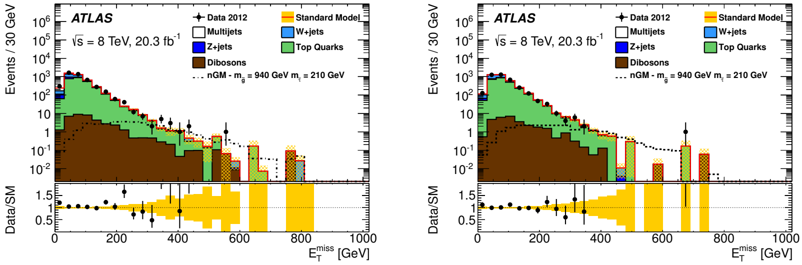

(g) τ+e – nGM

(h) τ+μ – nGM

Figure 10.32: Kinematic distributions defining the signal regions in the τ+lepton analyses [4].

Table 10.14: Summary of Standard Model background expectations and data yield for all the analysis signal regions.

	2τ GMSB	2τ nGM	2τ bRPV	2τ Inclusive
Multijet	$0.062 \pm 0.045 \pm 0.021$	$0.066 \pm 0.045 \pm 0.032$	$0.11 \pm 0.05 \pm 0.04$	$0.12 \pm 0.05 \pm 0.06$
W + jets	$0.14 \pm 0.07 \pm 0.18$	$0.78 \pm 0.31 \pm 0.47$	$0.48 \pm 0.15 \pm 0.31$	$1.26 \pm 0.33 \pm 0.54$
Z + jets	$0.037 \pm 0.020 \pm 0.042$	$0.65 \pm 0.28 \pm 0.94$	$0.18 \pm 0.07 \pm 0.21$	$0.54 \pm 0.15 \pm 0.64$
Top	$0.050 \pm 0.031 \pm 0.053$	$1.65 \pm 0.38 \pm 0.65$	$0.32 \pm 0.10 \pm 0.19$	$0.57 \pm 0.14 \pm 0.32$
Diboson	0 ± 0	0 ± 0	0 ± 0	$0.39 \pm 0.19 \pm 0.30$
Total background	$0.28 \pm 0.10 \pm 0.22$	$3.1 \pm 0.5 \pm 0.9$	$1.09 \pm 0.19 \pm 0.39$	$2.9 \pm 0.4 \pm 0.7$
Data	0	1	1	3

	τ+e GMSB	τ+e nGM	τ+e bRPV	τ+e mSUGRA
Multijet	< 0.2	< 0.1	< 0.3	< 0.4
W + jets	$0.25 \pm 0.11 \pm 0.31$	$0.45 \pm 0.14 \pm 0.28$	$1.61 \pm 0.54 \pm 0.58$	$0.96 \pm 0.22 \pm 0.46$
Z + jets	$0.28 \pm 0.12 \pm 0.29$	$0.11 \pm 0.06 \pm 0.11$	$0.20 \pm 0.09 \pm 0.81$	$0.15 \pm 0.07 \pm 0.16$
Top	$0.52 \pm 0.26 \pm 0.54$	$2.98 \pm 0.82 \pm 1.93$	$1.99 \pm 0.59 \pm 0.81$	$7.43 \pm 1.31 \pm 2.52$
Diboson	$0.29 \pm 0.13 \pm 0.28$	$0.73 \pm 0.21 \pm 0.21$	$0.22 \pm 0.12 \pm 0.12$	$1.47 \pm 0.30 \pm 0.32$
Total background	$1.34 \pm 0.33 \pm 0.80$	$4.3 \pm 0.9 \pm 2.0$	$4.0 \pm 0.8 \pm 1.3$	$10.0 \pm 1.4 \pm 3.0$
Data	1	8	3	14

	τ+μ GMSB	τ+μ nGM	τ+μ bRPV	τ+μ mSUGRA
Multijet	< 0.01	< 0.04	< 0.04	< 0.01
W + jets	$0.32 \pm 0.13 \pm 0.08$	$0.39 \pm 0.15 \pm 0.42$	$0.82 \pm 0.32 \pm 0.70$	$0.75 \pm 0.20 \pm 0.38$
Z + jets	$0.33 \pm 0.24 \pm 0.5$	$0.06 \pm 0.03 \pm 0.07$	$0.29 \pm 0.13 \pm 0.16$	$0.07 \pm 0.03 \pm 0.07$
Top	$0.02 \pm 0.02 \pm 0.01$	$2.80 \pm 0.83 \pm 0.97$	$1.22 \pm 0.46 \pm 0.57$	$8.36 \pm 1.40 \pm 2.90$
Diboson	$0.29 \pm 0.13 \pm 0.16$	$0.32 \pm 0.14 \pm 0.28$	$0.22 \pm 0.12 \pm 0.10$	$0.72 \pm 0.21 \pm 0.55$
Total background	$0.98 \pm 0.31 \pm 0.35$	$3.6 \pm 0.9 \pm 1.2$	$2.5 \pm 0.6 \pm 1.0$	$9.9 \pm 1.5 \pm 3.3$
Data	2	2	7	9

Table 10.15: Overview of the signal regions used to make the combined limits.

Combined limit	1τ SR	2τ SR	τ+lepton SR
GMSB	Tight	GMSB	GMSB
bRPV	Tight	bRPV	bRPV
nGM	-	nGM	nGM
mSUGRA	Tight	-	mSUGRA

the observed data with respect to the background only expectation in the τ+e and 2τ bRPV signal regions. Likewise, the deviations are not seen only within one of the analysis channels, possibly indicating a preferred final state particle content of the hypothesised Supersymmetric signal, either through the model flavour, preferred decays and branching ratios or mass hierarchies. In the case of the light lepton mainly originating from a τ decay in the signal models we would also expect similar observed excesses in the 2τ analysis channel. However, the two largest observed excesses are observed in signal regions targeting different final state kinematics (nGM and bRPV signal regions) and different final state particle content (τ+μ and τ+e), lending support to the interpretation of the deviations as statistical fluctuations of the background processes.

Since no significant excess is seen across the signal regions 95% CL upper limits are set in the GMSB, mSUGRA, bRPV and nGM grids by combining results from the four search channels. Like for the 1τ channel in the previous section information on the background and signal yields and systematics across the four grids are included in a total likelihood for the four channels. Table 10.15 shows the signal regions, one from each analysis channel, used to construct the combined limit. For the combined result for the mSUGRA and nGM grids no signal region from the 1τ and 2τ search channels respectively are included in the total likelihood due to lack of sensitivity to these models. Where possible, the complementarity of the search channels are exploited by combining signal regions with different regions of sensitivity resulting in the strongest expected combined exclusion. The individual contributions to the combined limit can be seen in Figure 10.33. In particular the combined exclusion in the mSUGRA and bRPV signal grids are seen to benefit from the complementarity of the specific signal regions at low m_0 and $m_{1/2}$ in particular.

The HistFitter package [181] was used to construct the exclusion limits using the Asymptotic approximation along with the CL_S criterion and the

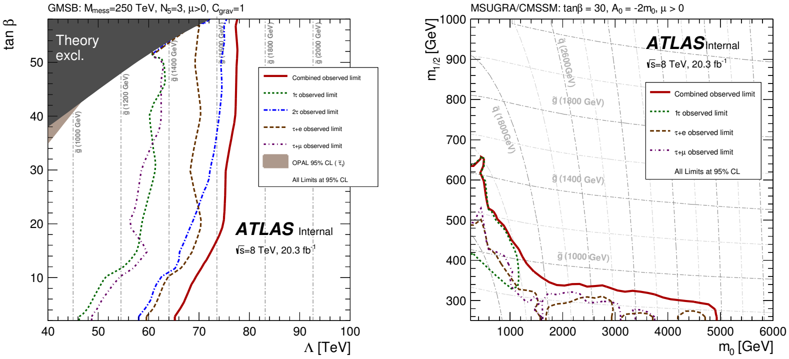

(a) GMSB (b) mSUGRA

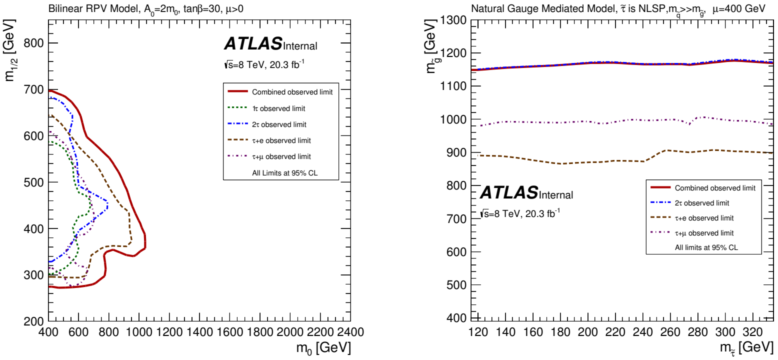

(c) bRPV (d) nGM

Figure 10.33: Individual 95% CL upper limits on the GMSB, bRPV and mSUGRA signal grids.

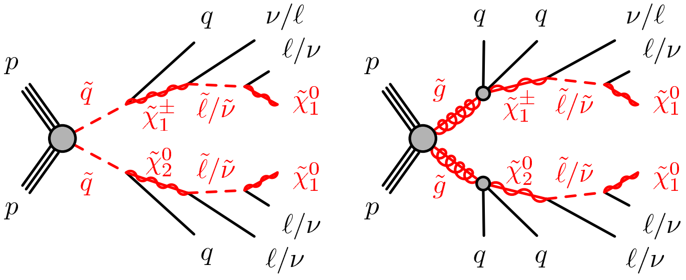

(a) squark-pair production (b) gluino-pair production

Figure 10.34: Decay topologies in simplified model with two-step decays and a slepton in the decay chain. In the model interpretation presented here the slepton is a $\tilde{\tau}$.

Profile Likelihood test statistic. Generator systematics and the luminosity uncertainty are taken to be fully correlated between the analysis channels, while all other systematics are treated as uncorrelated. Correlations between background and signal uncertainties are also taken into account. The effects of different choices for the treatment of nuisance parameter correlations were investigated, with results generally found not to be very sensitive to the selected treatment.

The final combined exclusion limits obtained in the four signal grids can be seen in Figure 10.35. Looking at the conservative estimate of the observed exclusion corresponding to the signal cross section shifted downwards according to its theoretical uncertainty, a lower limit on the SUSY breaking scale Λ of 63 TeV is determined independent of the value of $\tan\beta$ for the GMSB model. For $\tan\beta > 20$ the limit on Λ increases to 73 TeV, which corresponds to excluding gluino masses below about 1.6 TeV in this model. For the mSUGRA model, values of $m_{1/2}$ up to 640 GeV are excluded for low m_0, while for $m_0 > 2$ TeV values of $m_{1/2}$ up to 300 GeV are excluded. For the bRPV model values of $m_{1/2}$ up to 680 GeV are excluded for low m_0 while for $m_{1/2} = 360$ GeV the exclusion in m_0 reaches 920 GeV. In the interpretation of the nGM model gluino masses below 1090 GeV are excluded independent of the $\tilde{\tau}$ mass. These results are seen to be significant improvements, both for the individual analysis channel exclusions and the combined limits, on the preliminary ones published in [2] using the same dataset. The preliminary results are shown in Figure B.12.

In addition to interpreting results in the GMSB, mSUGRA, bRPV and nGM models in [4], the results obtained in the analysis was presented in

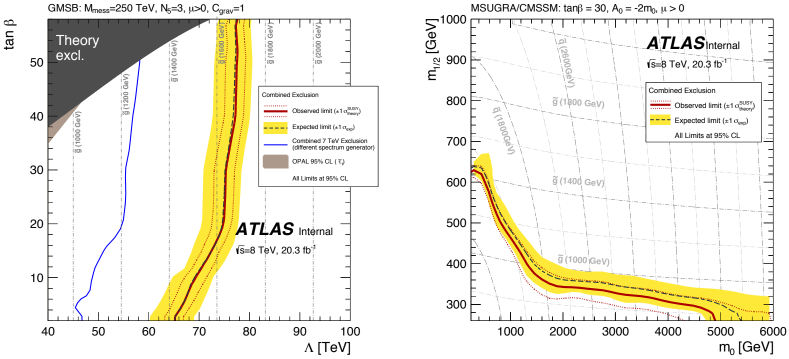

(a) GMSB (b) mSUGRA

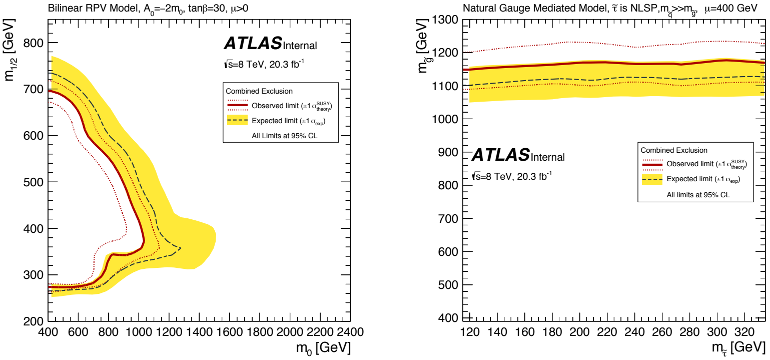

(c) bRPV (d) nGM

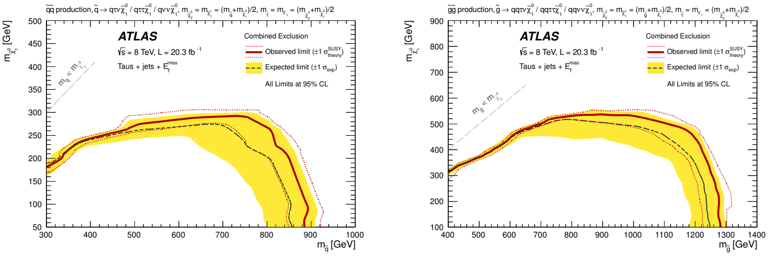

(e) squark-pair production [5] (f) gluino-pair production [5]

Figure 10.35: 95% CL upper limits on the GMSB, bRPV and mSUGRA signal grids and the two-step simplified model with pair production of squarks and gluinos.

papers summarising the findings of all run I searches for strongly produced supersymmetry [5], and re-interpreted in the context of pMSSM [6]. Interpretations were made in two simplified models where pairs for squarks or gluinos are produced and decay into a neutralino LSP in two steps, as shown in Figure 10.34. To ensure τ content in the final state the decay was forced to be via a $\tilde{\tau}$. Results from the 1τ and 2τ analysis channels were combined to obtain the final limit in these grids. For the 1τ analysis channel the loose signal region was found to be the most performant, while the nGM signal region resulted in the strongest limits for the 2τ analysis channel. The limits obtained when combining these two signal regions are shown in Figure 10.35. For the squark-pair production grid the observed exclusion reaches a maximal neutralino mass of about 270 GeV and a maximal squark mass of around 850 GeV. The corresponding values for the gluino-pair production model is a maximal exclusion in LSP masses up to about 480 GeV and gluino masses of 1220 GeV.

Chapter 11

Conclusions and Analysis Context

The searches presented here constitute the final results on searches for strongly produced SUSY in τ final states using data collected during the first LHC run period. As observations were in agreement with the Standard Model only expectations, stringent limits were set on new physics contributions and selected supersymmetric models. Despite the strong limits set by this search alone, it is important to consider the analysis in context of the broader SUSY search programme, both within ATLAS and particle physics in general. Care should also be taken in interpreting the search results and their implications on the viability of SUSY as a whole.

Figure 11.1 shows a comparison between a selection of ATLAS analyses interpreted in the four supersymmetric models investigated in the analysis presented here. The strong production τ analysis is seen to result in competitive exclusion reaches in all the models compared – in particular for high $\tan\beta$ in GMSB and at low m_0 in both the R-parity conserving and violating mSUGRA models. These regions exemplify the particular targeted SUSY scenarios of large jet activity and enhanced τ content. Going towards higher $\tan\beta$ in GMSB yields more events with a τ. Similarly, the enhanced reach of the SS/3L analysis reach at low $\tan\beta$ is due to the $\widetilde{\ell}$ replacing the $\widetilde{\tau}$ as the NLSP in this region resulting in enhanced decay into light leptons. In the mSUGRA grid the analysis exclusion reach is relatively strong compared to other analyses particularly at low m_0 where the $\widetilde{\tau}$ is the NLSP, resulting in τ final states.

Even though the exclusions in Figure 11.1 appear to be largely overlapping it is important to keep in mind that complementary information is often gleaned even by searches of similar exclusion reach for a given model. Taking the GMSB results of Figure 11.1 as an example, where similar exclusion

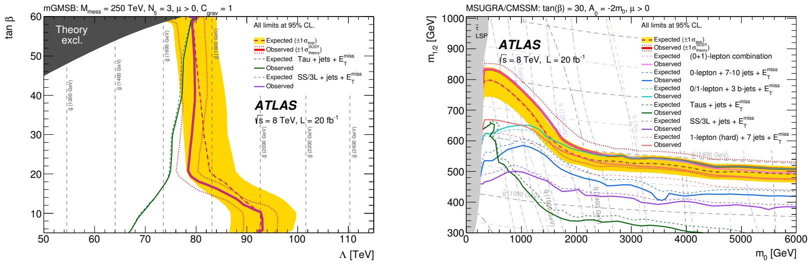

(a) GMSB (b) mSUGRA

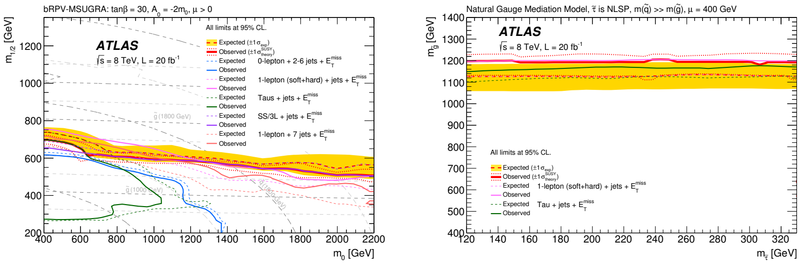

(c) bRPV (d) nGM

Figure 11.1: 95% CL upper limits on the GMSB, bRPV and mSUGRA signal grids for the most sensitive ATLAS searches [5].

power is seen in the two analyses, but the events selected by the two analyses are largely of distinct categories. When going towards higher values of Λ in the GMSB model plane, weak production of supersymmetric events start to be the dominant production mode. These events have very different detector signatures and kinematic properties from the strongly produced events the τ analysis is aimed at. The SS/3L analysis sensitivity, however, has a significant contribution from such events. As is seen from Figure 11.2 the overlap between the two analyses is only 51% for selected pMSSM events. In this way, similar exclusion reaches in a model can be obtained by analyses sensitive to widely different SUSY phenomenologies. Care should as such be taken in using exclusion reach in a specific model as a figure of merit when comparing analysis results, as the results do not necessarily generalise to a generic signal process or SUSY model.

The ATLAS SUSY search programme is rich with analyses designed to cover the wide range of possible phenomenologies of supersymmetric theory.

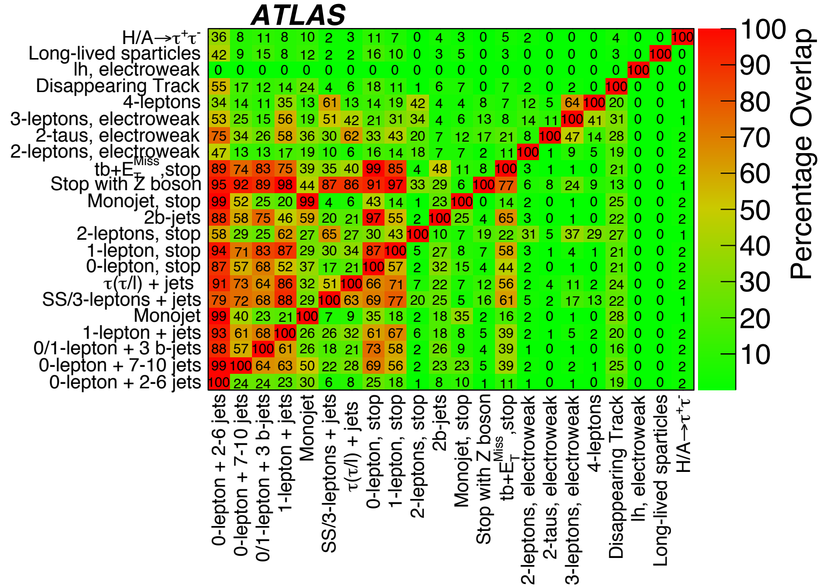

	0-lepton + 2-6 jets	0-lepton + 7-10 jets	0/1-lepton + 3 b-jets	1-lepton + jets	Monojet	SS/3-leptons + jets	τ(τ/l) + jets	0-lepton, stop	1-lepton, stop	2-leptons, stop	2b-jets	Monojet, stop	Stop with Z boson	$tb+E_T^{Miss}$,stop	2-leptons, electroweak	2-taus, electroweak	3-leptons, electroweak	4-leptons	Disappearing Track	lh, electroweak	Long-lived sparticles	$H/A\rightarrow\tau^+\tau^-$
$H/A\rightarrow\tau^+\tau^-$	36	8	11	8	10	2	3	11	7	0	4	3	0	5	2	0	0	0	4	0	0	100
Long-lived sparticles	42	9	15	8	12	2	2	16	10	0	3	5	0	3	0	0	0	0	3	0	100	0
lh, electroweak	0	0	0	0	0	0	0	0	0	0	0	0	0	0	0	0	0	0	0	100	0	0
Disappearing Track	55	17	12	14	24	4	6	18	11	1	6	7	0	7	2	0	2	0	100	0	0	0
4-leptons	34	14	11	35	13	61	13	14	19	42	4	4	8	7	12	5	64	100	20	0	0	1
3-leptons, electroweak	53	25	15	56	19	51	42	21	31	34	4	6	13	8	14	11	100	41	31	0	0	1
2-taus, electroweak	75	34	26	58	36	30	62	33	43	20	7	12	17	21	8	100	47	14	28	0	0	2
2-leptons, electroweak	47	13	13	17	19	10	6	16	14	18	7	7	2	11	100	1	9	5	19	0	0	2
$tb+E_T^{Miss}$,stop	89	74	83	75	39	35	40	99	85	4	48	11	8	100	3	1	1	0	21	0	0	2
Stop with Z boson	95	92	89	98	44	87	86	91	97	33	29	6	100	77	6	8	24	9	13	0	0	1
Monojet, stop	99	52	25	20	99	4	6	43	14	1	23	100	0	14	2	0	1	0	25	0	0	2
2b-jets	88	58	75	46	59	20	21	97	55	2	100	25	4	65	3	0	1	0	22	0	0	2
2-leptons, stop	58	29	25	62	27	65	27	30	43	100	10	7	19	22	31	5	37	29	27	0	0	1
1-lepton, stop	94	71	83	87	29	30	34	87	100	5	27	8	7	58	3	1	4	1	21	0	0	2
0-lepton, stop	87	57	68	52	37	17	21	100	57	2	32	15	4	44	2	0	1	0	21	0	0	2
τ(τ/l) + jets	91	73	64	86	32	51	100	66	71	7	22	7	12	56	2	4	11	2	24	0	0	2
SS/3-leptons + jets	79	72	68	88	29	100	63	69	77	20	25	5	16	61	5	2	17	13	22	0	0	1
Monojet	99	40	23	21	100	7	9	35	18	2	18	35	2	16	2	0	1	0	28	0	0	1
1-lepton + jets	93	61	68	100	26	26	32	61	67	6	18	8	5	39	2	1	5	2	20	0	0	2
0/1-lepton + 3 b-jets	88	57	100	61	26	18	21	73	58	2	26	9	4	39	1	0	1	0	16	0	0	2
0-lepton + 7-10 jets	99	100	64	63	50	22	28	69	56	2	23	23	5	39	2	0	2	1	25	0	0	2
0-lepton + 2-6 jets	100	24	24	23	30	6	8	25	18	1	8	10	1	11	1	0	1	0	19	0	0	2

Figure 11.2: Complementarity between searches for Supersymmetry in ATLAS [6]. The figure shows the percentage of model points excluded by a given search also excluded by another.

For example, direct searches are constructed to target specific production modes, sparticle mass spectra and branching fractions in both full and simplified SUSY models with varied detector signatures. Figure 11.2 shows the overlap between a selection of these analyses given as the percentage of model points excluded by a given analysis that is also excluded by another. It is clear that many of the analyses have significant overlap with the very inclusive 0-lepton search that benefit from the generic SUSY signature that is searched for. More targeted final states will, however, increase the sensitivity to more specialised corners of SUSY parameter space, such as very τ rich signals. In general little overlap is seen between the electroweak and strong production analyses, as is expected from how these are constructed. Highly specialised searches for long-lived sparticles, disappearing tracks and supersymmetric Higgs bosons are seen to have little overlap with other searches. For the analysis presented here the largest overlap is seen to be with the 0-lepton and 1-lepton searches, while overlap with other analyses is signifi-

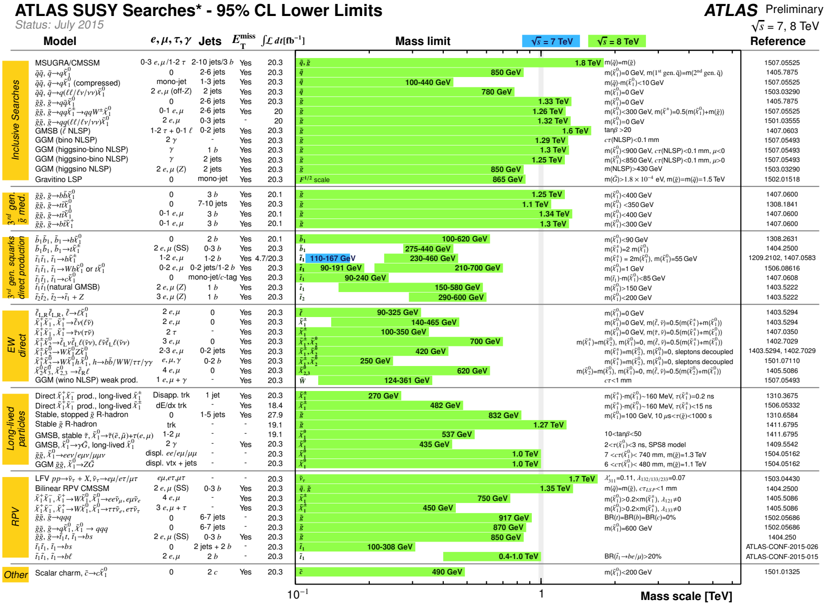

*Only a selection of the available mass limits on new states or phenomena is shown. All limits quoted are observed minus 1σ theoretical signal cross section uncertainty.

Figure 11.3: Summary of searches for Supersymmetry in ATLAS exemplified by the model dependent observed 95% CL lower limits on sparticle masses obtained in the respective searches [182].

cantly lower. Around 90% of the models excluded by the τ analysis are also excluded by the 0-lepton and 1-lepton searches.

Results presented as the maximal sparticle mass excluded of the same searches are shown in Figure 11.3. The results presented here yield a maximal gluino mass exclusion of 1.6 TeV at high $\tan\beta$ in the GMSB model plane. Again, one should be careful not to interpret these as general limits on sparticles masses – in addition to being highly model dependent, the obtained exclusion reach in sparticle masses depend strongly on the sparticle properties, such as the mass splitting between the initial sparticle produced in the collision and the LSP and preferred decay modes.

Although the data collected in the period 2010-2012 did not reveal any signs of new physics beyond the Standard Model, important steps towards constraining natural supersymmetric models have been taken. In addition to null results of direct searches for sparticles at colliders, precision measurements of rare processes in flavour physics, and measurements of the Higgs Boson properties further limit the room for possible contributions from physics beyond the Standard Model. Through these precision measurements properties of new physics, even at energy scales beyond the reach of searches, can be inferred and probed to provide both limits and possible hints towards physics beyond the Standard Model. This interplay between searches and precision measurements will continue in the second run period of the LHC, which will see almost a doubling of the centre of mass collision energy and more than a tenfold increase in the amount of collected data expected. This could open the doors towards discovery of new particles previously too massive or rarely produced to be seen, or further push the boundaries of supersymmetric theory and put natural SUSY models to a stringent test. In doing so the experience, expertise, know-how along with methods and techniques obtained and developed through the first LHC run period will be invaluable, and important lessons will be learned about possible beyond the Standard Model physics.

Part III

Searching for WIMP Dark Matter with CTA

Chapter 12

Searching the Skies for Dark Matter

The first part of this thesis concerned searches for supersymmetric dark matter produced in the laboratory through collider experiments. An alternative, and largely complementary approach to searching for dark matter is so-called indirect detection experiments. These experiments aim to detect remnants of naturally occurring dark matter through decay, or annihilation, products of the as of yet unobserved type of matter. The decay products could be neutrinos, electrons, protons, photons or other Standard Model particles, with several existing experiments tailored to observe one of these dark matter remnants. One virtue of such experiments is that they are potentially sensitive to very high mass dark matter candidates, where collider experiments are limited by the collision energies obtained. Furthermore, there is generally little model dependence in the signatures searched for, and consequently in the obtained results as well. The following chapters are dedicated to discussing the prospect of discovering WIMP dark matter at the next generation gamma-ray observatory – the Cherenkov Telescope Array.

The Cherenkov Telescope Array will be the latest installment in Imaging Atmospheric Cherenkov Telescopes (IACTs) that are based on the detection of Cherenkov light emitted when gamma-rays hit the atmosphere. It aims to significantly improve upon the performance of current experiments such as VERITAS in the U.S, MAGIC in the Canary Islands and HESS situated in Namibia. Chapter 13 will introduce both the scientific objectives of the experiment and outline the experimental design.

There are several ways of producing gamma-rays from the annihilation of WIMP dark matter, each resulting in distinct energy distributions of the resulting photons. Figure 12.1 exemplifies such annihilation diagrams for a supersymmetric WIMP, whereas analogous diagrams would occur in other

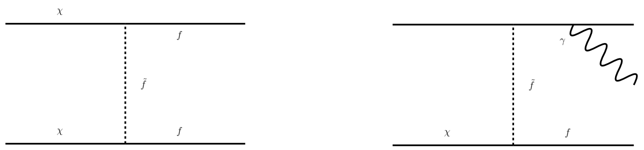

(a) Slepton/squark (b) Bremsstrahlung

(c) Higgs boson (d) Chargino

Figure 12.1: Neutralino annihilation diagrams to Standard Model particles.

beyond the Standard Model theories with WIMP dark matter candidates. Although these final states do not produce photons directly, the standard model decay products frequently produce neutral pions through hadronisation or interactions with matter. These pions in turn decay into photons that exhibit a continuous energy distribution. In addition bremsstrahlung photons in annihilations into electrically charged final states will also result in photons with a continuous energy distribution. At one-loop level, however, annihilations of the form $\chi\chi \to \gamma\gamma$, as shown in Figure 12.2, and $\chi\chi \to Z\gamma$ are allowed. Again taking the supersymmetric neutralino as an example WIMP. These annihilation processes would provide a "smoking-gun" signal for WIMP dark matter as the photons produced would be monochromatic – which is not easily mimicked by astrophysical background processes producing photons.

Chapter 14 presents an evaluation of the sensitivity of Cherenkov Telescope Array (CTA) in a model-independent search for monochromatic gamma-rays from WIMP dark matter annihilations. The analysis focuses on the Galactic Centre region, since this constitutes the largest nearby concentration of dark matter. Furthermore, since no astrophysical processes are expected to yield monochromatic gamma photons, the analysis is not expected to be overly sensitive to uncertainties related to the gamma ray background from sources in the Galactic Centre region.

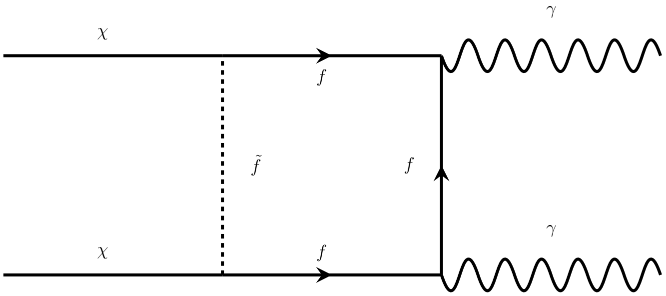

(a) fermion-sfermion loop

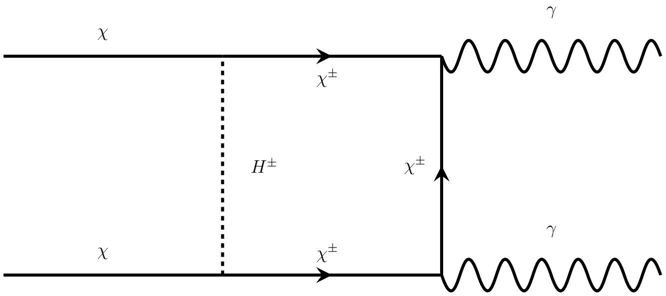

(b) charged-Higgs-chargino loop

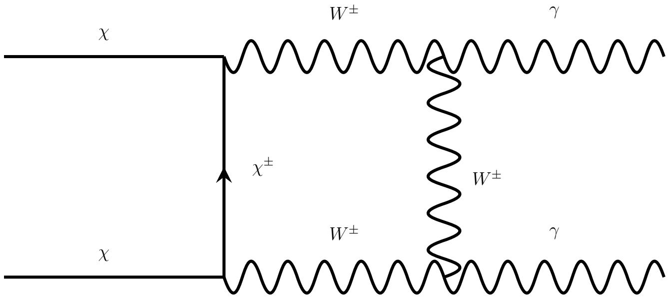

(c) chargino-W-boson loop

Figure 12.2: One-loop neutralino annihilations to photons.

Chapter 13

The Cherenkov Telescope Array

The Cherenkov Telescope Array (CTA) will provide valuable physics results in a wide range of areas within astrophysics and fundamental physics as it explores the universe in high energy gamma-rays. Among its aims is to study the origin of cosmic rays by observing both galactic and black hole particle accelerators through studies of extragalactic gamma rays, as well as aiming to address fundamental physics questions by searching for remnants of dark matter. The information in this chapter is primarily taken from [183] where a more thorough description of both the science case and design of the experiment can be found.

13.1 Science and Performance Objectives

The design goals of CTA include increasing the sensitivity of deep observations around 1 TeV by about an order of magnitude, while the large detection area and improved angular resolution will allow for observations of faint and short lived phenomena as well as resolving the details of extended sources. Additionally, the large detection area makes an energy coverage ranging from $\mathcal{O}(10~\text{GeV})$ to $\mathcal{O}(100~\text{TeV})$ possible. To achieve these goals and provide full sky coverage CTA consists of two sites – a main site in the southern hemisphere, and one in the northern hemisphere. The site in the southern hemisphere is the one responsible for observing the central region of the galaxy, while the northern site is dedicated to astrophysics studies. Furthermore, CTA will be an open observatory, making pre-processed versions of its data publicly available.

Gamma-ray energy photons are too energetic to be produced thermally by

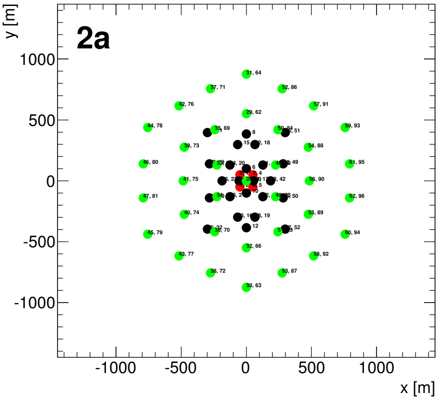

Figure 13.1: Array configuration used in Monte Carlo simulations. The array consists of three different telescope sizes, LST (red), MST (black), and SST (green). Key parameters for the telescopes are given in Table 13.1.

hot objects, but are rather produced either by relativistic particles interacting with matter and electromagnetic fields, or by decays or annihilations of new, heavy particles such as dark matter. The appealing aspect of observing gamma-rays is that, unlike cosmic rays, their origin can be traced, as the fact that they are electrically neutral means they are not influenced by interstellar magnetic fields. In other words, the source of high energy particles can be determined through observing the gamma-rays produced by the cosmic rays.

Rather than being observed directly, the gamma-rays are reconstructed from the light that is emitted as the gamma-ray traverses the earth's atmosphere. As the gamma-rays hit the atmosphere secondary showers of particles are induced. The speeds of the particles in the shower are higher than the speed of light in the air and the particles therefore emit Cherenkov radiation. By measuring the Cherenkov light on the ground both the energy and direction of the initial gamma-ray can be reconstructed. The large sensitive area allowed for by using an array of telescopes means that much lower fluxes at higher energies can be studied compared to what is possible with satellite-based detectors. The energy range covered by CTA is therefore largely complementary to that of satellite-based experiments, such as Fermi-LAT, while at the same time extending to higher energies and improving upon the sensitivity and angular resolution of current ground-based telescopes (HESS, MAGIC, VERITAS, etc.).

13.2 Experimental Design

This thesis focuses on searches for dark matter in the Galactic Centre region. For this purpose the telescope array situated at the southern site, which has full energy coverage, is most relevant. The main characteristics of this array and its constituent telescopes will be outlined in the following section.

Array Layout

The ideal layout of the CTA telescope array depends on the photon energy under consideration and requires different considerations to be taken into account. At low energies, below ~ 100 GeV, event rates are high, meaning that systematic uncertainties are the limiting factors in the sensitivity achieved. The high event rates allow the area of the array relevant for this energy regime to be small. By using a few large telescopes, rather than many small ones, to cover this energy range the low light yields of low energy gamma-rays can be efficiently collection. At intermediate energies ($\mathcal{O}(100\text{ GeV}) - \mathcal{O}(10\text{ TeV})$) medium sized telescopes are deployed with a spacing of about 100 m [183]. The higher number of medium sized telescopes with respect to current experimental facilities ensures increased sensitivity both due to the increase in the area covered, as well as better shower reconstruction as showers are usually simultaneously measured by multiple telescopes. At high energies, above ~ 10 TeV, the main factor limiting sensitivity is the gamma-ray flux, making a large instrumented area necessary to combat the low number of gamma-rays collected. The light yield, on the other hand, is large due to the high energy of the gamma-ray. This means that a suitable choice for detecting such gamma-rays are many small telescopes deployed with a wide spacing (100-200 m) [183].

The array used for simulating the detector response in the study presented here is shown in Figure 13.1. It consists of 63 telescopes of three different types. This array is referred to as configuration 2A. The core of the array consists of four Large Size Telescopes (LST) of 24 m diameter. Surrounding these are 24 Medium Size Telescopes (MST) of 12.3 m diameter. LST and MST are the main contributors to the sensitivity in the energy range relevant for dark matter searches. In addition to these telescopes there are 35 Small Size Telescopes (SST) of 7.4 m diameter spread out over a area close to 3 km^2 to increase the high energy capability of the array.

Table 13.1: Key figures for the three telescope sizes and cameras used in the simulated array [184] .

	LST	MST	SST
Diameter (m)	24.0	12.3	7.4
Dish shape	Parabolic	Davies-Cotton	Davies-Cotton
Mirror area (m^2)	412	100	37
Focal length (m)	31.2	15.6	11.2
Field of view (deg)	5	8	10
Number of pixels	2841	1765	1417
Pixel field of view (deg)	0.09	0.18	0.25

Telescope Characteristics

The main performance measures of a Cherenkov telescope is its ability to collect light, resolve image details and the size of the area observed by the telescope. The former depends on the telescope's mirror area, and on the photon collection efficiency of the PMTs of the telescope camera. Furthermore, it is necessary for the telescope triggering system to reject background photons during operation, in addition to being able to distinguish between gamma and cosmic-ray (excluding electrons) induced showers at analysis level. Key figures for the different telescope types are presented in Table 13.1 and will be introduced in the following.

The telescopes' field of view (FOV) is particularly important for the small telescopes, necessary for detection of high-energy gamma-rays, due to how widely they are spaced. A large field of view also allows for studies of extended sources, sky surveys and simultaneous study of multiple sources. The obtained FOV is limited by the number of detector pixels and read-out channels required, along with technical and mechanical difficulties of the optics of the telescope. The best imaging at large FOV using a single mirror is obtained using a Davies-Cotton [185] or elliptical dish geometry. These geometries introduce time dispersion of the measured light, which has detrimental effects on the trigger performance, effectively limiting dish sizes to less than 15 m [183].

Although the pixel size is primarily limited by cost considerations it also affects the trigger implementation. Unlike for large pixels, low-energy gamma-ray showers imaged with small pixels could have gaps between pixels with above-threshold deposits, making simple topological triggers inapplicable [183]. The pixel size is chosen to be smallest for the large telescopes and increasing with diminishing telescope sizes. This allows low-energy showers, mainly detected by the large telescopes, to be measured with high resolution at the same time as the number of night-sky background photons in each pixel is reduced. At high energies, where large FOVs are required, the decrease in resolution from the larger pixels is offset by the increased energy deposit by the shower photons, and the elongation of the shower images due to increased impact distances [183]. An important component of the image analysis is the shape and timing information of the recorded signal. By using this information, backgrounds from hadronic showers and secondary muons can be better distinguished from gamma-ray induced signals [186]. Furthermore, it allows variable signal integration windows to be used, thus reducing the noise from night-sky background photons in the image, as was done in MAGIC analyses [187].

The envisioned triggering system of the array needs to take into account coincidences between the individual telescopes in order for the data rate to be manageable. There are several possible implementations that could achieve this – ranging from each telescope triggering separately and looking for trigger coincidences between neighbouring telescopes, to using pixel level information from collections of telescopes to make the trigger decisions. While the former approach limits the energy threshold of the experiment, the latter allows for a lower threshold at the cost of introducing additional complexity to the system. The structure of the trigger would as such be hierarchical, where the first trigger level is based on pixels or collections of pixels, before image topology and finally array topology is taken into account [183]. Another important consideration is the speed of the triggering system. The array-wide triggering decision must be made within ms to μs to avoid deadtime caused by storage of telescope trigger information [188]. A fast approach would involve local trigger decisions based on information from neighbouring groups of telescopes, to a centralised decision based on the full array that would be slower, but highly flexible. Finally, the trigger should be software based to allow for easy customisation as the various operational modes required for the wide range of scientific objectives of the experiment require different triggering strategies. The southern array trigger rates are expected to be of $\mathcal{O}$(10kHz), with data rates in the range $\mathcal{O}$(100MB/s) - $\mathcal{O}$(1000MB/s) [188]. The lower bound on the data rate corresponds to a integrated signal over a short time window (15 ns), while for the upper bound the signal shape is sampled (at 1 GHz) over the same time window for all pixels.

In the following the expected response of CTA to gamma-rays hitting the atmosphere is taken from CTA Monte Carlo simulations [184]. The detector response derived from the simulations were optimised for 5 and 50 hours observation times, respectively, of a point source with a zenith angle of 20 degrees. The energy resolution and effective area from the simulations are given in a binned format, with 21 energy bins uniformly distributed on a log scale from 16 GeV to 160 TeV. Figure 13.2 shows the relative energy resolution and effective collection area for the considered southern site array.

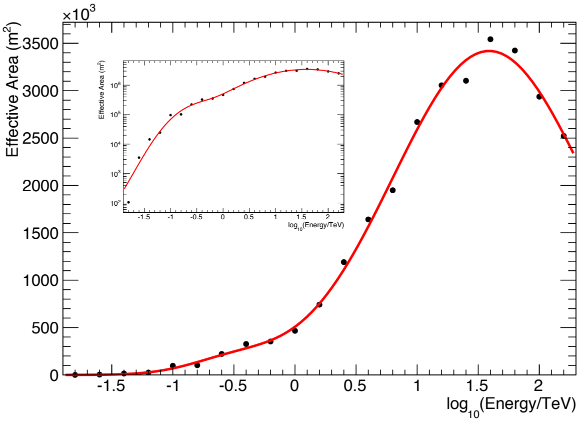

(a) Effective area

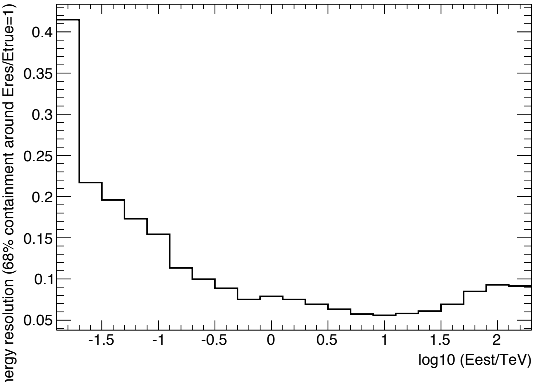

(b) Energy resolution

Figure 13.2: Simulated CTA response from [184] for 50 hour observation time. The red line shows the fit of two Gaussians to the effective area (top) described in the text.

Chapter 14

Sensitivity to WIMP DM Annihilating to a Photon Pair

The Galactic Centre has the highest concentration of dark matter in our galaxy, and is therefore a natural choice as the target region for a dark matter search. The presence of other gamma ray sources in the Galactic Centre is, however, a great challenge for most searches. In searching for a line emission, the background from other sources is less of an issue due to the characteristic shape of the signal that is searched for with respect to typical astrophysical backgrounds. An overview of the gamma-rays originating from the Galactic Centre can be found in [189] and [183]. These emissions are a complex mixture of extended and point sources and consist of gamma-rays produced by various astrophysical mechanisms. Although the Galactic Centre activity is not yet fully understood, experiments such as Chandra, HESS and INTEGRAL and others have greatly increased our knowledge of the Galactic Centre.

14.1 Modelling of Background and Signal

The Galactic Centre is located at a distance of approximately 8 kpc and is about 600 pc × 300 pc in size, corresponding to $\sim 4^\circ \times 2^\circ$ in galactic coordinates. It is dominated by a super-massive black hole with an estimated mass of $4 \times 10^6 M_\odot$ [189]. It also contains a radio source Sgr A^*, X-ray binaries, supernova remnants, dense molecular clouds, stellar clusters of young stars, pulsar wind nebulae and hot gas. Coupled with intense gravitational and magnetic fields it paints a picture of an intricate region where there are ample mechanisms for producing and accelerating particles. HESS is the experiment that has provided most of the information on the very high energy gamma-rays from the Galactic Centre that is relevant for CTA. Among other things it located a constant, point-like source close to Sgr A^* [190] emitting radiation following a power-law spectrum. The source is thought to originate from accelerated leptons or hadrons, but the mechanism of acceleration remains unknown, and several alternative hypotheses have been proposed [189]. Furthermore, HESS also observed a diffuse emission around the Galactic Centre of unknown origin and production mechanism [191, 192].

Following [193] and the above discussion the background is modelled by four components

$$\frac{dJ_{BG}}{dE} = \frac{dJ_{\text{proton}}}{dEd\Omega} + \frac{dJ_{\text{electron}}}{dEd\Omega} + \frac{dJ_{\text{HESS}}}{dE} + \frac{dJ_{\text{diffuse}}}{dE}, \tag{14.1}$$

where $\Delta\Omega$ is the solid angle spanned by our observational target area of the Galactic Centre. The first term represents background from hadronic cosmic rays; the second background from electron cosmic rays; the third the HESS source J1745-290; the fourth the diffuse photon emission measured by HESS in a $|\ell| \leq 0.8^\circ$ and $|b| \leq 0.3^\circ$ region around the Galactic Centre. These terms are given by

$$\frac{dJ_{\text{proton}}}{dEd\Omega} = 8.73 \cdot 10^{-9}\ (E/\text{TeV})^{-2.71}\ (\text{GeV cm}^2\text{ s sr})^{-1} \tag{14.2a}$$

$$\frac{dJ_{\text{HESS}}}{dE} = 2.3 \cdot 10^{-15}\ (E/\text{TeV})^{-2.25}\ (\text{GeV cm}^2\text{ s})^{-1} \tag{14.2b}$$

$$\frac{dJ_{\text{diffuse}}}{dE} = 5.1 \cdot 10^{-15}\ (E/\text{TeV})^{-2.29}\ (\text{GeV cm}^2\text{ s})^{-1} \tag{14.2c}$$

$$\frac{dJ_{\text{electron}}}{dEd\Omega} = \begin{cases} 1.17 \cdot 10^{-11}\ (E/\text{TeV})^{-3.0}\ (\text{GeV cm}^2\text{ s sr})^{-1}, & E \leq 1\text{ TeV} \\ 1.17 \cdot 10^{-11}\ (E/\text{TeV})^{-3.9}\ (\text{GeV cm}^2\text{ s sr})^{-1}, & E > 1\text{ TeV} \end{cases} \tag{14.2d}$$

The energy of the proton term is reduced by a factor 3 to take the reduced Cherenkov light output from hadronic showers into account [194]. Also following [193], we have multiplied the observed diffuse photon emission flux by a factor two as a conservative estimate on the extrapolation to our region of Galactic Centre observation. Furthermore, the reconstruction efficiency of protons is taken to be 1%, while for electrons and photons it is set to 80% as in [193].

The signal is modelled with a single Gaussian peak,

$$\Phi_{\text{sig}}(E) = \Phi_s e^{-(E-m_\chi)^2/2E_{\text{res}}^2(m_\chi)},$$

where m_χ is the WIMP mass hypothesis, and thus the energy of the photon from the annihilation, $E_{\text{res}}(m_\chi)$ is the energy resolution found from the array

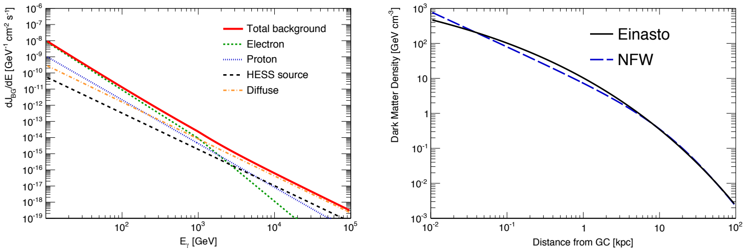

(a) Intrinsic background spectra (b) DM density profile

Figure 14.1: Intrinsic spectra composing the considered background and the Einasto and NFW Dark Matter profiles.

simulation described in Section 13.2, and Φ_s is a flux factor which is varied to estimate the sensitivity for observing the signal. The width of the Gaussian peak is set to the energy resolution of the detector, since the intrinsic energy spread of the emitted photon is expected to be only $\sim 10^{-3}$ [195]. The energy resolution at $m_\chi = 100$ GeV is ~15% for the CTA array considered in this analysis.

The observed signal flux for annihilation into two photons is related to the annihilation cross section as [196]

$$\Phi = \frac{\langle v\sigma\rangle}{2\pi m_\chi^2} \int_{\Delta\Omega} d\Omega \int_{\text{line of sight}} \rho^2(s) ds,$$

where $\langle v\sigma\rangle$ is the thermally averaged annihilation cross section, $\Delta\Omega$ is the solid angle which is observed, $\rho(s)$ is the dark matter density profile of the target region and s is the coordinate along the line of sight. The density profile of dark matter in the Galactic Centre is not well determined, since neither observations nor numerical simulations have sufficient resolution, and a number of proposed profiles are found in the literature, see e.g. [197, 198, 199]. The present analysis assumes the Einasto density profile [197]

$$\rho(r) = \rho_s \exp\left\{-\frac{2}{\alpha}\left[\left(\frac{r}{r_s}\right)^\alpha - 1\right]\right\}$$

with

$$r = \sqrt{s^2 + R_\odot^2 - 2sR_\odot \cos\ell \cos b},$$

$r_s = 20$ kpc and $\alpha = 0.17$ [200]. Here ℓ and b are the galactic longitude and latitude, respectively, $R_\odot = 8.5$ kpc the distance from our solar system to the centre of the galaxy, ρ_s is determined by setting $\rho(R_\odot) = 0.4$ GeV/cm^3 the

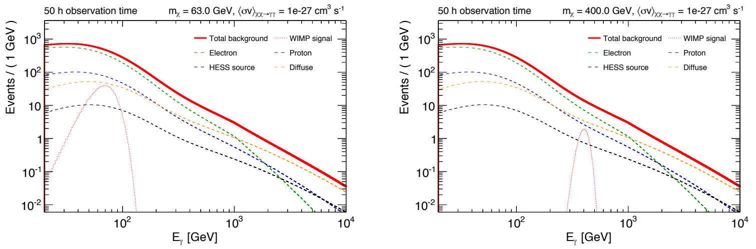

(a) $m_\chi = 63$ GeV (b) $m_\chi = 400$ GeV

Figure 14.2: Example observed signal and background spectra expected for 50 hours observation time with CTA assuming the intrinsic spectra shown in Figure 14.1.

average dark matter density at distance $R_\odot$ from the Galactic Centre [201]. The integration along the line of sight runs over the range $0 < s < 150$ kpc, giving a total mass of the Milky way halo of $\sim 1.2 \times 10^{12} M_\odot$ in agreement with the measured mass [202]. Integration with the above factors yields for the part of the signal flux that only depend on astrophysical quantities

$$J = \int_{\Delta\Omega} d\Omega \int_{\text{line of sight}} \rho^2(s) ds = 8.28 \cdot 10^{21}\ \text{GeV}^2\ \text{cm}^{-5}.$$

Observed spectra are obtained by integrating the intrinsic spectra over the given observational solid angle and time multiplied with the effective area of the array. The effective area is parametrised by a fit of two Gaussians, one centered at low and the other at high energy, as indicated by the red line in Figure 13.2. The resulting observed spectra for 50 hours observation time are shown in Figure 14.2. In Figure 14.3 curves indicating the signal cross section where $S/B = 1\%$ and $S/\sqrt{B} = 2$ respectively are shown, where S is the number of signal events within two standard deviations from the signal peak and B is the background in the corresponding area.

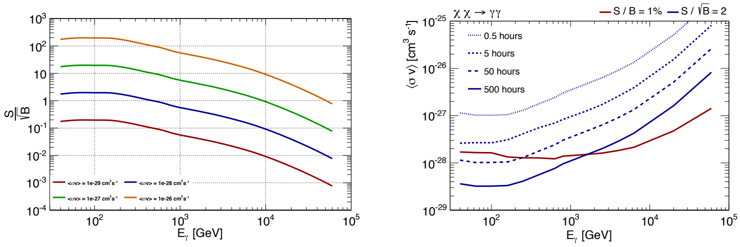

(a) S/$\sqrt{B}$

(b) Signal and background properties

Figure 14.3: S/$\sqrt{B}$ for versus WIMP mass for different annihilation cross sections assuming 50 hours observation time. Figure 14.3(b) shows the $S/B = 1\%$ curve and $S/\sqrt{B} = 2$ curves for a selection of observation times.

14.2 Sensitivity to Gamma Line Emission

To estimate the sensitivity a sliding window approach is adopted. Expected 95% CL exclusions are calculated for 12 WIMP mass hypotheses, chosen to have a linear spacing on a log scale, ranging from 40 GeV to 6 TeV. Pseudo data are generated from the total observed background spectrum, without any signal injected, within a window of three standard deviations of the WIMP mass hypothesis tested. Within each window the background is assumed to be well described by the product of a single power law and the effective area. The hypothesis of single power law background only within a window is then compared to hypothesis of an additional Gaussian signal, as described in the previous section. The resulting model, $f(x|\boldsymbol{\alpha})$, has three parameters ($\boldsymbol{\alpha}$) – the background normalisation and slope, and the signal cross section. Expressing the full list of parameters in terms of the parameter of interest, μ, which is the signal cross section and the other nuisance parameters as $\boldsymbol{\theta}$ we have $\boldsymbol{\alpha} = (\mu, \boldsymbol{\theta})$. The Poisson probability of observing n events given a total number of expected events, ν, is taken into account by the binned marked Poisson model

$$\boldsymbol{f}(\mathcal{D}|\nu, \boldsymbol{\alpha}) = \mathrm{Pois}(n|\nu) \prod_{i=1}^{m} f(x_i|\boldsymbol{\alpha}), \tag{14.3}$$

describing the probability density of a dataset, $\mathcal{D} = \{x_1, \ldots, x_m\}$, running over the m bins of the dataset. Throughout this work data is binned in 1 GeV bins.

The resulting binned extended likelihood function is then $L(\mu, \boldsymbol{\theta}; \mathcal{D}) = \boldsymbol{f}(\mathcal{D}|\mu, \boldsymbol{\theta})$. The maximum likelihood estimates are the values of the parame-

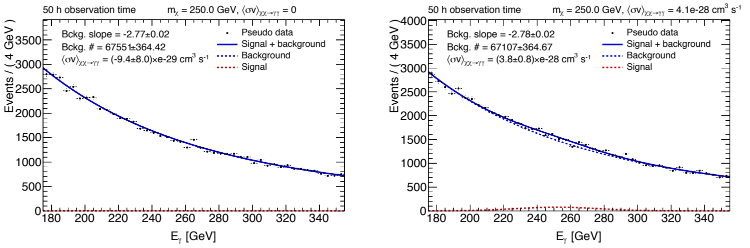

(a) Background only (b) $\langle v\sigma \rangle_{\chi\chi\rightarrow\gamma\gamma} = 4.1 \cdot 10^{-28} \mathrm{cm}^3\mathrm{s}^{-1}$

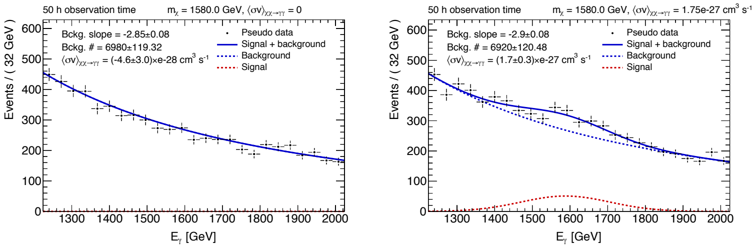

(c) Background only (d) $\langle v\sigma \rangle_{\chi\chi\rightarrow\gamma\gamma} = 1.75 \cdot 10^{-27} \mathrm{cm}^3\mathrm{s}^{-1}$

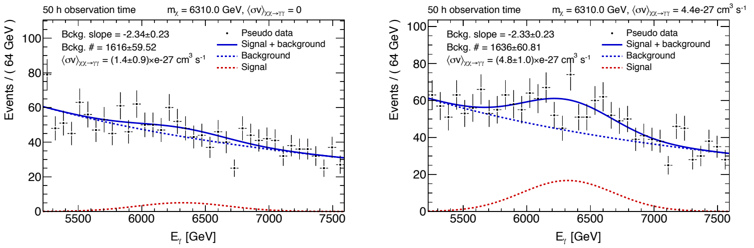

(e) Background only (f) $\langle v\sigma \rangle_{\chi\chi\rightarrow\gamma\gamma} = 4.4 \cdot 10^{-27} \mathrm{cm}^3\mathrm{s}^{-1}$

Figure 14.4: Toy datasets from background only within $\pm 3\sigma$ of the tested m_χ of 250 GeV (top), 1580 GeV(middle) and 6310 GeV(bottom). The solid lines show the unconditional maximum likelihood fit of the three parameter model described in the text to the toy data.

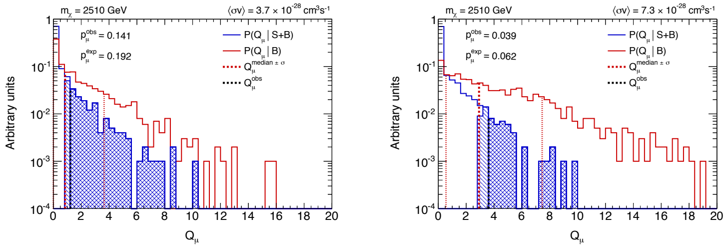

(a) $\langle v\sigma\rangle_{\chi\chi\to\gamma\gamma} = 3.7\cdot10^{-28}\mathrm{cm^3s^{-1}}$ (b) $\langle v\sigma\rangle_{\chi\chi\to\gamma\gamma} = 7.3\cdot10^{-28}\mathrm{cm^3s^{-1}}$

Figure 14.5: Example test statistic distributions obtained from toy Monte Carlo experiments for m_χ of 2510 GeV and two signal strength hypotheses. The hatched area indicates the integral corresponding to the p-value of the signal+background hypothesis that is tested when calculating the signal exclusion reach. The test statistic values used to calculate the expected p-value, with uncertainty, and the "observed" p-value for one of the toy experiments are also indicated.

ters maximising the likelihood function and are denoted by $\hat{\mu}$ and $\hat{\boldsymbol{\theta}}$. Figure 14.4 shows maximum likelihood fits of this model to pseudo data for hypothesised signal masses and signal strengths. Similarly, the conditional maximum likelihood estimate, $\hat{\hat{\boldsymbol{\theta}}}(\mu)$, is the value of $\boldsymbol{\theta}$ maximising the likelihood function for a given μ. Allowing the nuisance parameters to take on different values for each ν is commonly referred to as profiling, and is used to define the profile likelihood ratio

$$\lambda(\mu) = \frac{L(\mu, \hat{\hat{\boldsymbol{\theta}}}(\mu))}{L(\hat{\mu}, \hat{\boldsymbol{\theta}})}. \tag{14.4}$$

To set an upper limit on μ we define the test statistic

$$q_\mu = \begin{cases} -2\ln\lambda(\mu) & \hat{\mu} \le \mu \\ 0 & \hat{\mu} > \mu \end{cases} \tag{14.5}$$

The expected level of agreement between data and the hypothesised μ-value is quantified by the expected p-value

$$p_\mu = \int_{q_\mu^{\mathrm{median}}}^{\infty} f(q_\mu|\mu)dq_\mu, \tag{14.6}$$

where $f(q_\mu|\mu)$ is the pdf of q_μ for the hypothesised μ and q_μ^{median} is the median q-value of $f(q_\mu|0)$. Uncertainty on the expected p-value is obtained

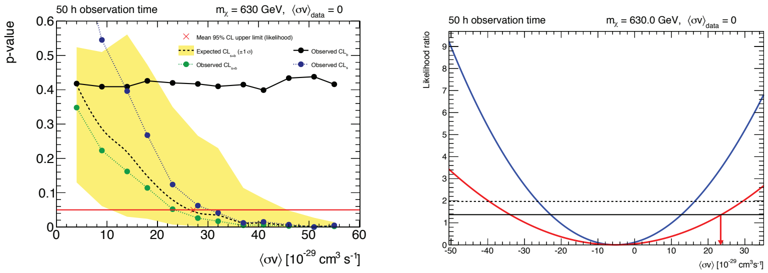

(a) Toy MC hypothesis test results (b) Likelihood ratios

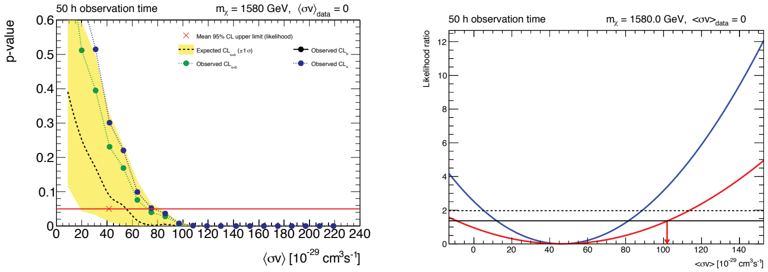

(c) Toy MC hypothesis test results (d) Likelihood ratios

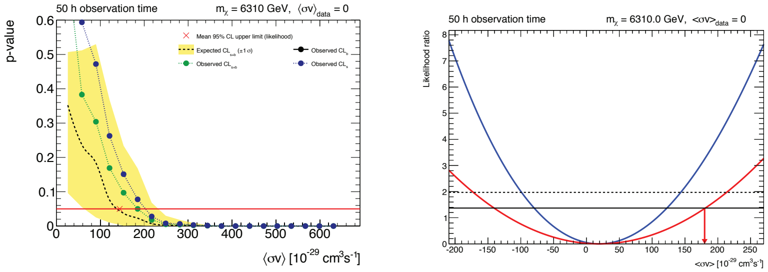

(e) Toy MC hypothesis test results (f) Likelihood ratios

Figure 14.6: Example results for calculating the 95% CL upper limit on a Dark Matter signal. The expected upper limit for the Toy Monte Carlo approach is the cross section where the dashed expected CL line reaches a p-value of 0.05, indicated by the red line. Uncertainties are obtained from the corresponding point for the upper and lower edges of the uncertainty band. The markers indicate the CL$_S$, CL$_{S+B}$ and CL$_B$ obtained from a single Toy Monte Carlo dataset. Figure (b) shows negative log likelihood ratios, red profile likelihood ratio and blue simple likelihood ratio, from a single Toy Monte Carlo dataset. The dashed and solid line indicate the 95% and 90% confidence intervals of the profile likelihood ratio respectively.

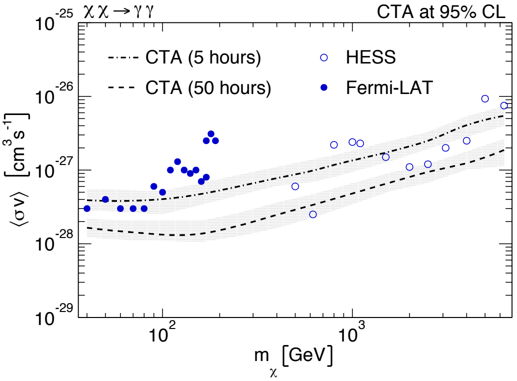

Figure 14.7: Expected 95% CL$_S$ upper limits on $\langle\sigma v\rangle_{\chi\chi\to\gamma\gamma}$ for CTA observation times of 5 h and 50 h with $\pm 1\sigma$ bands indicated by shaded areas. Markers show observed limits obtained by the HESS [203] and Fermi-LAT [196] experiments for comparison.

by replacing the median q_μ by the median value shifted by $\pm\sigma$. Distributions of $f(q_\mu|\mu)$ and $f(q_\mu|0)$ are obtained by generating 1000 Toy Monte Carlo datasets from background only and background plus signal from the full model shown in Figure 14.2. For each mass point this procedure is repeated, and a p-value for the signal plus background hypothesis calculated, for twelve hypothesised cross sections. The upper limit on μ at confidence level CL$_{S+B} = 1-\alpha$ is the value of μ for which the p-value is $p_\mu = \alpha$. To find the value of μ that gives $p_\mu = 0.05$, corresponding to the 95% CL upper limit, p-values are linearly interpolated between the tested cross sections. Figure 14.6 shows the p-value dependence on the signal cross section for a WIMP mass of 630 GeV. Also shown in the figure are values for a single Toy Monte Carlo dataset along with the quantities CL$_B$ and CL$_S$. CL$_B$ is calculated from the background only p-value

$$p_b = 1 - \int_{q_\mu^{\text{obs.}}}^{\infty} f(q_\mu|0)dq_\mu, \tag{14.7}$$

while to calculate CL$_S$ a ratio of the two p-values is used

$$p'_\mu = \frac{p_\mu}{1-p_b}. \tag{14.8}$$

As a cross-check of the above method, upper limits were calculated from a likelihood-based approach where one-sided 95% CL upper limits were determined from the profile likelihood ratio of background only pseudo data. The median upper limit is taken from 1000 background only Toy Monte Carlo datasets for each WIMP mass point. Figure 14.6 shows an example upper limit calculated from the profile likelihood ratio of one such toy dataset. The widening of the profile likelihood ratio relative to the simple likelihood ratio is due to the profiling of the nuisance parameters.

Figure 14.7 shows the obtained 95% CL_S upper limits on the signal cross section in the range 40 GeV to 6 TeV for 5 and 50 hours of CTA observational time. Compared to results from current experiments, HESS [203] and Fermi-LAT [196], CTA should be able to produce competitive results after 5 hours of observation. With an observation time of 50 hours CTA should provide significant improvements, up to a an order of magnitude, to the current exclusion reach across the whole mass range considered.

14.3 Interpretation and Discussion

The evaluation of the expected sensitivity to dark matter annihilating in the Galactic Centre region through the process $\chi\chi \to \gamma\gamma$ shows that the CTA reach is expected to be competitive with current experiments with data from only 5 hours of observation time. An observation time of 50 hours should see significant improvements with respect to current experimental limits over a wide WIMP mass range. The exclusion reach at 95% CL for 50 hours observation time is expected to be $\langle \sigma v \rangle_{\chi\chi\to\gamma\gamma} = (1-2)\cdot 10^{-28}\mathrm{cm}^3\mathrm{s}^{-1}$ for WIMP masses between 40 GeV and 200 GeV. At a WIMP mass around 5 TeV the exclusion is expected to be approximately an order of magnitude weaker for the same observation time. Further improvements could be envisioned not only through an increase in observation time, but also through for example improved separation between gamma-rays and charged cosmic rays, which is the main background component at low energies, along with improved energy reconstruction and collection efficiency.

Systematic effects have not been evaluated due to a lack of detailed understanding of their nature at the present time. Such effects are expected to be of the order a few percent of the observed background contributions at energies above 100 GeV[183]. Due to the distinct nature of the signal shape searched for the systematic uncertainties are not expected to significantly alter the results obtained in the previous sections in this region. However, below 100 GeV systematic uncertainties could be the limiting factor for the achieved sensitivity [183]. In particular the uncertainties related to contributions from charged cosmic rays could become significant, as it grows progressively more difficult to distinguish these from gamma rays at low energies. This is especially relevant for the results presented in this study due

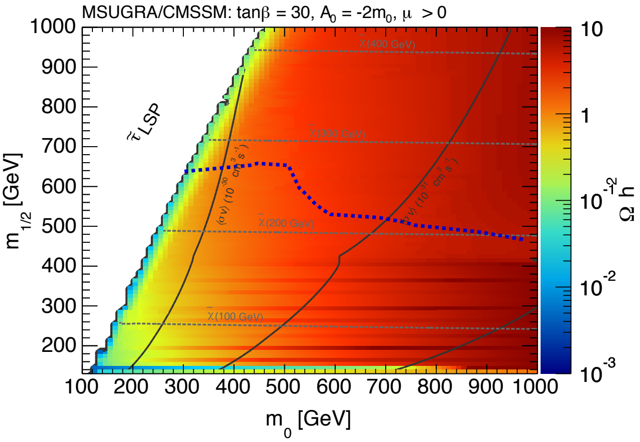

Figure 14.8: Quantities relevant to the search for WIMP dark matter annihilating to a monochromatic photon pair in the Higgs-aware mSUGRA grid studied in the ATLAS search for supersymmetry in τ final states. In addition to the dark matter relic density the neutralino LSP mass contours are indicated by the dashed grey lines, and the neutralino annihilation cross section into two photons is shown as solid lines. The exclusion limit obtained in the 8 TeV strong τ analysis is indicated by the dashed blue line.

to the general way in which the charged cosmic ray backgrounds have been treated. The lack of a dedicated detector response function for hadrons together with no detailed information on the method to be applied for hadron rejection, means that the obtained results at low energies (< 100 GeV) could be subject to significant change once a more detailed understanding of the experiment and its uncertainties is achieved.

To compare results with those obtained in Part II and exemplify the quantities relevant for indirect detection experiments in supersymmetry the mSUGRA model was investigated. To compute the supersymmetric dark matter properties the fortran package `DarkSUSY 5.1.1` [204, 205] was used. DarkSUSY uses `ISAJET 7.81` [206], that contains ISASUGRA, for the running of renormalisation group equations and `FeynHiggs 2.9.4` [207, 208, 209, 210, 211] to calculate Higgs masses and properties. Along with sparticle mass spectra and properties in the MSSM DarkSUSY is able to calculate astrophysical properties of supersymmetric dark matter and quantities related to both direct and indirect detection experiments. This includes, but is not limited to, the dark matter relic density [212, 213, 213] and neutralino annihilation cross sections into photons [214, 215].

Figure 14.8 shows the so-called Higgs-aware mSUGRA grid [216] as described Part II with dark matter related quantities as calculated by DarkSUSY. The coloured area shows the dark matter relic density where the narrow band of allowed values, indicated by the transition between green and blue colouring, is predominantly part of the $\chi - \tilde{\tau}$ co-annihilation region. The neutralino mass, indicated by the horisontal, grey, dashed lines, increases with $m_{1/2}$. The vertical, black, solid lines are the contours indicating the neutralino annihilation cross section into photons. The annihilation cross section reaches $10^{-30}\text{cm}^3\text{s}^{-1}$ in parts of the above mentioned co-annihilation region and is roughly increasing with decreasing values of m_0. As a reference, the observed limit obtained in the ATLAS analysis of 8 TeV data searching for strongly produced supersymmetry in τ final states presented in Chapter 10 is superimposed (blue dashed line). Figure 14.9 shows the annihilation cross section into photons against the neutralino mass for selected mSUGRA models, both in the Higgs-aware grid and for a more general selection of mSUGRA points from [217]. It is again clear how the ATLAS exclusion reach decreases towards higher neutralino masses, while the projected CTA exclusion is close to flat across the considered range. Furthermore, the models with a reasonable dark matter relic density are situated towards the higher annihilation cross section values obtained. Looking at the randomly sampled mSUGRA points, and those satisfying experimental constraints and discoverability criteria in τ SUSY search channels at ATLAS [217], show that annihilation cross sections around $10^{-29}\text{cm}^3\text{s}^{-1}$ for WIMP masses around 100-200 GeVare possible.

Although the annihilation cross sections obtained here are likely outside the reach of CTA, the figure nevertheless illustrate the complementarity between the two experimental approaches. Whereas the reach of accelerator searches are limited to lower sparticle masses and values of m_0 and $m_{1/2}$, the annihilation cross section is largely independent of these masses, thus potentially making WIMP masses of several hundred GeV and above accessible. In the context of the grid studied here accelerator experiments can exclude large values of $m_{1/2}$ for moderate m_0, whereas the opposite is true for CTA, where sensitivity is highest at moderate $m_{1/2}$, but with a potential to reach large values of m_0. As such the two approaches exhibit complementarity that would be important in both probing different regions of supersymmetric parameter space, as well as pinpointing the nature of supersymmetry should it be discovered.

As mentioned, the annihilation cross sections here appear to be outside the reach of CTA, however, a broader study of the MSSM has found that

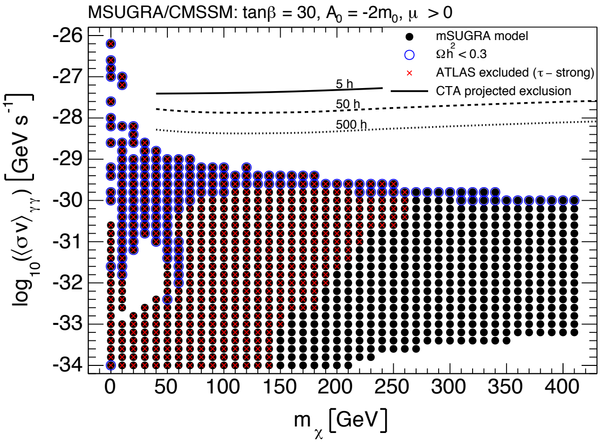

(a) Higgs-aware mSUGRA

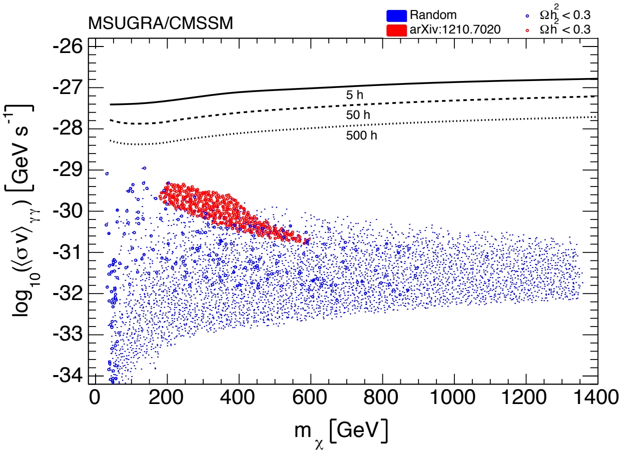

(b) mSUGRA

Figure 14.9: Annihilation cross section versus WIMP mass for selected mSUGRA models in a) the Higgs-aware grid, and b) randomly sampled mSUGRA models (blue) and models required to satisfy experimental constraints and discoverability criteria in τ channels at accelerators (red) from [217]. Solid discs are models, while circles are models with a reasonable dark matter relic density. a) also indicate models excluded by the search presented in Chapter 10 by red crosses. The projected CTA limits are also indicated. The result for 500 hours is obtained by extrapolating the 50 hour result assuming the relative increase in sensitivity is equal going from 50 to 500 hours, as from 5 to 50 hours.

values in the region $10^{-29} - 10^{-28}\mathrm{cm}^3\mathrm{s}^{-1}$ are possible across a large range of neutralino masses. In particular values around $10^{-28}\mathrm{cm}^3\mathrm{s}^{-1}$ are obtained for higgsino-like neutralinos with masses around 500 GeV [218]. The latter would likely be difficult to observe at collider experiments, but could be within the reach of CTA. Furthermore, both models with significant annihilations into photon pairs [219, 220, 221], and mechanism for increased line rates [222] have been proposed. Additionally the line flux could be increased by astrophysical factors, for example the signal strength could be boosted by the profile and distribution of sub-halos [223, 224, 225] possible by up to a factor 10 [226].

Chapter 15

Concluding Comments and Outlook

The first period of LHC running was very successful both in terms of operations, performance and, most importantly, in terms of the achieved physics results. The discovery of the Higgs boson was the undisputed high point, meaning that all of the particles postulated by the Standard Model have now been discovered. However, the data collected during this period did not show any hints of supersymmetry or other new physics beyond the Standard Model. The search for supersymmetry in τ final states presented in this thesis is only one out of many new physics searches found to be in good agreement with the Standard Model predictions. These results are nevertheless valuable in narrowing down and restricting the paramater space left for supersymmetry, or other new physics, to hide in. Many constrained models that were popular prior to the LHC startup, such as mSUGRA, have been heavily constrained and the room for natural supersymmetry has been reduced.

At the time of writing, the second run period is well underway, with collision energies almost doubled with respect to the data studied in this thesis. It is, however, important to keep in mind that the LHC, and the experiments associated with it, are only at the very beginning of their lifespans. The LHC is anticipated to collect more than two orders of magnitude more data than currently available in the coming ten to twenty years. While the increased energy means that new physics discoveries could be just around the corner, the history of particle physics has shown the rewards of patience. The road forward for particle physics today is perhaps less clear than during the several decades spanned from formulation to experimental completion of the Standard Model due to the lack of hints towards new physics from the domain of particle physics. Nevertheless, both the long term schedule of the

LHC and the statistical nature of particle physics discoveries reflect the fact that new physics phenomena are not necessarily readily discoverable nor as expected at the outset.

In this context, one should also bear in mind that despite the historical success and importance of collider experiments, the search for dark matter, connecting the domains of subatomic and galactic physics, underlines the need for additional search approaches that reflect this interconnection. Results from indirect and direct detection experiments complement those obtained by colliders and will be crucial to determine the nature of dark matter. The Cherenkov Telescope Array should improve significantly upon the sensitivity of current experiments in a wide range of fundamental physics and astrophysics. In particular, it will bring improved reach in searches for WIMP dark matter annihilations into pairs of photons once it is operational, also in regions not accessible to the ATLAS experiment at the LHC. With CTA just around the corner and the LHC running smoothly at record energy, the two experimental facilities promise to produce exciting physics results for many years to come.

Appendix A

Additional Material for the 7 TeV ATLAS Analysis

A.1 Monte Carlo Samples

Sample ID	Name	Generator	LO [pb]	k-factor	FE	NNLO [pb]	# events
107680	WenuNp0	AlpgenJimmy	6930.5	1.196		8288.88	3458883
107681	WenuNp1	AlpgenJimmy	1305.3	1.196		1561.14	2499645
107682	WenuNp2	AlpgenJimmy	378.13	1.196		452.24	3768632
107683	WenuNp3	AlpgenJimmy	101.86	1.196		121.82	1008947
107684	WenuNp4	AlpgenJimmy	25.68	1.196		30.71	250000
107685	WenuNp5	AlpgenJimmy	6.99	1.196		8.36	69999
144022	WenuNp6_pt20	AlpgenJimmy	1.55	1.196		1.85	145000
144196	WenuNp1_susyfilt	AlpgenJimmy	1305	1.1955	0.005659	8.83	180899
144197	WenuNp2_susyfilt	AlpgenJimmy	378	1.1955	0.01652	7.47	134998
144198	WenuNp3_susyfilt	AlpgenJimmy	101.9	1.1955	0.03404	4.15	139999
144199	WenuNp4_susyfilt	AlpgenJimmy	25.7	1.1955	0.05639	1.73	75000
107690	WmunuNp0	AlpgenJimmy	6932.4	1.195		8284.22	3462942
107691	WmunuNp1	AlpgenJimmy	1305.9	1.195		1560.55	2498593
107692	WmunuNp2	AlpgenJimmy	378.07	1.195		451.79	3768737
107693	WmunuNp3	AlpgenJimmy	101.85	1.195		121.71	1008446
107694	WmunuNp4	AlpgenJimmy	25.72	1.195		30.74	254950
107695	WmunuNp5	AlpgenJimmy	7	1.195		8.37	70000
144023	WmunuNp6_pt20	AlpgenJimmy	1.55	1.195		1.85	145000
144200	WmunuNp1_susyfilt	AlpgenJimmy	1305	1.1955	0.005422	8.46	171000
144201	WmunuNp2_susyfilt	AlpgenJimmy	378	1.1955	0.016234	7.34	139900
144202	WmunuNp3_susyfilt	AlpgenJimmy	101.9	1.1955	0.033596	4.09	139899
144203	WmunuNp4_susyfilt	AlpgenJimmy	25.7	1.1955	0.056165	1.73	70000
107700	WtaunuNp0	AlpgenJimmy	6931.8	1.195		8283.50	3418296
107701	WtaunuNp1	AlpgenJimmy	1304.9	1.195		1559.36	2499194
107702	WtaunuNp2	AlpgenJimmy	377.93	1.195		451.63	3750986
107703	WtaunuNp3	AlpgenJimmy	101.96	1.195		121.84	1009946
107704	WtaunuNp4	AlpgenJimmy	25.71	1.195		30.72	249998
107705	WtaunuNp5	AlpgenJimmy	7	1.195		8.37	65000
144024	WtaunuNp6_pt20	AlpgenJimmy	1.55	1.195		1.85	150000
144204	WtaunuNp1_susyfilt	AlpgenJimmy	1305	1.1955	0.008387	13.08	265000
144205	WtaunuNp2_susyfilt	AlpgenJimmy	378	1.1955	0.024476	11.06	204999
144206	WtaunuNp3_susyfilt	AlpgenJimmy	101.9	1.1955	0.050024	6.09	209900
144207	WtaunuNp4_susyfilt	AlpgenJimmy	25.7	1.1955	0.081906	2.52	104999

Table A.1: Simulated W+jets Monte Carlo samples with their corresponding sample ID, event generator, LO cross section, k-factor, filter efficiency, NNLO cross section [227], and number of generated events.

Sample ID	Name	Generator	LO [pb]	k-factor	FE	NNLO [pb]	# events
107650	ZeeN0p	AlpgenJimmy	669.6	1.24345		832.61	6618284
107651	ZeeN1p	AlpgenJimmy	134.55	1.24345		167.31	1334897
107652	ZeeN2p	AlpgenJimmy	40.65	1.24345		50.55	2004195
107653	ZeeN3p	AlpgenJimmy	11.26	1.24345		14.00	549949
107654	ZeeN4p	AlpgenJimmy	2.84	1.24345		3.53	149948
107655	ZeeN5p	AlpgenJimmy	0.76	1.24345		0.95	50000
107660	ZmumuN0p	AlpgenJimmy	669.6	1.24345		832.61	6615230
107661	ZmumuN1p	AlpgenJimmy	134.55	1.24345		167.31	1334296
107662	ZmumuN2p	AlpgenJimmy	40.65	1.24345		50.55	1999941
107663	ZmumuN3p	AlpgenJimmy	11.26	1.24345		14.00	549896
107664	ZmumuN4p	AlpgenJimmy	2.84	1.24345		3.53	150000
107665	ZmumuN5p	AlpgenJimmy	0.76	1.24345		0.95	50000
107670	ZtautauN0p	AlpgenJimmy	669.6	1.24345		832.61	10613179
107671	ZtautauN1p	AlpgenJimmy	134.55	1.24345		167.31	3334137
107672	ZtautauN2p	AlpgenJimmy	40.65	1.24345		50.55	1004847
107673	ZtautauN3p	AlpgenJimmy	11.26	1.24345		14.00	509847
107674	ZtautauN4p	AlpgenJimmy	2.84	1.24345		3.53	144999
107675	ZtautauN5p	AlpgenJimmy	0.76	1.24345		0.95	45000
107710	ZnunuNp0	AlpgenJimmy	3572	1.2604	0.011091	49.93	54949
107711	ZnunuNp1	AlpgenJimmy	738.73	1.2604	0.6112	569.09	909848
107712	ZnunuNp2	AlpgenJimmy	222.91	1.2604	0.88158	247.68	169899
107713	ZnunuNp3	AlpgenJimmy	61.874	1.2604	0.96751	75.45	144999
107714	ZnunuNp4	AlpgenJimmy	15.635	1.2604	0.99205	19.55	309899
107715	ZnunuNp5	AlpgenJimmy	4.3094	1.2604	0.99854	5.42	189998

Table A.2: Simulated $Z+$jets Monte Carlo samples with their corresponding sample ID, event generator, LO cross section, k-factor, filter efficiency, NNLO cross section [227], and number of generated events.

Sample ID	Generator	Final state	NLO [pb]	No. of events
105921	McAtNlo_JIMMY	$W^+W^- \to e\nu e\nu$	0.51	199949
105922	McAtNlo_JIMMY	$W^+W^- \to e\nu\mu\nu$	0.51	200000
105923	McAtNlo_JIMMY	$W^+W^- \to e\nu\tau\nu$	0.51	200000
105924	McAtNlo_JIMMY	$W^+W^- \to \mu\nu\mu\nu$	0.51	199000
105925	McAtNlo_JIMMY	$W^+W^- \to \mu\nu e\nu$	0.51	199949
105926	McAtNlo_JIMMY	$W^+W^- \to \mu\nu\tau\nu$	0.51	200000
105927	McAtNlo_JIMMY	$W^+W^- \to \tau\nu\tau\nu$	0.51	499676
105928	McAtNlo_JIMMY	$W^+W^- \to \tau\nu e\nu$	0.51	199950
105929	McAtNlo_JIMMY	$W^+W^- \to \tau\nu\mu\nu$	0.51	200000
105930	McAtNlo_JIMMY	$ZZ \to \ell\ell q\bar{q}$	0.270	25000
105931	McAtNlo_JIMMY	$ZZ \to \ell\ell\ell\ell$	0.026	99999
105932	McAtNlo_JIMMY	$ZZ \to \ell\ell\nu\nu$	0.077	99999
106036	McAtNlo_JIMMY	$ZZ \to 2\ell 2\tau$	1.695	25000
106037	McAtNlo_JIMMY	$ZZ \to 4\tau$	0.164	25000
113192	McAtNlo_JIMMY	$ZZ \to \tau\tau\nu\nu$	0.514	24950
113193	McAtNlo_JIMMY	$ZZ \to \tau\tau q\bar{q}$	0.928	25000
105940	McAtNlo_JIMMY	$W^+Z \to \ell\nu q\bar{q}$	0.090	100000
105941	McAtNlo_JIMMY	$W^+Z \to \ell\nu\ell\ell$	0.28	100000
105942	McAtNlo_JIMMY	$W^+Z \to q\bar{q}'\ell\ell$	0.086	25000
106024	McAtNlo_JIMMY	$W^+Z \to \tau\nu\ell\ell$	0.082	25000
106025	McAtNlo_JIMMY	$W^+Z \to \ell\nu\tau\tau$	0.043	199950
106026	McAtNlo_JIMMY	$W^+Z \to \tau\nu\tau\tau$	0.047	25000
113190	McAtNlo_JIMMY	$W^+Z \to q\bar{q}'\tau\tau$	0.045	25000
105970	McAtNlo_JIMMY	$W^-Z \to \ell\nu q\bar{q}$	0.0234	200000
105971	McAtNlo_JIMMY	$W^-Z \to \ell\nu\ell\ell$	0.0129	25000
105972	McAtNlo_JIMMY	$W^-Z \to q\bar{q}'\ell\ell$	0.0065	25000
106027	McAtNlo_JIMMY	$W^-Z \to \tau\nu\ell\ell$	0.2568	199949
106028	McAtNlo_JIMMY	$W^-Z \to \ell\nu\tau\tau$	0.1397	200000
106029	McAtNlo_JIMMY	$W^-Z \to \tau\nu\tau\tau$	0.0386	200000
113191	McAtNlo_JIMMY	$W^-Z \to q\bar{q}'\tau\tau$	0.1348	199950

Table A.3: Simulated diboson Monte Carlo samples with their corresponding sample ID, event generator, final state, NLO cross section, and number of generated events.

Sample ID	Name	Generator	LO [pb]	No. of events
105009	J0	Pythia	12030000000	999997
105010	J1	Pythia	807266000	999993
105011	J2	Pythia	48048000	999999
105012	J3	Pythia	2192900	999992
105013	J4	Pythia	87701	989992
105014	J5	Pythia	2350.1	999987
105015	J6	Pythia	33.61	999974
105016	J7	Pythia	0.13744	998955
105017	J8	Pythia	0.000006	998948

Table A.4: Simulated dijet Monte Carlo samples with their corresponding sample ID, event generator, cross section and number of generated events.

Sample ID	Name	Generator	LO [pb]	k-factor	NNLO [pb]	# events
116250	ZeeNp0Mll10to40	AlpgenJimmy	3054.7	1.24345	3798.37	994949
49 116251	ZeeNp1Mll10to40	AlpgenJimmy	84.91	1.24345	105.58	299998
116252	ZeeNp2Mll10to40	AlpgenJimmy	41.19	1.24345	51.22	999946
116253	ZeeNp3Mll10to40	AlpgenJimmy	8.35	1.24345	10.38	149998
116254	ZeeNp4Mll10to40	AlpgenJimmy	1.85	1.24345	2.30	40000
116255	ZeeNp5Mll10to40	AlpgenJimmy	0.46	1.24345	0.57	10000
116260	ZmumuNp0Mll10to40	AlpgenJimmy	3054.9	1.24345	3798.62	999849
49 116261	ZmumuNp1Mll10to40	AlpgenJimmy	84.78	1.24345	105.42	300000
116262	ZmumuNp2Mll10to40	AlpgenJimmy	41.13	1.24345	51.14	999995
116263	ZmumuNp3Mll10to40	AlpgenJimmy	8.34	1.24345	10.37	150000
116264	ZmumuNp4Mll10to40	AlpgenJimmy	1.87	1.24345	2.33	39999
116265	ZmumuNp5Mll10to40	AlpgenJimmy	0.46	1.24345	0.57	10000
116270	ZtautauNp0Mll10to40	AlpgenJimmy	3054.8	1.24345	3798.49	999649
49 116271	ZtautauNp1Mll10to40	AlpgenJimmy	84.88	1.24345	105.54	299999
116272	ZtautauNp2Mll10to40	AlpgenJimmy	41.28	1.24345	51.33	498899
116273	ZtautauNp3Mll10to40	AlpgenJimmy	8.35	1.24345	10.38	150000
116274	ZtautauNp4Mll10to40	AlpgenJimmy	1.83	1.24345	2.28	39999
116275	ZtautauNp5Mll10to40	AlpgenJimmy	0.46	1.24345	0.57	10000

Table A.5: Simulated Drell-Yan Monte Carlo samples with their corresponding sample ID, event generator, LO cross section, k-factor, NNLO cross section [227], and number of generated events.

Sample ID	Name	Generator	NLO [pb]	k-factor	NNLO [pb]	No. of events
105200	$t\bar{t}$ semileptonic (T1)	MCAtNLOJimmy	79.01	1.146	90.57	14983835
105204	$t\bar{t}$ full hadronic	MCAtNLOJimmy	66.48	1.146	76.23	1199034
117360	t-channel $t \to e\nu$	AcerMCPythia	8.06	0.865	6.97	999295
117361	t-channel $t \to \mu\nu$	AcerMCPythia	8.06	0.865	6.97	999948
117362	t-channel $t \to \tau\nu$	AcerMCPythia	8.05	0.855	6.97	998995
108343	s-channel $t \to e\nu$	MCAtNLOJimmy	0.47	1.064	0.50	299948
108344	s-channel $t \to \mu\nu$	MCAtNLOJimmy	0.47	1.064	0.50	299998
108345	s-channel $t \to \tau\nu$	MCAtNLOJimmy	0.47	1.064	0.50	299899
108346	single top Wt	MCAtNLOJimmy	14.79	1.064	15.74	899694

Table A.6: Simulated $t\bar{t}$ and single t Monte Carlo samples with their corresponding sample ID, event generator, NLO cross section [227] and number of generated events.

Sample ID	Name	Generator	NLO [pb]	k-factor	NNLO [pb]	No. of events
105890	ttbarlnlnNp0	AlpgenJimmy	3.466	1.69	5.86	194499
105891	ttbarlnlnNp1	AlpgenJimmy	3.3987	1.69	5.74	159999
105892	ttbarlnlnNp2	AlpgenJimmy	2.1238	1.69	3.59	336897
117897	ttbarlnlnNp3	AlpgenJimmy	0.94698	1.69	1.60	148000
117898	ttbarlnlnNp4	AlpgenJimmy	0.33409	1.69	0.56	60000
117899	ttbarlnlnNp5	AlpgenJimmy	0.12753	1.69	0.22	25000
105894	ttbarlnqqNp0	AlpgenJimmy	13.764	1.77	24.36	647396
105895	ttbarlnqqNp1	AlpgenJimmy	13.608	1.77	24.09	652997
105896	ttbarlnqqNp2	AlpgenJimmy	8.4181	1.77	14.90	1145892
117887	ttbarlnqqNp3	AlpgenJimmy	3.7759	1.77	6.68	652495
117888	ttbarlnqqNp4	AlpgenJimmy	1.3361	1.77	2.36	118999
117889	ttbarlnqqNp5	AlpgenJimmy	0.50399	1.77	0.89	79997

Table A.7: Alternative simulated $t\bar{t}$ samples with their corresponding sample ID, event generator, NLO cross section [227] and number of generated events. Used for studies of systematic uncertainties.

Sample ID	Generator	Final state	NLO [pb]	No. of events
125950	Sherpa	Ztoee2JetsEW2JetsQCD15GeVM40	0.44702	199999
125951	Sherpa	Ztomm2JetsEW2JetsQCD15GeVM40	0.44585	181200
125952	Sherpa	Ztott2JetsEW2JetsQCD15GeVM40	0.44445	199899
125956	Sherpa	Ztoee2JetsEW2JetsQCD15GeVM07to40	0.47727	100000
125957	Sherpa	Ztomm2JetsEW2JetsQCD15GeVM07to40	0.47712	100000
125958	Sherpa	Ztott2JetsEW2JetsQCD15GeVM07to40	0.46924	99900
128810	Sherpa	WWlnulnu	2.9832	1999697
128811	Sherpa	WZlllnu	0.36164	299950
128812	Sherpa	WZlllnuLowMass	1.0209	299949
128813	Sherpa	ZZllll	0.26622	100000
128814	Sherpa	ZZllnn	0.23838	349900
143062	Sherpa	WZlnnn	0.71868	100000
143063	Sherpa	WZqqnn	1.4249	99900
143064	Sherpa	Wtolnu2JetsEW1JetQCD	24.537	99900
143065	Sherpa	Ztonunu2JetsEW1JetQCD	1.3368	99999

Table A.8: Alternative simulated diboson Monte Carlo samples with their corresponding sample ID, event generator, final state, NLO cross section, and number of generated events. Used for studies of systematic uncertainties.

A.2 Signal Acceptance and Efficiency

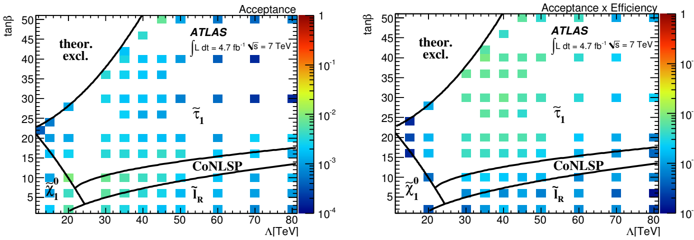

(a) Acceptance (b) Acceptance × efficiency

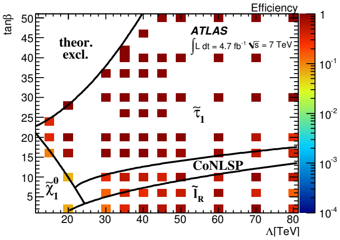

(c) Efficiency

Figure A.1: Acceptance, efficiency and acceptance × efficiency for the 7 TeV analysis [1].

A.3 Event Displays

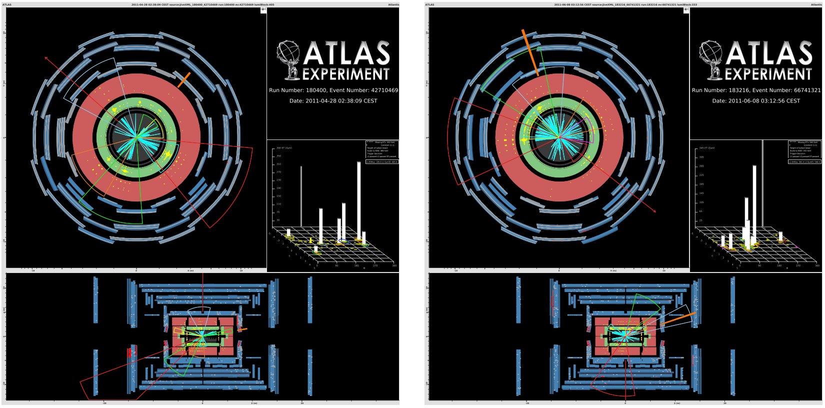

(a) Run #: 180400, Event #: 42710469 (b) Run #: 183216, Event #: 66741321

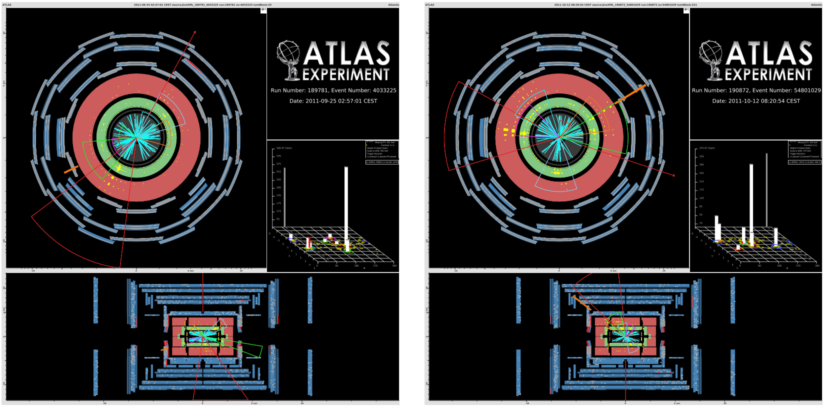

(c) Run #: 189781, Event #: 4033225 (d) Run #: 190872, Event #: 54801029

Figure A.2: Event displays for the signal region events observed in the data for the 7 TeV analysis [1]. Jets are shown as cones, and the τ jet is additionally indicated by a thick orange line. The red arrow illustrates the $E_{\mathrm{T}}^{\mathrm{miss}}$ observed in the event.

A.4 Exclusion Limit Comparisons

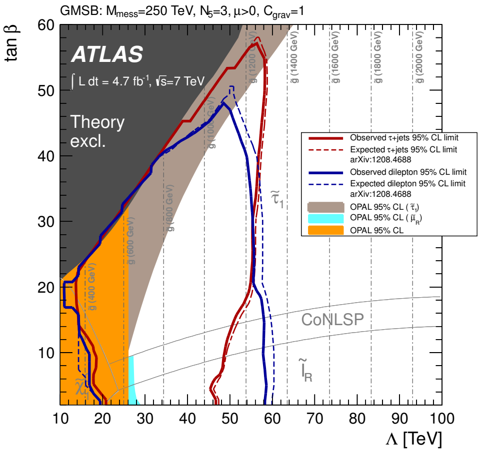

(a) two lepton comparison

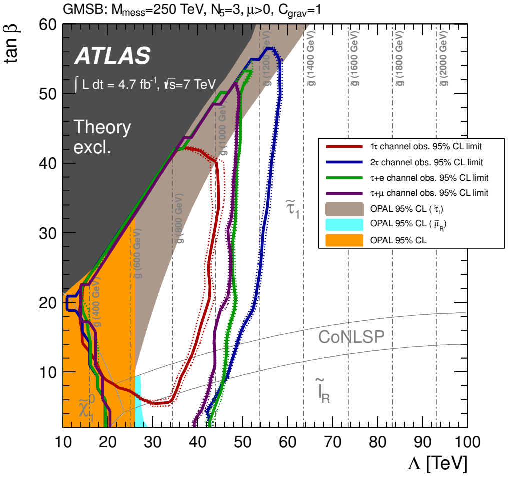

(b) Individual limits

Figure A.3: Comparison of 95% CL exclusion limits. Comparison between combined τ limits and two lepton analysis limits (top) [173], and individual τ limits (bottom) [1].

Appendix B

Additional Material for the 8 TeV ATLAS Analysis

B.1 Monte Carlo Samples

Sample ID	Name	Generator	xsec [pb]	k-factor	filter eff.	No. of events
117050	ttbar NoAllHad	PowhegPythia+AFII	253.00	1	0.543	74947917
108343	SingleTopSChanWenu	McAtNloJimmy	0.56	1.074	1.0	169183
108344	SingleTopSChanWmunu	McAtNloJimmy	0.56	1.074	1.0	169100
108345	SingleTopSChanWtaunu	McAtNloJimmy	0.56	1.074	1.0	169061
108346	SingleTopWtChanIncl	McAtNloJimmy	20.57	1.083	1.0	1766958
117360	t-channel $t \to e\nu$	AcerMCPythia	8.60	1.10	1.0	256853
117361	t-channel $t \to \mu\nu$	AcerMCPythia	8.60	1.10	1.0	256914
117362	t-channel $t \to \tau\nu$	AcerMCPythia	8.60	1.10	1.0	251341

Table B.1: Baseline $t\bar{t}$ and single t MC samples with their corresponding sample ID, event generator, cross section[228], k-factor, filter efficiency and number of generated events.

Sample ID	Name	Generator	LO [pb]	k-factor	No. of events
164440	ttbarlnlnNp0__baseline	AlpgenJimmy	4.7930	1.737	799897
164441	ttbarlnlnNp1__baseline	AlpgenJimmy	5.0680	1.737	808897
164442	ttbarlnlnNp2__baseline	AlpgenJimmy	3.2570	1.737	529996
164444	ttbarlnlnNp3__baseline	AlpgenJimmy	1.5211	1.737	410000
164445	ttbarlnlnNp4p__baseline	AlpgenJimmy	0.7710	1.737	187997
164450	ttbarlnqqNp0__baseline	AlpgenJimmy	19.190	1.809	3359080
164451	ttbarlnqqNp1__baseline	AlpgenJimmy	20.290	1.809	3398787
164452	ttbarlnqqNp2__baseline	AlpgenJimmy	13.090	1.809	2209980
164454	ttbarlnqqNp3__baseline	AlpgenJimmy	6.0815	1.809	1499794
164455	ttbarlnqqNp4p__baseline	AlpgenJimmy	3.0844	1.809	556989
116108	ttbbincl	AlpgenJimmy	1.4345	1.689	299998
116109	ttccincl	AlpgenJimmy	2.7150	1.689	499997

Table B.2: Alternative $t\bar{t}$ samples with their corresponding sample ID, event generator, NLO cross section and number of generated events.

Sample ID	Name	$p_{\mathrm{T}}^{\mathrm{low}}$ [GeV]	$p_{\mathrm{T}}^{\mathrm{high}}$ [GeV]	Flavor Filter	AFII/FS	NLO [pb]	k-factor	filter eff.	No. of events
167749	Zee	0		BFilter	AFII	1110.7	1.12	0.028034	3999000
167750	Zee	0		CFilterBVeto	AFII	1109.6	1.12	0.28341	2999995
167751	Zee	0		CVetoBVeto	AFII	1107.1	1.12	0.68621	4978999
167752	Zmumu	0		BFilter	AFII	1109.8	1.12	0.027996	3997997
167753	Zmumu	0		CFilterBVeto	AFII	1112	1.12	0.28307	2987995
167754	Zmumu	0		CVetoBVeto	AFII	1108.7	1.12	0.6897	4413999
167755	Ztautau	0		BFilter	AFII	1109.1	1.12	0.02782	3997994
167756	Ztautau	0		CFilterBVeto	AFII	1110.2	1.12	0.28373	2998998
167757	Ztautau	0		CVetoBVeto	AFII	1112.1	1.12	0.68884	4979999
167758	Znunu	0		BFilter	AFII	5990.8	1.12	0.029387	24992972
167759	Znunu	0		CFilterBVeto	AFII	5988.3	1.12	0.28017	19957480
167760	Znunu	0		CVetoBVeto	AFII	5987.5	1.12	0.69045	23359980
180543	Zee	40	70	BFilter	AFII	70.493	1.12	0.070638	600000
180544	Zee	40	70	CFilterBVeto	AFII	70.53	1.12	0.34197	600000
180545	Zee	40	70	CVetoBVeto	AFII	70.431	1.12	0.58761	1049998
180546	Zmumu	40	70	BFilter	AFII	70.511	1.12	0.070707	599000
180547	Zmumu	40	70	CFilterBVeto	AFII	70.469	1.12	0.34141	599000
180548	Zmumu	40	70	CVetoBVeto	AFII	70.534	1.12	0.58768	1398999
180549	Ztautau	40	70	BFilter	AFII	70.441	1.12	0.070859	598999
180550	Ztautau	40	70	CFilterBVeto	AFII	70.538	1.12	0.34163	600000
180551	Ztautau	40	70	CVetoBVeto	AFII	70.528	1.12	0.58755	1399996
167797	Zee	70	140	BFilter	AFII	29.494	1.12	0.082517	1396999
167798	Zee	70	140	CFilterBVeto	AFII	29.487	1.12	0.35497	999999
167799	Zee	70	140	CVetoBVeto	AFII	29.491	1.12	0.56262	1999998
167800	Zmumu	70	140	BFilter	AFII	29.491	1.12	0.082585	1159000
167801	Zmumu	70	140	CFilterBVeto	AFII	29.447	1.12	0.35488	1000000
167802	Zmumu	70	140	CVetoBVeto	AFII	29.521	1.12	0.56196	1996998
167803	Ztautau	70	140	BFilter	FS	29.489	1.12	0.082563	1199396
167804	Ztautau	70	140	CFilterBVeto	FS	29.499	1.12	0.35509	979998
167805	Ztautau	70	140	CVetoBVeto	FS	29.494	1.12	0.56247	1999693
167806	Znunu	70	140	BFilter	AFII	166.63	1.12	0.084058	5078993
167807	Znunu	70	140	CFilterBVeto	AFII	166.64	1.12	0.35211	2998998
167808	Znunu	70	140	CVetoBVeto	AFII	166.62	1.12	0.5636	4999996
167809	Zee	140	280	BFilter	AFII	3.9901	1.12	0.095235	200000
167810	Zee	140	280	CFilterBVeto	AFII	3.9811	1.12	0.36919	399999
167811	Zee	140	280	CVetoBVeto	AFII	3.989	1.12	0.53431	600000
167812	Zmumu	140	280	BFilter	AFII	3.9842	1.12	0.095389	200000
167813	Zmumu	140	280	CFilterBVeto	AFII	3.9911	1.12	0.36999	389000
167814	Zmumu	140	280	CVetoBVeto	AFII	3.9841	1.12	0.53441	599500
167815	Ztautau	140	280	BFilter	FS	3.9878	1.12	0.095807	199900
167816	Ztautau	140	280	CFilterBVeto	FS	3.988	1.12	0.36953	399999
167817	Ztautau	140	280	CVetoBVeto	FS	3.9871	1.12	0.53328	598897
167818	Znunu	140	280	BFilter	AFII	22.512	1.12	0.096855	1000000
167819	Znunu	140	280	CFilterBVeto	AFII	22.52	1.12	0.36786	1989998
167820	Znunu	140	280	CVetoBVeto	AFII	22.514	1.12	0.53462	2979999

Table B.3: Baseline Sherpa Z+jets MC samples with their corresponding sample ID, event generator, p_{T}slices, flavor filter, detector simulation, NLO cross section, k-factor, filter efficiency and number of generated events. (continued in table B.4)

Sample ID	Name	$p_{\mathrm{T}}^{\mathrm{low}}$ [GeV]	$p_{\mathrm{T}}^{\mathrm{high}}$ [GeV]	Flavor Filter	AFII/FS	NLO [pb]	k-factor	filter eff.	No. of events
167821	Zee	280	500	BFilter	FS	0.24182	1.12	0.10851	20000
167822	Zee	280	500	CFilterBVeto	FS	0.24128	1.12	0.38744	49899
167823	Zee	280	500	CVetoBVeto	FS	0.24158	1.12	0.50617	39999
167824	Zmumu	280	500	BFilter	FS	0.24219	1.12	0.10802	19900
167825	Zmumu	280	500	CFilterBVeto	FS	0.24169	1.12	0.38643	50000
167826	Zmumu	280	500	CVetoBVeto	FS	0.24272	1.12	0.50549	50000
167827	Ztautau	280	500	BFilter	FS	0.2412	1.12	0.10653	19999
167828	Ztautau	280	500	CFilterBVeto	FS	0.24102	1.12	0.38481	50000
167829	Ztautau	280	500	CVetoBVeto	FS	0.24147	1.12	0.5072	49899
167830	Znunu	280	500	BFilter	FS	1.3533	1.12	0.10893	199999
167831	Znunu	280	500	CFilterBVeto	FS	1.3555	1.12	0.38402	239999
167832	Znunu	280	500	CVetoBVeto	FS	1.3527	1.12	0.50667	999892
167833	Zee	500		Bfilter	FS	0.013235	1.12	0.11573	9600
167834	Zee	500		CFilterBVeto	FS	0.013454	1.12	0.39846	10000
167835	Zee	500		CVetoBVeto	FS	0.013307	1.12	0.4848	50000
167836	Zmumu	500		BFilter	FS	0.013161	1.12	0.11408	10000
167837	Zmumu	500		CfilterBVeto	FS	0.01348	1.12	0.39857	10000
167838	Zmumu	500		CVetoBVeto	FS	0.013264	1.12	0.48689	10000
167839	Ztautau	500		BFilter	FS	0.013231	1.12	0.11524	10000
167840	Ztautau	500		CFilterBVeto	FS	0.013308	1.12	0.39316	10000
167841	Ztautau	500		CvetoBVeto	FS	0.013284	1.12	0.48562	50000
167842	Znunu	500		BFilter	FS	0.073103	1.12	0.11776	49999
167843	Znunu	500		CFilterBVeto	FS	0.073347	1.12	0.39631	50000
167844	Znunu	500		CVetoBVeto	FS	0.073278	1.12	0.48436	199699

Table B.4: Baseline Sherpa Z+jets MC samples continued from table B.3.

Sample ID	Name	$p_{\mathrm{T}}^{\mathrm{low}}$ [GeV]	$p_{\mathrm{T}}^{\mathrm{high}}$ [GeV]	Flavor Filter	AFII/FS	NLO [pb]	k-factor	filter eff.	No. of events
167740	Wenu	0		BFilter	AFII	10973	1.11	0.012778	14977980
167741	Wenu	0		CFilterBVeto	AFII	10971	1.11	0.049039	9998989
167742	Wenu	0		CVetoBVeto	AFII	10987	1.11	0.93804	48415976
167743	Wmunu	0		BFilter	AFII	10973	1.11	0.012823	14989485
167744	Wmunu	0		CFilterBVeto	AFII	10970	1.11	0.04254	9872485
167745	Wmunu	0		CVetoBVeto	AFII	10981	1.11	0.94461	48856968
167746	Wtaunu	0		BFilter	AFII	10974	1.11	0.012791	14850862
167747	Wtaunu	0		CFilterBVeto	AFII	10971	1.11	0.046082	9993984
167748	Wtaunu	0		CVetoBVeto	AFII	10969	1.11	0.94065	49640972

Table B.5: Baseline Sherpa W+jets MC samples with their corresponding sample ID, event generator, p_{T}slices, flavor filter, detector simulation, NLO cross section, k-factor, filter efficiency and number of generated events. (continued in table B.6)

Sample ID	Name	$p_\mathrm{T}^\mathrm{low}$ [GeV]	$p_\mathrm{T}^\mathrm{high}$ [GeV]	Flavor Filter	AFII/FS	NLO [pb]	k-factor	filter eff.	No. of events
180534	Wenu	40	70	BFilter	AFII	652.82	1.11	0.034473	1100000
180535	Wenu	40	70	CFilterBVeto	AFII	652.83	1.11	0.17142	899999
180536	Wenu	40	70	CVetoBVeto	AFII	653.16	1.11	0.79335	16947492
180537	Wmunu	40	70	BFilter	AFII	652.73	1.11	0.034565	1097999
180538	Wmunu	40	70	CFilterBVeto	AFII	653.14	1.11	0.16599	900000
180539	Wmunu	40	70	CVetoBVeto	AFII	653.06	1.11	0.79983	16978984
180540	Wtaunu	40	70	BFilter	AFII	652.84	1.11	0.034574	1099999
180541	Wtaunu	40	70	CFilterBVeto	AFII	652.58	1.11	0.16931	889999
180542	Wtaunu	40	70	CVetoBVeto	AFII	652.99	1.11	0.79616	15166494
167761	Wenu	70	140	BFilter	AFII	250.55	1.11	0.045931	2000000
167762	Wenu	70	140	CFilterBVeto	AFII	250.71	1.11	0.20099	2996497
167763	Wenu	70	140	CVetoBVeto	AFII	250.43	1.11	0.75298	14908986
167764	Wmunu	70	140	BFilter	AFII	250.55	1.11	0.045919	1988999
167765	Wmunu	70	140	CFilterBVeto	AFII	250.57	1.11	0.19889	2995999
167766	Wmunu	70	140	CVetoBVeto	AFII	250.77	1.11	0.75855	14931984
167767	Wtaunu	70	140	BFilter	FS	250.57	1.11	0.045942	1999893
167768	Wtaunu	70	140	CFilterBVeto	FS	250.61	1.11	0.19889	2999890
167769	Wtaunu	70	140	CVetoBVeto	FS	250.6	1.11	0.75485	14928649
167770	Wenu	140	280	BFilter	AFII	31.155	1.11	0.063159	999999
167771	Wenu	140	280	CFilterBVeto	AFII	31.189	1.11	0.22196	1999997
167772	Wenu	140	280	CVetoBVeto	AFII	31.112	1.11	0.71496	2000000
167773	Wmunu	140	280	BFilter	AFII	31.164	1.11	0.063069	997497
167774	Wmunu	140	280	CFilterBVeto	AFII	31.165	1.11	0.21647	1985998
167775	Wmunu	140	280	CVetoBVeto	AFII	31.173	1.11	0.7203	1993999
167776	Wtaunu	140	280	BFilter	FS	31.162	1.11	0.063078	989797
167777	Wtaunu	140	280	CFilterBVeto	FS	31.151	1.11	0.22015	1998688
167778	Wtaunu	140	280	CVetoBVeto	FS	31.176	1.11	0.71609	1999994
167779	Wenu	280	500	BFilter	FS	1.8413	1.11	0.082886	99998
167780	Wenu	280	500	CFilterBVeto	FS	1.837	1.11	0.23454	199898
167781	Wenu	280	500	CVetoBVeto	FS	1.8426	1.11	0.682	499891
167782	Wmunu	280	500	BFilter	FS	1.838	1.11	0.082902	100000
167783	Wmunu	280	500	CFilterBVeto	FS	1.8395	1.11	0.22845	199998
167784	Wmunu	280	500	CVetoBVeto	FS	1.8433	1.11	0.68776	499698
167785	Wtaunu	280	500	BFilter	FS	1.8362	1.11	0.083026	100000
167786	Wtaunu	280	500	CFilterBVeto	FS	1.8395	1.11	0.23271	199998
167787	Wtaunu	280	500	CVetoBVeto	FS	1.8368	1.11	0.68397	499998
167788	Wenu	500		BFilter	FS	0.10188	1.11	0.099655	10000
167789	Wenu	500		CFilterBVeto	FS	0.10101	1.11	0.2444	10000
167790	Wenu	500		CVetoBVeto	FS	0.10093	1.11	0.65741	10000
167791	Wmunu	500		BFilter	FS	0.10163	1.11	0.10004	10000
167792	Wmunu	500		CFilterBVeto	FS	0.1021	1.11	0.23852	10000
167793	Wmunu	500		CVetoBVeto	FS	0.10186	1.11	0.65837	49700
167794	Wtaunu	500		BFilter	FS	0.10208	1.11	0.099663	10000
167795	Wtaunu	500		CFilterBVeto	FS	0.10139	1.11	0.24221	10000
167796	Wtaunu	500		CVetoBVeto	FS	0.10201	1.11	0.66004	49998

Table B.6: Baseline Sherpa W+jets MC samples continued from table B.5.

Sample ID	Name	Generator	LO [pb]	k-factor	filter eff.	No. of events
107680	WenuNp0	AlpgenJimmy	8037.1	1.186	1	3459718
107681	WenuNp1	AlpgenJimmy	1579.2	1.186	1	2499797
107682	WenuNp2	AlpgenJimmy	477.2	1.186	1	3769889
107683	WenuNp3	AlpgenJimmy	133.9	1.186	1	1009965
107684	WenuNp4	AlpgenJimmy	35.6	1.186	1	249999
107685	WenuNp5	AlpgenJimmy	10.5	1.186	1	70000
107690	WmunuNp0	AlpgenJimmy	8040.0	1.186	1	3469591
107691	WmunuNp1	AlpgenJimmy	1580.3	1.186	1	2499893
107692	WmunuNp2	AlpgenJimmy	477.5	1.186	1	3769890
107693	WmunuNp3	AlpgenJimmy	133.9	1.186	1	1009896
107694	WmunuNp4	AlpgenJimmy	35.6	1.186	1	255000
107695	WmunuNp5	AlpgenJimmy	10.5	1.186	1	20000
107700	WtaunuNp0	AlpgenJimmy	8035.8	1.186	1	3364789
107701	WtaunuNp1	AlpgenJimmy	1579.8	1.186	1	2449991
107702	WtaunuNp2	AlpgenJimmy	477.5	1.186	1	3719888
107703	WtaunuNp3	AlpgenJimmy	133.7	1.186	1	1009993
107704	WtaunuNp4	AlpgenJimmy	35.5	1.186	1	249898
107705	WtaunuNp5	AlpgenJimmy	10.5	1.186	1	65000
117284	WccNp0	AlpgenJimmy	150.19	1.186	1	1274998
117285	WccNp1	AlpgenJimmy	132.68	1.186	1	1049997
117286	WccNp2	AlpgenJimmy	71.80	1.186	1	552899
117287	WccNp3	AlpgenJimmy	30.26	1.186	1	170000
117293	WcNp0	AlpgenJimmy	807.89	1.186	1	6489181
117294	WcNp1	AlpgenJimmy	267.61	1.186	1	2069695
117295	WcNp2	AlpgenJimmy	69.82	1.186	1	519999
117296	WcNp3	AlpgenJimmy	20.54	1.186	1	110000
117297	WcNp4	AlpgenJimmy	4.30	1.186	1	20000
107280	WbbNp0	AlpgenJimmy	55.68	1.186	1	474999
107281	WbbNp1	AlpgenJimmy	45.24	1.186	1	359999
107282	WbbNp2	AlpgenJimmy	23.24	1.186	1	174999
107283	WbbNp3	AlpgenJimmy	11.14	1.186	1	50000
172001	WenuNp1_susyfilt	AlpgenJimmy	12.70	1.186	1	1999991
172002	WenuNp2_susyfilt	AlpgenJimmy	8.95	1.186	1	1492993
172003	WenuNp3_susyfilt	AlpgenJimmy	4.33	1.186	1	1249989
172004	WenuNp4_susyfilt	AlpgenJimmy	1.70	1.186	1	399498
172005	WenuNp5_susyfilt	AlpgenJimmy	0.55	1.186	1	109899
172006	WenuNp6_susyfilt	AlpgenJimmy	0.19	1.186	1	20000
172011	WmunuNp1_susyfilt	AlpgenJimmy	12.68	1.186	1	1999795
172012	WmunuNp2_susyfilt	AlpgenJimmy	8.96	1.186	1	1499993
172013	WmunuNp3_susyfilt	AlpgenJimmy	4.33	1.186	1	1249296
172014	WmunuNp4_susyfilt	AlpgenJimmy	1.70	1.186	1	399898
172015	WmunuNp5_susyfilt	AlpgenJimmy	0.56	1.186	1	109998
172016	WmunuNp6_susyfilt	AlpgenJimmy	0.19	1.186	1	20000
172021	WtaunuNp1_susyfil	AlpgenJimmy	46.38	1.186	0.3475	3994886
172022	WtaunuNp2_susyfil	AlpgenJimmy	34.30	1.186	0.3349	2794687
172023	WtaunuNp3_susyfil	AlpgenJimmy	17.05	1.186	0.3269	1234793
172024	WtaunuNp4_susyfil	AlpgenJimmy	6.55	1.186	0.3360	549496
172025	WtaunuNp5_susyfil	AlpgenJimmy	2.04	1.186	0.3543	150000
172026	WtaunuNp6_susyfil	AlpgenJimmy	0.66	1.186	0.3812	30000

Table B.7: Alternative W+jets MC samples with their corresponding sample ID, event generator, LO cross section, k-factor, and number of generated events.

Sample ID	Name	Generator	LO [pb]	k-factor	No. of events
107650	ZeeNp0	AlpgenJimmy	711.7700	1.23	6608782
107651	ZeeNp1	AlpgenJimmy	155.1700	1.23	1335000
107652	ZeeNp2	AlpgenJimmy	48.74500	1.23	404499
107653	ZeeNp3	AlpgenJimmy	14.22500	1.23	110000
107654	ZeeNp4	AlpgenJimmy	3.759500	1.23	30000
107655	ZeeNp5	AlpgenJimmy	1.094500	1.23	10000
107660	ZmumuNp0	AlpgenJimmy	712.1100	1.23	6619489
107661	ZmumuNp1	AlpgenJimmy	154.7700	1.23	1334706
107662	ZmumuNp2	AlpgenJimmy	48.91200	1.23	404997
107663	ZmumuNp3	AlpgenJimmy	14.22600	1.23	110000
107664	ZmumuNp4	AlpgenJimmy	3.783800	1.23	30000
107665	ZmumuNp5	AlpgenJimmy	1.114800	1.23	10000
107670	ZtautauNp0	AlpgenJimmy	711.8100	1.23	6619683
107671	ZtautauNp1	AlpgenJimmy	155.1300	1.23	1334996
107672	ZtautauNp2	AlpgenJimmy	48.80400	1.23	404997
107673	ZtautauNp3	AlpgenJimmy	14.16000	1.23	110000
107674	ZtautauNp4	AlpgenJimmy	3.774400	1.23	30000
107675	ZtautauNp5	AlpgenJimmy	1.116300	1.23	10000
126414	ZeeccNp0	AlpgenJimmy	15.65400	1.23	604899
126415	ZeeccNp1	AlpgenJimmy	6.894600	1.23	259999
126416	ZeeccNp2	AlpgenJimmy	2.920400	1.23	109999
126417	ZeeccNp3	AlpgenJimmy	1.141100	1.23	40000
126418	ZmumuccNp0	AlpgenJimmy	15.64900	1.23	599397
126419	ZmumuccNp1	AlpgenJimmy	6.893000	1.23	265000
126420	ZmumuccNp2	AlpgenJimmy	2.917600	1.23	115000
126421	ZmumuccNp3	AlpgenJimmy	1.137700	1.23	39999
117706	ZtautauccNp0	AlpgenJimmy	15.652000	1.23	599999
117707	ZtautauccNp1	AlpgenJimmy	6.897900	1.23	264999
117708	ZtautauccNp2	AlpgenJimmy	2.910000	1.23	115000
117709	ZtautauccNp3	AlpgenJimmy	1.134000	1.23	39999
109300	ZeebbNp0	AlpgenJimmy	8.377700	1.23	150000
109301	ZeebbNp1	AlpgenJimmy	3.252900	1.23	80000
109302	ZeebbNp2	AlpgenJimmy	1.190200	1.23	45000
109303	ZeebbNp3	AlpgenJimmy	0.502780	1.23	4999
109305	ZmumubbNp0	AlpgenJimmy	8.374200	1.23	149900
109306	ZmumubbNp1	AlpgenJimmy	3.254000	1.23	80000
109307	ZmumubbNp2	AlpgenJimmy	1.181000	1.23	45000
109308	ZmumubbNp3	AlpgenJimmy	0.506690	1.23	5000
109310	ZtautaubbNp0	AlpgenJimmy	8.375700	1.23	149900
109311	ZtautaubbNp1	AlpgenJimmy	3.242700	1.23	79999
109312	ZtautaubbNp2	AlpgenJimmy	1.193800	1.23	45000
109313	ZtautaubbNp3	AlpgenJimmy	0.497910	1.23	5000

Table B.8: Alternative Z+jets MC samples for Z decaying to charged leptons listed with their corresponding sample ID, event generator, LO cross section, k-factor, filter efficiency and number of generated events.

Sample ID	Name	Generator	LO [pb]	k-factor	No. of events
147105	ZeeNp0	AlpgenPythia	718.97	1.18	6298988
147106	ZeeNp1	AlpgenPythia	175.7	1.18	8199476
147107	ZeeNp2	AlpgenPythia	58.875	1.18	3175991
147108	ZeeNp3	AlpgenPythia	15.636	1.18	814995
147109	ZeeNp4	AlpgenPythia	4.0116	1.18	348597
147110	ZeeNp5Incl	AlpgenPythia	1.2592	1.18	219700
147113	ZmumuNp0	AlpgenPythia	719.16	1.18	6288796
147114	ZmumuNp1	AlpgenPythia	175.74	1.18	8088384
147115	ZmumuNp2	AlpgenPythia	58.882	1.18	3175488
147116	ZmumuNp3	AlpgenPythia	15.673	1.18	844799
147117	ZmumuNp4	AlpgenPythia	4.0057	1.18	378200
147118	ZmumuNp5Incl	AlpgenPythia	1.2544	1.18	179200
147121	ZtautauNp0	AlpgenPythia	718.87	1.18	16797868
147122	ZtautauNp1	AlpgenPythia	175.76	1.18	10679582
147123	ZtautauNp2	AlpgenPythia	58.856	1.18	3740893
147124	ZtautauNp3	AlpgenPythia	15.667	1.18	1011994
147125	ZtautauNp4	AlpgenPythia	4.0121	1.18	378798
147126	ZtautauNp5Incl	AlpgenPythia	1.256	1.18	209799
200332	ZeebbNp0	AlpgenPythia	0.45959	1.18	1629895
200333	ZeebbNp1	AlpgenPythia	0.33059	1.18	619997
200334	ZeebbNp2	AlpgenPythia	0.14807	1.18	170000
200335	ZeebbNp3Incl	AlpgenPythia	0.079647	1.18	109997
200340	ZmuumbbNp0	AlpgenPythia	0.45871	1.18	1529994
200341	ZmumubbNp1	AlpgenPythia	0.33007	1.18	449700
200342	ZmumubbNp2	AlpgenPythia	0.14886	1.18	219999
200343	ZmumubbNp3Incl	AlpgenPythia	0.079763	1.18	109499
200348	ZtautaubbNp0	AlpgenPythia	0.45949	1.18	259999
200349	ZtautaubbNp1	AlpgenPythia	0.32987	1.18	90000
200350	ZtautaubbNp2	AlpgenPythia	0.14796	1.18	50000
200351	ZtautaubbNp3Incl	AlpgenPythia	0.079949	1.18	50000
200432	ZeeccNp0	AlpgenPythia	0.41161	1.18	279998
200433	ZeeccNp1	AlpgenPythia	0.29829	1.18	169499
200434	ZeeccNp2	AlpgenPythia	0.13703	1.18	100000
200435	ZeeccNp3Incl	AlpgenPythia	0.07637	1.18	50000
200440	ZmuumccNp0	AlpgenPythia	0.4114	1.18	289798
200441	ZmumuccNp1	AlpgenPythia	0.29799	1.18	190000
200442	ZmumuccNp2	AlpgenPythia	0.13717	1.18	90000
200443	ZmumuccNp3Incl	AlpgenPythia	0.07637	1.18	40000
200448	ZtautauccNp0	AlpgenPythia	0.41194	1.18	269999
200449	ZtautauccNp1	AlpgenPythia	0.29787	1.18	159900
200450	ZtautauccNp2	AlpgenPythia	0.13705	1.18	100000
200451	ZtautauccNp3Incl	AlpgenPythia	0.07655	1.18	49999

Table B.9: Alternative Z+jets MC samples for Z decaying to charged leptons listed with their corresponding sample ID, event generator, LO cross section, k-factor and number of generated events.

Sample ID	Name (event generator: AlpgenJimmy)	NLO [pb]	k-factor	filter eff.	No. of events
156803	ZnunuNp0_filt1jet	4151.5	1.23	0.00646	5000
156804	ZnunuNp1_filt1jet	892.4	1.23	0.455	85000
156808	ZnunuNp1_met70_filt1jet	69.51	1.0	0.999	75000
156805	ZnunuNp1_met140_filt1jet	6.032	1.0	1.0	95000
156806	ZnunuNp1_met280_filt1jet	0.243	1.0	1.0	25000
156807	ZnunuNp1_met500_filt1jet	0.00895	1.0	1.0	5000
156809	ZnunuNp2_filt1jet	282.1	1.23	0.761	40000
156813	ZnunuNp2_met70_filt1jet	60.97	1.0	0.991	100000
156810	ZnunuNp2_met140_filt1jet	8.00	1.0	1.0	150000
156811	ZnunuNp2_met280_filt1jet	0.46	1.0	1.0	50000
156812	ZnunuNp2_met500_filt1jet	0.0229	1.0	1.0	13000
156814	ZnunuNp3_filt1jet	82.0	1.23	0.906	15000
156818	ZnunuNp3_met70_filt1jet	27.54	1.0	0.986	75000
156815	ZnunuNp3_met140_filt1jet	5.244	1.0	1.0	110000
156816	ZnunuNp3_met280_filt1jet	0.392	1.0	1.0	50000
156817	ZnunuNp3_met500_filt1jet	0.0227	1.0	1.0	13000
156819	ZnunuNp4_filt1jet	21.6	1.23	0.965	4000
156823	ZnunuNp4_met70_filt1jet	9.432	1.0	0.993	25000
156820	ZnunuNp4_met140_filt1jet	2.347	1.0	1.0	120000
156821	ZnunuNp4_met280_filt1jet	0.220	1.0	1.0	45000
156822	ZnunuNp4_met500_filt1jet	0.0142	1.0	1.0	10000
156824	ZnunuNp5_filt1jet	6.6	1.23	0.989	8000
156828	ZnunuNp5_met70_filt1jet	3.352	1.0	0.998	19000
156825	ZnunuNp5_met140_filt1jet	1.042	1.0	1.0	30000
156826	ZnunuNp5_met280_filt1jet	0.121	1.0	1.0	17000
156827	ZnunuNp5_met500_filt1jet	0.00876	1.0	1.0	4000

Table B.10: Alternative MC samples for Z+jets with the Z decaying to neutrino pairs, generated with AlpgenJimmy and listed with their corresponding sample ID, LO cross section, k-factor, filter efficiency, NNLO cross section,and number of generated events.

Sample ID	Generator	Final state	NLO [pb]	k-factor	No. of events
126892	Sherpa	$W^+W^- \to \ell\nu\ell\nu$	5.50	1.06	2699994
126893	Sherpa	W$^{\pm}Z \to \ell\ell\ell\nu$	9.75	1.05	2699893
126894	Sherpa	$ZZ \to \ell\ell\ell\ell$	8.74	1.00	3799491
126895	Sherpa	$ZZ \to \ell\ell\nu\ell\nu$	0.496	1.05	899899

Table B.11: Baseline diboson MC samples with their corresponding sample ID, event generator, final state, NLO cross section, k-factor and number of generated events.

Sample ID	Name (event generator: Powheg+Pythia8)	NLO [pb]	k-factor	filter eff.	No. of events
126928	WpWm_ee	0.598	1.078	1.000	599700
126929	WpWm_me	0.597	1.079	1.000	600000
126930	WpWm_te	0.598	1.079	1.000	580000
126931	WpWm_em	0.598	1.078	1.000	589999
126932	WpWm_mm	0.597	1.079	1.000	600000
126933	WpWm_tm	0.597	1.079	1.000	599798
126934	WpWm_et	0.597	1.080	1.000	580000
126935	WpWm_mt	0.598	1.079	1.000	599999
126936	WpWm_tt	0.598	1.079	1.000	580000
126937	ZZ_4e_mll4_2pt5	0.077	1.000	0.908	1099997
126938	ZZ_2e2mu_mll4_2pt5	0.176	1.000	0.827	1599696
126939	ZZ_2e2tau_mll4_2pt5	0.175	1.000	0.583	1079798
126940	ZZ_4mu_mll4_2pt5	0.077	1.000	0.912	1099798
126941	ZZ_2mu2tau_mll4_2pt5	0.175	1.000	0.587	1069799
126942	ZZ_4tau_mll4_2pt5	0.077	1.000	0.106	299999
126949	ZZllnunu_ee_mll4	0.054	3.000	1.000	299400
126950	ZZllnunu_mm_mll4	0.054	3.000	1.000	300000
126951	ZZllnunu_tt_mll4	0.054	3.000	1.000	299999
129477	WZ_Wm11Z11_mll0p250d0_2LeptonFilter5	1.407	1.122	0.295	190000
129478	WZ_Wm11Z13_mll0p4614d0_2LeptonFilter5	0.938	1.122	0.352	190000
129479	WZ_Wm11Z15_mll3p804d0_2LeptonFilter5	0.175	1.122	0.167	75999
129480	WZ_Wm13Z11_mll0p250d0_2LeptonFilter5	1.399	1.122	0.294	159999
129481	WZ_Wm13Z13_mll0p4614d0_2LeptonFilter5	0.954	1.122	0.351	190000
129482	WZ_Wm13Z15_mll3p804d0_2LeptonFilter5	0.175	1.122	0.169	76000
129483	WZ_Wm15Z11_mll0p250d0_2LeptonFilter5	1.399	1.122	0.143	70000
129484	WZ_Wm15Z13_mll0p4614d0_2LeptonFilter5	0.938	1.122	0.183	76000
129485	WZ_Wm15Z15_mll3p804d0_2LeptonFilter5	0.172	1.122	0.059	9000
129486	WZ_W11Z11_mll0p250d0_2LeptonFilter5	0.980	1.144	0.297	189899
129487	WZ_W11Z13_mll0p4614d0_2LeptonFilter5	0.639	1.144	0.353	190000
129488	WZ_W11Z15_mll3p804d0_2LeptonFilter5	0.113	1.144	0.160	76000
129489	WZ_W13Z11_mll0p250d0_2LeptonFilter5	0.936	1.144	0.298	190000
129490	WZ_W13Z13_mll0p4614d0_2LeptonFilter5	0.649	1.144	0.354	190000
129491	WZ_W13Z15_mll3p804d0_2LeptonFilter5	0.113	1.144	0.160	76000
129492	WZ_W15Z11_mll0p250d0_2LeptonFilter5	0.936	1.144	0.148	76000
129493	WZ_W15Z13_mll0p4614d0_2LeptonFilter5	0.639	1.144	0.187	75999
129494	WZ_W15Z15_mll3p804d0_2LeptonFilter5	0.111	1.144	0.057	19000
178411	ZZ_2e2tau_mll4_taufilter	0.175	1.000	0.084	100000
178412	ZZ_2mu2tau_mll4_taufilter	0.175	1.000	0.082	100000
178413	ZZ_4tau_mll4_taufilter	0.077	1.000	0.324	299998
179385	WZ_Wm11Z15_mll3p80d40_taufilter	0.175	1.122	0.163	76000
179386	WZ_Wm13Z15_mll3p80d40_taufilter	0.175	1.122	0.164	66000
179387	WZ_Wm15Z11_mll0p250d0_taufilter	1.399	1.122	0.053	19000
179388	WZ_Wm15Z13_mll0p4614d0_taufilter	0.938	1.122	0.058	19000
179389	WZ_Wm15Z15_mll3p804d0_taufilter	0.172	1.122	0.198	19000
179390	WZ_W11Z15_mll3p80d40_taufilter	0.113	1.144	0.151	75999
179391	WZ_W13Z15_mll3p80d40_taufilter	0.113	1.144	0.152	76000
179392	WZ_W15Z11_mll0p250d0_taufilter	0.936	1.144	0.057	19000
179393	WZ_W15Z13_mll0p4614d0_taufilter	0.639	1.144	0.066	19000
179394	WZ_W15Z15_mll3p804d0_taufilter	0.111	1.144	0.183	19000

Table B.12: Alternative Powheg+Pythia8 diboson MC samples with their corresponding sample ID, final state, NLO cross section, k-factor filter efficiency and number of generated events.

Sample ID	Name	Generator	LO [pb]	FE	No. of events
147900	jetjet_JZ0	Pythia8	72.85×10^{9}	0.985	1000000
147901	jetjet_JZ1	Pythia8	72.85×10^{9}	0.014	999877
147902	jetjet_JZ2	Pythia8	26.4×10^{6}	0.108	999996
147903	jetjet_JZ3	Pythia8	544070	0.064	999996
147904	jetjet_JZ4	Pythia8	6445.4	0.031	999777
147905	jetjet_JZ5	Pythia8	39.74	0.034	999609
147906	jetjet_JZ6	Pythia8	0.416	0.063	997663
147907	jetjet_JZ7	Pythia8	0.041	0.015	997854

Table B.13: Baseline multijet MC samples with their corresponding sample ID, event generator, cross section, filter efficiency and number of generated events.

Sample ID	Name	Generator	LO [pb]	k-factor	# events
146830	ZeeNp0Excl_Mll10to60	AlpgenJimmy	3477.2	1.19	999998
146831	ZeeNp1Excl_Mll10to60	AlpgenJimmy	108.8	1.19	299999
146832	ZeeNp2Excl_Mll10to60	AlpgenJimmy	52.8	1.19	469999
146833	ZeeNp3Excl_Mll10to60	AlpgenJimmy	11.3	1.19	144500
146834	ZeeNp4Excl_Mll10to60	AlpgenJimmy	2.59	1.19	36300
146835	ZeeNp5Incl_Mll10to60	AlpgenJimmy	0.693	1.19	79619
146840	ZmumuNp0Excl_Mll10to60	AlpgenJimmy	3477.1	1.19	999999
146841	ZmumuNp1Excl_Mll10to60	AlpgenJimmy	108.7	1.19	299998
146842	ZmumuNp2Excl_Mll10to60	AlpgenJimmy	52.7	1.19	469998
146843	ZmumuNp3Excl_Mll10to60	AlpgenJimmy	11.2	1.19	144499
146844	ZmumuNp4Excl_Mll10to60	AlpgenJimmy	2.60	1.19	36300
146845	ZmumuNp5Incl_Mll10to60	AlpgenJimmy	0.69	1.19	79740
146850	ZtautauNp0Excl_Mll10to60	AlpgenJimmy	3477.1	1.19	999898
146851	ZtautauNp1Excl_Mll10to60	AlpgenJimmy	108.7	1.19	299999
146852	ZtautauNp2Excl_Mll10to60	AlpgenJimmy	52.7	1.19	469999
146853	ZtautauNp3Excl_Mll10to60	AlpgenJimmy	11.33	1.19	144399
146854	ZtautauNp4Excl_Mll10to60	AlpgenJimmy	2.59	1.19	218400
146855	ZtautauNp5Incl_Mll10to60	AlpgenJimmy	0.692	1.19	79979

Table B.14: Drell-Yan samples with their corresponding sample ID, event generator, LO cross section, k-factor, NNLO cross section,and number of generated events.

B.2 Signal Contamination in Background Control Regions

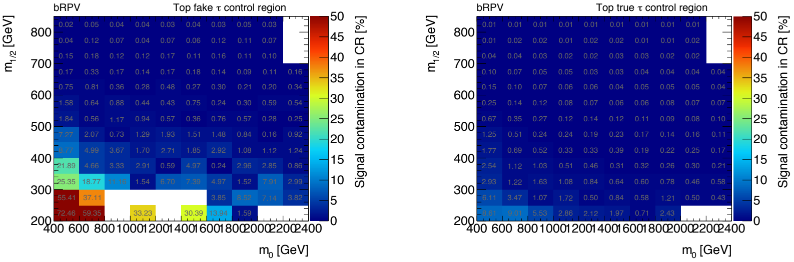

(a) Top fake CR (b) Top true CR

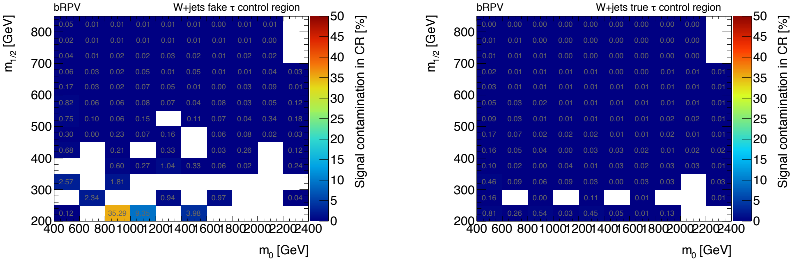

(c) W/Z fake CR (d) W/Z true CR

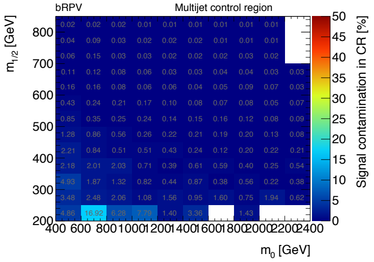

(e) QCD Multijet CR

Figure B.1: Contamination in the Standard Model background control regions from the bRPV grid evaluated in the analysis.

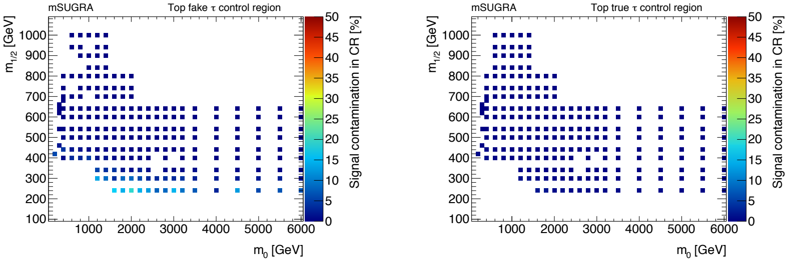

(a) Top fake CR (b) Top true CR

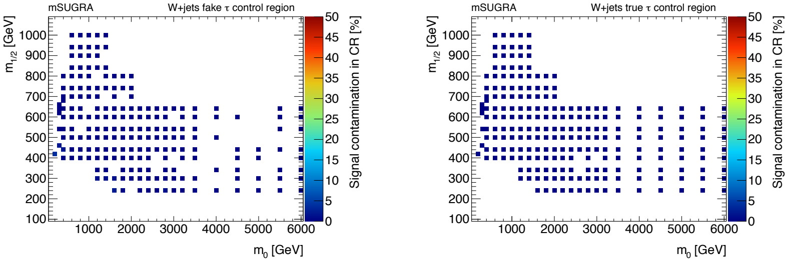

(c) W/Z fake CR (d) W/Z true CR

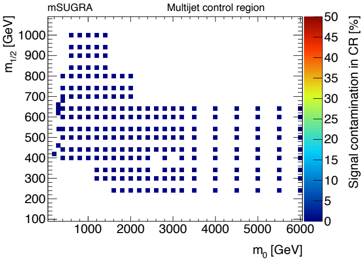

(e) QCD Multijet CR

Figure B.2: Contamination in the Standard Model background control regions from the mSUGRA grid evaluated in the analysis.

B.3 Generator Comparisons

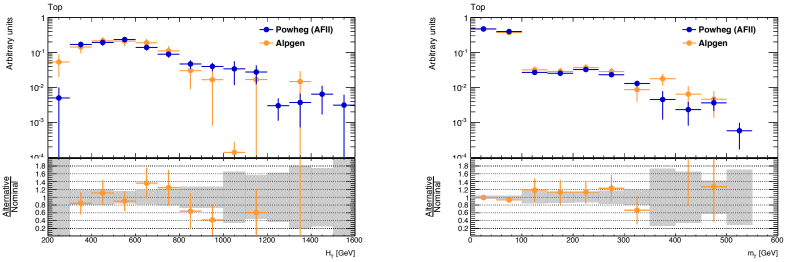

(a) H_{T} (b) m_{T}

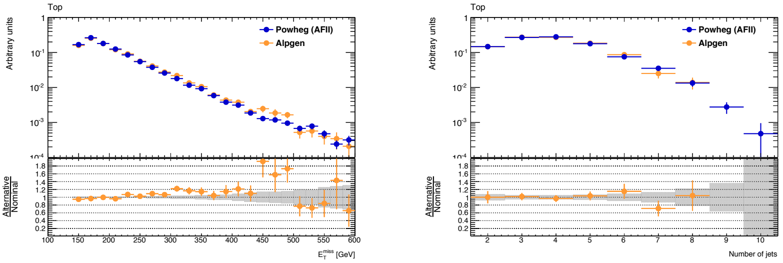

(c) $E_{\mathrm{T}}^{\mathrm{miss}}$ (d) number of jets

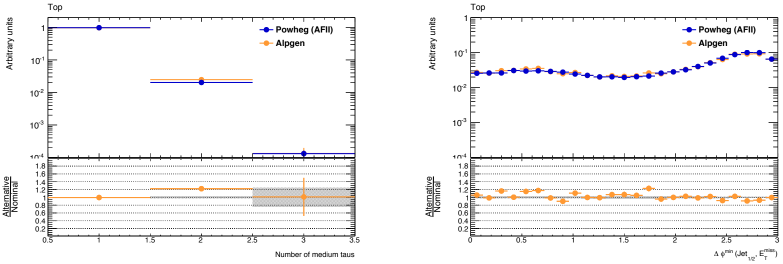

(e) number of τ leptons (f) $\Delta\Phi(\mathrm{jet}, E_{\mathrm{T}}^{\mathrm{miss}})$

Figure B.3: Comparison of the nominal (blue) and alternative (orange) $t\bar{t}$ generators. The distributions are normalised to unity.

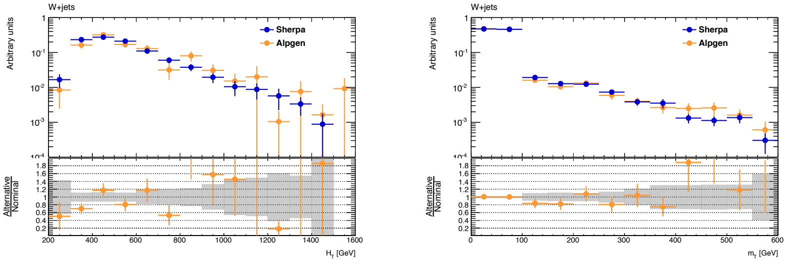

(a) H_{T} (b) m_{T}

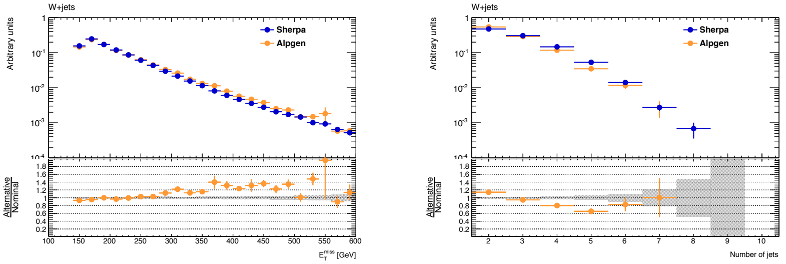

(c) $E_{\mathrm{T}}^{\mathrm{miss}}$ (d) number of jets

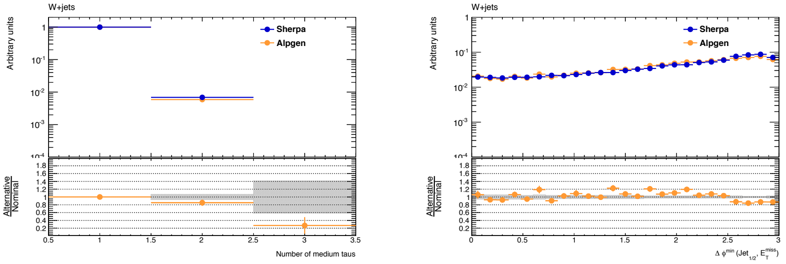

(e) number of τ leptons (f) $\Delta\Phi(\mathrm{jet}, E_{\mathrm{T}}^{\mathrm{miss}})$

Figure B.4: Comparison of the nominal (blue) and alternative (orange) W+jets generators. The distributions are normalised to unity.

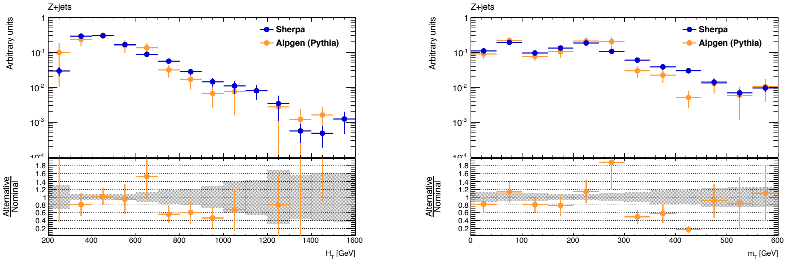

(a) H_{T} (b) m_{T}

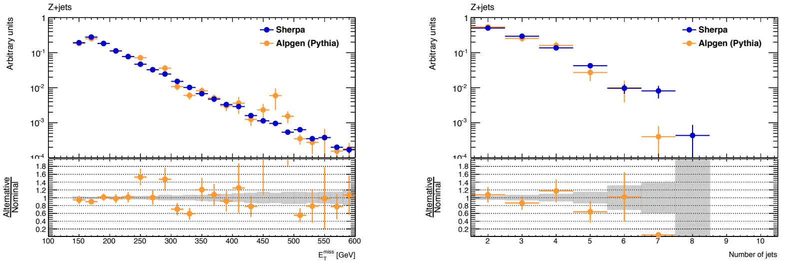

(c) $E_{\mathrm{T}}^{\mathrm{miss}}$ (d) number of jets

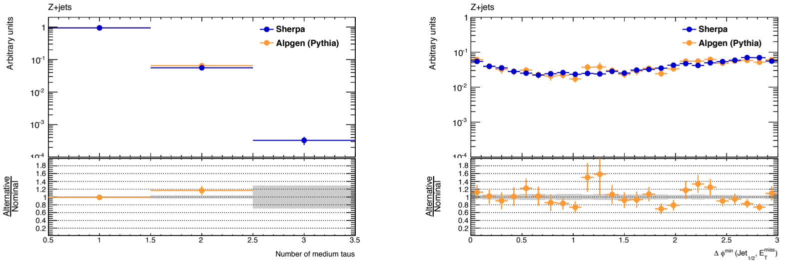

(e) number of τ leptons (f) $\Delta\Phi(\mathrm{jet}, E_{\mathrm{T}}^{\mathrm{miss}})$

Figure B.5: Comparison of the nominal (blue) and alternative (orange) Z+jets generators. The distributions are normalised to unity.

B.4 Signal Efficiency and Acceptance

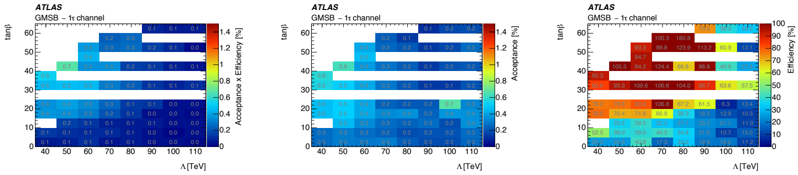

(a) Efficiency × acceptance (b) Acceptance (c) Efficiency

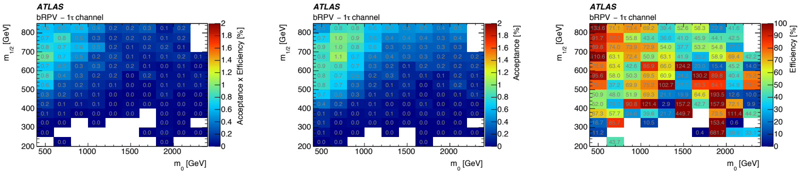

(d) Efficiency × acceptance (e) Acceptance (f) Efficiency

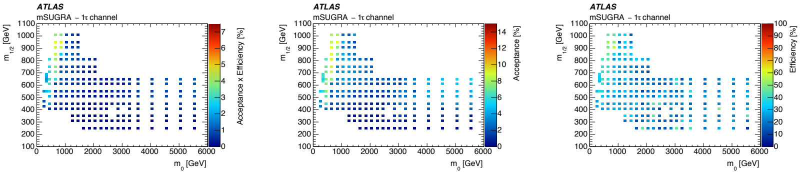

(g) Efficiency × acceptance (h) Acceptance (i) Efficiency

Figure B.6: Signal region selection efficiencies for the tight signal region in the GMSB (top), bRPV (middle) and mSUGRA (bottom) signal grids.

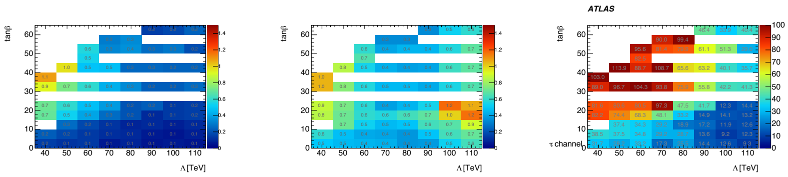

(a) Efficiency × acceptance (b) Acceptance (c) Efficiency

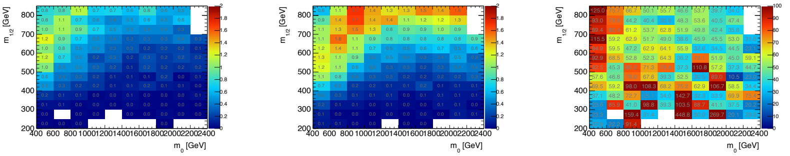

(d) Efficiency × acceptance (e) Acceptance (f) Efficiency

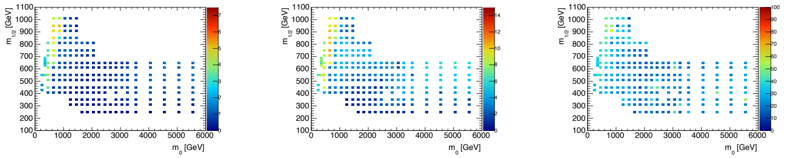

(g) Efficiency × acceptance (h) Acceptance (i) Efficiency

Figure B.7: Signal region selection efficiencies for the loose signal region in the GMSB (top), bRPV (middle) and mSUGRA (bottom) signal grids.

B.5 Signal Uncertainties

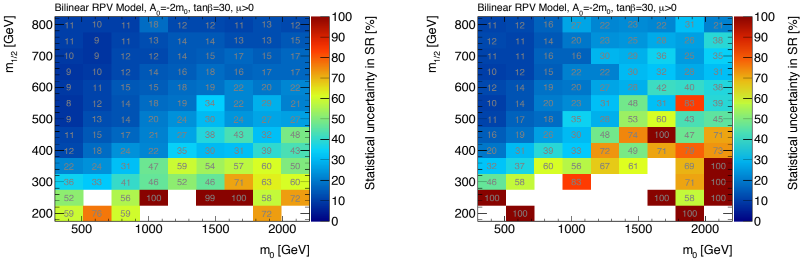

(a) Statistical uncertainty (b) Statistical uncertainty

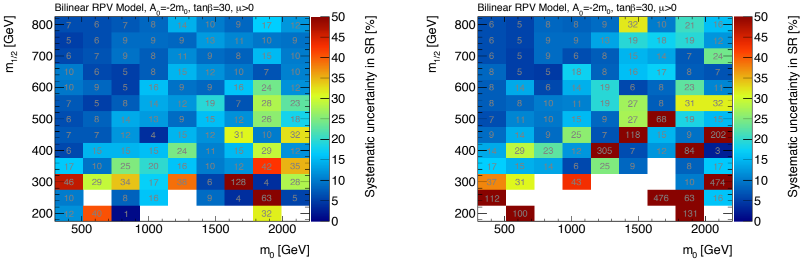

(c) Systematic uncertainty (d) Systematic uncertainty

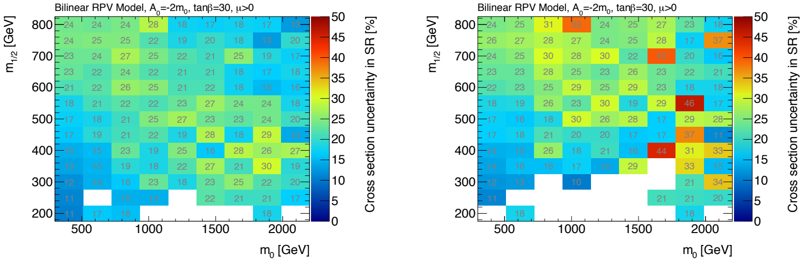

(e) Cross-section uncertainty (f) Cross-section uncertainty

Figure B.8: Relative signal region uncertainties for the bRPV grid. The left hand column show uncertainties in the loose signal region, while the tight signal region uncertainties are to the right.

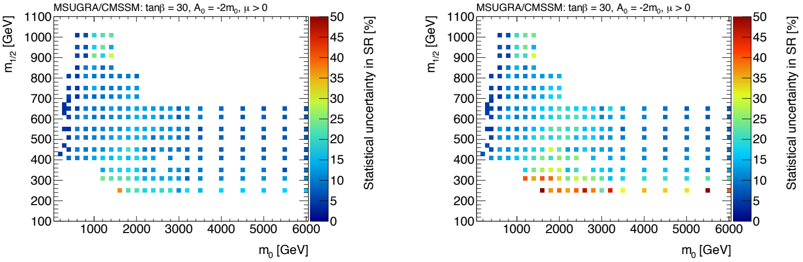

(a) Statistical uncertainty (b) Statistical uncertainty

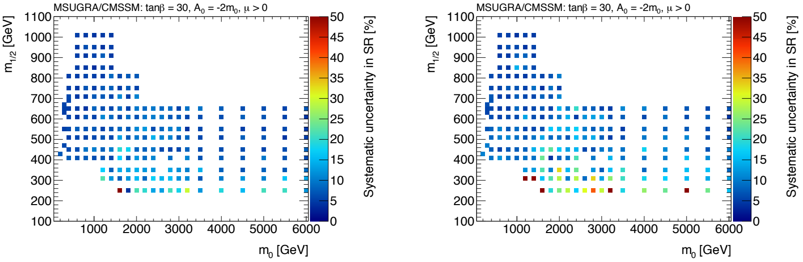

(c) Systematic uncertainty (d) Systematic uncertainty

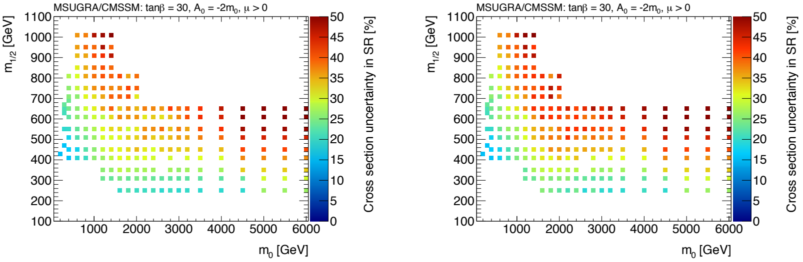

(e) Cross-section uncertainty (f) Cross-section uncertainty

Figure B.9: Relative signal region uncertainties for the mSUGRA grid. The left hand column show uncertainties in the loose signal region, while the tight signal region uncertainties are to the right.

B.6 Event Displays

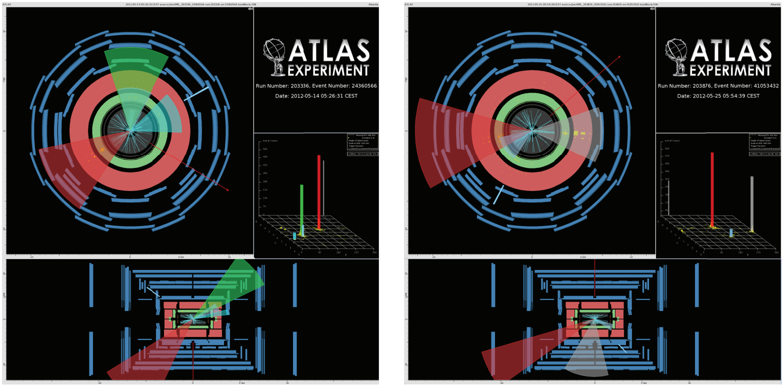

(a) Event #: 203336, Run #: 24360566 (b) Event #: 203876, Run #: 41053432

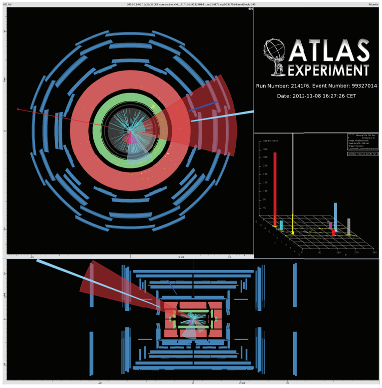

(c) Event #: 214176, Run #: 99327014

Figure B.10: Selected event displays for tight signal regions events observed in the data. Jets are indicated by cones, while the hadronic τ is shown as a thick light blue line. The red arrow illustrates the $E_{\mathrm{T}}^{\mathrm{miss}}$ observed in the event.

B.7 Signal Grid CLs Values

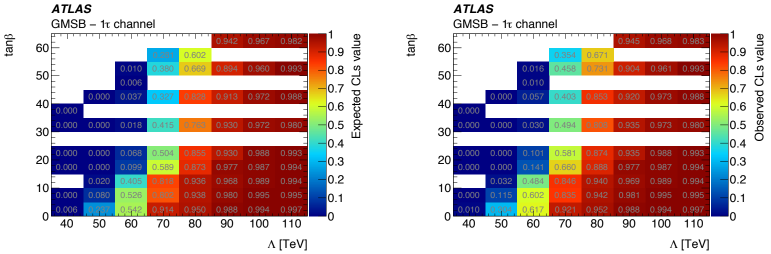

(a) GMSB (b) GMSB

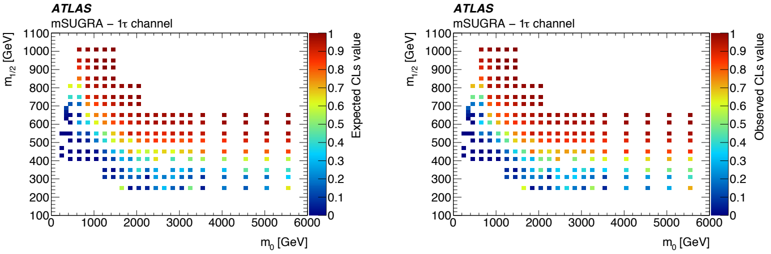

(c) mSUGRA (d) mSUGRA

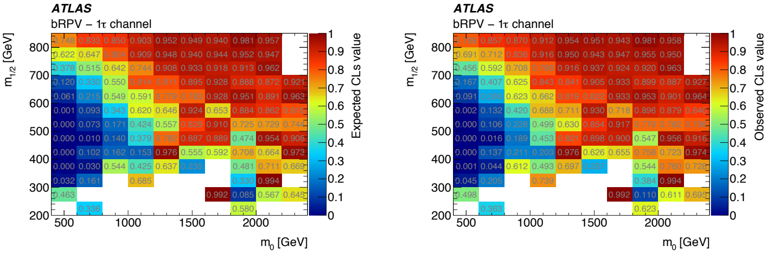

(e) bRPV (f) bRPV

Figure B.11: Expected (left) and observed (right) CLs values for the GMSB, mSUGRA and bRPV signal grids.

B.8 Preliminary 8 TeV Results

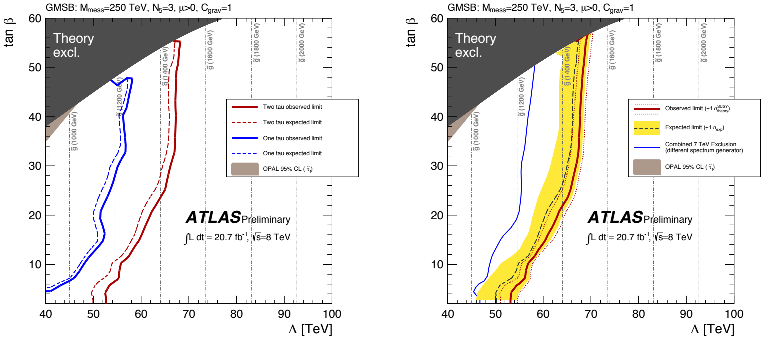

(a) GMSB (individual) (b) GMSB (combined)

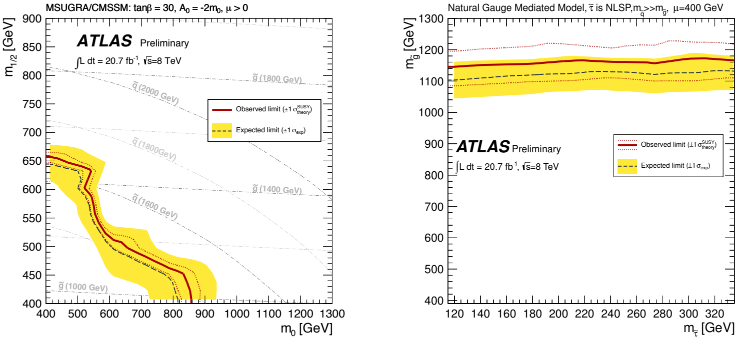

(c) mSUGRA (d) nGM

Figure B.12: Preliminary results published using the full 2012 dataset.

Bibliography

[1] ATLAS Collaboration, G. Aad et al., *Search for Supersymmetry in Events with Large Missing Transverse Momentum, Jets, and at Least One Tau Lepton in 7 TeV Proton-Proton Collision Data with the ATLAS Detector*, Eur. Phys. J. **C72** (2012) 2215, `arXiv:1210.1314 [hep-ex]`.

[2] ATLAS Collaboration, *Search for Supersymmetry in Events with Large Missing Transverse Momentum, Jets, and at Least One Tau Lepton in 21 fb^{-1} of $\sqrt{s} = 8$ TeV Proton-Proton Collision Data with the ATLAS Detector*, ATLAS-CONF-2013-026. `http://cdsweb.cern.ch/record/1525882`.

[3] ATLAS Collaboration, O. Dale, *Search for supersymmetry in events with large missing transverse momentum, jets, and at least one tau lepton in 21 fb^{-1} of 8 TeV proton-proton collision data with the ATLAS detector*, PoS **EPS-HEP2013** (2013) 079.

[4] ATLAS Collaboration, G. Aad et al., *Search for supersymmetry in events with large missing transverse momentum, jets, and at least one tau lepton in 20 fb^{-1} of $\sqrt{s} = 8$ TeV proton-proton collision data with the ATLAS detector*, JHEP **09** (2014) 103, `arXiv:1407.0603 [hep-ex]`.

[5] ATLAS Collaboration, G. Aad et al., *Summary of the searches for squarks and gluinos using $\sqrt{s} = 8$ TeV pp collisions with the ATLAS experiment at the LHC*, JHEP **10** (2015) 054, `arXiv:1507.05525 [hep-ex]`.

[6] ATLAS Collaboration, G. Aad et al., *Summary of the ATLAS experiment's sensitivity to supersymmetry after LHC Run 1 – interpreted in the phenomenological MSSM*, JHEP **10** (2015) 134, `arXiv:1508.06608 [hep-ex]`.

[7] P. F. Salvatore et al., *Search for Events with Large Missing Transverse Momentum, Jets, and Leptons (e/mu/tau) in 7 TeV Proton-Proton Collision Data with the ATLAS Detector*, ATL-PHYS-INT-2012-081. `https://cdsweb.cern.ch/record/1484637`.

[8] P. Bechtle et al., *Search for Events with Large Missing Transverse Momentum, Jets, and Leptons (e/mu/tau) in 8 TeV Proton-Proton Collision Data with the ATLAS Detector*, ATL-COM-PHYS-2013-1086. `https://cds.cern.ch/record/1568012`.

[9] S. P. Martin, *A Supersymmetry primer*, `arXiv:hep-ph/9709356 [hep-ph]`. [Adv. Ser. Direct. High Energy Phys.18,1(1998)].

[10] S. Weinberg, *A Model of Leptons*, Phys. Rev. Lett. **19** (1967) 1264–1266. `http://link.aps.org/doi/10.1103/PhysRevLett.19.1264`.

[11] S. L. Glashow, *Partial-symmetries of weak interactions*, Nuclear Physics **22** no. 4, (1961) 579 – 588. `http://www.sciencedirect.com/science/article/pii/0029558261904692`.

[12] V. Barger and R. Phillips, *Collider Physics*. Frontiers in physics. Addison-Wesley Publishing Company, 1997. `https://books.google.no/books?id=k-iBmqBk6y4C`.

[13] G. Bertone, D. Hooper, and J. Silk, *Particle dark matter: Evidence, candidates and constraints*, Phys.Rept. **405** (2005) 279–390, `arXiv:hep-ph/0404175 [hep-ph]`.

[14] G. Jungman, M. Kamionkowski, and K. Griest, *Supersymmetric dark matter*, Phys. Rept. **267** (1996) 195–373, `arXiv:hep-ph/9506380 [hep-ph]`.

[15] F. Zwicky, *Die Rotverschiebung von extragalaktischen Nebeln*, Helv. Phys. Acta **6** (1933) 110–127.

[16] X. ray: NASA/CXC/CfA/M.Markevitch et al.; Optical: NASA/STScI; Magellan/U.Arizona/D.Clowe et al.; Lensing Map: NASA/STScI; ESO WFI; Magellan/U.Arizona/D.Clowe et al., 2006. `http://chandra.harvard.edu/photo/2006/1e0657/`.

[17] D. Clowe, M. Bradac, A. H. Gonzalez, M. Markevitch, S. W. Randall, C. Jones, and D. Zaritsky, *A direct empirical proof of the existence of*

dark matter, Astrophys. J. **648** (2006) L109–L113, `arXiv:astro-ph/0608407 [astro-ph]`.

[18] N. A. Bahcall and X.-h. Fan, *The Most massive distant clusters: Determining omega and sigma*$_8$, Astrophys. J. **504** (1998) 1, `arXiv:astro-ph/9803277 [astro-ph]`.

[19] A. Kashlinsky, *Determining* Ω *from the cluster correlation function*, Physics Reports **307** no. 1-4, (1998) 67 – 73. `http://www.sciencedirect.com/science/article/pii/S0370157398000507`.

[20] R. G. Carlberg, H. K. C. Yee, S. L. Morris, H. Lin, E. Ellingson, D. Patton, M. Sawicki, and C. W. Shepherd, *The* Ω_M*-*Ω_Λ *Dependence of the Apparent Cluster* Ω, The Astrophysical Journal **516** no. 2, (1999) 552. `http://stacks.iop.org/0004-637X/516/i=2/a=552`.

[21] K. G. Begeman, A. H. Broeils, and R. H. Sanders, *Extended rotation curves of spiral galaxies: Dark haloes and modified dynamics*, Mon. Not. Roy. Astron. Soc. **249** (1991) 523.

[22] V. C. Rubin, N. Thonnard, and W. K. Ford, Jr., *Rotational properties of 21 SC galaxies with a large range of luminosities and radii, from NGC 4605 /R = 4kpc/ to UGC 2885 /R = 122 kpc/*, Astrophys. J. **238** (1980) 471.

[23] W. J. G. de Blok, S. S. McGaugh, A. Bosma, and V. C. Rubin, *Mass density profiles of LSB galaxies*, Astrophys. J. **552** (2001) L23–L26, `arXiv:astro-ph/0103102 [astro-ph]`.

[24] K. Olive and P. D. Group, *Review of Particle Physics*, Chinese Physics C **38** no. 9, (2014) 090001. `http://stacks.iop.org/1674-1137/38/i=9/a=090001`.

[25] NASA / WMAP Science Team, “The Microwave Sky, c. 1965.” `http://wmap.gsfc.nasa.gov/media/030635/index.html`. [Online; accessed November 2015].

[26] NASA / WMAP Science Team, “COBE to WMAP Sky.” `http://wmap.gsfc.nasa.gov/media/030653/index.html`. [Online; accessed November 2015].

[27] NASA / WMAP Science Team, *Nine Year Microwave Sky*, 2013. `http://map.gsfc.nasa.gov/media/121238/index.html`. [Online; accessed November 2015].

[28] ESA and the Planck Collaboration, *PLANCK CMB*, 2012. `http://www.esa.int/spaceinimages/Images/2013/03/Planck_CMB`. [Online; accessed November 2015].

[29] C. L. Bennett, D. Larson, J. L. Weiland, N. Jarosik, G. Hinshaw, N. Odegard, K. M. Smith, R. S. Hill, B. Gold, M. Halpern, E. Komatsu, M. R. Nolta, L. Page, D. N. Spergel, E. Wollack, J. Dunkley, A. Kogut, M. Limon, S. S. Meyer, G. S. Tucker, and E. L. Wright, *Nine-year Wilkinson Microwave Anisotropy Probe (WMAP) Observations: Final Maps and Results*, The Astrophysical Journal Supplement Series **208** no. 2, (2013) 20. `http://stacks.iop.org/0067-0049/208/i=2/a=20`.

[30] Planck Collaboration, P. A. R. Ade et al., *Planck 2013 results. I. Overview of products and scientific results*, Astron. Astrophys. **571** (2014) A1, `arXiv:1303.5062 [astro-ph.CO]`.

[31] ESA and the Planck Collaboration, *Power spectrum of temperature fluctuations in the Cosmic Microwave Background*, 2013. `http://sci.esa.int/planck/51555-planck-power-spectrum-of-temperature-fluctuations-in-the-cosmic-microwave-background/`. [Online; accessed November 2015].

[32] Planck Collaboration, P. A. R. Ade et al., *Planck 2013 results. XV. CMB power spectra and likelihood*, Astron. Astrophys. **571** (2014) A15, `arXiv:1303.5075 [astro-ph.CO]`.

[33] B. Paczynski, *Gravitational microlensing by the galactic halo*, Astrophys. J. **304** (1986) 1–5.

[34] K. Griest, *Galactic Microlensing as a Method of Detecting Massive Compact Halo Objects*, Astrophys. J. **366** (1991) 412–421.

[35] F. D. Paolis, G. Ingrosso, P. Jetzer, and M. Roncadelli, *A Case for a Baryonic Dark Halo*, Phys. Rev. Lett. **74** (1995) 14–17. `http://link.aps.org/doi/10.1103/PhysRevLett.74.14`.

[36] S. Dodelson and L. M. Widrow, *Sterile-neutrinos as dark matter*, Phys. Rev. Lett. **72** (1994) 17–20, `arXiv:hep-ph/9303287 [hep-ph]`.

[37] J. R. Ellis, T. Falk, K. A. Olive, and M. Srednicki, *Calculations of neutralino-stau coannihilation channels and the cosmologically relevant region of MSSM parameter space*, Astropart. Phys. **13** (2000) 181–213, `arXiv:hep-ph/9905481 [hep-ph]`.

[38] L. Bergstrom, *Dark Matter Candidates*, New J. Phys. **11** (2009) 105006, `arXiv:0903.4849 [hep-ph]`.

[39] A. Neveu and J. H. Schwarz, *Factorizable dual model of pions*, Nucl. Phys. **B31** (1971) 86–112.

[40] Y. A. Golfand and E. P. Likhtman, *Extension of the Algebra of Poincare Group Generators and Violation of p Invariance*, JETP Lett. **13** (1971) 323–326.

[41] P. Ramond, *Dual Theory for Free Fermions*, Phys. Rev. **D3** (1971) 2415–2418.

[42] D. V. Volkov and V. P. Akulov, *Is the Neutrino a Goldstone Particle?*, Phys. Lett. **B46** (1973) 109–110.

[43] J. Wess and B. Zumino, *Supergauge Transformations in Four-Dimensions*, Nucl. Phys. **B70** (1974) 39–50.

[44] R. Barbieri and G. Giudice, *Upper Bounds on Supersymmetric Particle Masses*, Nucl. Phys. **B306** (1988) 63.

[45] B. de Carlos and J. Casas, *One loop analysis of the electroweak breaking in supersymmetric models and the fine tuning problem*, Phys. Lett. **B309** (1993) 320–328, `arXiv:hep-ph/9303291`.

[46] P. Fayet, *Supersymmetry and Weak, Electromagnetic and Strong Interactions*, Phys. Lett. **B64** (1976) 159.

[47] P. Fayet, *Spontaneously Broken Supersymmetric Theories of Weak, Electromagnetic and Strong Interactions*, Phys. Lett. **B69** (1977) 489.

[48] G. R. Farrar and P. Fayet, *Phenomenology of the Production, Decay, and Detection of New Hadronic States Associated with Supersymmetry*, Phys. Lett. **B76** (1978) 575–579.

[49] P. Fayet, *Relations Between the Masses of the Superpartners of Leptons and Quarks, the Goldstino Couplings and the Neutral Currents*, Phys. Lett. **B84** (1979) 416.

[50] S. Dimopoulos and H. Georgi, *Softly Broken Supersymmetry and SU(5)*, Nucl. Phys. **B193** (1981) 150.

[51] A. H. Chamseddine, R. Arnowitt, and P. Nath, *Locally Supersymmetric Grand Unification*, Phys. Rev. Lett. **49** (1982) 970.

[52] R. Barbieri, S. Ferrara, and C. A. Savoy, *Gauge Models with Spontaneously Broken Local Supersymmetry*, Phys. Lett. **B119** (1982) 343.

[53] L. E. Ibanez, *Locally Supersymmetric SU(5) Grand Unification*, Phys. Lett. **B118** (1982) 73.

[54] L. J. Hall, J. D. Lykken, and S. Weinberg, *Supergravity as the Messenger of Supersymmetry Breaking*, Phys. Rev. **D27** (1983) 2359–2378.

[55] N. Ohta, *Grand Unified Theories Based on Local Supersymmetry*, Prog. Theor. Phys. **70** (1983) 542.

[56] G. L. Kane, C. F. Kolda, L. Roszkowski, and J. D. Wells, *Study of constrained minimal supersymmetry*, Phys. Rev. **D49** (1994) 6173–6210.

[57] M. Dine and W. Fischler, *A Phenomenological Model of Particle Physics Based on Supersymmetry*, Phys. Lett. **B110** (1982) 227.

[58] L. Alvarez-Gaume, M. Claudson, and M. B. Wise, *Low-Energy Supersymmetry*, Nucl. Phys. **B207** (1982) 96.

[59] C. R. Nappi and B. A. Ovrut, *Supersymmetric Extension of the SU(3)×SU(2)×U(1) Model*, Phys. Lett. **B113** (1982) 175.

[60] M. Dine and A. E. Nelson, *Dynamical supersymmetry breaking at low-energies*, Phys. Rev. **D48** (1993) 1277–1287, `arXiv:hep-ph/9303230`.

[61] M. Dine, A. E. Nelson, and Y. Shirman, *Low-energy dynamical supersymmetry breaking simplified*, Phys. Rev. **D51** (1995) 1362–1370, `arXiv:hep-ph/9408384`.

[62] M. Dine, A. E. Nelson, Y. Nir, and Y. Shirman, *New tools for low-energy dynamical supersymmetry breaking*, Phys. Rev. **D53** (1996) 2658–2669, `arXiv:hep-ph/9507378`.

[63] J. Rich, D. Lloyd Owen, and M. Spiro, *Experimental particle physics without accelerators*, Phys. Rept. **151** (1987) 239–364.

[64] P. F. Smith, *Terrestrial Searches for New Stable Particles*, Contemp. Phys. **29** (1988) 159–186.

[65] T. K. Hemmick et al., *A Search for Anomalously Heavy Isotopes of Low Z Nuclei*, Phys. Rev. **D41** (1990) 2074–2080.

[66] T. Falk, K. A. Olive, and M. Srednicki, *Heavy sneutrinos as dark matter*, Phys. Lett. **B339** (1994) 248–251, `arXiv:hep-ph/9409270 [hep-ph]`.

[67] SLD Electroweak Group, SLD Heavy Flavor Group, LEP Electroweak Working Group, DELPHI, LEP, ALEPH, OPAL, L3 Collaboration, *A Combination of preliminary electroweak measurements and constraints on the standard model*, `arXiv:hep-ex/0312023 [hep-ex]`.

[68] J. Ellis and K. A. Olive, *Supersymmetric Dark Matter Candidates*, `arXiv:1001.3651 [astro-ph.CO]`.

[69] D. Albornoz Vasquez, G. Belanger, and C. Boehm, *Revisiting light neutralino scenarios in the MSSM*, Phys. Rev. **D84** (2011) 095015, `arXiv:1108.1338 [hep-ph]`.

[70] Ø. Dale, *Discovering SUSY with $\tau^+\tau^-$ over $t\bar{t}$ Background – Evaluation of ATLAS Potential with 2010 Data*, Master's thesis, University of Bergen, 2011.

[71] T. Buanes, T. Burgess, Ø. Dale, A. Kastanas, A. Lipniacka, and T. Sjursen, *Search for supersymmetry in the coannihilation region with taus, jets and missing transverse energy in the final state.*, Tech. Rep. ATL-COM-PHYS-2011-1304, CERN, Geneva, Oct, 2011. `https://cds.cern.ch/record/1385579`.

[72] ATLAS Collaboration, *Search for Supersymmetry with Jets, Missing Transverse Momentum and at Least One Hadronically Decaying Tau Lepton in Proton-Proton Collisions at $\sqrt{s} = 7$ TeV with the ATLAS Detector*, Phys. Lett. **B 714** (2012) 197, `arXiv:1204.3852 [hep-ex]`.

[73] ATLAS Collaboration, *Search for Events with Large Missing Transverse Momentum, Jets and at Least Two Tau Leptons in 7 TeV Proton-Proton Collision Data with the ATLAS Detector*, Phys. Lett. **B 714** (2012) 180, `arXiv:1203.6580 [hep-ex]`.

[74] L. Evans and P. Bryant, *LHC Machine*, JINST **3** (2008) S08001.

[75] ATLAS Collaboration, G. Aad et al., *The ATLAS Experiment at the CERN Large Hadron Collider*, Journal of Instrumentation **3** no. 08, (2008) S08003. `http://stacks.iop.org/1748-0221/3/i=08/a=S08003`.

[76] C. Lefevre, “LHC: the guide.” Brochure, Feb, 2009. `https://cds.cern.ch/record/1165534`.

[77] ATLAS Collaboration. Standard Model public results. `https://twiki.cern.ch/twiki/bin/view/AtlasPublic/StandardModelPublicResults`. [Online; accessed September 2015].

[78] ATLAS Collaboration. Luminosity public results. `https://twiki.cern.ch/twiki/bin/view/AtlasPublic/LuminosityPublicResults`. [Online; accessed September 2015].

[79] J. Pequenao, “Computer generated image of the whole ATLAS detector.” CDS, Mar, 2008. `http://cds.cern.ch/record/1095924`.

[80] J. Pequenao and P. Schaffner, “An computer generated image representing how ATLAS detects particles.” CDS, Jan, 2013. `https://cds.cern.ch/record/1505342`.

[81] M. Cacciari, G. P. Salam, and G. Soyez, *The Anti-k(t) jet clustering algorithm*, JHEP **04** (2008) 063, `arXiv:0802.1189 [hep-ph]`.

[82] T. Gleisberg, S. Hoeche, F. Krauss, M. Schonherr, S. Schumann, F. Siegert, and J. Winter, *Event generation with SHERPA 1.1*, JHEP **02** (2009) 007, `arXiv:0811.4622 [hep-ph]`.

[83] ATLAS Collaboration, *ATLAS detector and physics performance: Technical Design Report, 2*. Technical Design Report ATLAS. CERN, Geneva, 1999. `https://cds.cern.ch/record/391177`.

[84] A. Buckley et al., *General-purpose event generators for LHC physics*, Phys. Rept. **504** (2011) 145–233, `arXiv:1101.2599 [hep-ph]`.

[85] A. Martin, W. Stirling, R. Thorne, and G. Watt, *Parton distributions for the LHC*, The European Physical Journal C **63** no. 2, (2009) 189–285. `http://dx.doi.org/10.1140/epjc/s10052-009-1072-5`.

[86] S. Agostinelli et al., *Geant4 — a simulation toolkit*, Nuclear Instruments and Methods in Physics Research Section A: Accelerators, Spectrometers, Detectors and Associated Equipment **506** no. 3, (2003) 250 – 303. `http://www.sciencedirect.com/science/article/pii/S0168900203013688`.

[87] ATLAS Collaboration, *ATLAS detector and physics performance: Technical Design Report, 1*. Technical Design Report ATLAS. CERN, Geneva, 1999. `http://cds.cern.ch/record/391176`.

[88] ATLAS Collaboration, G. Aad et al., *The ATLAS Simulation Infrastructure*, Eur. Phys. J. **C70** (2010) 823–874, `arXiv:1005.4568 [physics.ins-det]`.

[89] *Identification of the Hadronic Decays of Tau Leptons in 2012 Data with the ATLAS Detector*, Tech. Rep. ATLAS-CONF-2013-064, CERN, Geneva, Jul, 2013. `https://cds.cern.ch/record/1562839`.

[90] ATLAS Collaboration, G. Aad et al., *Identification and energy calibration of hadronically decaying tau leptons with the ATLAS experiment in pp collisions at* $\sqrt{s}$*=8 TeV*, Eur. Phys. J. **C75** no. 7, (2015) 303, `arXiv:1412.7086 [hep-ex]`.

[91] *Determination of the tau energy scale and the associated systematic uncertainty in proton-proton collisions at* $\sqrt{s} = 8$ *TeV with the ATLAS detector at the LHC in 2012*, Tech. Rep. ATLAS-CONF-2013-044, CERN, Geneva, Apr, 2013. `https://cds.cern.ch/record/1544036`.

[92] ATLAS Collaboration. Tau public results. `https://twiki.cern.ch/twiki/bin/view/AtlasPublic/TauPublicCollisionPlots`. [Online; accessed October 2015].

[93] SUSY object definitions. `https://twiki.cern.ch/twiki/bin/view/AtlasProtected/SusyObjectDefintions`. [Online; accessed January 2016].

[94] SUSY Tools. `https://svnweb.cern.ch/trac/atlasoff/browser/PhysicsAnalysis/SUSYPhys/SUSYTools`. [Online; accessed January 2016].

[95] ATLAS Collaboration, G. Aad et al., *Jet energy measurement and its systematic uncertainty in proton-proton collisions at* $\sqrt{s} = 7$ *TeV with the ATLAS detector*, Eur. Phys. J. **C75** (2015) 17, `arXiv:1406.0076 [hep-ex]`.

[96] W. Lampl, S. Laplace, D. Lelas, P. Loch, H. Ma, S. Menke, S. Rajagopalan, D. Rousseau, S. Snyder, and G. Unal, *Calorimeter Clustering Algorithms: Description and Performance*, Tech. Rep. ATL-LARG-PUB-2008-002. ATL-COM-LARG-2008-003, CERN, Geneva, Apr, 2008. `http://cds.cern.ch/record/1099735`.

[97] C. Cojocaru et al., *Hadronic calibration of the {ATLAS} liquid argon end-cap calorimeter in the pseudorapidity region in beam tests*,

Nuclear Instruments and Methods in Physics Research Section A: Accelerators, Spectrometers, Detectors and Associated Equipment **531** no. 3, (2004) 481 – 514. `http://www.sciencedirect.com/science/article/pii/S0168900204012884`.

[98] C. Issever, K. Borras, and D. Wegener, *An improved weighting algorithm to achieve software compensation in a fine grained LAr calorimeter*, Nuclear Instruments and Methods in Physics Research A **545** (2005) 803–812, `physics/0408129`.

[99] ATLAS Collaboration, G. Aad et al., *Jet energy measurement with the ATLAS detector in proton-proton collisions at* $\sqrt{s} = 7$ *TeV*, Eur. Phys. J. **C73** no. 3, (2013) 2304, `arXiv:1112.6426 [hep-ex]`.

[100] M. Cacciari and G. P. Salam, *Pileup subtraction using jet areas*, Phys. Lett. **B659** (2008) 119–126, `arXiv:0707.1378 [hep-ph]`.

[101] ATLAS Collaboration, G. Aad et al., *Performance of b-Jet Identification in the ATLAS Experiment*, `arXiv:1512.01094 [hep-ex]`.

[102] ATLAS Collaboration, *Commissioning of the ATLAS high-performance b-tagging algorithms in the 7 TeV collision data*, Tech. Rep. ATLAS-CONF-2011-102, CERN, Geneva, Jul, 2011. `https://cds.cern.ch/record/1369219`.

[103] ATLAS Collaboration, *Measurement of the b-tag Efficiency in a Sample of Jets Containing Muons with 5* fb^{-1} *of Data from the ATLAS Detector*, Tech. Rep. ATLAS-CONF-2012-043, CERN, Geneva, Mar, 2012. `https://cds.cern.ch/record/1435197`.

[104] Medium++ electron ID. `https://twiki.cern.ch/twiki/bin/view/AtlasProtected/IsEMIdentification`. [Online; accessed January 2016].

[105] ATLAS Collaboration, G. Aad et al., *Electron performance measurements with the ATLAS detector using the 2010 LHC proton-proton collision data*, Eur. Phys. J. **C72** (2012) 1909, `arXiv:1110.3174 [hep-ex]`.

[106] ATLAS Collaboration, G. Aad et al., *Electron reconstruction and identification efficiency measurements with the ATLAS detector using the 2011 LHC proton-proton collision data*, Eur. Phys. J. **C74** no. 7, (2014) 2941, `arXiv:1404.2240 [hep-ex]`.

[107] SUSY object definitions 8 TeV. `https://twiki.cern.ch/twiki/bin/view/AtlasProtected/SusyObjectDefinitionsr178TeV`. [Online; accessed January 2016].

[108] Electron cleaning and object quality. `https://twiki.cern.ch/twiki/bin/view/AtlasProtected/LArCleaningAndObjectQuality#Object_Quality`. [Online; accessed February 2016].

[109] ATLAS Collaboration, G. Aad et al., *Muon reconstruction efficiency and momentum resolution of the ATLAS experiment in proton-proton collisions at* $\sqrt{s} = 7$ *TeV in 2010*, Eur. Phys. J. **C74** no. 9, (2014) 3034, `arXiv:1404.4562 [hep-ex]`.

[110] ATLAS Collaboration, G. Aad et al., *Measurement of the muon reconstruction performance of the ATLAS detector using 2011 and 2012 LHC proton-proton collision data*, Eur. Phys. J. **C74** no. 11, (2014) 3130, `arXiv:1407.3935 [hep-ex]`.

[111] ATLAS Collaboration, G. Aad et al., *Performance of Missing Transverse Momentum Reconstruction in Proton-Proton Collisions at 7 TeV with ATLAS*, Eur. Phys. J. **C72** (2012) 1844, `arXiv:1108.5602 [hep-ex]`.

[112] ATLAS Collaboration Collaboration, *Performance of primary vertex reconstruction in proton-proton collisions at* $\sqrt{s} = 7$ *TeV in the ATLAS experiment*, Tech. Rep. ATLAS-CONF-2010-069, CERN, Geneva, Jul, 2010. `https://cds.cern.ch/record/1281344`.

[113] ATLAS Collaboration, G. Aad et al., *Characterisation and mitigation of beam-induced backgrounds observed in the ATLAS detector during the 2011 proton-proton run*, JINST **8** (2013) P07004, `arXiv:1303.0223 [hep-ex]`.

[114] Jet cleaning 2012. `https://twiki.cern.ch/twiki/bin/viewauth/AtlasProtected/HowToCleanJets2012`. [Online; accessed January 2016].

[115] Calorimeter Dead Cell Correction. `https://twiki.cern.ch/twiki/bin/view/AtlasProtected/DeadCellCorrection`. [Online; accessed January 2016].

[116] Calorimeter Dead Cell Shape Correction. `https://twiki.cern.ch/twiki/bin/view/AtlasProtected/JetMomentsForBadCells`. [Online; accessed January 2016].

[117] Jet cleaning 2011. `https://twiki.cern.ch/twiki/bin/viewauth/AtlasProtected/HowToCleanJets2011`. [Online; accessed January 2016].

[118] Fake MET Estimator. `https://twiki.cern.ch/twiki/bin/view/AtlasProtected/FakeMetEstimator`. [Online; accessed January 2016].

[119] W. Beenakker, R. Hopker, M. Spira, and P. M. Zerwas, *Squark and gluino production at hadron colliders*, Nucl. Phys. **B492** (1997) 51–103, `arXiv:hep-ph/9610490 [hep-ph]`.

[120] A. Kulesza and L. Motyka, *Threshold resummation for squark-antisquark and gluino-pair production at the LHC*, Phys. Rev. Lett. **102** (2009) 111802, `arXiv:0807.2405 [hep-ph]`.

[121] W. Beenakker, S. Brensing, M. Kramer, A. Kulesza, E. Laenen, and I. Niessen, *Soft-gluon resummation for squark and gluino hadroproduction*, JHEP **12** (2009) 041, `arXiv:0909.4418 [hep-ph]`.

[122] W. Beenakker, S. Brensing, M. n. Kramer, A. Kulesza, E. Laenen, L. Motyka, and I. Niessen, *Squark and Gluino Hadroproduction*, Int. J. Mod. Phys. **A26** (2011) 2637–2664, `arXiv:1105.1110 [hep-ph]`.

[123] M. Kramer, A. Kulesza, R. van der Leeuw, M. Mangano, S. Padhi, T. Plehn, and X. Portell, *Supersymmetry production cross sections in pp collisions at* $\sqrt{s} = 7$ *TeV*, `arXiv:1206.2892 [hep-ph]`.

[124] ALEPH Collaboration, A. Heister et al., *Search for gauge mediated SUSY breaking topologies in* e^+e^- *collisions at center-of-mass energies up to 209-GeV*, Eur. Phys. J. **C25** (2002) 339–351, `arXiv:hep-ex/0203024 [hep-ex]`.

[125] DELPHI Collaboration, J. Abdallah et al., *Search for supersymmetric particles in light gravitino scenarios and sleptons NLSP*, Eur. Phys. J. **C27** (2003) 153–172, `arXiv:hep-ex/0303025 [hep-ex]`.

[126] OPAL Collaboration, G. Abbiendi et al., *Searches for gauge-mediated supersymmetry breaking topologies in e+ e- collisions at LEP2*, Eur. Phys. J. **C46** (2006) 307–341, `arXiv:hep-ex/0507048 [hep-ex]`.

[127] ATLAS Collaboration, G. Aad et al., *Observation of a new particle in the search for the Standard Model Higgs boson with the ATLAS detector at the LHC*, Phys. Lett. **B716** (2012) 1–29, `arXiv:1207.7214 [hep-ex]`.

[128] CMS Collaboration, S. Chatrchyan et al., *Observation of a new boson at a mass of 125 GeV with the CMS experiment at the LHC*, Phys. Lett. **B716** (2012) 30–61, `arXiv:1207.7235 [hep-ex]`.

[129] ATLAS Collaboration and CMS Collaboration Collaboration, G. Aad et al., *Combined Measurement of the Higgs Boson Mass in pp Collisions at* $\sqrt{s} = 7$ *and 8 TeV with the ATLAS and CMS Experiments*, Phys. Rev. Lett. **114** (2015) 191803. `http://link.aps.org/doi/10.1103/PhysRevLett.114.191803`.

[130] Planck Collaboration, P. A. R. Ade et al., *Planck 2013 results. XVI. Cosmological parameters*, Astron. Astrophys. **571** (2014) A16, `arXiv:1303.5076 [astro-ph.CO]`.

[131] G. Hinshaw, D. Larson, E. Komatsu, D. N. Spergel, C. L. Bennett, J. Dunkley, M. R. Nolta, M. Halpern, R. S. Hill, N. Odegard, L. Page, K. M. Smith, J. L. Weiland, B. Gold, N. Jarosik, A. Kogut, M. Limon, S. S. Meyer, G. S. Tucker, E. Wollack, and E. L. Wright, *Nine-year Wilkinson Microwave Anisotropy Probe (WMAP) Observations: Cosmological Parameter Results*, The Astrophysical Journal Supplement Series **208** no. 2, (2013) 19. `http://stacks.iop.org/0067-0049/208/i=2/a=19`.

[132] M. Hirsch, M. A. Diaz, W. Porod, J. C. Romao, and J. W. F. Valle, *Neutrino masses and mixings from supersymmetry with bilinear R parity violation: A Theory for solar and atmospheric neutrino oscillations*, Phys. Rev. **D62** (2000) 113008, `arXiv:hep-ph/0004115 [hep-ph]`. [Erratum: Phys. Rev.D65,119901(2002)].

[133] F. de Campos et al., *Probing bilinear R-parity violating supergravity at the LHC*, JHEP **0805** (2008) 048, `arXiv:0712.2156 [hep-ph]`.

[134] Y. Grossman and S. Rakshit, *Neutrino masses in R-parity violating supersymmetric models*, Phys. Rev. **D69** (2004) 093002, `arXiv:hep-ph/0311310 [hep-ph]`.

[135] D. F. Carvalho, M. E. Gomez, and J. C. Romao, *Charged lepton flavor violation in supersymmetry with bilinear R-parity violation*, Phys. Rev. **D65** (2002) 093013, `arXiv:hep-ph/0202054 [hep-ph]`.

[136] W. Porod, M. Hirsch, J. Romao, and J. W. F. Valle, *Testing neutrino mixing at future collider experiments*, Phys. Rev. **D63** (2001) 115004, `arXiv:hep-ph/0011248 [hep-ph]`.

[137] J. Barnard, B. Farmer, T. Gherghetta, and M. White, *Natural gauge mediation with a bino NLSP at the LHC*, `arXiv:1208.6062 [hep-ph]`.

[138] M. Buican, P. Meade, N. Seiberg, and D. Shih, *Exploring General Gauge Mediation*, JHEP **03** (2009) 016, `arXiv:0812.3668 [hep-ph]`.

[139] Glen Cowan. Discovery sensitivity for a counting experiment with background uncertainty. `https://www.pp.rhul.ac.uk/~cowan/stat/notes/medsigNote.pdf`. [Online; accessed January 2016].

[140] G. Cowan, K. Cranmer, E. Gross, and O. Vitells, *Asymptotic formulae for likelihood-based tests of new physics*, Eur. Phys. J. **C71** (2011) 1554, `arXiv:1007.1727 [physics.data-an]`. [Erratum: Eur. Phys. J.C73,2501(2013)].

[141] G. Cowan, K. Cranmer, E. Gross, and O. Vitells, *Asymptotic Formulae for Likelihood-Based Tests of new Physics*, Eur. Phys. J. **C71** (2011) 1554, `arXiv:1007.1727`.

[142] ATLAS statistics forum. ABCD method in searches. `https://twiki.cern.ch/twiki/pub/AtlasProtected/ATLASStatisticsFAQ/ABCD.pdf`.

[143] K. Cranmer, *Practical Statistics for the LHC*, in *Proceedings, 2011 European School of High-Energy Physics (ESHEP 2011).* 2014. `arXiv:1503.07622 [physics.data-an]`. `http://inspirehep.net/record/1356277/files/arXiv:1503.07622.pdf`.

[144] ATLAS Collaboration, G. Aad et al., *Jet energy resolution in proton-proton collisions at* $\sqrt{s} = 7$ *TeV recorded in 2010 with the ATLAS detector*, Eur. Phys. J. **C73** no. 3, (2013) 2306, `arXiv:1210.6210 [hep-ex]`.

[145] ATLAS Collaboration, G. Aad et al., *Single hadron response measurement and calorimeter jet energy scale uncertainty with the ATLAS detector at the LHC*, Eur. Phys. J. **C73** no. 3, (2013) 2305, `arXiv:1203.1302 [hep-ex]`.

[146] ATLAS Collaboration, *Jet energy measurement with the ATLAS detector in proton-proton collisions at sqrt(s) = 7 TeV*, `arXiv:1112.6426 [hep-ex]`.

[147] ATLAS Collaboration, G. Aad et al., *Improved luminosity determination in pp collisions at sqrt(s) = 7 TeV using the ATLAS detector at the LHC*, Eur. Phys. J. **C73** no. 8, (2013) 2518, `arXiv:1302.4393 [hep-ex]`.

[148] J. Neyman and E. S. Pearson, *On the Problem of the Most Efficient Tests of Statistical Hypotheses*, Philosophical Transactions of the Royal Society of London A: Mathematical, Physical and Engineering Sciences **231** no. 694-706, (1933) 289–337, `http://rsta.royalsocietypublishing.org/content/231/694-706/289.full.pdf`. `http://rsta.royalsocietypublishing.org/content/231/694-706/289`.

[149] S. S. Wilks, *The Large-Sample Distribution of the Likelihood Ratio for Testing Composite Hypotheses*, Ann. Math. Statist. **9** no. 1, (1938) 60–62. `http://dx.doi.org/10.1214/aoms/1177732360`.

[150] A. Wald, *Tests of Statistical Hypotheses Concerning Several Parameters When the Number of Observations is Large*, Transactions of the American Mathematical Society **54** no. 3, (1943) 426–482. `http://www.jstor.org/stable/1990256`.

[151] A. L. Read, *Presentation of search results: the CL s technique*, Journal of Physics G: Nuclear and Particle Physics **28** no. 10, (2002) 2693. `http://stacks.iop.org/0954-3899/28/i=10/a=313`.

[152] M. L. Mangano, M. Moretti, F. Piccinini, R. Pittau, and A. D. Polosa, *ALPGEN, a generator for hard multiparton processes in hadronic collisions*, JHEP **07** (2003) 001, `arXiv:hep-ph/0206293 [hep-ph]`.

[153] J. Pumplin, D. R. Stump, J. Huston, H. L. Lai, P. M. Nadolsky, and W. K. Tung, *New generation of parton distributions with uncertainties from global QCD analysis*, JHEP **07** (2002) 012, `arXiv:hep-ph/0201195 [hep-ph]`.

[154] S. Frixione and B. R. Webber, *Matching NLO QCD computations and parton shower simulations*, JHEP **06** (2002) 029, `arXiv:hep-ph/0204244 [hep-ph]`.

[155] S. Frixione, P. Nason, and B. R. Webber, *Matching NLO QCD and parton showers in heavy flavor production*, JHEP **08** (2003) 007, `arXiv:hep-ph/0305252 [hep-ph]`.

[156] S. Frixione, E. Laenen, P. Motylinski, and B. R. Webber, *Single-top production in MC@NLO*, JHEP **03** (2006) 092, `arXiv:hep-ph/0512250 [hep-ph]`.

[157] H.-L. Lai, M. Guzzi, J. Huston, Z. Li, P. M. Nadolsky, J. Pumplin, and C.-P. Yuan, *New parton distributions for collider physics*, Phys. Rev. D **82** (2010) 074024. `http://link.aps.org/doi/10.1103/PhysRevD.82.074024`.

[158] J. M. Butterworth, J. R. Forshaw, and M. H. Seymour, *Multiparton interactions in photoproduction at HERA*, Z. Phys. **C72** (1996) 637–646, `arXiv:hep-ph/9601371 [hep-ph]`.

[159] G. Corcella, I. G. Knowles, G. Marchesini, S. Moretti, K. Odagiri, P. Richardson, M. H. Seymour, and B. R. Webber, *HERWIG 6: An Event generator for hadron emission reactions with interfering gluons (including supersymmetric processes)*, JHEP **01** (2001) 010, `arXiv:hep-ph/0011363 [hep-ph]`.

[160] S. Jadach, Z. Was, R. Decker, and J. Kuhn, *The τ decay library TAUOLA, version 2.4*, Computer Physics Communications **76** no. 3, (1993) 361 – 380. `http://www.sciencedirect.com/science/article/pii/001046559390061G`.

[161] P. Golonka, B. Kersevan, T. Pierzchala, E. Richter-Was, Z. Was, and M. Worek, *The Tauola photos F environment for the TAUOLA and PHOTOS packages: Release. 2.*, Comput. Phys. Commun. **174** (2006) 818–835, `arXiv:hep-ph/0312240 [hep-ph]`.

[162] T. Sjostrand, S. Mrenna, and P. Z. Skands, *PYTHIA 6.4 Physics and Manual*, JHEP **05** (2006) 026, `arXiv:hep-ph/0603175 [hep-ph]`.

[163] *ATLAS tunes of PYTHIA 6 and Pythia 8 for MC11*, Tech. Rep. ATL-PHYS-PUB-2011-009, CERN, Geneva, Jul, 2011. `https://cds.cern.ch/record/1363300`.

[164] A. Sherstnev and R. S. Thorne, *Parton Distributions for LO Generators*, Eur. Phys. J. **C55** (2008) 553–575, `arXiv:0711.2473 [hep-ph]`.

[165] F. E. Paige, S. D. Protopopescu, H. Baer, and X. Tata, *ISAJET 7.69: A Monte Carlo event generator for pp, anti-p p, and e+e- reactions*, `arXiv:hep-ph/0312045 [hep-ph]`.

[166] M. Bahr et al., *Herwig++ Physics and Manual*, Eur. Phys. J. **C58** (2008) 639–707, `arXiv:0803.0883 [hep-ph]`.

[167] ATLAS Collaboration, G. Aad et al., *Measurement of the production cross section for Z/gamma* in association with jets in pp collisions at $\sqrt{s} = 7$ TeV with the ATLAS detector*, Phys. Rev. **D85** (2012) 032009, `arXiv:1111.2690 [hep-ex]`.

[168] ATLAS Collaboration, G. Aad et al., *Measurement of the inclusive $W^{\pm}$ and Z/gamma cross sections in the electron and muon decay channels in pp collisions at $\sqrt{s} = 7$ TeV with the ATLAS detector*, Phys. Rev. **D85** (2012) 072004, `arXiv:1109.5141 [hep-ex]`.

[169] ATLAS Collaboration, G. Aad et al., *Measurement of the charge asymmetry in top quark pair production in pp collisions at $\sqrt{s} = 7$ TeV using the ATLAS detector*, Eur. Phys. J. **C72** (2012) 2039, `arXiv:1203.4211 [hep-ex]`.

[170] B. P. Kersevan and E. Richter-Was, *The Monte Carlo event generator AcerMC versions 2.0 to 3.8 with interfaces to PYTHIA 6.4, HERWIG 6.5 and ARIADNE 4.1*, Comput. Phys. Commun. **184** (2013) 919–985, `arXiv:hep-ph/0405247 [hep-ph]`.

[171] ATLAS Collaboration, *Luminosity Determination in pp Collisions at sqrt(s) = 7 TeV using the ATLAS Detector in 2011*, Tech. Rep. ATLAS-CONF-2011-116, CERN, Geneva, Aug, 2011.

[172] ATLAS Collaboration, *Search for Supersymmetry in Events with Large Missing Transverse Momentum, Jets, and at Least One Tau Lepton in 7 TeV Proton-Proton Collision Data with the ATLAS Detector*, Eur. Phys. J. **C 72** (2012) 2215, `arXiv:1210.1314 [hep-ex]`.

[173] ATLAS Collaboration, G. Aad et al., *Further search for supersymmetry at $\sqrt{s} = 7$ TeV in final states with jets, missing transverse momentum and isolated leptons with the ATLAS detector*, Phys. Rev. **D86** (2012) 092002, `arXiv:1208.4688 [hep-ex]`.

[174] ATLAS Collaboration, G. Aad et al., *Measurements of normalized differential cross sections for $t\bar{t}$ production in pp collisions at*

$\sqrt{s} = 7$âĂĽâĂĽTeV using the ATLAS detector, Phys. Rev. **D90** no. 7, (2014) 072004, `arXiv:1407.0371 [hep-ex]`.

[175] ATLAS Collaboration, G. Aad et al., *Search for pair-produced third-generation squarks decaying via charm quarks or in compressed supersymmetric scenarios in pp collisions at $\sqrt{s} = 8$ TeV with the ATLAS detector*, Phys. Rev. **D90** no. 5, (2014) 052008, `arXiv:1407.0608 [hep-ex]`.

[176] P. M. Nadolsky et al., *Implications of CTEQ global analysis for collider observation*, Phys. Rev. **D78** (2008) 013004, `arXiv:0802.0007 [hep-ph]`.

[177] *Summary of ATLAS Pythia 8 tunes*, Tech. Rep. ATL-PHYS-PUB-2012-003, CERN, Geneva, Aug, 2012. `https://cds.cern.ch/record/1474107`.

[178] P. Z. Skands, *Tuning Monte Carlo Generators: The Perugia Tunes*, Phys. Rev. **D82** (2010) 074018, `arXiv:1005.3457 [hep-ph]`.

[179] S. Owen, *Data-driven estimation of the QCD multijet background to SUSY searches with jets and missing transverse momentum at ATLAS using jet smearing*, ATL-PHYS-INT-2012-008. `http://cdsweb.cern.ch/record/1423310`.

[180] ATLAS Collaboration, G. Aad et al., *Search for squarks and gluinos with the ATLAS detector in final states with jets and missing transverse momentum using 4.7 fb^{-1} of $\sqrt{s} = 7$ TeV proton-proton collision data*, Phys. Rev. **D87** no. 1, (2013) 012008, `arXiv:1208.0949 [hep-ex]`.

[181] M. Baak, G. J. Besjes, D. Cote, A. Koutsman, J. Lorenz, and D. Short, *HistFitter software framework for statistical data analysis*, Eur. Phys. J. **C75** (2015) 153, `arXiv:1410.1280 [hep-ex]`.

[182] ATLAS Collaboration. Supersymmetry public results. `https://twiki.cern.ch/twiki/bin/view/AtlasPublic/SupersymmetryPublicResults`. [Online; accessed June 2015].

[183] M. Actis, G. Agnetta, F. Aharonian, A. Akhperjanian, J. Aleksić, E. Aliu, D. Allan, I. Allekotte, F. Antico, L. A. Antonelli, and et al., *Design concepts for the Cherenkov Telescope Array CTA: an advanced facility for ground-based high-energy gamma-ray astronomy*,

Experimental Astronomy **32** (2011) 193–316, `arXiv:1008.3703 [astro-ph.IM]`.

[184] K. Bernlohr, A. Barnacka, Y. Becherini, O. B. Bigas, E. Carmona, et al., *Monte Carlo design studies for the Cherenkov Telescope Array*, `arXiv:1210.3503 [astro-ph.IM]`.

[185] J. M. Davies and E. S. Cotton, *The Proceedings of the Solar Furnace Symposium Design of the quartermaster solar furnace*, Solar Energy **1** no. 2, (1957) 16 – 22. `http://www.sciencedirect.com/science/article/pii/0038092X57901160`.

[186] R. Mirzoyan, D. Sobczynska, E. Lorenz, and M. Teshima, *Tagging single muons and other long-flying relativistic charged particles by ultrafast timing in air Cherenkov telescopes*, Astropart. Phys. **25** (2006) 342–348, `arXiv:astro-ph/0605091 [astro-ph]`. [,469(2006)].

[187] MAGIC Collaboration, J. Albert et al., *FADC signal reconstruction for the MAGIC Telescope*, Nucl. Instrum. Meth. **A594** (2008) 407–419, `arXiv:astro-ph/0612385 [astro-ph]`.

[188] CTA Consortium Collaboration, M. P. Arribas, U. Schwanke, and R. Wischnewski, *Trigger and data rates expected for the CTA Observatory*, AIP Conf. Proc. **1505** (2012) 781–784, `arXiv:1211.3061 [astro-ph.IM]`.

[189] A. Goldwurm, *An Overview of the High-Energy Emission from the Galactic Center*, `arXiv:1007.4174 [astro-ph.HE]`.

[190] H.E.S.S. Collaboration Collaboration, F. Aharonian et al., *H.E.S.S. observations of the Galactic Center region and their possible dark matter interpretation*, Phys.Rev.Lett. **97** (2006) 221102, `arXiv:astro-ph/0610509 [astro-ph]`.

[191] H.E.S.S. Collaboration Collaboration, F. Aharonian et al., *Discovery of very-high-energy gamma-rays from the galactic centre ridge*, Nature **439** (2006) 695–698, `arXiv:astro-ph/0603021 [astro-ph]`.

[192] E. Wommer, F. Melia, and M. Fatuzzo, *Diffuse TeV Emission at the Galactic Centre*, Mon. Not. Roy. Astron. Soc. **387** (2008) 987, `arXiv:0804.3111 [astro-ph]`.

[193] T. Bringmann, F. Calore, G. Vertongen, and C. Weniger, *On the Relevance of Sharp Gamma-Ray Features for Indirect Dark Matter*

Searches, Phys.Rev. **D84** (2011) 103525, `arXiv:1106.1874 [hep-ph]`.

[194] D. Fegan, *gamma/hadron separation at TeV energies*, J.Phys. **G23** (1997) 1013–1060.

[195] L. Bergström and G. Bertone, *Gamma-rays*, in *Particle Dark Matter: Observations, Models and Searches.* Cambridge University Press, 2010.

[196] LAT Collaboration Collaboration, M. Ackermann et al., *Fermi LAT Search for Dark Matter in Gamma-ray Lines and the Inclusive Photon Spectrum*, Phys.Rev. **D86** (2012) 022002, `arXiv:1205.2739 [astro-ph.HE]`.

[197] J. Einasto, *Kinematics and dynamics of stellar systems*, Trudy Inst. Astrofiz. Alma-Ata **51** (1965).

[198] J. N. Bachall and R. Soneira, *The Universe at Faint Magnitudes. I. Models for the Galaxy and the Predicted Star Counts*, Astrophysical Journal Suppl **44** (1980).

[199] J. F. Navarro, C. S. Frenk, and S. D. White, *A Universal density profile from hierarchical clustering*, Astrophys.J. **490** (1997) 493–508, `arXiv:astro-ph/9611107 [astro-ph]`.

[200] J. F. Navarro, A. Ludlow, V. Springel, J. Wang, M. Vogelsberger, et al., *The Diversity and Similarity of Cold Dark Matter Halos*, `arXiv:0810.1522 [astro-ph]`.

[201] R. Catena and P. Ullio, *A novel determination of the local dark matter density*, JCAP **1008** (2010) 004, `arXiv:0907.0018 [astro-ph.CO]`.

[202] SDSS Collaboration Collaboration, X. Xue et al., *The Milky Way's Circular Velocity Curve to 60 kpc and an Estimate of the Dark Matter Halo Mass from Kinematics of 2400 SDSS Blue Horizontal Branch Stars*, Astrophys.J. **684** (2008) 1143–1158, `arXiv:0801.1232 [astro-ph]`.

[203] H.E.S.S. Collaboration Collaboration, A. Abramowski et al., *Search for photon line-like signatures from Dark Matter annihilations with H.E.S.S*, Phys.Rev.Lett. **110** (2013) 041301, `arXiv:1301.1173 [astro-ph.HE]`.

[204] P. Gondolo, J. Edsjo, P. Ullio, L. Bergstrom, M. Schelke, and E. A. Baltz, *DarkSUSY: Computing supersymmetric dark matter properties numerically*, JCAP **0407** (2004) 008, `arXiv:astro-ph/0406204 [astro-ph]`.

[205] P. Gondolo, J. EdsjÃű, L. Ullio, P. amd BergstrÃűm, M. Schelke, E. Baltz, T. Bringmann, and G. Duda, 2015. `http://www.darksusy.org`.

[206] F. E. Paige, S. D. Protopopescu, H. Baer, and X. Tata, *ISAJET 7.69: A Monte Carlo event generator for pp, anti-p p, and e+e- reactions*, `arXiv:hep-ph/0312045 [hep-ph]`.

[207] T. Hahn, S. Heinemeyer, W. Hollik, H. Rzehak, and G. Weiglein, *High-Precision Predictions for the Light CP -Even Higgs Boson Mass of the Minimal Supersymmetric Standard Model*, Phys. Rev. Lett. **112** no. 14, (2014) 141801, `arXiv:1312.4937 [hep-ph]`.

[208] M. Frank, T. Hahn, S. Heinemeyer, W. Hollik, H. Rzehak, and G. Weiglein, *The Higgs Boson Masses and Mixings of the Complex MSSM in the Feynman-Diagrammatic Approach*, JHEP **02** (2007) 047, `arXiv:hep-ph/0611326 [hep-ph]`.

[209] G. Degrassi, S. Heinemeyer, W. Hollik, P. Slavich, and G. Weiglein, *Towards high precision predictions for the MSSM Higgs sector*, Eur. Phys. J. **C28** (2003) 133–143, `arXiv:hep-ph/0212020 [hep-ph]`.

[210] S. Heinemeyer, W. Hollik, and G. Weiglein, *The Masses of the neutral CP - even Higgs bosons in the MSSM: Accurate analysis at the two loop level*, Eur. Phys. J. **C9** (1999) 343–366, `arXiv:hep-ph/9812472 [hep-ph]`.

[211] S. Heinemeyer, W. Hollik, and G. Weiglein, *FeynHiggs: A Program for the calculation of the masses of the neutral CP even Higgs bosons in the MSSM*, Comput. Phys. Commun. **124** (2000) 76–89, `arXiv:hep-ph/9812320 [hep-ph]`.

[212] P. Gondolo and G. Gelmini, *Cosmic abundances of stable particles: improved analysis.*, Nuclear Physics B **360** (1991) 145–179.

[213] J. Edsjo, M. Schelke, P. Ullio, and P. Gondolo, *Accurate relic densities with neutralino, chargino and sfermion coannihilations in mSUGRA*, JCAP **0304** (2003) 001, `arXiv:hep-ph/0301106 [hep-ph]`.

[214] L. Bergstrom and P. Ullio, *Full one loop calculation of neutralino annihilation into two photons*, Nucl. Phys. **B504** (1997) 27–44, `arXiv:hep-ph/9706232 [hep-ph]`.

[215] P. Ullio and L. Bergstrom, *Neutralino annihilation into a photon and a Z boson*, Phys. Rev. **D57** (1998) 1962–1971, `arXiv:hep-ph/9707333 [hep-ph]`.

[216] S. Martin, T. Sarangi, and X. Portell, "Considering scenarios with higgs constraints." `HTTPS://INDICO.CERN.CH/GETFILE.PY/ACCESS?CONTRIBID=14&SESSIONID=1&RESID=0&MATERIALID=SLIDES&CONFID=188153`.

[217] T. Burgess, J. O. Lindroos, A. Lipniacka, and H. Sandaker, *Finding viable Models in SUSY Parameter Spaces with Signal Specific Discovery Potential*, `arXiv:1210.7020 [hep-ph]`.

[218] L. Bergstrom, P. Ullio, and J. H. Buckley, *Observability of gamma-rays from dark matter neutralino annihilations in the Milky Way halo*, Astropart. Phys. **9** (1998) 137–162, `arXiv:astro-ph/9712318 [astro-ph]`.

[219] J. Hisano, S. Matsumoto, M. M. Nojiri, and O. Saito, *Non-perturbative effect on dark matter annihilation and gamma ray signature from galactic center*, Phys. Rev. **D71** (2005) 063528, `arXiv:hep-ph/0412403 [hep-ph]`.

[220] M. Gustafsson, E. Lundström, L. Bergström, and J. Edsjö, *Significant Gamma Lines from Inert Higgs Dark Matter*, Phys. Rev. Lett. **99** (2007) 041301. `http://link.aps.org/doi/10.1103/PhysRevLett.99.041301`.

[221] Y. Mambrini, *A Clear Dark Matter gamma ray line generated by the Green-Schwarz mechanism*, JCAP **0912** (2009) 005, `arXiv:0907.2918 [hep-ph]`.

[222] J. Hisano, S. Matsumoto, and M. M. Nojiri, *Unitarity and higher order corrections in neutralino dark matter annihilation into two photons*, Phys. Rev. **D67** (2003) 075014, `arXiv:hep-ph/0212022 [hep-ph]`.

[223] L. Bergstrom, T. Bringmann, and J. Edsjo, *Complementarity of direct dark matter detection and indirect detection through gamma-rays*, Phys. Rev. **D83** (2011) 045024, `arXiv:1011.4514 [hep-ph]`.

[224] V. Springel, S. D. M. White, C. S. Frenk, J. F. Navarro, A. Jenkins, M. Vogelsberger, J. Wang, A. Ludlow, and A. Helmi, *A blueprint for detecting supersymmetric dark matter in the Galactic halo*, `arXiv:0809.0894 [astro-ph]`.

[225] M. Kuhlen, J. Diemand, and P. Madau, *The Dark Matter Annihilation Signal from Galactic Substructure: Predictions for GLAST*, Astrophys. J. **686** (2008) 262, `arXiv:0805.4416 [astro-ph]`.

[226] J. Diemand, M. Kuhlen, and P. Madau, *Dark matter substructure and gamma-ray annihilation in the Milky Way halo*, Astrophys. J. **657** (2007) 262–270, `arXiv:astro-ph/0611370 [astro-ph]`.

[227] J. Butterworth, E. Dobson, U. Klein, B. Mellado Garcia, T. Nunnemann, J. Qian, D. Rebuzzi, and R. Tanaka, "Single boson and diboson production cross sections in pp collisions at $\sqrt{s}$=7 tev." ATL-PHYS-INT-2011-078, Aug, 2011.

[228] ATLAS Top Group, *2012 Top Cross Sections*, Tech. Rep. Link: `https://twiki.cern.ch/twiki/bin/viewauth/AtlasProtected/TopCommonParametersMC12`, Revision 12, August, 2013.